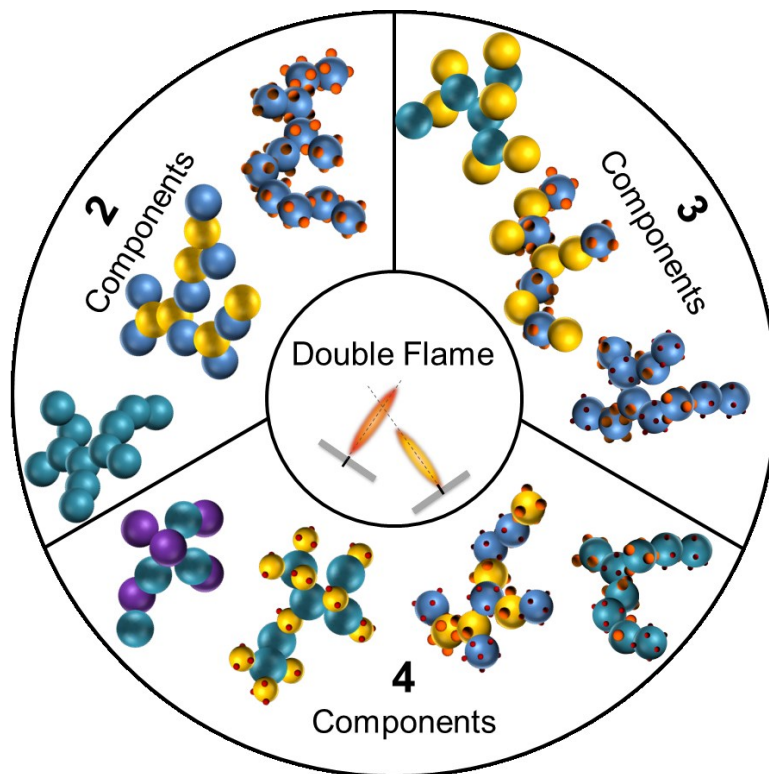

Tailored aerosol synthesis of nanosized multicomponent catalysts



Vom Fachbereich Produktionstechnik der UNIVERSITÄT BREMEN

zur Erlangung des Grades Doktor-Ingenieur genehmigte

Dissertation

von Dipl.-Ing. Henrike Großmann

1. Gutachter: Prof. Dr.-Ing. habil. Lutz Mädler (Universität Bremen)
2. Gutachter: Prof. Dr. Anker D. Jensen (DTU - Technical University of Denmark)

Tag der mündlichen Prüfung: 29. Januar 2018

Zusammenfassung

Der Einsatz von nanopartikulären Multikomponentensystemen spielt eine Schlüsselrolle in der Entwicklung neuartiger Materialien. Diese Materialien sind essentiell um z.B. als heterogene Katalysatoren die wirtschaftliche Implementierung ungenutzter und bisher unwirtschaftlicher Energiewandlungsprozesse zu ermöglichen.

Die Idee ist dabei, mehrere Komponenten zu kombinieren und so nicht nur die Summe der einzelnen Eigenschaften der Materialien zu erhalten, sondern zusätzlich neue Materialeigenschaften zu generieren. Die vorliegende Arbeit beinhaltet eine detaillierte Zusammenstellung der theoretischen Grundlagen und eine Diskussion zu Anwendungsbeispielen, Synthesemethoden und Charakterisierungsgrundlagen von Multikomponenten-Partikelsystemen.

Die Flammen-Sprüh-Pyrolyse (FSP) ist eine Synthesemethode zur Herstellung von Metalloxidkatalysatoren im Nanometerbereich. Sie wird als ein aerosolbasierter Hochtemperatur-Prozess im Detail vorgestellt. FSP synthetisiert, basierend auf der Gas zu Partikel Umwandlung, Oxide nahezu aller Metalle und Übergangsmetalle [1, 2]. Beschränkungen gibt es jedoch u.a. bei der gezielten Positionierung einer katalytisch aktiven Komponente auf einem Trägermaterial. Die in der Arbeit genutzte Doppel-Flammensprühpyrolyse (DFSP) ist eine Erweiterung der üblicherweise verwendeten Einzelflammensprühpyrolyse. Sie stellt eine vielversprechende neuartige Herstellungsmethode für Multikomponentensysteme dar. Die Partikel werden hier in zwei gegenüberliegenden Flammen synthetisiert. Im Gegensatz zur Einzelflamme können in der Doppelflamme, durch gezielte Wahl der geometrischen Parameter, die einzelnen Partikeltypen während der Synthese kontrolliert in Interaktion gebracht und somit die Eigenschaften des neuen Multikomponenten-Materials gezielt gesteuert werden.

Zwei Beispiele zeigen die sehr hohe Flexibilität der Doppelflammensynthese auf. Kapitel 4.2 beschreibt den Syntheseprozess für einen binären Fischer-Tropsch (FT) Katalysator, der aus stabil geträgertem Kobaltoxid (CoO_x) und einem Aluminiumoxid Träger (Al_2O_3) besteht. Die Doppelflamme ermöglicht, bei geeigneter Einstellung der Syntheseparameter zum einen die erfolgreiche Unterdrückung von inaktivem Kobalt-Aluminium-Spinell und zum anderen eine hohe Sinterstabilität des geträgerten Kobaltoxids. Mittels einer experimentellen Studie werden die optimalen geometrischen Prozessparameter für die Synthese von hoch aktiven Fischer-Tropsch Katalysatoren im Doppelflammprozess bestimmt.

Kapitel 4.4 beschreibt das zweite Synthesebeispiel, einen ternärer Katalysator für die präferenzielle Oxidation von Kohlenstoffmonoxid (CO-PrOx). Der untersuchte CO-PrOx Katalysator besteht aus Cer (CeO_2) und Eisenoxidpartikeln (FeO_x), die auf Partikelebene miteinander vermischt werden. Der Doppelflammen-Prozess ermöglicht hier zum einen die Unterdrückung von unerwünschtem Eisendoping in den Cerpartikeln und zum anderen die gezielte und exklusive Aufbringung von metallischem Platin (Pt) auf der Eisenkomponente. Im einstufigen Doppelflammenprozess besteht die Möglichkeit, das Design des Katalysators gezielt einzustellen und somit neuartige Modellkatalysatoren reproduzierbar zu synthetisieren. Dies hilft wiederum um ein besseres Verständnis der CO-PrO_x Mechanismen bei FeO_x -basierten Katalysator zu erhalten.

Die Schwierigkeit bezüglich des gezielten Designs von Multikomponenten-Katalysatoren liegt im Wissen über die Steuerung des vorherrschenden Temperaturprofils im Syntheseprozess. Das erforderliche Profil ist dabei stark abhängig von den zu synthetisierenden Materialien und der angestrebten Produktcharakteristik. Kapitel 5.1 beschreibt erstmalig den Einfluss der Interaktionsdistanz auf das resultierende Temperaturprofil im Doppelflammenprozess. Falls die Interaktion der Flammen bei kleinen Distanzen stattfindet (Bereiche in denen sich der Precursor noch in der Gasphase befindet), ergibt sich eine Mischung der Komponenten auf atomarer Ebene. Die Ausbildung eines Mischkristalls, ähnlich wie bei der Einzelflammensynthese, kann dann das Ergebnis sein. Falls das Temperaturprofil und somit das Reaktionsprofil im Interaktionsbereich es zulässt, kann es auch zu einer partiellen Sinterung von Partikeln untereinander oder zu oberflächenbeschichteten Trägerpartikeln kommen. Bei größeren Interaktionsdistanzen bilden sich individuelle Oxidpartikel der einzelnen Materialien aus, die auf Partikelebene gut vermischt sind. Weiterhin wird auf Basis zweier unterschiedlichen Materialsysteme eine Platin- (Pt) bzw. Wolframoxid- (WO_3) und jeweils eine Titanoxidpartikel (TiO_2) produzierende Flamme, der Einfluss des Interaktionswinkels auf die individuellen Partikeleigenschaften und die Vermischungscharakteristik der Partikelströme untersucht (Kapitel 5.2 und 5.3). Es werden universelle Richtlinien für die Flammenausrichtung im Doppelflammenprozess festgelegt und erstmalig detaillierte Erkenntnisse zum Mischprozess des Verfahrens präsentiert.

Eng verbunden mit der Synthese von Mehrkomponenten-Nanomaterialien ist die Bestimmung des Mischungsgrades der unterschiedlichen Komponenten. Diese ist auf Nanoebene sehr schwierig, da viele der bekannten Charakterisierungsmethoden auf dieser Größenskala nur begrenzt anwendbar sind. Diese Arbeit führt daher zwei neue Verfahren zur quantitativen Bestimmung des Mischungsgrades in geträgerten (z.B.

aktive Komponente auf Träger) und aggregierten Partikelsystemen (z.B. Mischung zweier partikulärer Halbleiter) ein und validiert diese.

Die vorliegende Arbeit unterbreitet weiterhin eine umfassende Darstellung der unterschiedlichen Prozessparameter im Doppelflammenprozess und belegt dies mit Beispielen aus dem Bereich der heterogenen Katalyse.

Summary

Nanoparticles consisting of multiple components play a key role in the development of new materials. They can be applied e.g. as heterogeneous catalysts in novel types of energy conversion processes. The idea of such systems is the combination of different components which results not only in the addition of their individual properties, but furthermore generates novel ones. The thesis presents a detailed overview on the theoretical basis of such multicomponent particle systems and discusses catalytic applications, synthesis methods as well as the essentials for the characterization of these kinds of particle systems.

Flame Spray Pyrolysis (FSP) is a well investigated high temperature aerosol technique for synthesizing nanosized metal oxide catalysts from almost all metals and transition metals by gas-to-particle conversion [1, 2]. However, specific designs of multicomponent catalysts and a controlled dispersion of catalytically active material on supports are limited in this one-step approach. Thus, this thesis investigates the adjustment of two single flames in a so-called double flame set up and reveals that this process has the potential for a specific design and controlled particle dispersion. The individual metal oxide precursors reacting in two opposing spray flames and the intersection of the flames is adjusted to a well-defined temperature range. The proper setting of the geometric process parameters allows tailoring the characteristic of the synthesized multicomponent material. If the flames intersect at small distances where both precursors are still in vapor phase, a mixture of oxides on atomic scale and the formation of mixed metal oxides are possible. Tailoring the flame geometries, e.g. increase the intersection distance, results in the formation of individual oxide particles which are mixed on particle scale. A further increase in intersection distance result in the formation of particle clusters up to a mixture on agglomerate scale.

Two examples, a binary Fischer-Tropsch (FT) catalyst and a ternary catalyst for the preferential oxidation of CO (CO-PrOx) demonstrate the flexibility of the double flame synthesis for the production of tailored multicomponent catalysts. In chapter 4.2, the double flame approach is used to deposit cobalt (Co) on an alumina (Al_2O_3) support, which reduces the formation of an undesired atomic mixture with varying flame parameters. An experimental study determines the optimal geometric process parameters of the two flames for the synthesis of highly active Fischer-Tropsch catalysts. The double flame approach provides the synthesis conditions for a mixture on particle scale within the high temperature environment. This enables a stable material interphase

between the Al_2O_3 support and the CoO_x phase and results in a high sinter stability of the catalytic material. The sinter stability is an essential requirement to face harsh reaction conditions during the Fischer-Tropsch process. Chapter 4.4 presents investigations regarding the CO-PrOx activity of a ternary catalyst system, containing the reducible supports ceria (CeO_2) and iron oxide (FeO_x) and the catalytic active component platinum (Pt). To achieve the desired high activities at low reaction temperatures, a mixture of CeO_2 and FeO_x on particle scale is aspired. The intimate crystalline interface between the CeO_2 and FeO_x particles enables in this connection the required oxygen mobility between the two components. The application of the double flame process further enables the exclusive deposition of metallic platinum (Pt) particles on the iron oxide (FeO_x) component. So far, little is known on the details of the reaction mechanism hindering a specific design of the catalyst and therefore, an essential increase in activity and selectivity. The tailored synthesis of catalysts with different particle characteristics helps to understand the interplay between the different support components CeO_2 and FeO_x and to gain a deeper understanding of the CO-PrOx mechanisms.

The thesis investigates besides the synthesis of the two specific catalyst systems the underlying process conditions during the synthesis. The temperature profile of the intersecting flames is one of the key parameters in the DF process which significantly influences the final material composition. Chapter 5.1 includes a detailed study and description of the temperature profile during the double flame synthesis process and discusses the influence of the interaction distance on the temperature profile for the first time in detail. Closely linked with the synthesis of multicomponent nanomaterials is the determination of the degree of mixing between the different components and the uniformity of the mixing state throughout the synthesized sample. A quantitative characterization becomes complex since easy accessible characterization methods are rarely applicable on nanoscale. Two novel image based methods for the determination of the degree of mixing in deposited systems (e.g. active component on support) and aggregated systems (e.g. two types of support) are developed. Their application helps to quantify the influence of the geometric configuration of the flames on the degree of mixing and the uniformity of the sample. Chapter 5.2 present the results of the intersection of a platinum (Pt) and a titania (TiO_2) flame (deposited system) and 5.3 of a tungsten-oxide (WO_3) and a titania (TiO_2) flame (aggregated system). Universal guidelines for an ideal process adjustment are established and insights into the mixing process are presented.

Table of content

Zusammenfassung	I
Summary	IV
Table of content	VI
Table of abbreviations.....	VIII
Table of symbols.....	IX
Glossary	X
Preface	XIV
1 Introduction.....	1
2 Multicomponent nanoparticles applied as heterogeneous catalysts	6
2.1 Requirements of nanoparticulate multicomponent catalysts.....	7
2.2 Design and application of nanoparticulate multicomponent catalysts	13
2.2.1 Mixing states within a primary particle.....	16
2.2.2 Mixing state within a particle collective.....	18
2.3 Characterization techniques for multicomponent catalysts.....	21
2.3.1 X-ray powder diffraction	21
2.3.2 Adsorption based methods to determine particle sizes	22
2.3.3 Electron microscopy.....	24
2.3.4 Temperature-Programmed Reduction.....	26
2.4 Degree of mixing in multicomponent particle systems.....	27
2.4.1 Approaches to determine the uniformity of a particulate mixture	27
2.4.2 Parameter to quantify the uniformity of a particulate mixture	28
3 Synthesis techniques for multicomponent nanoparticles	32
3.1 Bottom up synthesis methods	33
3.1.1 Liquid-phase techniques	35
3.1.2 Gas-phase techniques	36
3.1.3 Surface deposition methods.....	39
3.2 Flame spray pyrolysis	40
3.2.1 Particle formation process	41
3.2.2 Temperature profile and synthesis parameters	48
3.2.3 Synthesis of multicomponent particles	50
3.3 Double flame spray pyrolysis	52
4 Synthesis of multicomponent catalysts using the double flame	56
4.1 Fundamentals of the Fischer-Tropsch-synthesis	56
4.1.1 Fischer-Tropsch-catalysts.....	58
4.1.2 Flame made Fischer-Tropsch-catalysts	58
4.2 Flame synthesis of a supported catalysts for the Fischer-Tropsch reaction	59
4.2.1 Synthesis and characterization of binary Al ₂ O ₃ / Co catalysts	60
4.2.2 Sinter stability and catalytic performance in the FT reaction.....	69
4.2.3 Conclusion	71
4.3 Catalysts for the preferential oxidation of carbon monoxide	73

4.3.1	CO-PrOx- catalysts	74
4.3.2	Flame made CO-PrOx- catalysts.....	75
4.4	Flame synthesis of ternary catalysts for CO-PrOx.....	75
4.4.1	Synthesis and characterization of ternary Fe+Pt / Ce catalysts	77
4.4.2	Catalytic performance in the PrOx- reaction.....	82
4.4.3	Conclusion	83
4.5	Evaluation of the DF set-up for the synthesis of multicomponent catalysts.....	85
5	Characterization of the mixing process during the DF synthesis of heterostructured nanoparticles	86
5.1	Temperature profile and mixing characteristic in the DF process	88
5.2	Analysis of the DF mixing process in a deposited system	95
5.3	Analysis of the DF mixing process in an aggregated system.....	106
5.4	Conclusions	112
6	Scope and potential of the double flame system	114
	Bibliography	X
	Danksagung	XXIV
	Studentische Arbeiten	XXVI
	Erklärung	XXVII
	Appendix	i
I.	Experimental procedures	i
I.I.	Experimental procedures for chapter 4.2 reprinted from ref. [4].....	i
I.II.	Experimental procedures for chapter 4.4 reprinted from ref. [5].....	iv
I.III.	Experimental procedures for chapter 5.1 partly reprinted from ref. [3]	vi
II.	Additional material chapter 5.2:	xi
III.	Additional material chapter 6:.....	xii

Table of abbreviations

AAS	Atomic absorption spectroscopy
ADF	Annular dark-field imaging
AFM	Atomic force microscopy
AFS	Aerosol flame synthesis
ALD	Atomic layer deposition
APM	Aerosol particle mass
BET	Brunauer, Emmet, and Teller
BTL	Biomass to liquid
CFD	Computational fluid dynamics
CO-PrOx	Preferential oxidation of carbon monoxide
CS	Critical supersaturation level
CTL	Coal to liquid
CTY	Cobalt-time yield
CVD	Chemical vapor deposition
DF	Double flame
DFSP	Double flame spray pyrolysis
DMA	Differential mobility analyzer
EDC	Eddy dissipation concept
EELS	Electron energy loss spectroscopy
EFTEM	energy-filtered transmission electron microscope
FASP	Flame- assisted spray pyrolysis
FID	Flame ionization detector
FSP	Flame spray pyrolysis
FT	Fischer Tropsch
FTIR	Fourier-transform infrared
GTL	Gas to liquid
HAADF	High-angle annular dark-field
IPC	Inductively coupled plasma
IWI	Incipient wetness impregnation
LAFS	Liquid-fed aerosol flame synthesis
MMC	Metal matrix composite
PEMFC	Polymer electrolyte membrane fuel cell
PVD	Physical vapor deposition
SAED	Selected-area electron diffraction
SEM	Scanning electron microscope
SF	Single flame
SSA	Specific surface area
STEM	Scanning transmission electron microscope
TCD	Thermal conductivity detector
TEM	Transmission electron microscope
TPR	Temperature programmed reduction
UV-Vis	Ultraviolet- visible diffuse reflectance
VAFS	Vapor-fed aerosol flame synthesis
WGS	Water-gas-shift

XPS	X-ray photoelectron spectroscopy
XRD	X-ray diffraction

Table of symbols

d_X	m	Particle diameter of component X
d_Y	m	Particle diameter of component Y
N_s	-	Number of taken samples
D_f	-	Fractal dimension
D_{fm}	-	Mass-mobility exponent
d_m	m	Mobility diameter
d_{mean}	m	Geometric mean
i	-	Value of the measured component
l_D	m	Inner diameter
k_f	-	Fractal prefactor
k_m	-	Constant prefactor
N_p	-	Number of primary particles
r	m	Radius
R	$J mol^{-1} K^{-1}$	Universal gas constant
r_c	m	Critical nucleus size
R_g	m	Gyration radius of the aggregate
s	-	Standard deviation
S	-	Saturation ratio
s^2	-	Empirical variance
T	$^{\circ}C$	Temperature
V_m	$m^3 mol^{-1}$	Molar volume
x	-	Expectancy
α_0	-	Level of significance
γ	Nm^{-1}	Surface tension
ΔG	Nm^{-1}	Cluster free energy
λ	m	Wavelengths
σ^2	-	Variance
σ_g	-	Geometric standard deviation

Glossary

Compilation of used terms and their definition within the thesis

agglomerate	An agglomerate contains at least two aggregates which are physically bonded.
aggregate	An aggregate consists of several chemically bonded (sintered) primary particles.
aggregated system	An aggregated system describes a mixture of different types of primary particles (X and Y) within an aggregate which have a ratio between the particle diameters of $d_X/d_Y > 0.5$ (with $d_X \leq d_Y$).
center axis	The center axis is the vertical axis in the double flame set up, passing through the intersection point of the flames.
core-shell particles	Basis for this structure is a primary particle, which consists of at least two components, that forms two different crystal/ amorphous phases. In this structure, one phase covers the surface of a particle containing the second phase. Core shell particle are a special type of polycrystalline particles.
degree of mixing	The degree of mixing is an indicator how many hetero contacts between the different components are present in a particle aggregate. By definition, the degree of mixing is the highest when the maximum number of possible hetero-contacts is present for all primary particles within an aggregate. Both in a deposited and in an aggregated system, this is the case for a mixture on particle scale. The degree of mixing is the highest for mixtures on particle scale > cluster scale > agglomerate scale.
deposited systems	A deposited system describes a mixture of two different types of primary particles (X and Y) which have a ratio between the particle diameters of $d_X/d_Y \leq 0.5$ (with $d_X < d_Y$). The component X is called deposit while component Y is the support.
doped crystal structure	Basis for this structure is a primary particle, with a crystal structures (M-AO _X) where the host component (AO _X) keeps its

crystal structure and the second component, the dopant (M), migrates in this so called “host structure” without a change of its crystal structure.

flame axis	The flame axis connects the particular centers of the nozzles with the geometric intersection point of the two flames and varies with the intersection angle.
hetero contact	A hetero contact describes the interphase between two different types of primary particles. This interphase (hetero contact) is required to take advantage of the properties of both components including the special properties of the interphase.
heterojunction	A heterojunction describes the chemical formed interface between two different crystalline semiconductor particles, where the difference in the position of the particular conduction and valance bands results in a transfer of the photo excited electrons and holes.
homo contact	A homo contact describes the chemical formed interphase between two particles that are of the same type of primary particle.
intersection distance	The intersection distances is the shortest distance from the center of the nozzle to the geometric intersection point of the two flames and is adjusted by the distance between the two nozzles and the intersection angle.
intersection point	The two flame axes and the vertical axis geometrically intersect in the intersection point.
mixed metal oxide particles	A mixed metal oxide contains cations of more than one element (A and B) that have a covalent binding with oxygen. Basis for this structure is a primary particle, with a crystal structure e.g. of the form ABO_x .
mixing process	The mixing process describes the interaction of the two flame jets. The status of the mixing process gives insight on the probability distribution of the components within the reaction zone. The

	<p>mixing process is in progress as long as one component's probability of presence changes with the position in the reaction zone. The mixing process is completed, when both components have the same probability of presence within the whole reaction zone.</p>
mixing state	<p>A mixing state describes the distribution of different chemical components within a primary particle or a particle collective.</p>
mixture on agglomerate scale	<p>This mixture describes agglomerates which consists of at least two different types of aggregates. A single aggregate always contains the same type of primary particle.</p>
mixture on atomic scale	<p>This mixture describes a primary particle which consists of at least two components that are mixed on atomic length scale, meaning they form either a mixed metal oxide or a doped crystal structure.</p>
mixture on inner particulate scale	<p>This mixture describes a primary particle which consists of at least two components that have two different (crystalline or amorphous) phases.</p>
mixture on particle cluster scale	<p>This mixture describes an aggregate which consists of at least two different types of particle clusters. A single particle cluster always contains primary particles of the same type.</p>
mixture on particle scale	<p>This mixture describes an aggregate which consists of at least two different types of primary particle.</p>
particle cluster size	<p>The particle cluster size is the number of primary particles within an aggregate which have the same type and are connected with each other via a homo contact.</p>
particle cluster	<p>A particle cluster includes all particles which are of the same type of primary particle and are connected with each other via a homo contacts.</p>
particle collective	<p>A particle collective describes the accumulation of at least two different types of primary particles in form of an aggregate or agglomerate.</p>

particle type	A particle type describes the characteristic of a primary particle. A primary particle can consist either of a single oxide component or multiple components. A primary particle with multiple components can exhibit two different mixing states (mixture on atomic scale or mixture on inner particulate scale).
polycrystalline particles	Basis for this structure is a primary particle which consists of at least two components with different phases. In a polycrystalline structure are the two different phases of disordered nature.
primary particle	A primary particle is a single particle within an aggregate. The primary particles can be of different types (see particle type).
reaction zone	In the flame spray pyrolysis (FSP) process is the reaction zone for the particle synthesis equivalent with the flame zone.
uniformity of a mixture	Whereas the degree of mixing describes the mixing state within an aggregate, comprised the uniformity of the mixture all (deposited) aggregates within a sample. A sample is defined as uniform in cases where only one mixing state is present on aggregate scale throughout the whole sample.

Preface

This dissertation describes the results obtained during my time as PhD-student from November 2011 until December 2015 at the University of Bremen under the supervision of Prof. Dr.-Ing. habil. Lutz Mädler.

The thesis contains only my own research, if not explicitly stated otherwise.

Single chapters of this thesis have been peer-reviewed and published as followed:

Chapter 5:

The data and results have been published in the peer-reviewed Journal "Journal of Nanoparticle Research". The content is original research from H.K. Grossmann and part of the thesis.

[3] Grossmann, H. K., Grieb, T., Meierhofer, F., Hodapp, M. J., Noriler, D., Gröhn, A., Meier, H. F., Fritsching, U., Wegner, K. and Mädler, L. (2015). "Nanoscale mixing during double-flame spray synthesis of heterostructured nanoparticles." *Journal of Nanoparticle Research* 17(4): 1-16.

H. K. Grossmann is the responsible author of the overall manuscript. She carried out the experimental work including temperature diagnostics, particle synthesis and characterisation and mixing characterization. A. Gröhn at ETH Zürich has supported the Fourier transform infrared spectroscopy (FTIR) measurements and F. Meierhofer the thermocouple measurements. M. J. Hodapp and D. Noriler conducted all CFD simulations. Particle analysis using (S)TEM was supported by T. Grieb.

Chapter 4.2:

[4] Grossmann, H. K., Minnermann, M., Pokhrel, S., Thiel, K., Hagelin-Weaver, H., Bäumer, M. and Mädler, L. (2013). "Double flame spray pyrolysis as a novel technique to synthesize alumina-supported cobalt Fischer–Tropsch catalysts." *Catalysis Today* 214: 90-99

H. K. Grossmann carried out the particle synthesis and the particle characterization (BET, XRD and UV-Vis). M. Minnermann conducted the STEM/ EDX, the TPR and the catalytic measurements. H. K. Grossmann and M. Minnermann are equally sharing the responsibility for the overall manuscript.

Chapter 4.4:

[5] Dreyer, J. A. H., Grossmann, H. K., Chen, J., Grieb, T., Gong, B. B., Sit, P. H. L., Mädler, L. and Teoh, W. Y. (2015). "Preferential oxidation of carbon monoxide over Pt–FeO_x/CeO₂ synthesized by two-nozzle flame spray pyrolysis." *Journal of Catalysis* 329: 248-261.

H. K. Grossmann carried out the particle synthesis and supported the particle characterization (BET, XRD and TEM) and the discussion regarding the structural properties of the catalysts. J. A. H Dreyer conducted all the TPR and catalytic measurements and is the responsible author of the overall manuscript.

The figures within all three chapters have been published as presented and only minor adaptations are carried out to keep the overall flow of the thesis. The experimental procedures of the three chapters are directly adopted from the publications and reprinted in the attachment.

1 Introduction

One of the main challenges of the 21st century is the phasing out of our nuclear and fossil fuel based energy supply. This departure is motivated in the limited availability of crude oil, but it covers also issues such as energy wars, climate change and the obligation towards future generations to economize farseeing with existing energy resources. For realizing this turnaround, the sustainable implementation of renewables is essential. So far, 80.9% of the energy supply is based on fossil fuels and nuclear power. The overall percentage of renewables is only 19.1%, including 9% of traditional biomass, used primarily for cooking and heating. However, the use of modern renewables is continuously increasing in the resent years. The resources for the energy generation are quite diversified in their actual resources; covering water, wind, biofuels and solar energy (see Figure 1). This diversity of the renewable is essential to implement a stable and forward-looking energy supply which considers the local availability of resources. This diversity also avoids the dependence on certain selected resources that is often accompanied with political conflicts. The technologies for the energy generation from renewables are divers in exactly the same way as the renewable resources itself. While the wind and water based energy supply requires mechanical solutions; the enhancements of biofuels and photocatalytic application are depended on the development of new (photo-) catalytic active materials.

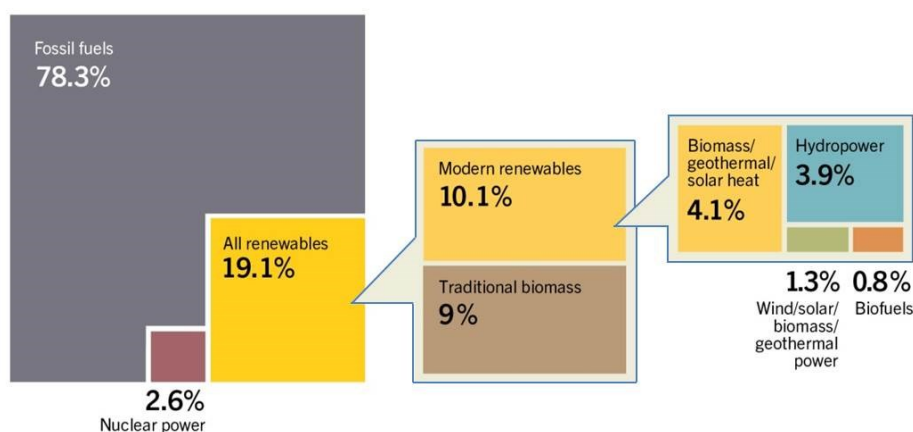


Figure 1: Estimated Renewable Energy Share of Global Final Energy Consumption, 2013 [6].

For the implementation of new technologies, the availability of existing infrastructure has to be considered. A huge part of our resent energy supply, especially in the field of transportation and heating is oil or gas based. The usage of nonpetroleum based alternative biofuels is a way of taking use of the existing infrastructure. The synthesis of fuels from renewable recourses is a solution which adjusts well to the fuel based system

and is therefore, subject of current research [7-9]. One way for the synthesis of fuels from renewable resources is the Fischer-Tropsch (FT) reaction, where syngas (CO and H₂) react under certain reaction conditions to ordered energy rich hydrocarbon chains [10-12]. In the past, this synthesis route was mostly used for the coal liquefaction [13-15]. The utilization of biomass as CO and H₂ resource for the required syngas, converts the Fischer-Tropsch reaction to a potential solution in this field. The drawback of this approach is, however, that it is directly competitive with food production, since biomass is involved. The production of sustainable syngas (H₂ and CO) based on H₂O and CO₂ using photocatalyst, offers a production route that offers the potential to overcome this drawback. Here, H₂O is separated in H₂ and O₂ [16-18] using a photo catalyst and solar light. Exhausted CO₂ gas can further be photocatalytically reduced to CO or methanol [19-22].

Other renewable approaches, next to gas and fuel based Fischer-Tropsch reactions, are hydrogen based transportation scenarios. One example in this field is the Polymer Electrolyte Membrane Fuel Cell (PEMFC) technology [23, 24], where the chemical energy of hydrogen fuel is directly transformed into electrical energy with high efficiency and low emission of pollutants. Here, the challenge of a particular clean production of H₂ plays a decisive role. To cover this issue, the technology is associated with a complex gas pre-treatment, to secure stable process condition. One important gas pre-treatment technology is the preferential oxidation of carbon monoxide (CO-PrOx). This technology helps to reduce the amount of poisoning CO residues in the H₂ fuel and provides stable process conditions in the fuel cell.

The Fischer-Tropsch reaction, the photocatalytic water or CO₂ splitting approach, and the preferential oxidation of CO (CO-PrOx) are promising building blocks for a future renewable energy supply. Most technologies are, however, still on the research stage and not fully industrial implemented. Next to extensive process innovation, all approaches need further fundamental knowledge on the involved reaction mechanisms. The bottleneck for the implementation of a competitive energy supply based on these technologies is the development of novel high-performance catalysts. These tailored catalysts are the key for achieving a cost and energy competitive production compared to a fossil fuel based feedstock. Catalysts are the core of the reaction, since they accelerate the rate of reaction by interacting with the reactants. As presented in Figure 2a, a catalyst enables scenarios, where significantly less energy is required to perform the reaction, compared to a scenario without catalyst. The application of a catalyst results, thus, in much faster reaction rates and a significant increase in efficiency. In

addition, the application of a catalyst reduces the required reaction temperature and applied pressure during the reaction since the required activation energy decreases. By definition, the catalyst is not consumed during the reaction and does not influence the thermodynamic equilibrium of the reactants and products [25]. The ideal catalyst for the particular reaction is further highly selective. This means, it favors the formation of the desired product and suppresses undesirable side products [26].

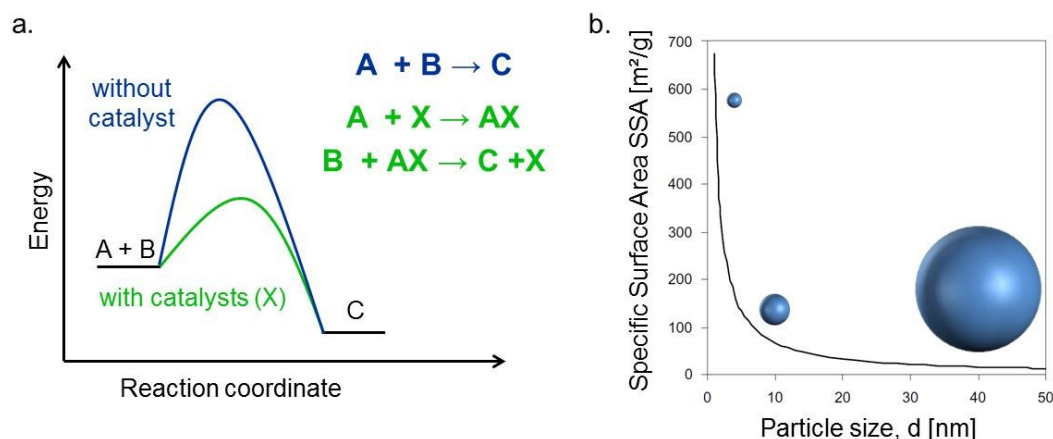


Figure 2: a. Schematic representation how a catalyst influences the reaction path cf. [26] and b. Specific surface area as a function of particle size (for nickel particles with a density of $\rho=8900 \text{ kg/m}^3$) cf. [27].

Today, catalysts play a crucial role in 90% of all commercially produced chemical products and are the key for emissions control e.g. in automotive. Most of the applied catalysts are heterogeneous catalyst. The main advantage of using a heterogeneous catalyst is that, being a solid material, it is easy to separate from the gas and/or liquid reactants and products of the overall catalytic reaction [28]. Since the reaction in such a heterogeneous system takes place at the surface of a solid, the surface to volume ratio of the applied catalyst is essential. The surface to volume ratio is particularly high for nanoparticles compared to that of traditional bulk and micrometer-sized ones. For particles with a diameter of 30 nm, 10 % of the atoms are placed on the surface and are available as active sites. For particle with a 3 nm diameter, already 50 % of the atoms are placed on the surface and can actively take part at the reaction. Figure 2b illustrates the significant increase of specific surface area with decreasing particle size. This allows to build the reactors smaller and to reduce investment costs for large equipment. In addition, this fact reduces the number of "unused atoms" inside the particles. The latter one is especially important when expensive catalyst materials, such as the precious metals (platinum or rhodium) are used.

Nanoparticles further gained great scientific attention in the recent years as they build a bridge between the properties of bulk materials and atomic or molecular structures. Whereas the physical properties of bulk materials are not significantly influenced due to variations in the size, nanoparticles possess size dependent properties. In the nano regime quantum effects play a dominating role leading to unique mechanical, electrical, magnetic, optical and chemical properties of the particles [29].

Nanomaterials are further expected to possess many improved properties over those of bulk and micrometer-sized ones, due to different effects in terms of volume, quantum size, surface defects, and macroscopic quantum tunnel [29, 30]. Since a catalyst particle in the nano range contains only of a few atoms, this catalysts can be assigned in the border area between molecular (homogeneous) and solid-state (heterogeneous) catalysts [26]. Nanoparticulate catalysts offer due to their special properties the potential to have a high selectivity, an extremely high activity, low energy consumption and a long lifetime. To realize this potential, a precisely adjustment of the size, shape, spatial distribution, surface composition and electronic structure is required. In addition, the thermal and chemical long-term stability of the individual components must be ensured. All these features are also of high importance when the particles are applied not as catalyst but as advanced energetic, electronic, photonic, magnetic and biomedical materials [31] and are, therefore, of high importance.

All the heterogeneous catalysts, which are applied in the above described approaches e.g. the Fischer-Tropsch (FT) reaction, are typically highly complex multicomponent materials, where each of the materials plays a certain role in the chemical conversion process, for example, as active component, support, or oxygen storage component [16, 32]. Although surface science studies in the recent years have contributed significant progress on the fundamental understanding of catalysis, most of the applied commercial catalysts are still produced by "mixing, shaking and baking" of several components [33]. The specific design of nanoscale structures is hard to control and synthesis-structure-performance relationships are not fully understood. A further considerable issue regarding nanomaterials is the limited possibility to characterize these structures. Because of its complex physico-chemical properties and the considerably small size in the nanometer scale, the characterization of these catalysts is highly challenging. The detailed characterization is, however, indispensable to develop and enhance production processes which allow a tailored design of catalyst.

Flame Spray Pyrolysis (FSP) is, for example, a suitable method for the production of nanosized metal oxide catalysts. It is a high temperature aerosol technique and is suitable for the synthesis of metal oxide catalysts from almost all metals and transition metals [1]. The extension of the normal Flame Spray Pyrolysis to the Double Flame (DF) approach allows the specific designs of multicomponent catalysts and the controlled dispersion of catalytic material on a support. In this case, the combustion of two different metal oxide precursors takes place in two individual flames which are aligned so that they intersect at a defined temperature range. The temperature profile of these intersecting flames is the key parameter when designing the final multicomponent catalyst. A variety of different catalyst formations is realizable ranging from a mixture of oxides on the atomic scale to the formation of surface deposited particles. Additionally, the modification of properties such as particle size, shape, and specific surface area is possible for each component individually by adjusting the flames separately. Currently few other synthesis routes can offer this flexibility in multicomponent catalysts design, which makes the Double Flame Spray Pyrolysis (DFSP) to an attractive approach. DF synthesized catalyst can, thus, contribute in the decoding of structure-reactivity relationships due to the possibility of a tailored catalyst design. In addition, flame synthesized catalyst have enormous potential to show an increased efficiency compared to commercial catalysts. Therefore, this thesis investigates the fundamentals of the DF process and for the first time identifies guidelines for ideal process adjustments based on the intensive study of different material systems.

2 Multicomponent nanoparticles applied as heterogeneous catalysts

Since the end of the 1990s, and with the development of nanoscience, nanocatalysis has clearly emerged as a domain at the interface between homogeneous and heterogeneous catalysis which offers unique solutions to answer the demanding need for catalyst improvement [33]. Nanocatalysts offer special properties due to its nanodimension as discussed e.g. in the review of Wang et al.:

- “surface and interface effect (unusual properties of extremely small crystals that arise from the damage of a boundary between a material and its surrounding environment)
- small size effect (novel properties of extremely small crystals that arise from the decrease of the atom's density of amorphous nanoparticles near the surface layer)
- quantum size effect (unusual properties of extremely small crystals that arise from confinement of electrons to small regions of space in one, two, or three dimensions)
- macroscopic quantum tunnel effect (when the total energy is less than the barrier height, extremely small crystals can still pass through the barrier) [34]”.

Since the heart of a heterogeneous catalyst involves the active sites at the surface of the solid, an appropriate catalyst design includes a support. This support helps to maximize the surface area and stabilizes the catalyst material against sintering. The combination of a catalytic material and a support system describes, therefore, one of the most common multicomponent systems in catalysis. The application of a support increases not only the surface area of the catalyst; it can further influence the reaction pathway to a great extent [35]. The interface between the two components plays a critical role in catalysis, since interfacial phenomena, such as strong metal–support interactions (SMSI) are present. This SMSIs favor e.g. the chemisorption properties of group VIII metals at elevated temperatures when supported on reducible oxides [36]. So the development of multi component structures is motivated by the fact that resulting structures will combine the single properties and may give rise to novel collective properties [37].

Chapter 2.1 describes the required properties of nanoparticulate multicomponent catalysts in more detail. Chapter 2.2 gives an insight in the description of different types of multicomponent arrangements and highlights applications of the different catalyst designs. Chapter 2.3 presents the applied characterization techniques for the later

investigated multi component particles and chapter 2.4 summarizes the approaches for the characterization of the degree of mixing in multicomponent catalyst systems.

2.1 Requirements of nanoparticulate multicomponent catalysts

The general criteria to characterize heterogeneous catalysts are their activity and selectivity, the thermal and mechanical properties, their stability, morphology and its costs. The activity of a catalyst is the property of the catalyst to form the desired product under certain reaction conditions (temperature, pressure etc.). Conversion is the indicator for the overall catalyst activity and related to a specific chemical reaction. The definition of conversion is the number of moles product converted per number of moles reactant. In most of the catalytic reactions, several reaction paths are present in parallel to the desired product and the formation of by-products takes place. Therefore, the selectivity of a catalyst plays an essential role. Its definition is the percentage of the desired product formed in relation to all formed products.

Reaction mechanism: Reactions involving heterogeneous catalyst are always located on the surface of the catalytically active material. The atoms of the catalyst surface play a key role in the reaction procedure, since their function is to break the bonds between the reacting species and to build new bonds to form the product species [26, 33, 38, 39].

There are two main mechanisms in heterogeneous catalysis [40] represented in Figure 3: In the Langmuir-Hinshelwood-mechanism, where both reactants A and B must be adsorbed from the gas phase (I) onto the catalyst surface (II). The adsorbed species diffuse on the surface of the catalyst and a bonding between A and B takes place (III). The last step in this mechanism is the desorption process of product C from the catalyst surface (IV). In the Eley-Rideal-mechanism, reactant A adsorbs onto the catalyst surface (I). The reactant B, which stays in the gas phase (II), reacts with the adsorbed reactant A and a stable bonding between the components is formed (III). The last step is again the desorption process of the product C from the catalyst surface (IV). Whether a catalytic reaction proceeds via a Langmuir-Hinshelwood, Eley-Rideal or another less prominent mechanism has significant implications on the reaction kinetic. Theoretical studies have demonstrated that the surface structure of the catalyst, which changes within a multi component catalyst due to the particular composition, can influence which of the mechanism is the predominate one [41]. However, at present it is postulated that the most frequent reaction mechanism is Langmuir-Hinshelwood [42].

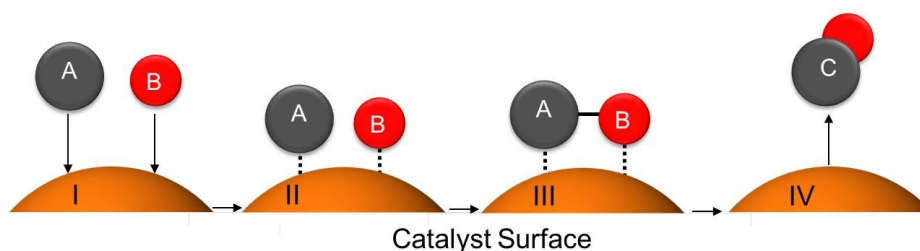
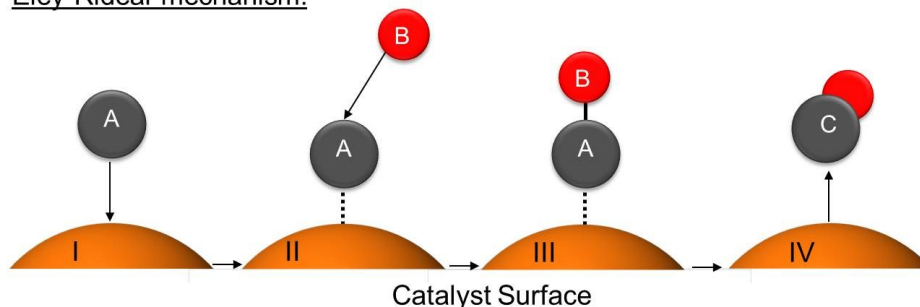
Langmuir-Hinshelwood-mechanism:Eley-Rideal-mechanism:

Figure 3: Schematic presentation of the two main mechanisms in heterogeneous catalysis including the educts A and B and the product C.

Size effects: The overall active surface for the catalytic reaction increases due to a reduction in particle size, because the number of “unused” atoms, which are present in the bulk, significantly decreases. Certain effects e.g. the surface, interface and quantum size effects get dominant. Lopez et al. demonstrated that gold (Au) particles in the nano dimension are considerably more reactive than extended Au surfaces, because of the low coordinated Au atoms, which can interact stronger with adsorbates. Additionally, gold nanoparticle have sites with a geometry that are particularly well suited for reactions involving bond breaking (and formation) in small molecules [43].

Catalytic particles in the nano dimension have further a benefit when expensive and rare active components e.g. Pt, Pd, or Au are applied, since the overall amount of the utilize material is significantly reduced. The dispersion gives an insight, how high the percentage of actual catalytically effective atoms on the surface is in relation to the total number the atoms of the component. A dispersion of 1 (or 100%) indicates that all atoms of the material are accessible on the surface. Typical catalytic materials have a dispersion between 0.5 (particle sizes of less than one nanometer) and 0.1 for particle sizes around 10 nm.

Sinter effects: One challenge with nanocatalyst is, however, the deactivation due to sintering, also called aging. This issue is especially high when nanocatalysts are applied, since the very high surface area to volume ratio of nanoparticles comes with the challenge that the individual particles will tend to coalesce and form larger particles to reduce the total surface energy [44]. This leads to a significant decrease of catalytic activity due to a loss of active surface area. Deactivation by sintering occurs due to high reaction temperatures especially above the Tamman temperature of the solid. The Tamman temperature is the temperature where atoms of a solid become mobile. One way to face this issue is a specific catalyst design, which ensures a high thermal stability of the active component during the reaction process. Since the active component often has a low heat-resistance, the deposition of the active component on a thermal stable support material reduces sintering significantly. The particles of the catalytically active component are fixed onto a high surface area support in such a way that inter particle contacts between the active component are hindered. A stable interface between the support and active component is essential to prevent coalescence, especially at harsh reaction conditions. For a high catalytic activity, a uniform dispersion of the active component on the support is required. This maximizes the distance between the individual particles of the active components deposited on the support particle.

The support is, however, not only a stabilizer for the active component, its chemical and physical properties also influences the catalytic activity of the reaction system significantly [45, 46]. The mechanical strength, the thermal stability and the porosity of the support are important with respect of its catalytic application [47]. A central issue in catalyst design is that educt and product molecules can approach and leave the catalyst surface fast and without undesired limitations [38]. The same applies for the formed products, so that they can leave the catalyst surface unhindered, even if their molecule diameter is significant larger than the one of their educts. It is further essential that the entire provided surface is also accessible to the reactant molecules, which can approach, either from the gas phase or from the liquid phase. The porosity and the minimal pore size of the catalyst system should be high enough to ensure a constant reactant and product flow. Further the individual adjustment of the particle size of the support and the active component is an important issue for all catalytic applications, since it influences the catalytic activity significantly [48]. In all cases, the ideal particle size of the individual component is highly depended on the particular reaction.

Strong metal-support interaction: As already stated earlier, the interaction between support and catalytic material is a further key to tune the catalytic activity. Interfacial

phenomena, such as strong metal–support interactions (SMSI) are only present in multicomponent systems. They are dependent on the choice of the support material and significantly influence the activity and selectivity. When group VIII metals (Fe, Ni, Rh, Pt, Pd, and Ir) are supported on reducible oxides (TiO_2 , CeO_2 etc.), the adsorption of H_2 and CO is drastically reduced, but competitive hydrogenation versus hydrogenolytic reactions are greatly favored [49]. So methanation production from CO or CO_2 and H_2 is enhanced by three orders of magnitude [50].

Spillover effects: The spillover effect is only present in multicomponent system and can also influence the catalytic performance. Spillover involves the transport of active species adsorbed or formed on a first surface (donor phase) onto another surface (acceptor) that does not adsorb or form the active species under the same conditions [51]. The result is the reaction of this species on the second phase either with other adsorbing gases and / or the reaction with or the activation of the second phase [52]. Figure 4 illustrates a schematic of the spillover effect on a multicomponent system including three components: 1. metal catalyst, 2. support and 3. an additional reactive phase. The example on the right illustrates hydrogen spillover from a metal onto its support and a second spillover to an additional reactive surface (in this case a reducible metal oxide). On this surface it may react with a hydroxyl to produce water ($\text{OH} + \text{H} \rightarrow \text{H}_2\text{O}$) [53]. In this reaction step, the metal of the metal oxide support is exposed and creates adsorption or catalytic sites.

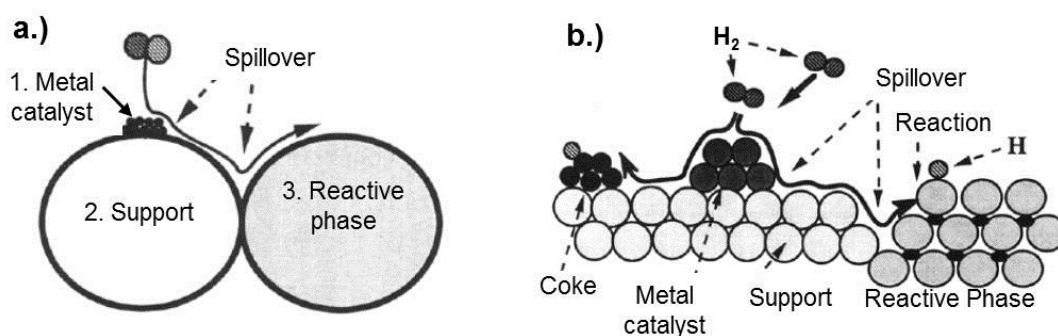


Figure 4: a.) Schematic representation of spillover: from a metal absorbing surface onto a support; and then onto another surface in contact with the support and b.) Pathway of a hydrogen spillover both reprinted with permission of [53].

Boudart et al. choose “spillover” to describe the migration of hydrogen atoms (H) from metal particles to its support, because the H atoms spill over from hydrogen-rich to hydrogen-poor surfaces [54]. Deutschmann further discussed that besides hydrogen

spillover, oxygen spillover may play an important role in oxidation reactions catalyzed by multi component oxides. One example is the addition of antimony (Sb) oxide to a selective oxidation catalyst. “This addition enhances the catalytic activity at high levels of selectivity by a factor of up to five relative to the Sb-free system, although antimony oxide itself is completely inactive [25]. So far, the experimental verification of the exact physical nature of spillover processes is very rare. In summary the term “spillover” is typically used to explain nonlinear effects (synergistic effects) on the performance, when chemically different components of a catalytic materials are combined [25].

Photocatalysis: A special type of reaction with heterogeneous catalysts is photocatalysis. The approach of this reaction type has expanded rapidly within the last four decades, since it offers promising approaches for energy and environmentally related problems. Solar water splitting and the purification of air and water that contain low concentrations of pollutants are the major applications so far [55]. The photocatalyst, which mainly consists of a transition metal oxide (e.g. TiO_2 , WO_3 and BiVO_4) or another semiconducting material, absorbs light ($h\nu$). The size of the bandgap, determines which wavelengths of the light spectra can be absorbed. The energy of the absorbed light must be equal to or greater than the band-gap energy E_g ($h\nu \geq E_g$) to generate a free photoelectron in the conduction band and a photo-hole in the valence band. The excited electron reacts with an oxidant and produces a reduced product. The reaction between the generated holes and a reductant results in an oxidized product. Both reactions take place at the surface of the catalyst. Figure 5 schematically presents the reaction steps for the photocatalytic water-splitting process. Which types of surface reactions are energetically realizable highly depends on the energetic positioning of the valence and the conduction band.

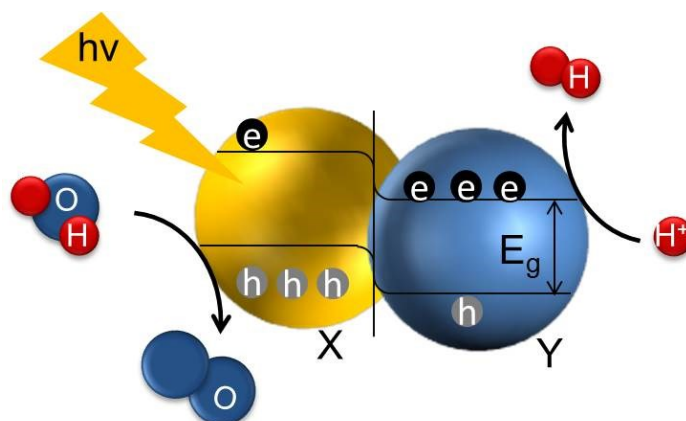


Figure 5: Photocatalytic water-splitting process using heterojunctions.

The characteristic parameter for the catalytic efficiency of a photocatalyst is the quantum yield. This is by definition equal to the ratio of the reaction rate in molecules per second to the photonic flux in photons per second [56]. The quantum yield can significantly decrease due to the recombination of excited electrons and holes. When a recombination takes place, the energy gained from the excitation of the electron is released as undesired heat. Following well known design aspects help to reduce the probability of such a recombination event and leads to an increasing electron lifetime [55]:

- a high crystallinity and a low defect concentration to avoid recombination in the bulk;
- a small particle size to minimize the length of the diffusion path of the excited electrons and holes to the surface.

Within the recent years, the focus within photocatalysis shifts more and more in direction of multicomponent materials, since single materials e.g. pure TiO_2 or Fe_2O_3 fail in reaching the requested activity. One approach is the combination of a photocatalyst and a co-catalyst in a multicomponent system. The deposition of noble metal co-catalysts e.g. platinum (Pt) or rhodium (Rh) on the photocatalyst surface can reduce the recombination significantly, since it improves the charge separation within the semiconductor and reduces the overall recombination rate.

Quite more challenging and a relatively novel and promising strategy to reduce the recombination rate is the formation of heterojunctions [57] as presented in Figure 5. A heterojunction describes the interface between two different crystalline semiconductors, where the difference in the position of the particular conduction bands results in a transfer of the photo-excited electrons from conduction band of component X to the conduction band of component Y. The hole transfer takes place simultaneously from the valence band of component Y to the valence band of component X. This results in a spatial separation of photo generated electrons and holes [58]. These photocatalytic multicomponent catalysts are, however, very complex systems and highly sensitive to surface defects which result in undesired recombination. The challenge is to implement a robust synthesis method which results in defect free particles and a stable and a nearly defect free interface between the two components to avoid recombination.

A third promising approach to achieve a highly active catalyst is a mixture of two components on atomic scale, since this so called mixed metal oxides offer promising positions of the conduction and the valence band, which are not present in single

material system. A suitable position of the bands is, however, necessary to utilize light with wavelengths in the visible light region, since this represents the main part of the solar spectrum.

All the discussed issues within this paragraph, including the influence of particle size, support interaction, surface accessibility, sinter stability and so forth give an idea of the enormous complexity of a real catalyst system. The next section defines the different combinations of materials in a multi component system and introduces the different mixing states investigated in the experimental part.

2.2 Design and application of nanoparticulate multicomponent catalysts

Multi component nanoparticle catalysts can exhibit a variety of different mixing states. A **mixing state** describes the distribution of the chemical components within a particulate system. The investigated particulate systems within this thesis are aggregates. An aggregate contains several primary particles that are chemically bonded (sintered) [59]. The formation of these fractal-like aggregates is characteristic for the aerosol synthesis of nanoparticles, described in detail in chapter 3.2.

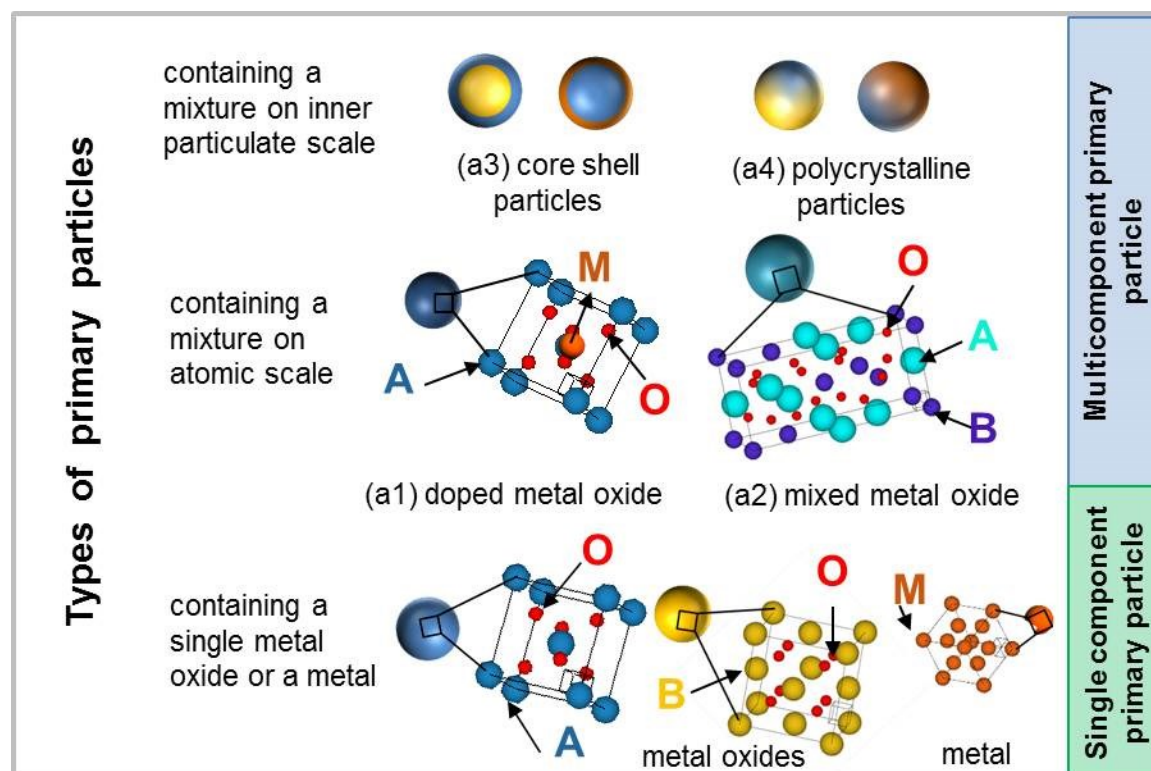


Figure 6: Illustration of different types of primary particles, which contain either a single or multiple components.

A **primary particle** is a single particle, which consist either of a single component (bottom row) or of multiple components (middle and top row) as illustrated in Figure 6. Multiple component primary particles are further divided in particles which contain a mixture on atomic scale and a mixture on inner particulate scale, explained in detail in chapter 2.2.1.

These primary particles are the building blocks for further mixing states within a so-called particle collective. A **particle collective** describes the accumulation of at least two different types of primary particles in form of an aggregate or an agglomerate (physically bonded aggregates) [59]. Figure 8 schematically illustrates 10 different mixing states, which are of high importance within the following chapters. In a first step, following distinctions are done:

a. Mixing states within a primary particle (bottom / blue color code)

and **mixing states within a particle collective (top)**.

The mixing states within a particle collective are further divided in:

b. Mixing states within a deposited system (orange color code)

c. Mixing states within an aggregated system (yellow color code)

A **deposited system** describes a mixture of at least two different types of primary particles (X and Y) which have a ratio between the diameter of the particles X and Y of $d_x/d_y \leq 0.5$ (with $d_x \leq d_y$). For a ratio, $d_x/d_y > 0.5$ the system is called **aggregated system**.

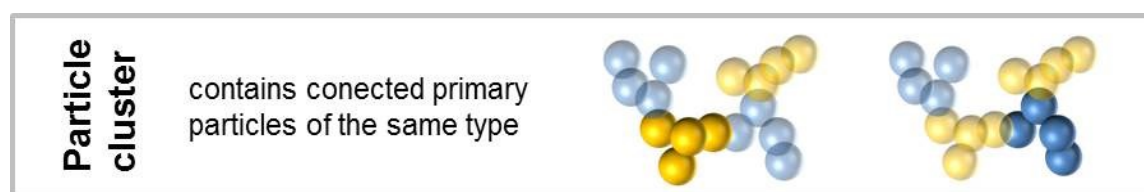


Figure 7: Illustration of different particle clusters with a cluster size of four particles.

Within an aggregate, primary particles of the same type can form particle cluster. A particle cluster includes all particles which are of the same type of primary particle and are connected with each other via a homo contacts. A **homo contact** denotes the particle contact between two primary particles of the same type. The cluster size

represents the number of particles which are connected via a homo contacts illustrated in Figure 7.

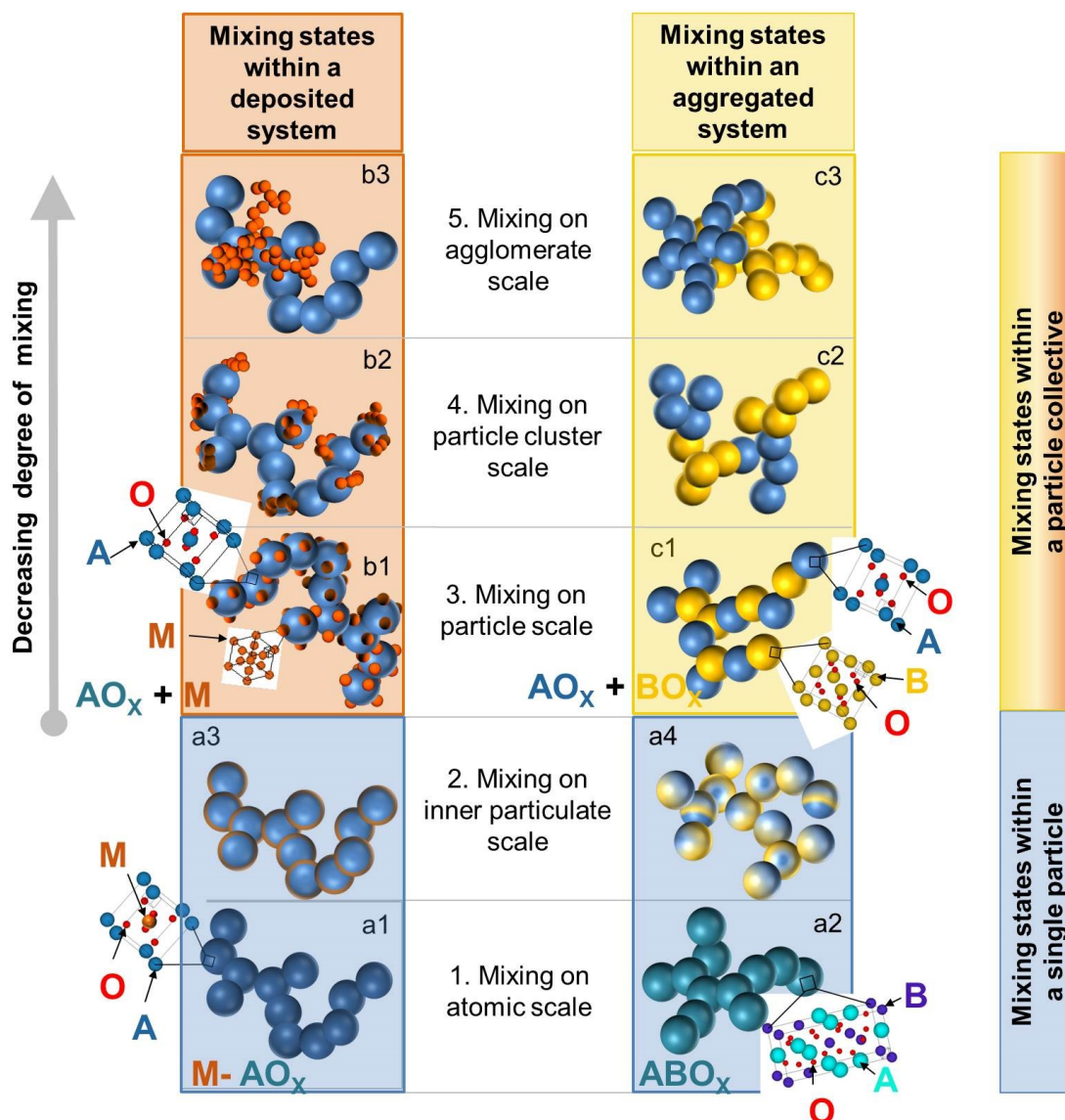


Figure 8: Schematic illustration of different mixing states within multi component catalysts: Mixing states within a primary particle (blue color code) including a1 a doped crystal structure, a2 a mixed metal oxides a3 a core shell structure and a4 polycrystalline particles. The boxes for the mixing states a1 and a2 as well as a3 and a4 are interconvertible between the deposited and the aggregated system. Mixing states within a particle collective describe either a deposited system (b1-3, orange color code) or an aggregated system (c1-3 yellow color code). The degree of mixing within a particle collective is decreasing from a mixture on particle scale to a mixture on agglomerate scale.

The degree of mixing is an indicator how many hetero contacts between the different components are present and related to a particle collective. A **hetero contact** denotes the interphase between two different types of primary particles. This interphase (hetero

contact) is required to take advantage of the properties of both components including the special properties of the interphase.

By definition, the ***degree of mixing*** is the highest when the maximum number of possible hetero-contacts is present for all primary particles within a particle collective. Both in a deposited and in an aggregated system, this is the case for a mixture on particle scale.

Degree of mixing in particle collectives: particle scale > cluster scale > agglomerate scale

Whereas the degree of mixing describes the mixing state within a particle collective, comprised the ***uniformity of the mixture*** all particle collectives within a sample. A sample is defined as uniform in cases where only one mixing state is present on aggregate scale throughout the whole sample. The uniformity of the mixture is the highest when the hetero-contacts are uniformly distributed within the sample. The presence of particle collectives within the sample, where e.g. a mixture on particle scale exists next to a region with a mixture on agglomerate scale significantly decreases the uniformity of the mixture. It is possible to have a uniform mixture with a low degree of mixing, when two types of aggregates are uniformly mixed on agglomerate scale throughout the whole sample.

Table 1 lists specific examples for all the different mixing stages according to the number of components involved. Roman numerals introduce the arrangements and the related capabilities as heterogeneous catalyst in the text. A supplementation and extension of this presented list of particle arrangements is possible by include e.g. more than four components.

2.2.1 Mixing states within a primary particle

Mixing of two or more components within a primary particle can take place on two main mixing scales: Mixing on atomic and mixing on inner particulate scale. The formed aggregates consist of primary particles which have all the same mixing state.

1. Mixing on atomic scale

The mixture of two or more components on atomic scale can lead either to the formation of a mixed metal oxide or to a doped crystal structure.

Mixed metal oxides (a2) consist of a crystal structure of at least two different elements, where all metal atoms (A and B) have a covalent binding to the oxygen. Possible are binary, ternary and quaternary systems of amorphous or crystalline nature. Typical stoichiometric forms are perovskites (ABO_3), scheelites (ABO_4), or spinels (AB_2O_4). Table 1 includes a variety of examples where mixed metal oxides are applied in a catalytic system (I, IV, VII, VIII and X) and highlights the reason for the application of a multicomponent material. Of special interest is also the synthesis of metastable mixed metal oxide phases because of their superior catalytic properties [60, 61].

In **doped crystal structures** ($M-AO_x$) (a1), the host component keeps its crystal structure and the second component migrates in this so called “host structure” without a change of its crystal structure. The dopant (M) can be either a noble metal atom e.g. Platinum (Pt) or a metal atom e.g. Titan (Ti).

Within the recent years, the application of doping and especially the application of mixed-metal oxides gained more and more interest in the field of catalysis, since e.g. surface properties or bandgap positions differ significantly from single component materials. This offers various advantages compared to single materials.

In multicomponent materials, the specific surface properties, which influence the catalytic activity significantly, can be tuned from acid–base to redox properties. This is realizable due to adjustments in material composition of the mixed metal oxide or due to variations of the doping content [62, 63]. Mixed metal oxides (I) further exhibits unique bandgap positions compared to single material semiconductors [64]. Doping (I) is successfully applied to modify the bandgap size and position of semiconductors [65]. This bandgap modifications are beneficial e.g. for the photo-oxidation capability [66].

2. Mixing on inner particulate scale

This mixture describes a primary particle which consist of at least two components that form two different crystal phases (e.g. crystalline and amorphous):

This can either be in form of so called **core-shell particles** (a3), where one phase covers the surface of a particle containing the second phase or in form of **polycrystalline particles** of disordered structure (a4) [67]. The different phases, in core shell and polycrystalline particles, can either contain two metal oxide phases or a noble metal and a metal oxide. One example is the flame synthesis of particles with an inner ceria core of spherical shape that is encapsulated by a 1 to 2 nm shell of amorphous

titania. Core-shell nanocatalysts can exhibit unique catalytic properties that are not present in either the core or the shell materials [68].

One example for a disordered system is a “raisin–bun”-type nanocomposite containing e.g. MoO₃ and SiO₂ particles. This special system can consist of 1.0 nm sized MoO₃ particles, which are homogeneously dispersed in 23 nm silica spheres. The nanocomposite exhibits enhanced catalytic activities and good reusability, attributed to the unique structure [69].

2.2.2 Mixing state within a particle collective

For mixtures extending the single particle scale, the distinction between deposited (b, orange color code) and aggregated (c, yellow color code) systems is used and presented in Figure 8. In both systems the degree of mixing varies based on the scale the two different types of particles are mixed:

3. Mixing on particle scale: This mixture describes a particle collective which consists of at least two different types of primary particles. The two types of particles form a high number of hetero contacts.
4. Mixing on cluster scale: This mixture describes a particle collective e.g. an aggregate which consists of at least two different types of particle clusters. Compared to a mixture on particle scale the number of hetero contacts is decreasing while the number of homo contacts is increasing in a mixture on cluster scale.
5. Mixing on agglomerate scale: This mixture covers at least two types of aggregates which consist only of one type of primary particles and are mixed within an agglomerate.

Particle mixing in a deposited system: The main characteristic of deposited systems, also called decorated systems, is the significant difference between the particle sizes of the different components. In this thesis, the critical value for the ratio in diameter between the primary particle size of component X (d_x) and component Y (d_y) is set to $d_x/d_y = 0.5$. Therefore, a deposited system represents a ratio where $d_x/d_y \leq 0.5$. In cases, where the ratio between deposit and support particle tends towards zero, the system has certain similarities to nanocomposite materials, where nanoparticles are deposited e.g. in a continuous polymer matrix [70].

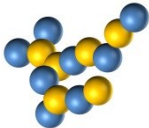
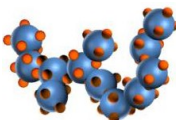
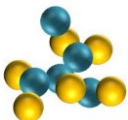
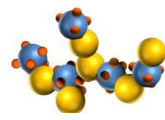
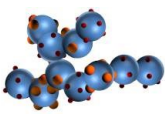
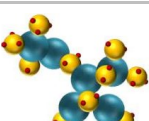
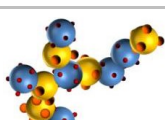
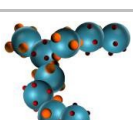
In deposited systems commonly small (noble-) metals (M) and in certain cases other oxides of the form BO_x, are dispersed on a support metal oxide particle AO_x (III). This

deposition can also be partial on one of the support component, when more than one type of support particle is present (V and VIII). When two types of deposits exist, they are either decorated on one component (VI) or partially on different supports (IX and X). A typical catalyst / support structure is the most prominent example for a deposited system where particles of the active component, are deposited on a particulate support [71]. This deposition increases the sinter stability of the active component, compared to the single material systems and offers an enhanced catalytic performance because of e.g. spillover effects. A co-catalyst, which is deposited on a semiconductor surface to reduce the charge recombination, is another prominent example for the advantages of multi component materials [17]. Zhang et al. demonstrated that the deposition of PdO on Co_3O_4 (III) particles adjust band-gap and Fermi energy levels which finally has significant influences on hazard potential of the particles [72]. Shimizu et al. increased the NO sensing properties of gas sensors due to the deposition of 5.0 wt.% Cr_2O_3 on SnO_2 (III) which results in the formation of micro p-n junctions [73].

Particle mixing in aggregated systems ($\text{AO}_x + \text{BO}_x$): This case describes a mixture, where two particles of nearly equal particle diameters are mixed within an aggregate ($d_x/d_y > 0.5$). Compared to physically mixed particle systems, sintering ensures a stable interface between the two different types of metal oxides particles in an aggregated system. The two types of particles can e.g. consist of two different oxides (II, V, IX), of a single and a mixed metal oxide (IV, VIII) or two mixed metal oxides (VII). Heterojunctions described by Marschall et al. are representative for this particle system [58]. Sasikala et al. demonstrated that heterophase structured TiO_2 and SnO_2 (II) particles showed enhanced photocatalytic activity for hydrogen generation compared to pure TiO_2 due to the enhanced charge separation in the composite system [74]. Jia et al. investigated successfully the BiVO_4 - SrTiO_3 :Rh heterojunction (VIII) system and indicated that a stable interface between both components is essential for the charge separation [75]. Another example where particle mixing in aggregated systems is beneficial compared to a single component material is the presence of an additional oxygen storage component, as presented in the work of Strobel et al. for a NOx storage-reduction system (V und VIII) [76, 77]. Particle mixing in aggregated systems also plays an important role for sensors, where p-type nanoparticles percolate between n-type particles (II, IV and VII) [78].

The compositional and structural complexity of the described catalyst components offer many degrees of freedom for tuning their catalytic properties for the desired application [32]. Table 1 presents specific examples and their catalytic applications for different types of mixtures according to the number of involved components.

Table 1: Specific examples and catalytic applications for different types of mixtures according to the amount of involved components

	graphic presentation	description of the structure	examples for catalytic application
2 components (binary systems)	I 	One type of mixed metal oxide or doped particles	- LaCrO ₃ : organic reactions [62] - CaWO ₄ , SrWO ₄ : photocatalysis [64] - Fe- doped TiO ₂ : photo oxidation [66]
	II 	Two different types of metal oxides particles (sintered interface)	- MnO _x // Al ₂ O ₃ and FeO _x // Al ₂ O ₃ : partial oxidation of methane [79] SnO ₂ on TiO ₂ : hydrogen generation [74]
	III 	Small (noble) metal particles dispersed on one metal oxide particles	- PdO // Co ₃ O ₄ : cellular redox homeostasis [72] - Pt // TiO ₂ : photocatalytic mineralisation of sucrose [80] Cr ₂ O ₃ // SnO ₂ : NOx Sensing [73]
3 components (ternary systems)	IV 	Mixed metal oxide and single metal oxide particles (sintered interface)	- CoMo // Al ₂ O ₃ : hydrotreating [81]
	V 	Two different types of metal oxides particles, one type decorated with a noble metal	- Pt- BaCO ₃ // Al ₂ O ₃ : NOx storage-reduction [76]
	VI 	Two different types of (noble) metals decorated on a metal oxide	- (Ru, Rh, Pt, Pd) // Al ₂ O ₃ : partial oxidation of methane [82]
4 components (quaternary systems)	VII 	Two different types of mixed metal oxides particles (sintered interface)	-Ba ₅ Ta ₄ O ₁₅ // Ba ₃ Ta ₅ O ₁₅ : hydrogen generation [83], - CaFe ₂ O ₄ // MgFe ₂ O ₄ degradation of isopropyl alcohol and hydrogen production from water [84]
	VIII 	Mixed metal oxide and single metal oxide particles decorated with a noble metal	- Pt- BaCO ₃ // Ce _x Zr _{1-x} O ₂ :NOx storage-reduction [77]
	IX 	Two different types of metal oxides particles, both decorated with different noble metals	- BiVO ₄ :Ru // SrTiO ₃ :Rh: visible light photocatalysis [75]
	X 	One mixed metal oxide particle decorated with two types of noble metals	- Pt // Ru // Y ₂ Ta ₂ O ₅ N ₂ : water reduction and oxidation [85]
	 metal oxides	 mixed metal oxides	 (noble) metals

2.3 Characterization techniques for multicomponent catalysts

Catalytic activity and performance of heterogeneous catalysts are highly dependent on structural characteristic e.g. particle size, crystallinity, reducibility and especially for multi component systems the material dispersion. The knowledge, how the material morphology influences the catalytic performance is the key to tailor catalysts for its application. The following section introduces a selection of established characterization techniques.

2.3.1 X-ray powder diffraction

X-ray powder diffraction (XRD) is a frequently applied analytical technique for phase identification of a crystalline material and provides information on unit cell dimensions. XRD rapidly gives information on the crystal structures, on crystallite size (grain size) and preferred orientations in polycrystalline or powdered solid samples using Rietveld refinement [86]. It can further be used to determine modal amounts of oxides (quantitative analysis). Regarding the catalytic performance XRD gives first insights on composition and structure e.g. on atomic mixing (ABO_x) or separate phases ($AO_x + BO_x$). It further gives an indication on the crystallinity of the sample which is an additional parameter for the catalytic performance.

The X-rays are generated by a cathode ray tube, filtered to produce monochromatic radiation, focused and directed towards the sample. The technique bases on constructive interference of monochromatic X-rays and the crystalline sample. Scattered monochromatic X-rays that are in phase, result in constructive interferences when conditions satisfy the Bragg's Law :

$$n \cdot \lambda = 2d \sin \theta \quad (1)$$

Here is n an integer called the order of the reflection ($n=1,2,3,\dots$), λ the wavelength of the X-rays, d the distance between two planes in the atomic lattice, and θ the angle between the incident ray and the scattering planes [86]. Scanning the sample within a range of 2θ angles, detecting and counting the X-rays, results in characteristic X-ray scans, which cover all possible diffraction directions of the lattice due to the random orientation of the powdered material. Conversion of the diffraction peaks to d -spacing allows identification of the material because each material has a set of unique d -spacing. The results are compared with standard reference patterns in the so-called Rietveld refinement.

The limitations of the techniques are a possible peak overlay for small particles which hinder a distinct characterization. Further, the system cannot detect amorphous particles and has a detection limit for mixed materials in the range of ~ 2-5%. Hence, one can never be sure that there are no other phases present than the ones detected with XRD [86].

2.3.2 Adsorption based methods to determine particle sizes

Since the reaction in heterogeneous systems takes place on the surface of the particulate catalysts, the specific surface area is one of the key parameter. Especially in multicomponent systems (catalyst /support system), the distinction between the total surface area and the specific surface area of the active phase plays an important role.

The Brunauer-Emmett-Teller (BET) method helps to determine the overall specific surface area, based on the phenomenon of physical adsorption of gases on the external and internal surfaces of a solid material. When an active component is deposited on an inert support, chemisorption is applied to determine the specific surface area of the active phase. The main differences between physisorption and chemisorption are described in the following section:

Main characteristics of physisorption:

- describes the formation of physical bonds with a surface
- is a reversible process with low bonding forces
- is not limited to certain materials
- includes multi-layer adsorption
- takes place with all gases below their critical temperature

In 1938, Stephen Brunauer, Paul Hugh Emmett and Edward Teller published the first article about the BET theory [87]. The presented approach allows the determination of the specific surface area (SSA) based on the amount of adsorbed gas at a given pressure. BET systems utilize inert probing gases such as nitrogen for the quantification of the SSA. The principal assumption of the BET theory is the application of the Langmuir equation to every adsorption layer [88]. The connection between relative vapor pressure and amount of adsorbed gas at a constant temperature results in the so called adsorption isotherm and is describes by the linear relation between $\frac{P}{n^a(P_0-P)}$ and $\frac{P}{P_0}$, where P is the actual vapor pressure, P₀ is the vapor pressure at saturation and n^a the total amount of absorbed gas [89]. In practice is the range of application is limited to 0,1 -

0,3 for $\frac{P}{P_0}$ [90]. With the help of the adsorption isotherm, the specific surface area (SSA) of the material can be determined. Based on the assumption of monodisperse spherical primary particles (which often deviates from the actual particle form) a so-called BET equivalent diameter d_{BET} can be generated from the SSA with the help of the material density ρ_p , see equation (2):

$$d_{\text{BET}} = \frac{6}{\text{SSA} \cdot \rho_p} \quad (2)$$

Especially since most of the catalyst systems deviate from a spherical shape and the actual density of the synthesized material can be unknown, discussions based on the BET equivalent diameter d_{BET} involve uncertainties. A discussion based on the SSA is a reasonable alternative.

In order to determine the ratio of the surface in a catalyst / support system, where the catalyst is chemically active, chemisorption is a suitable method.

Main characteristics of chemisorption:

- describes the formation of a chemical bond with a surface
- exhibits significant higher bonding forces compared to physisorption
- the nature of the bonding can be irreversible
- must overcome an activation energy
- is much slower than physical adsorption
- is limited to active species
- is limited to the formation of a monomolecular adsorbed layer
- needs the presence of certain reactive gases (typically H₂ or CO)

Chemisorption is a method to determine directly the number of reactive surface atoms, based on a measurement of the gas uptake. When the stoichiometry for the reaction of chemisorption is known, the quantity of the adsorbed gas on the active species gives the metal surface area and the metal dispersion. The dispersion can be determined based on two types of methods: static ones (such as volumetric and gravimetric) and dynamic ones which are based on gas thermal conductivity (continuous flow and pulse adsorption methods) [91].

In static chemisorption method, an isotherm of the total chemisorption (strong and weak interactions) is determined after a high temperature evacuation. In a low temperature evacuation, the weak physisorbed molecules are removed while the strong chemisorbed molecules remain at the surface. Then a second isotherm of the weak chemisorbed

species is determined. The subtraction of the weakly adsorbed number of molecules from the total adsorbed amount results in the amount of strongly and irreversible adsorbed gas. This strong chemisorption is the base for calculating the surface area and the metal dispersion [92]. In dynamic methods, an inert gas continuously flows over the solid. Stepwise pulses of adsorbing gas are injected into the gas flow. Recording the amount of injected gas compared to the amount of gas passing through the sample gives the adsorption. At the beginning, the active solid surface adsorbs the sample gas (strong interaction) until constant peaks appear and indicates saturation. The major difference between dynamic and static chemisorption methods is that the static method only considers the strongly adsorbed species, while the dynamic method measure strong and weakly chemisorbed species [93].

The metal dispersion D is calculated based on the ratio of the total number of metal atoms present at the surface of the catalyst (N_S) and the total number of metal atoms at the surface and in the bulk (N_T) see equation (3).

$$D = \frac{N_S}{N_T} \quad (3)$$

The value for the dispersion ranges from 0 to 1 (or 0 and 100%). Assuming spherical particles, relationships between metal dispersion, surface area and mean particle diameter can be established [91]. However, recent studies have demonstrated that the assumption of spherical particles and the non-observance of metal support interaction, can result in significant deviations from the real particle sizes [94].

2.3.3 Electron microscopy

Electron microscopy, a straightforward imaging technique, helps to determine the size and shape of single and multicomponent particle systems. This method uses a beam of accelerated electrons as a source of illumination [95]. Figure 9 illustrates the interaction between the sample and the primary electron beam, which has a characteristic wavelength of less than 1Å and enables monitoring close to atomic detail. Based on Chorkendorff et al. [86], detectable signals, when a primary electron beam of energies between 100 and 400 keV hits a sample in the following scenarios:

- “Electrons pass through the sample without suffering energy loss (depending on sample thickness)
- Electrons are diffracted by particles if these are favorably oriented towards the beam, enabling one to obtain crystallographic information

- Electrons collide with atoms in the sample and backscattering takes place. Backscattering becomes more effective with increasing mass of the atom (e.g. Pt has a higher yield of backscattered electrons compared to lighter TiO_2)
- Auger electrons and X-rays are formed in the relaxation of core-ionized atoms (Application: e.g. EDX)
- Electrons excite characteristic transitions in the sample which can be studied by analyzing the energy loss suffered by the primary electrons (Application: EELS) [86].

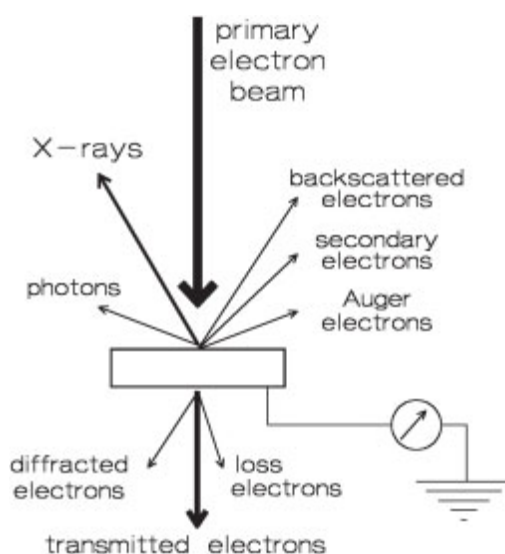


Figure 9: Interaction between the primary electron beam and the sample in an electron microscope leads to a number of detectable signals, reprinted with permission of ref. [86]

Transmission electron microscopy (TEM) images are based on transmitted electrons, have a resolution down to atomic scale ($1\text{-}2\text{\AA}$) and show many characteristics on the internal composition of the sample, such as size, shape and crystal structure. In TEM, the analysis only allows small amounts of the sample at a time. TEM is, thus, a relatively time consuming technique with a low throughput of samples.

Scanning electron microscope (SEM) images are based on scattered electrons have a lower resolution down to a range of $5\text{-}10\text{ nm}$ and focus on the sample surface and its composition. SEM allows the analysis of larger amount of sample at a time, however, at the cost of resolution. Compared to TEM, SEM provides a 3-dimensional image.

With respect to the analysis of multicomponent materials, however, both methods suffering from the fact that a fast identification of the components is challenging, when particle size and shape of the different materials are similar. The application of **scanning**

transmission electron microscope (STEM), which combines characteristics of TEM and SEM is, thus, a suitable alternative. Rasterize the beam across the sample makes these microscopes suitable to combine imaging with analysis techniques such as mapping by **energy dispersive X-ray (EDX)** spectroscopy and **electron energy loss spectroscopy (EELS)**. This allows a detailed elemental identification. Combining STEM and annular dark-field imaging (ADF-STEM), where images are formed using large angle scatter electrons, it is possible to form atomic resolution images, where the contrast is directly related to the atomic number (z-contrast image). For example, Pt particles appear significant brighter in STEM images compared to TiO_2 , due to the significant difference in atomic number.

Atomic force microscopy (AFM) is a scanning probe microscopes technique, which measures local properties of the sample surface, such as height, friction or magnetism using a sharp tip as a probe. Resolutions down to a few nanometers are realizable. To acquire an image, the probe performs raster-scans over a small area of the sample, measuring local properties simultaneously. Compared to TEM and SEM, it can provide three-dimensional images without an extensive sample preparation. If the nanoparticle materials have distinctly different morphologies, AFM imaging is theoretical able to differentiate between them. An AFM equipped with phase imaging capability (sensitive to variations in material properties such as adhesion or viscoelasticity), can also record a phase map along with the surface topography. This enables the mixing characterization of nanoparticles with similar size and morphology [31].

2.3.4 Temperature-Programmed Reduction

Temperature-Programmed Reduction (TPR) is a technique to characterize the reduction behavior of heterogeneous catalysts. TPR determines the number of reducible species and identifies the temperature when reduction takes place. Within the analyzing treatment a gas, typically hydrogen in an inert carrier gas such as nitrogen or argon passes the sample, while the temperature increases linearly with time. During the analyzing procedure, the consumption of hydrogen through adsorption/reaction is monitored based on changes within the concentration of the gas mixture downstream from the reaction cell. The resulting plot contains the hydrogen consumption over the temperature. The analysis of the diagram offers information on the amount of consumed gas and is therefore an indicator for the occurred reduction steps. For example, the reduction of Co_3O_4 takes place in two different steps: First the reduction of Co_3O_4 to three times CoO and in a second step the reduction of CoO to metallic cobalt. The consumed amount of H_2 differs in the ratio 1 to 3 from step one to two)

An important aspect of TPR analyses is that the sample does not need to have any special characteristics other than containing reducible metals.

2.4 Degree of mixing in multicomponent particle systems

Within the recent years, the interest in mixing and dispersing nanoscale particles has significantly increased. The uniformity of these nanoscale mixtures is essential to guarantee e.g. constant catalytic properties within the sample. However, the characterization of the contacts on nano scale presents a major challenge to the currently available measuring techniques [96] and the number of suitable methods which can provide a resolution on this length scale, is little.

Frequently applied methods to determine the uniformity of particle mixtures in the micrometer range are sieving and weighting or the determination of the material composition using chemical analysis. These approaches, however, fail on nanoscale due to their limited resolution. Currently only imaging techniques provide the necessary resolution and therefore, play an essential role in mixing characterization on nanoscale. Examples for imaging methods are transmission electron microscopy (TEM), scanning electron microscopy (SEM) and atomic force microscopy (AFM). Although these image-based methods are time consuming and suffer frequently from the challenge that a 3D object is investigated based on a 2D projection, they offer the possibility to determine the uniformity and the degree mixing in nanoparticulate qualitatively. The deviation resulting from applying a 2D examination is yet unknown and displays the need for a detailed evaluation concerning the suitability of the analysis.

Most of the studies, with respect to mixing on the length scale of nanosized aggregates discuss mixing only qualitatively, lacking of a suitable measure [31, 97]. The following two subsections present a selection of different image based approaches to determine the uniformity of nanosized mixtures and introduce parameters to quantify the uniformity and the related degree of mixing.

2.4.1 Approaches to determine the uniformity of a particulate mixture

Wei et al. [31] investigated several imaging methods and their results indicated that the capability of imaging techniques to determining the quality of nanoparticle mixing significant depends on the physical and chemical properties of the nanopowders. SEM was suitable for characterizing powder mixtures having a distinct difference in particle shape or a high difference in atomic number. Only EELS was able to characterize mixtures of components that are very similar in shape and atomic number. EDX provides

information on the uniformity of various material mixtures, but has to struggle with limited resolution. The work of Wei et al. further reveals that the AFM method is promising, however, has to be further optimized to successfully differentiate between different components and to reliably determine uniformity and the resulting degree of mixing [31].

Daumann et al. investigated the qualities of shear mixing tools for nanosized aggregates in the range of 140-300 nm and evaluated the uniformity with respect to the concentration of the components within TEM images [98, 99]. They suggested that parameters, such as fractal dimension or agglomerate size, are not suitable for the characterization of the mixing. They further stated that the determination of the mass concentration using energy dispersive X-ray spectroscopy (EDX) for the determination of the atomic concentration on spots of TEM images is the only correct way for the characterization of mixtures on aggregated scale. However, their approach to analyze the concentration of the components in aggregates lacks contact information on primary particle scale. In addition, the resolution of EDX is limited on the length scale of a few nanometers. Therefore, this approach is not suitable for the systematic analysis of the mixing characteristic on primary particle level.

One challenge in determining the uniformity of a sample is the choice of the evaluated length scale. A mixture may be described as uniform on a certain length scale, whereas investigations on a smaller length scale reveal segregation for the same evaluated system [100]. The suitable length scale varies from system to system and has to be statistically validated for each case [101].

2.4.2 Parameter to quantify the uniformity of a particulate mixture

Wei et al. stated in their review on mixing and characterization of nanosized powders that numerous studies, with respect to mixing of nanosized powders discuss uniformity and the degree of mixing only qualitatively [31]. To quantify the uniformity of nanoparticle mixtures, it is necessary to know which measured variables x constitute a suitable parameter [99].

Karnezis et al. introduced three different variables x to quantify the uniformity of a mixture in the field of Metal Matrix Composites (MMCs) based on TEM image analysis [102]: the nearest neighbor distance, the radial distribution function and the quadrat method. The nearest neighbor method determines the distance of the centers of gravity between one particle and its closest neighbor. The resulting distribution of the distances

gives insights on the uniformity of the samples. This method has its main weakness when particles clustering occur. The radial distribution function counts the number of particles, when a circular disc of radius r is centered on a particle. Again, the resulting distribution gives insights on the uniformity of the samples. The quadrat method divides images with a grid of square cells and counts the number of particles in each cell. The quadrat method, earlier investigated from Rogers [103], was found to be a suitable method for this approach. Kim et al. applied the method for the characterization of Metal Matrix (nano)-Composites (MMnCs) using TEM imaging [70]. These approaches have the potential to be transferred for the analysis of the uniformity in deposited systems.

An appropriate method to determine the uniformity in aggregated systems is to determine the average cluster size. As defined earlier, a cluster includes all particles within an aggregate / agglomerate that are of the same type and are in chemical contact. By definition, a cluster contains at least two primary particles of the same type. A large cluster size correlates with a low degree of mixing. The cluster size distribution gives again insights on the uniformity of the evaluated mixture.

Another method to examine particle mixing within aggregates is the analysis of the number of contacts (coordination number) between the different components. The coordination number is directly linked to the percolation and an indicator for the material functionalities [104]. A relative hetero coordination number \bar{c}_{Het} describes the number of contacts to a particle of a different component c_{Het} in relation to the overall number of contact, including hetero c_{Het} and homo contacts c_{Hom} (particle contact with the same component). Ayeni et al. [100] and Chandratilleke et al. [105-107] utilizing a comparable approach to analyze mixing in single particle systems. Both simulated the mixing dynamics of spherical non-aggregated particles for mixing in different shaped tumblers using the discrete element method (DEM). A high relative hetero coordination number \bar{c}_{Het} is linked with a high degree of mixing. The uniformity of the sample can be evaluated based on the variance of the hetero coordination number.

As mentioned most of the presented analyzing methods evaluate the uniformity of a sample based on the resulting distribution of the variables x . Kim et al. applied three different methods for the analysis of the received distributions: Morisita's index, the particle density, and the Skewness-Quadrat Method [70]. They found that the last one is the most suitable for a quantitative analysis of the uniformity of a nanoparticulate sample.

The image-based analysis of the degree of mixing in aggregated systems comes with the challenge to determine the boundaries of the aggregate. Therefore, the uniformity of

the overall sample can be used as a first indicator on the degree of mixing. However, for a more detailed analysis of the degree of mixing the distributions of single agglomerates can be analyzed. Independent which variable x is applied as parameter (nearest neighbor distance, particles per cell or the cluster size) the distributions of a uniform mixture has to match the following criteria both for deposited and aggregated systems, illustrated in Figure 10.

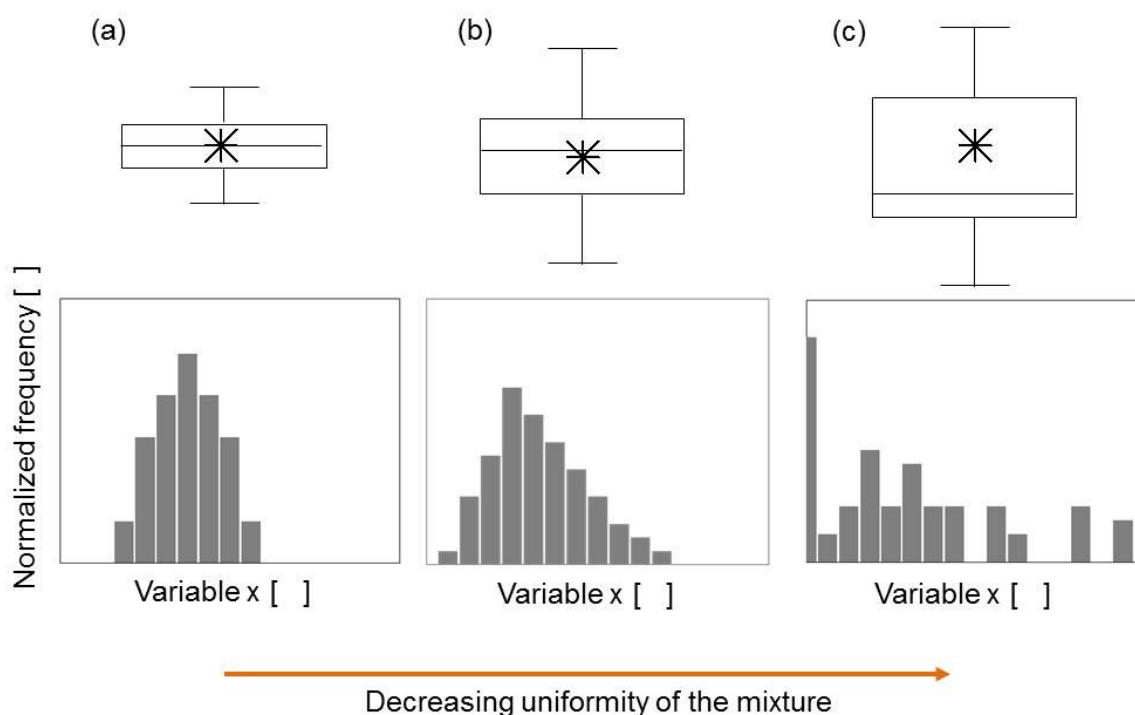


Figure 10: Different distributions describing the uniformity of a mixture, whereas a decrease in uniformity takes place from a to c.

(a) A distribution which is bell-shaped, has a high symmetry (the difference between the median and the arithmetic mean is small and the skewness approaches zero) and a small standard deviation indicates a uniform product quality.

Deposited system: Each support particle in the particle collective has nearly the same number of deposited particles.

Aggregated system: An aggregate / agglomerate consist of clusters which have all the same cluster size.

(b) An increase in the standard deviation and a slight skewness characterize a less uniform mixture.

Deposited system: The amount of deposited particles per support significantly varies.

Aggregated system: The size of the present cluster within an aggregate / agglomerate significantly varies.

(c) Large standard deviation and an asymmetric distribution with a high skewness of the distribution characterize a non-uniform sample.

Deposited system: Both the number of primary particles, which are decorated with a high number of deposits and the amount of support particles without a deposit significantly, increases.

Aggregated system: The sample contains regions with a mixture on particle scale next to regions with a mixture on aggregate scale.

Another appropriate procedure to evaluate the uniformity of a particulate mixture is to take a number of random samples (N_s) and determine the variance in their composition: the higher the uniformity of the mixture, the lower the expected variance [108].

$$\sigma^2 \approx s^2 = \frac{1}{N_s} \cdot \sum_{i=1}^{N_s} (x_i - x)^2 \quad (4)$$

Equation (4) represent the dependence of the variance σ^2 on the number of samples N_s ; the expectancy x and the values of the measured component i , x_i [99]. The number of samples N_s , which is required to determine the variance σ^2 , is theoretically infinite. Under real conditions, when costs and experimental time plays an important role, the empirical variance s^2 is determined based on the number of analyzed samples.

Dividing the empirical standard deviation s by the expectancy x , gives the variation coefficient, applied e.g. by Daumann et al [98, 99] and presented in equation (5).

$$v = \frac{\sqrt{\sigma^2(x_i, t_m)}}{x} \approx \frac{\sqrt{s^2}}{x} \quad (5)$$

3 Synthesis techniques for multicomponent nanoparticles

Nanocatalysts can be synthesized using two main approaches: top down and bottom up, see Figure 11. In top down methods, mechanical, chemical or another form of energy

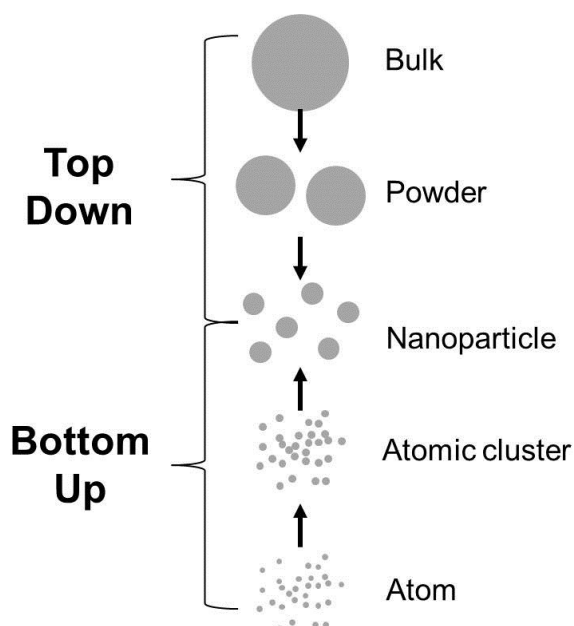


Figure 11: Top down and bottom up approach for the synthesis of nanoparticles.

disintegrates bulk material into smaller fractions. Micropatterning techniques such as Lithography (photo-, ion beam -, electron- or X-ray-lithography) and inkjet printing, cutting, etching and grinding are typical fabrication techniques. This physical technologies enable the design, fabrication and embedding of nanostructures in a functional host environment [109].

In bottom up methods, the synthesis process starts from single atoms or molecules that coalesce with other atoms and molecules to form larger nanostructures via chemical reactions.

Bottom up approaches utilize the concepts of molecular self-assembly and/or molecular recognition and are able to produce two-dimensional or three-dimensional products. They are often significantly cheaper than top-down methods, which makes them attractive for applications. However, the adjustment of the individual particle sizes and the mixing states of the final product are still challenging [109]. Especially in multicomponent particle systems, as investigated in this thesis, the individual size adjustment of the particles is essential for the product quality. The separate synthesis of the individual components combined with a subsequent mixing process is an approach that reduces the influencing synthesis parameter significantly. This enables an individual particle size adjustment. Procedures to subsequently intermix the different components after the synthesis are e.g. the ball milling process [110-113] or the lab scale application of pestle and mortar [114]. However, these approaches involve multi-step processing and can result in insufficient chemical bonding between the different components or non-uniform mixtures. Additionally, the process conditions in these processes can affect the particle size of the individual components subsequently and can lead to broad size distribution and varying particle shape or geometries. Further, the insertion of impurities in the system has a negative impact. Based on these reasons the direct synthesis of multicomponent materials is preferred. The following chapters present a selection of

bottom up synthesis methods and gives detailed information on the flame spray pyrolysis process.

3.1 Bottom up synthesis methods

Two main routes represent the bottom up methods and can realize a direct synthesis of multicomponent nanoparticles: the liquid and the gas-phase route. Liquid-phase methods apply chemical reactions in solvents and the formation of colloids. The formed nanoparticles can then be stabilized by surfactants or ligands against aggregation [115]. Gas-phase synthesis techniques are based on homogeneous nucleation in the gas phase and subsequent condensation and coagulation [116]. The applied synthesis technique in this thesis is the flame spray pyrolysis, which belongs to gas phase techniques.

Figure 12 gives an overview on the most common liquid (blue) and gas (red) phase synthesis methods. Especially the gas phase synthesis offers the opportunity to synthesize multicomponent systems in a single step. Even so, both methods are theoretically suitable for the synthesis of single and of multicomponent materials, the specific adjustment of the final product characteristic is, especially for the multi component materials, limited. Here, the application of surface deposition methods is a suitable approach (bottom part) to overcome these limitations, since the particle characteristic of both components is adjusted separately in this multi-step route. In surface deposition approaches, either atoms or small atomic clusters diffuse on the surface of previously, from liquid or a gas phase route synthesized support nanoparticles. They form the desired second or third component as a complete layer or as smaller particles on the support particle surface [37].

The following sections present a selection of the most common bottom up techniques. This includes a discussion of the advantages and disadvantages regarding the technology and the product quality and an overview regarding the ability to synthesize highly complex multicomponent materials without a subsequent mixing process. The focus of the second part of the chapter is the detailed description of the particle formation process and the process parameters applied in the single and double flame spray pyrolysis set-up.

Bottom Up synthesis methods for single and multicomponent material

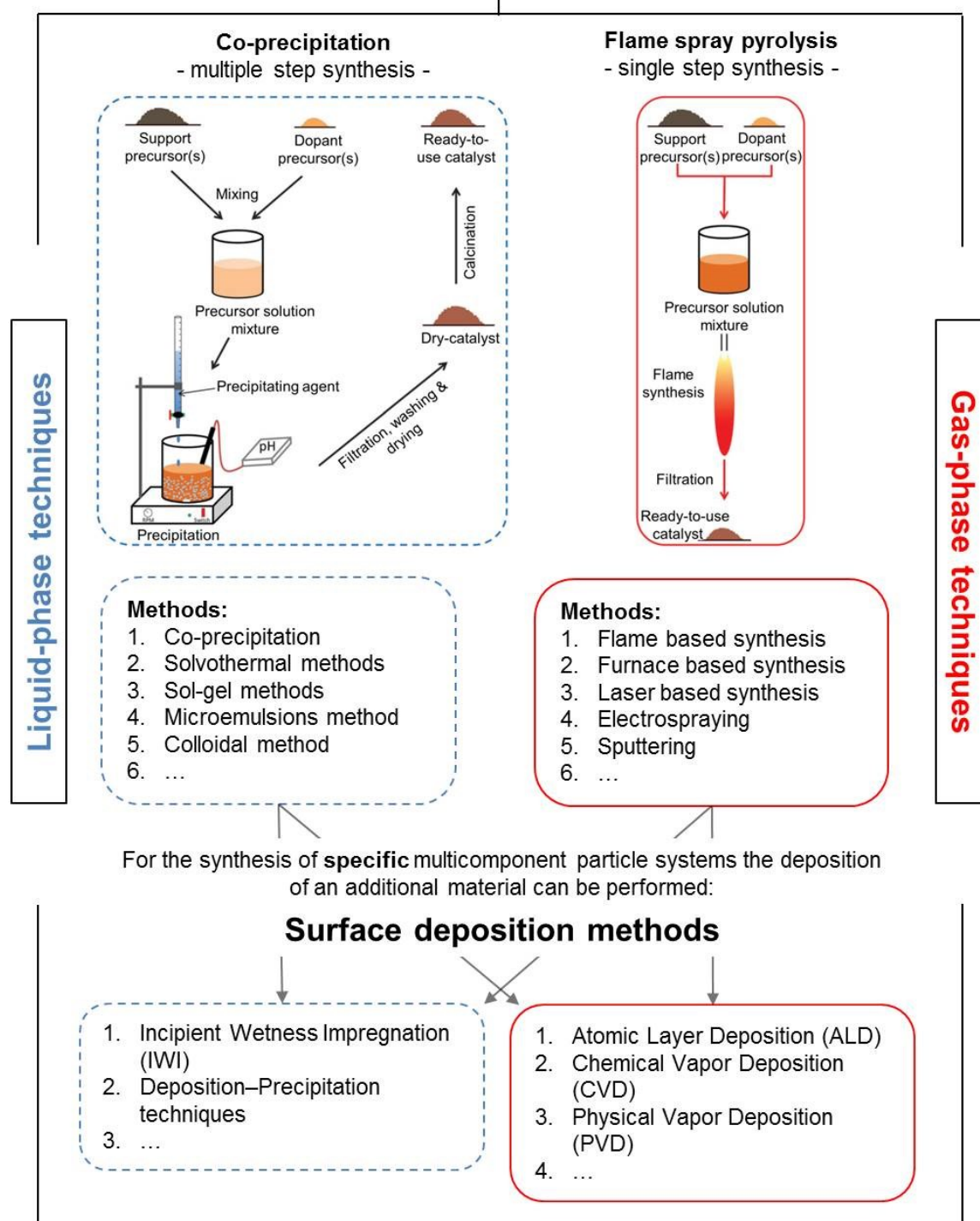


Figure 12: Illustration of common liquid (blue) and gas (red) phase synthesis method applied for the synthesis of single and multicomponent materials (top part). For the specific design of more complex multicomponent materials, one or more additional material(s) can be deposited on the surface of a (multicomponent) support (bottom part). The Co-precipitation and flame spray pyrolysis schematic are reprinted with permission of ref. [117]

3.1.1 Liquid-phase techniques

So far mostly liquid-phase or also called wet-phase techniques are applied for the industrial manufacturing of catalytic particle systems [118]. In liquid-phase methods chemical reactions in solvents lead to the formation of colloids. Figure 13 presents the fundamental steps within the liquid phase synthesis. The precursors are either present in the liquid phase or dispersed as a solid in the solvent. The reactants undergo liquid-phase or liquid-solid surface reaction and form intermediates. These intermediates can pass through further reaction steps until the final component develops in the liquid phase. Due to homogeneous or heterogeneous nucleation, primary particle growth starts and continues by condensation effects. A stabilization of the formed particles by surfactants or ligands in the liquid phase results in the formation of single nanoparticles. Limited stabilization leads to nanoparticles agglomerate [119, 120].

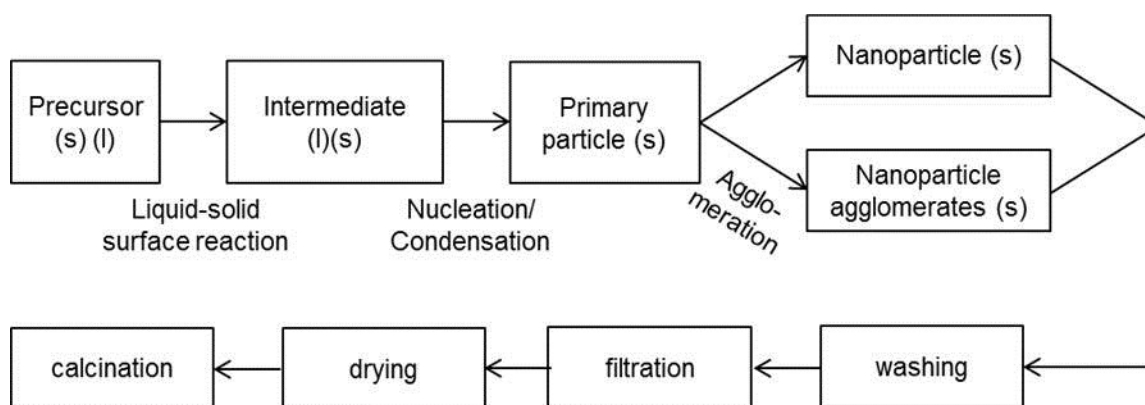


Figure 13: Fundamental steps within the liquid phase synthesis. Graphic is adapted from ref. [119, 120].

Common liquid phase synthesis methods are the following:

1. Co-precipitation
2. Solvothermal methods
3. Sol-gel methods
4. Microemulsions method
5. Colloidal method

The major advantages of all the liquid-phase techniques are the mainly cheap precursor and the synthesis of monodisperse particles. Further, the syntheses of highly porous materials with a high specific surface area (e.g. zeolites) are possible in these approaches.

However, as the applied temperature in liquid phase methods are low, this can result in a limited temperature stability of the products during following catalytic reaction. An applied thermal post-treatment increases the temperature stability of the catalysts. This thermal treatment further helps to achieve desired (crystalline) product phases, which may have not directly formed because of the low process temperatures during the synthesis. A post-treatment, however, bears the danger of a significant decrease in specific surface area and pore volume. The major disadvantage of these techniques are the high number of different process steps, such as filtration, purification, drying and calcination which makes a continuous process control very difficult to handle. Therefore, for most of the liquid-phase syntheses routes batch processing is inevitable.

Following examples give an insight for the suitability of liquid phase methods for the synthesis of multicomponent particle materials. Wang et al. reported on the preparation of ultra-small monodisperse $\text{MoO}_3/\text{SiO}_2$ nanocomposites using reverse microemulsions [69], where 1 nm small MoO_3 particles are uniformly distributed in 23 nm large silica particles. Dependent on the precursor and the material ratio, limited types of nanocomposites can also be synthesized using solvothermal methods as shown by Sun et al. for a WO_3/TiO_2 system [121]. In sol-gel methods, the synthesis of multi component materials can be prepared due to a controlled stoichiometry when mixing sols of different components. Li et al. presented a single step synthesis of the multicomponent system $\text{FeCo}/\text{Al}_2\text{O}_3$, where $\alpha\text{-FeCo}$ particles are homogeneously dispersed in the Al_2O_3 matrix [122]. Aerogels are also suitable substrate materials for subsequently produced multicomponent materials, since they offer a highly porous structure and the additional component can easily be deposited on the particle surface [123]. However, the individual size adjustment of the particles is very limited in this approach and highly related to the utilize concentration ratio.

3.1.2 Gas-phase techniques

In the recent years, the gas-phase synthesis gained increasing interest for the synthesis of nanomaterials [124, 125]. Already today, the large-scale production of singular nanoparticulate materials such as SiO_2 , TiO_2 and Al_2O_3 is industrial implemented [25]. Especially aerosol processes have furthermore the potential to produce multicomponent materials [116].

Figure 14 highlights the fundamental steps within the gas phase synthesis. The process starts with the evaporation of the precursor, followed by gas phase reactions and supersaturation effects until the primary particles formation takes place by homogeneous

or heterogeneous nucleation. The primary particles grow based on condensation and coagulation. A detailed concept of the particle formation steps in gas phase follows in chapter 3.2.

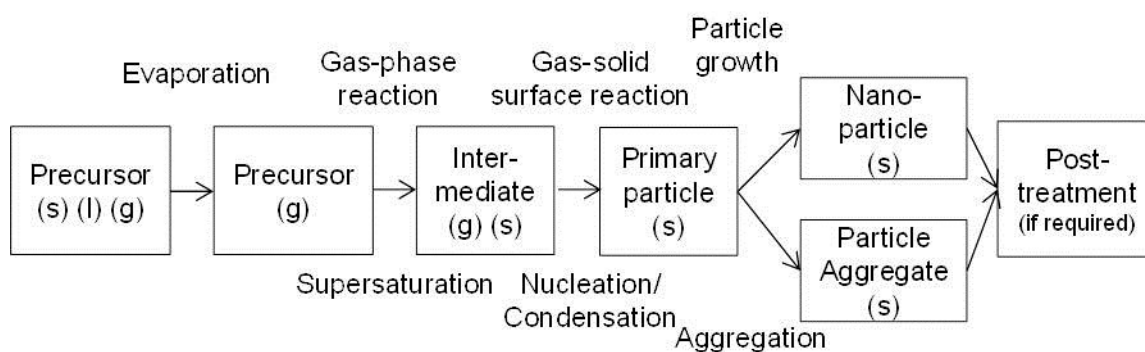


Figure 14: Fundamental steps within the gas phase synthesis. Graphic is adapted from ref. [119, 120].

Common gas phase synthesis methods are the following:

1. Flame based synthesis
2. Furnace based synthesis
3. Laser based synthesis
4. Electro spraying
5. Sputtering

The major advantage of the gas phase techniques compared to the liquid ones is that the implementation of continuous processes is more feasible. They are also a suitable method for the direct synthesis of multicomponent materials. A direct precipitation of nanoparticles from the gas phase to the support particles realizes the synthesis of coatings or the decoration of noble metals on support particles in a single step [126]. Figure 12 illustrates the potential of the flame process to synthesize these multicomponent materials in a continuous single step process [47, 127]. Compared to conventional preparation techniques such as the liquid-phase route, the aerosol technique enables continuous production, which is a significant benefit for large-scale productions. Additionally, it reduces the liquid volumes and surfactants required for high yield of high purity materials [128]. The reproducibility of continuous gas phase synthesized products is higher than in batch processes produced particles [116].

One challenge of the gas phase methods is that the separation of the products from relatively voluminous gas streams. This generates the demand of efficient filters or

cyclone systems. Further, the applied precursors require a high purity since a purification step during the synthesis step is not possible. This demand leads, however, also to the formation of purer products with fewer impurities compared to liquid phase synthesis. The prices of the applied precursors in the gas phase can be significantly higher than the one for the liquid phase. Current research already focuses on the development of precursors from cheaper raw materials through various routes. This should help to decrease the prices of the precursor in future [1].

One further advantage of gas-to-particle routes is the high external surface area of the nearly spherical and solid particles. They have a particle size in the range of micrometer to nanometer, depending on the process conditions. Next to the high purity, this is an important requirement for a high catalytic activity. Gas phase techniques tend to synthesize non-porous materials, since the formation process offers high temperatures and fast cooling rates. These are also the reasons why gas phase synthesized particles offer a high thermal stability and a good mass transfer during the catalytic reaction [47].

It has to be mentioned, that gas phase approaches often results in powders with a wide size distribution and only to a limited extent in monodisperse particle size distributions [129]. Under certain conditions, flame synthesis can result in the production of non-solid spherical, (e.g. hollow) particles as explained in section 3.2. A precise process control prohibits this circumstance. One major disadvantage of the flame methods is the formation of hard agglomerates which leads to difficulties in producing high-quality bulk materials [130]. This may be avoided by cooling the flame, for example, using a quenching ring [131].

Shim et al. investigated an ultrasonic spray pyrolysis process for the synthesis of $\text{Al}_2\text{O}_3/\text{ZrO}_2/\text{TiO}_2$ ceramic composite particles, where all the formation of all three phases took place in parallel [132]. Sourice et al. synthesized carbon-covered silicon nanoparticles in a continuous one-step process by applying a two stages laser pyrolysis reactor. In a first stage crystallized silicon cores form which are covered by a carbon continuous shell in the second stage [133]. The synthesis of multicomponent particles in a single step is further realizable based on the evaporation of multicomponent targets e.g. a mixture of metallic and ceramic targets [134]. However, the ideal adjustment of the resulting mixture is still challenging.

Especially the flame-based methods offer the potential for the synthesis of different types of multi component materials in a single step. Flame-Assisted Spray Pyrolysis (FASP) allows the synthesis of mixed oxides such as SrTiO_3 [135] and metastable $\beta\text{-SrMnO}_3$ and

NiMn₂O₄. Guo et al. synthesized composite materials e.g. Fe_xO_y/SiO₂ core-shell particles [136]. For the SiO₂ core, they applied silica colloidal with a particle size 10 nm. Multicomponent materials have also been synthesized with vapor-fed aerosol flame (VAFS) synthesis, for example, V₂O₅/Al₂O₃ [137] or V₂O₅/TiO₂/SiO₂ powders [138].

Flame spray pyrolysis (FSP) is the youngest of the flame based synthesis processes and the most heavily explored in recent years. It offers a high potential for the production of complex and functional nanomaterials in a single step [1]. Strobel et al. realized, for example, Pt deposited on Al₂O₃ support [139] and Schulz et al. presented an example with a SiO₂ coating on a Ce_xZr_{1-x}O₂ host particle [140]. Section 3.2.3 introduces the different configurations for the synthesis of multicomponent particles in more detail.

3.1.3 Surface deposition methods

Although nanosized multicomponent powders can be synthesized using liquid and gas phase synthesis methods, the ability to fully design and control them is still lacking [141]. Both methods have one major challenge in common: a high dependency between particle sizes and the initial material concentration in the synthesis process. This dependency conflicts with the circumstance, that the concentration ratio between the individual components is mostly predetermined. However, the methods offer the possibility to influence particles sizes with process parameters such as pH, time, temperature and flow rates. This adjustment gets more complex for an increasing number of different components in the synthesis process.

Therefore, the application of surface growth methods is a possible solution to form the desired material combination in complex systems, since particle properties like particle size can be adjusted separately in this multi-step process. In the surface deposition approaches, the production of the nanoparticulate components occurs firstly, by either a liquid or a gas phase synthesis route. The second component is then deposited in an additional step based on two main principals: by deposition of previously produced nanoparticles by diffusion, electrophoresis, thermophoresis, an inert force or by deposition of gaseous, liquid or solid precursors which are transformed to the product via heterogeneous nucleation on the surface [37].

There are several techniques which belong to the surface deposition methods. The methods can again be divided in liquid and gas phase techniques based on the physical conditions:

Liquid phase techniques:

1. Incipient Wetness Impregnation (IWI)
2. Deposition–Precipitation techniques

Gas phase techniques:

1. Atomic Layer Deposition (ALD)
2. Chemical Vapor Deposition (CVD)
3. Physical Vapor Deposition (PVD)

The appropriate surface deposition technique depends on the requirements of the multicomponent system. The applications last from methods which offer a high uniformity with the drawback of being time consuming and cost intensive to quicker and cheaper solutions. The later ones then have to cope with a non-uniform distribution or even individual clustering and can result in a limited chemical bonding between the different components. The main disadvantage of all these approaches is, however, that a multi-step processing is involved which can be prejudicial when it comes to industrial applications and large-scale production.

3.2 Flame spray pyrolysis

Section 3.1 introduces several methods for the synthesis of multi component materials and discusses their advantages and disadvantages. Flame spray pyrolysis (FSP) is one promising synthesis method which covers various requirements for the successful synthesis of multicomponent materials and is the applied synthesis technique within this thesis.

FSP is a high temperature aerosol method that converts a metal containing precursor into oxide or noble metal nanoparticles [1, 2]. Within this synthesis technique, a self-sustaining flame operates as the synthesis reactor [2, 47]. In the last years, the research interest on this synthesis method has increased significant. A short residence time, high temperatures and large temperature gradients characterize the process. The main advantages of the process are the production of multicomponent systems in one-step and the high production rates [142, 143]. Figure 15 presents the basic design of the experimental set up.

For the FSP synthesis, a metal precursor is dissolved in a combustible organic solvent. A two-phase nozzle atomizes this precursor solution using either air or pure O₂ [2, 47]. Since the combustion takes place in a self-sustaining flame, a rather small supporting flame of premixed methane and oxygen ignites and sustains the spray combustion.

Particle formation takes place as described in the following section. Filters, cyclones or electrostatic precipitators collect the flame-made particles. Alternatively, the flame products can also be deposited directly onto a substrate [144].

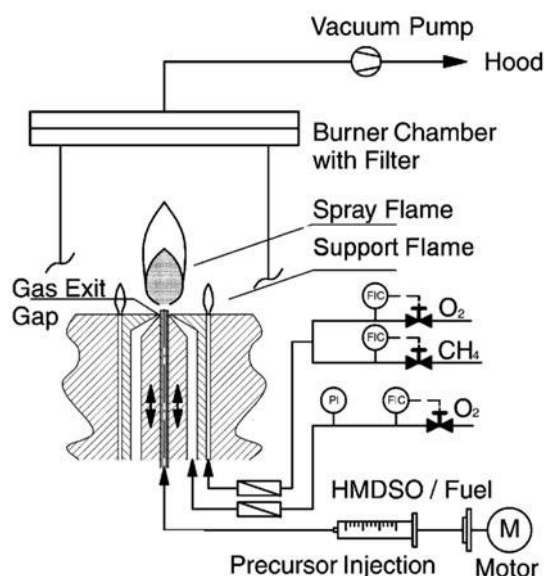


Figure 15: Experimental set-up of FSP using an air-assisted nozzle and a supporting CH₄/O₂ flame (Reprinted with permission of ref. [2]).

3.2.1 Particle formation process

The following section describes the main particle formation mechanisms, characterizing the synthesis of particles in the liquid and the gas phase (liquid to solid or the gas to solid route). Figure 16 illustrates the five main steps of the particle formation on the example of the FSP process. The reaction zone for the particle synthesis in the FSP process is the flame. Due to significant temperature gradients within the reaction zone, all described steps take place simultaneously distributed all over the flame reaction zone.

1. Precursor spray evaporation

A two-phase nozzle introduces the carbon-based precursors in the flame environment and the dispersion gas flow (air or pure O₂) atomizes the precursor solution. The gas has a velocity just below sonic speed at the nozzle outlet. For standard flame conditions, this procedure results in droplets of the range of 7-19 μm [145]. Gröhn et al. investigated the fluid-particle dynamics during the flame spray synthesis of ZrO₂ particles and demonstrated a hollow-cone spray structure at low height above the nozzle [145]. They further presented that 95% of the spray volume has already evaporated at 25 mm height

above the nozzle at standard conditions. Micro explosions attend the droplet evaporation and the chemical reaction, respectively a combustion of the gaseous precursors as investigated by Rosebrock et al. [146, 147]. The corresponding metal component transitions in the gas phase and oxidizes immediately. A supersaturation of the product vapors starts the nucleation process.

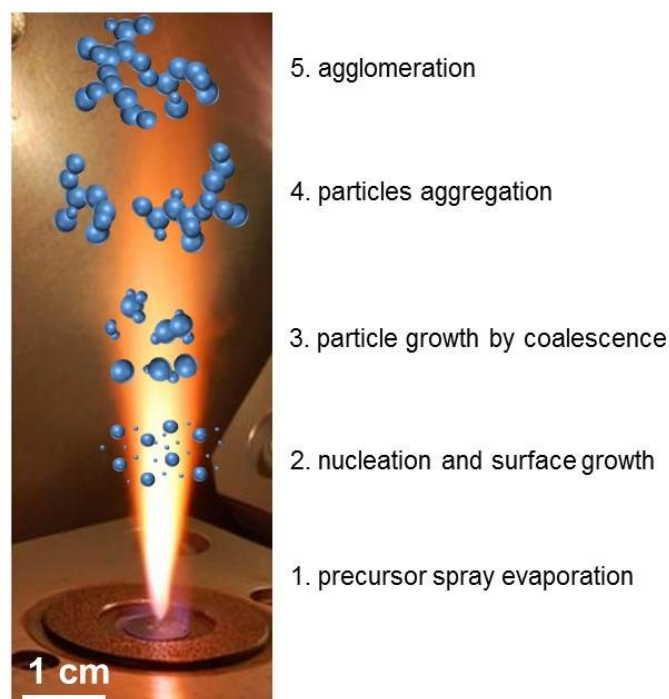


Figure 16: Illustration of the particle formation in the FSP process.

2. Nucleation and surface growth

Nucleation is a process where a metastable system, such as a supersaturated vapor, initiates a discontinuous phase transformation. Previous bonds of the precursor break and a clustering of the released metal atoms in the vapor phase creates a new phase. Homogenous and heterogeneous nucleation characterizes a nucleation process [148]. **Homogenous nucleation** occurs in the absence of any solid interface. Prior to the initiation of homogeneous nucleation, the concentration of the metal atoms respectively the metal oxide molecules increases with time leading to a supersaturation of the product vapor. The rapid cooling in the flame further accelerates the effect of supersaturation. Because the supersaturated vapor is not energetically stable, the atoms respectively the metal oxide molecules separate out and the formation of a nuclei in the gas phase starts. A nucleus indicates a small nanoparticle with less than 10^4 molecules or atoms, corresponding to a diameter of only a few nanometers [116]. For a given supersaturation, concentration in the gas phase a critical nucleus size exists. Nuclei with

sizes below are unstable and evaporate, beyond the critical size the nuclei are stable and continuously grow. The stability of a nucleus is determined considering the changes in Gibbs free energy associated with the process of nucleation [37]. The ratio of the partial pressure of a species to its saturated vapor pressure defines the saturation ratio S and the resulting critical radius r_c . In case $S > 1$, the nucleus grows; if $S < 1$, the nucleus dissolves; and if $S = 1$, nuclei and vapor are at equilibrium. Nuclei with a radius equal or greater than r_c are thermodynamically stable and can lower their free energies through continuous growth. Nuclei that smaller than r_c would dissolve to decrease the free energy.

Heterogeneous nucleation occurs preferentially at special sites of a surfaces (e.g. phase boundaries or impurities) on preexisting particles. The basic assumption is that at preferential sites the effective surface energy is lower which decreases the activation energy. As a result, nucleation at these preferential sites is preferable and occurs at lower saturation levels. As a result, heterogeneous nucleation occurs more often than homogeneous nucleation [37]. Nevertheless, under real existing reaction conditions it can be assumed that both kinds of nucleation occur consecutively and parallel [148].

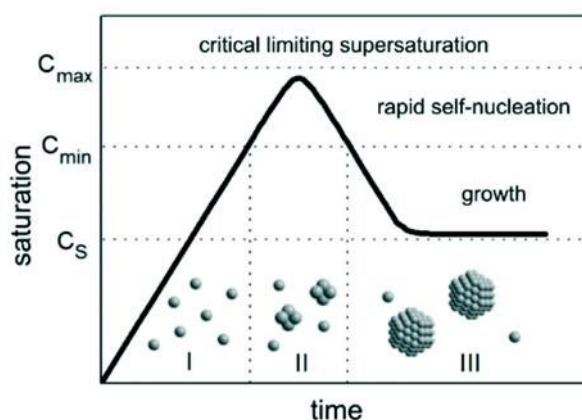


Figure 17: LaMer plot describing the nucleation principle for nanoparticles. The qualitative curve describes the atoms respectively molecule concentration c as a function of time. (Reprinted with permission of ref. [148]).

LaMer and his colleagues transferred the classical nucleation theory to the nanoparticle synthesis back in the 1950s. The basic idea of the concept is to separate nucleation and growth. Figure 17 displays the LaMer plot including the three characteristic stages[148].

- (I) The concentration of atoms respectively molecules increases and exceeds the critical supersaturation level (C_s) which is theoretically necessary to start homogeneous nucleation.

- (II) In praxis, rapid self-nucleation just starts after passing the level (C_{\min}) which indicates the required activation energy for nucleation. So-called burst nucleation takes place (metastable zone).
- (III) Due to the burst nucleation, the supersaturation level lowers immediately below its self-nucleation level C_{\min} . The nucleation process stops and the particle further grow by diffusion of further atoms respectively molecules from the vapor phase towards the particle surfaces. This surface growth can be interpreted as heterogeneous nucleation/growth and the nuclei grow up to a primary particle.

The expected corresponding nuclei or respectively the primary particle concentration with respect to time increases fast at the self-nucleation stage (II) and stays more or less constant during the final growth stage (III). Since the diffusion coefficient of atoms respectively molecules in the gas phase is three orders of magnitude larger than that in the liquid phase, the rate of growth by condensation is very rapid compared to liquid phase techniques [149].

Most common flame-made materials have spherically shaped primary particles. However, also cubic, polyhedral and rod like shapes have been synthesized using FSP [144]. Suzuki et al. investigated the formation of several oxides using an inductively coupled plasma (spray-ICP) method. They synthesized plate-, bar- and foil-like, polyhedral and cubical particles and confirmed that some oxides revealed a primary particle morphology characteristic of their crystal structures and the related surface energies [150]. They suggested that gas-solid reaction, occurring on the surface of nuclei, control predominantly particle growth of non-spherical particles. Atoms or molecules condense from the gas phase and not by coalescence as described in the next section. Tani et al. synthesized ZnO particles using FSP and observed a rod-like shape for primary particles at higher solution feed rates. They postulated that this rod-like particles may indicate that the ZnO particles are also predominantly formed by surface growth of the primary particles rather than by coalescence [151].

3. Particle growth by coalescence

Coagulation of particles takes place at high particle concentrations and is a consequence of particle collisions. The coagulation theory bases on collisions related to Brownian motion and field forces e.g. gravity and internal electric fields. Assuming strong adhesive forces, which are characteristic for small particles, these collisions result in the formation of particle accumulations. In these cases, where the reaction temperature in the flame is

still high enough, the primary particles further grow by coalescence. Coalescence describes the process when several particles merge in order to reduce their surface free energy. The reason is that the surface of the resulting particle is smaller than the sum of the individual particles. The temperature dependence of the material properties determines the particle coalescence significantly. Figure 18 illustrates the coalescence process schematically.

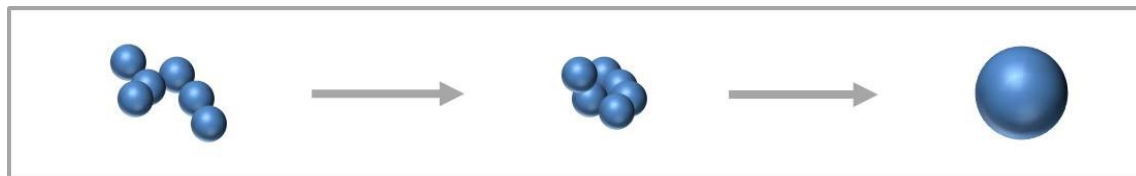


Figure 18: Particle coalescence

Self-preservation is a characteristic of particle size distributions attained in flame synthesis processes. Size distributions are self-preserving, in cases the different distribution fall on top of each other, when scaling them with factors, e.g. the average particle size. Since particle growth is controlled by Brownian coagulation, the geometric standard deviation of the self-preserving lognormal number distribution σ_{geo} for FSP synthesized particles is ~ 1.46 [152]. Particle size distributions which have a shape that is invariant with time and only depends on the collision frequency function, are characteristic for aerosols that undergo Brownian coagulation.

The relation between characteristic collision time and characteristic coalescence time describes the degree of coalescence [153]:

$T_{\text{coalescence}} < T_{\text{collision}} \rightarrow$ Spherical particle

$T_{\text{coalescence}} > T_{\text{collision}} \rightarrow$ Aggregate

In the case of a shorter coalescence time compared to the collision time, the aerosol consists of individual particles which completely coalesce after each collision. Whereas aggregates form when the collision time is shorter compared to the coalescence time [154], described in detail in the next section.

4. Particle aggregation

The complete coalescence, resulting in spherical particles, is only sufficiently fast in the high temperature zones of a flame reactor. In contrast, partial coalescence also known as the formation of sinter necks leads to the formation of aggregates. In this case, strong

covalent bonds connect the primary particles chemically. The driving force of these processes is again the reduction of surface area due to necking between particles. Figure 19 presents a schematic of the aggregation process, which results in the formation of so-called “hard agglomerates”.

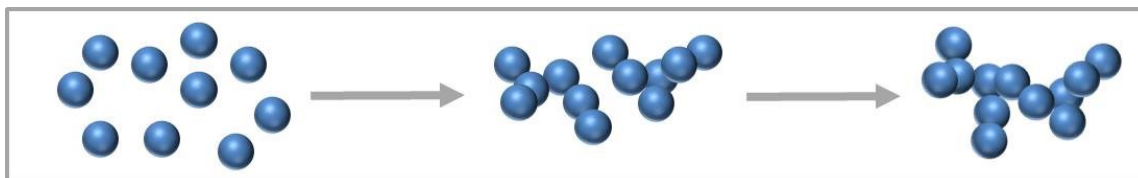


Figure 19: Formation process of aggregates

Windeler et al. postulated that the rate at which the coalescence time exceeds the collision time determines the particle shape and the extent of necking [155]. In these cases, the coalescence time exceeds the collision time and therefore, the shape of the individual particles retains. Subsequent collisions form aggregates composed of particles held together by weak van der Waals forces, represented in Figure 20 a. The degree of necking between the particles significantly increases when the coalescence time slowly becomes longer than the collision time. This formation of necks gives the resulting aggregate its strong hold.

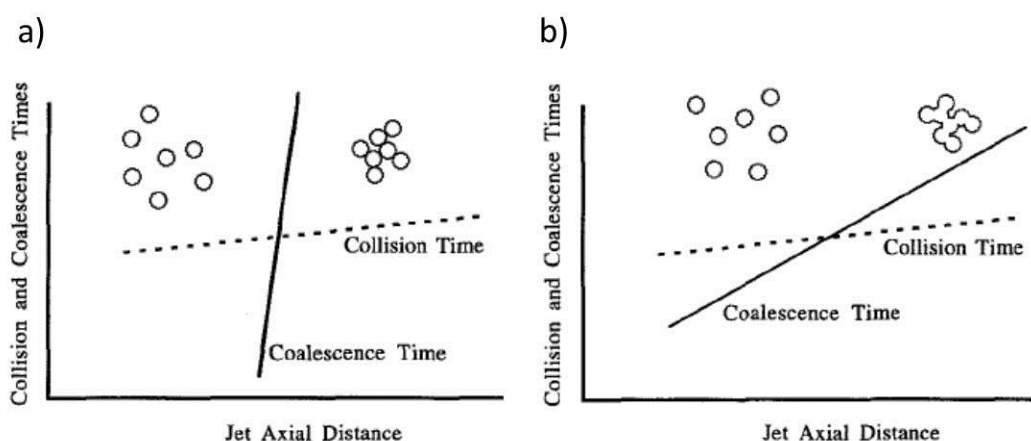


Figure 20: Schematic illustration of the Collision and Coalescence time a) Coalescence time quickly passes the collision time: weak van der Waals forces hold the particles together; b) Coalescence time slowly passes the collision time: particles form large necks (Reprinted with permission of ref. [155]).

In the examined flame process an aggregate is usually composed of a few to several hundred primary particles which are in the size range from 5 nm to 50 nm [156]. The fractal theory describes the structure of aggregates. Fractals are structures with

geometrically similar shapes at different levels of magnification as defined by Mandelbrot [157]. However, the scaling relationship for fractals is not fully accomplished for small aggregates since they contain only a few primary particles, therefore, their structure is considered as fractal-like. Particle cluster- particle cluster aggregation, where particle clusters containing a certain number of primary particle, coagulate with other particle clusters to form a larger aggregate is a suitable way to describe the formation of aggregates in the FSP process.

The fractal dimension D_f characterizes the structure and varies depending on the nature of the collision process. Chain-like agglomerates have a D_f of approximately 1 and for compact agglomerates, D_f approaches 3. Nanoparticle agglomerates synthesized by the FSP or other flame based methods result in a fractal dimension of $D_f = 1.8$ [154].

The number of primary particles (N_p) within an aggregate can be calculated based on the fractal dimension D_f , the radius of a primary particle (r), the gyration radius of the aggregate (R_g) and an experimentally determined fractal prefactor k_f as presented in equation (6).

$$N_p = k_f \left(\frac{R_g}{r} \right)^{D_f} \quad (6)$$

The fractal prefactor for FSP synthesized particle is $k_f = 1.3$ [154]. The ratio between full coalescence and neck sintering influences the average number of primary particles in an aggregate. The overall particle concentration and the residence time of the particles in the high temperature zone of the flame highly influence this ratio. Faster cooling rates and high temperatures favor the formation of less aggregated particles. Laser irradiation or electrical fields can also influence the degree of particle aggregation, generally resulting in less aggregated structures [144].

A more practically orientated method to determine the average number of primary particles (N_p) is based on the mobility diameter (d_m), as shown in equation (7). Eggersdorfer et al. determined experimentally the constant prefactor $k_m = 1$ and the mass-mobility exponent $D_{fm} = 2.15$ for FSP synthesized aggregates using differential mobility analyzer (DMA) and aerosol particle mass (APM) measurements [158].

$$N_p = k_m \left(\frac{d_m}{r} \right)^{D_{fm}} \quad (7)$$

Compared to the gyration radius, the mobility diameter d_m of the aggregates can be determined more easily in experiments. Here, the differential sedimentation in a sucrose gradient due to high rotation of the centrifuge gives rise to the mobility diameter of the

aggregate. Another method is the already mentioned differential mobility analyzer (DMA) which works based on a size-selective electrostatic precipitator.

In the recent years, detailed theoretical studies on the dynamics of the aggregation process of fractal elements have been published [159-163]. The studies using e.g. discrete element modeling (DEM) to investigate influencing parameters on the particle diameter and the extent of aggregation e.g. TiO_2 [164-166], SiO_2 [131], or ZrO_2 [158].

5. Agglomeration

In cases, the temperature in the flame drops below the sinter temperature of the oxide, the formation of so-called (soft) agglomerates starts. Agglomerates are groups of aggregates kept together by mainly physical bonds and can be broken up quite easily. Capillary forces, van der Waals forces and electrostatic forces dominate these physical bonds. Salameh et al. studied the rearrangement within agglomerate structures in detail and demonstrated an unfolding and breakage process of agglomerates [167]. This process starts with the formation of a roughly linear chain of aggregates until a breakage of a chain based on aggregate detachment at a primary particle –particle contact takes place. The identified specific kinetics during the aggregate rearrangement are rolling, sliding, or torsion. They also demonstrated that the established macroscopic models such as capillary forces and van der Waals forces are not sufficient to describe the acting contact forces correctly. A combination of non-continuous solvation forces and capillary forces describes the contact forces acting between the single primary particles/aggregates in the agglomerate more sufficiently.

The following chapter highlights the presence of significant temperature gradients within the reaction zone of the flame process. Therefore, it can be assumed that all presented reaction mechanisms (1-5) are coexistent within the flame reaction zone.

3.2.2 Temperature profile and synthesis parameters

Schulz et al. [168] and Gröhn et al. [145] performed fundamental work on the experimental investigation of the temperature and flow characteristics in the single flame spray process. Gröhn and coworkers additionally conducted Computational Fluid Dynamics (CFD) simulations of the single flame combustion process and combined this analysis with particle formation models. Noriler et al. investigated the FSP flame regarding the chemistry-turbulence interaction for the description of the combustion reactions [169].

Figure 21 presents the experimentally determined flame temperature of Schulz and coworkers [168]. A constant temperature region up to 2500°C characterizes the highly exothermal precursor combustion up to 5 cm above the burner. This constant region follows a significant temperature decrease with increasing height above the burner. This decrease results from the flame expansion due to air entrainment. The high gas velocities in the flame lead to short residence times of the synthesized particles of a few milliseconds.

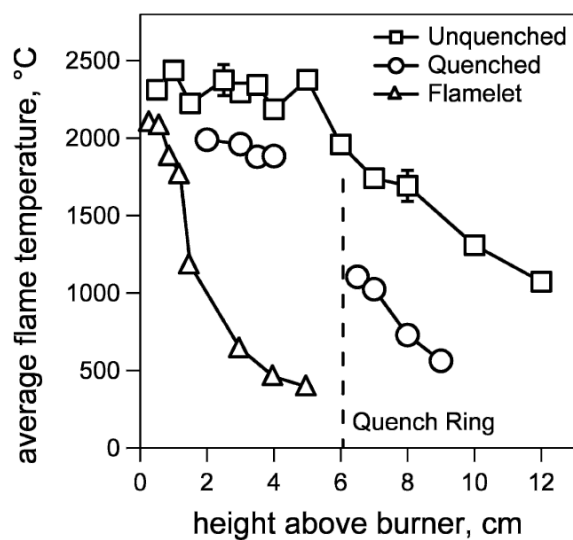


Figure 21: Temperature profile of the flame spray at standard conditions (squares), with quench ring installed at 6 cm (circles) and without precursor feed (triangles). (Reprinted with permission of ref. [168])

Adjustments of the synthesis conditions strongly influence the particle characteristics of FSP synthesized particles. The main parameters influencing the time/ temperature profile during the synthesis process are the following:

- Reactor geometry
- Mass flows of the precursor and dispersion gas
- Type of carrier gas
- Reaction pressure
- Precursor (e.g. different decomposition kinetics and reaction enthalpies)

The application of a quench ring also affects the temperature profile since it reduces the temperature significantly; see Figure 21 (circles). Its application stops the particle growth and lead to a reduced primary particle size and further suppresses the formation of aggregates.

A high precursor flow rate, leads to a high concentration of the precursor within the flame and an enlargement of the high temperature zone combined with an increase in particle size. Increasing the dispersion gas flow rate, in contrast, reduces the flame height. This shortens the residence time and results in smaller particles. This trend is demonstrated for different oxides e.g. bismuth oxide [170], ceria [171] and zinc oxide [151]. Mädler et al. [2] investigated the influence on the combustion enthalpy of the solvent and the choice of the dispersion gas in detail. Experiments have revealed that in cases the oxidant is oxygen, the droplets burn much faster than in air. The particles longer remain in the high temperature regime which results in an increase in particle size [2]. Next to the flame temperature has the choice of the precursor a huge influence on the particle characteristic since it influences, the nucleation process significantly.

The morphology of the synthesized particles further depends on the evaporation rate of the precursor solution. Spherical primary particles in an aggregate form when the evaporation time is short and the particle formation takes place as described in section 3.2.1. In contrast an incomplete droplet evaporation leads to hollow and shell-like micron-sized particles [144].

While most of FSP synthesized particles are metal oxides, the synthesis of metallic nanoparticles is possible under restrictive oxygen flame conditions. An inert gas-filled glove box, for example, provides an atmosphere with a reduced amount of O₂ which still has a sufficient amount of O₂ for the complete combustion of hydrocarbon fuels [1].

3.2.3 Synthesis of multicomponent particles

Dependent on the kinetics and the thermodynamics of the applied materials a synthesis of different types of multicomponent materials in the conventional FSP process is possible as illustrated in Figure 22.

Route I represents the typical formation route of a single material as described in detail in the previous section. In route II, a surface layer of one component fully coats a host particle. Schulz et al. presented an example with a SiO₂ coating on a Ce_xZr_{1-x}O₂ host particle [140]. When a full encapsulation is not attainable, either due to insufficient amount of the secondary component or due to phase segregation, small atomic clusters form on the surface of the other component. Route III presents this deposition on various metal oxide supports. It takes mostly place for fine noble metals (Ru, Rh, Pd, Ag, Pt to Au) or even alloys [1]. In most of the cases, the low boiling/sublimation points of the noble metals relative to that of the oxide supports allow sequential nucleation and growth

along the concentration gradient of the spray flame. The support metal oxide firstly nucleates at high temperature followed by a heterogeneous nucleation of the noble metals at cooler downstream gas temperature. The rapid quenching of the high flame temperatures and the short residence times, significantly prevent sintering of the noble metals on the support surface. The noble metal (or deposit) particles maintain their high surface dispersion. A strong interaction with the support limits the mobility of the deposits and its sintering. This leads to a high temperature stability of the multicomponent particles. Kydd et al. further have successfully deposited non-noble metal CuO on a CeO₂ support [172].

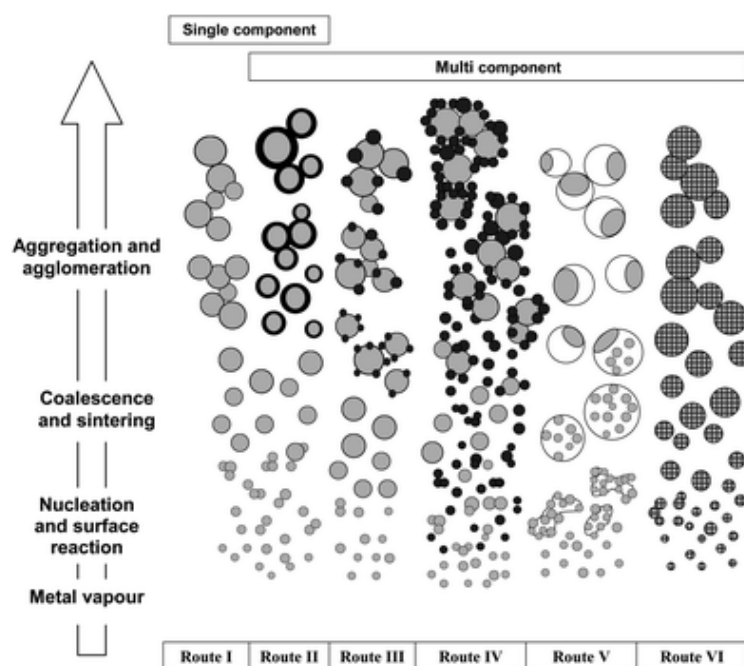


Figure 22: The formation of different types of multicomponent materials using the conventional FSP process (Reprinted with permission of ref. [1])

In some multicomponent systems, the different particle phases tend to segregate completely (Route IV). This results in a low miscibility of the components and a particle-particle mixture with only physical cohesion. However, this route is very unusual in a single flame process. It has so far only been reported for the CeO₂/Bi system applying a restrictive oxygen flame [173]. Route V represents the formation of polycrystalline particles. Here, two components e.g. SiO₂ / ZnO form individual phases within a single particle [174, 175]. Route VI describes homogeneous mixing in the form of mixed metal oxides and doped structures. A broad variety of materials has been synthesized using these methods reaching from Fe-doping of ZnO [176] or TiO₂ [177], solid solutions e.g. Ce_xZr_{1-x}O₂ [178] to mixed metal oxide phases e.g. BiVO₄ [179].

Especially the synthesis of particles using routes II-IV are somewhat limited by the thermodynamic properties, e.g. the differences of the vapor pressures. Difference in boiling points and solid-state phase miscibility of deposit-support materials play a central role in the synthesis process. This is particularly important when the deposits nucleate at high temperature and solid-state reaction, e.g. phase miscibility, formation of complex oxides with support materials cannot be neglected [1]. The double flame system introduced in the following section helps to avoid these limitations.

3.3 Double flame spray pyrolysis

The combination of two single FSP reactors to a double flame (DF) Spray Pyrolysis configuration offers the possibility to synthesis a variety of multicomponent materials.

In the DF set up the particle characteristic can be uncoupled from thermodynamic properties. This allows to tailor the mixing state and to tune the individual particle sizes. The particular materials nucleate in different flames and the intersection of the two flames at a defined distance and angle results in a certain mixing state. The geometric configuration and the corresponding process conditions (e.g. temperature) in the mixing zone influence the resulting material characteristic significantly. The concentration ratio of the sprayed components, the adjustment of the geometric flame parameters and the physical properties of the single components allow the tailored synthesis of mixing states within a single particle or within a deposited and an aggregated system presented in Figure 23.

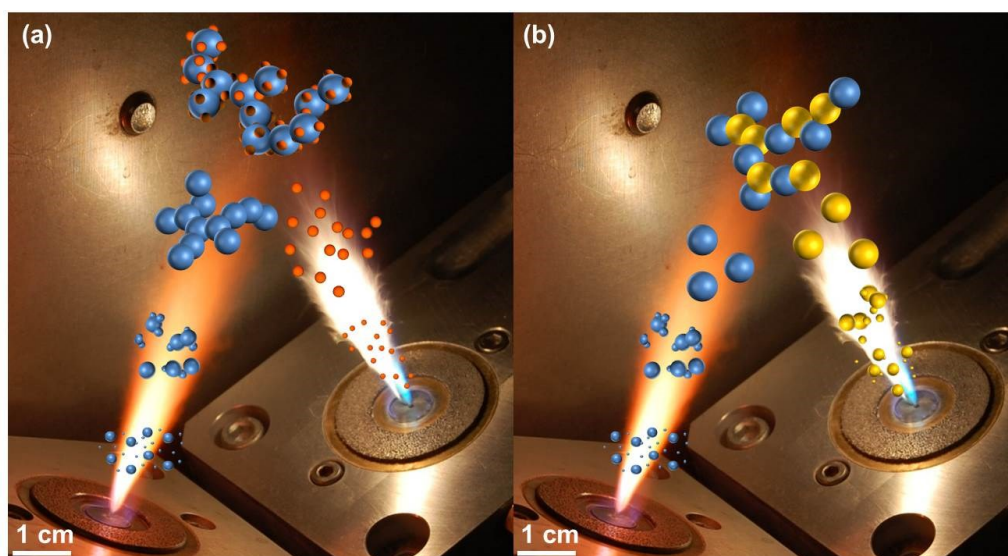


Figure 23: The DF configuration allows the synthesis of a deposited particle systems (a) or an aggregated system (b).

Table 1 on page 20 summarizes various possibilities for multicomponent catalysts ranging from binary to quaternary systems. A single step synthesis of these different mixing stages is realizable when applying the DF configuration. The DF enables the combination of two single flames in various combinations: One flame synthesizes mixed metal oxide particles containing two components (Route VI Figure 22) whereas the second flame synthesizes a deposited system (Route III). This type of combination enables e.g. the partial deposition of an active component on one of two different support components.

The number of publications reporting novel materials with DF Pyrolysis has increased considerably within the last couple of years demonstrating a broad range of applications [76, 77, 180-189]. Ernst et al. [181] separated the synthesis of carbon support and Pt particles into two flames allowing the surface deposition of Pt on carbon compared to carbon-coated Pt particles made in a single flame. Strobel et al. introduced the DF process for the synthesis of NO_x storage-reduction catalysts as it allows the preferential deposition of noble metals on either the support or the storage component, as shown for Pt/Ba/Al₂O₃ [76] and Pt/Ba/Ce_xZr_{1-x}O₂ [77]. Here, they have combined the synthesis of a deposited and an aggregated particle system using the DF approach. The elimination of an inactive spinel phase in the DF process was investigated by Høj et al. [184] and Tepluchin et al. [186]. Wang et al. synthesized an Al₂O₃/ SiO₂ support in one flame and palladium as the active component in the other flame and tested the catalysts for their hydrogenation of a model aromatic ketone acetophenone [185]. All studies highlight that the two individual flames allow a higher flexibility in tuning the resulting catalyst properties, final composition and size. The temperature profile along the flame axes, mainly adjusted by the intersection distance are the key parameter within the DFSP process and influence the composition of the synthesized material directly. So far, the focus of all the performed studies was mainly on the application of different material systems rather than a study of the process conditions themselves.

Figure 24 represents the ideal cases of the multicomponent particle formation in the DF process. The adjustment of the nozzle distance d and the intersection angle α define the intersection distance l . The intersection distance further influences the synthesized mixing state. The intersection angle α influences how uniform a certain mixing state is synthesized.

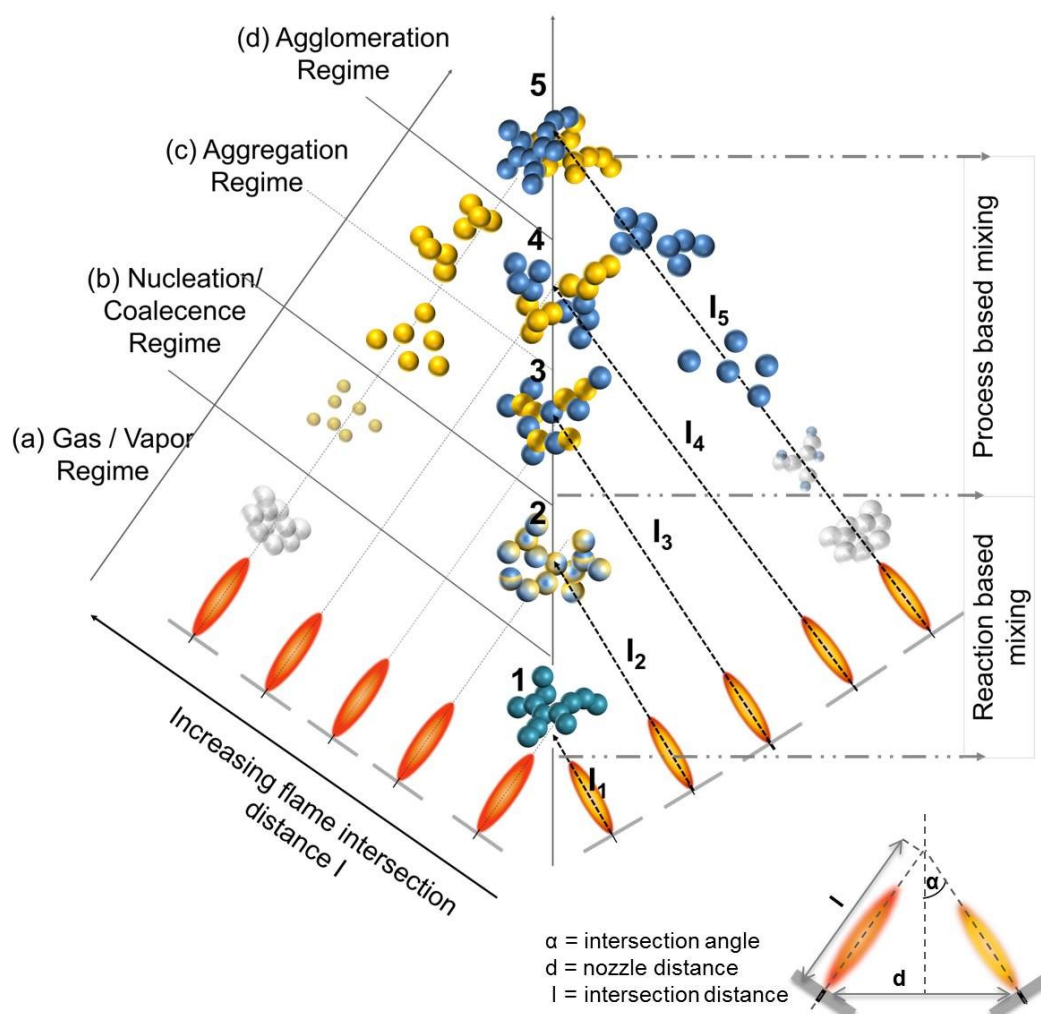


Figure 24: Illustration of the influence of the intersection distance on the resulting mixing state within an aggregated system. The schematic can be adopted for a deposited system.

(a) Intersection in the gas / vapor regime: The intersection distance of the flames, when both precursors are still in gas/ vapor phase, results in atomic mixing and the formation of mixed metal oxides or doping comparable with route VI in Figure 22. The intersection in the gas / vapor phase allows the synthesis of mixtures on atomic scale based on two immiscible precursors, which might be limited in the single flame approach.

(b) Intersection in the nucleation / coalescence regime: Mixing in a zone, where nucleation and primary particle formation starts, can result in the formation of polycrystalline particles, described in Route V in Figure 22. The characteristic of the synthesized particles highly depends on the miscibility of the material. When the two particle materials tend to segregate, the formation of individual primary particles is possible. A high miscibility favors the formation of polycrystalline particles up to a mixture on atomic scale, due to supplementary diffusion processes.

(c) Intersection in the aggregation regime: An increase in the flame intersection distance, up to the aggregation regime, favors the formation of individual oxide particles, which form a mixture on particle scale. Since the temperature at the intersection point is sufficient for partial sintering, the different primary particles are chemically bonded (sintered) at their interfaces.

(d) Intersection in the agglomeration regime: A further increase in intersection distance, associated with a decrease of the temperature in the mixing zone, leads to a mixture on agglomerate scale. A single aggregate contains primary particles of a single element / oxide or with the same mixing state. The aggregates exhibit physically bonding to each other.

The reaction zone is characterized by steep temperature gradients along the flame axis and in horizontal direction. Since the temperature induces the particle formation regime, it is assumed that the described regimes are present in parallel during the synthesis process.

4 Synthesis of multicomponent catalysts using the double flame

Multicomponent materials are the building blocks for novel efficient catalysts. Chapter 2 presents a discussion of the different types of multicomponent catalysts and summarizes their diversity and applications. Chapter 3 introduces the flame process as a suitable method for the single step design of multi component catalyst. The following chapter 4 presents in detail the tailored double flame synthesis of a binary and a ternary material system for two different catalytic applications.

The first study focuses on a flame made binary catalyst for the Fischer-Tropsch synthesis. Chapter 4.1 presents the basics of the Fischer-Tropsch reaction and highlights the state of the art catalysts for the process. Chapter 4.2 contains insights on the flame synthesis of the binary catalysts, which consist of small cobalt particles dispersed on an Al_2O_3 support and presents the catalytic results of the test reactions.

The second study investigates the tailored design of a ternary catalyst for the preferential oxidation of carbon monoxide (PrOx). Chapter 4.3 presents the basics of the PrOx reaction and highlights the state of the art catalysts for the process. In chapter 4.4 is the focus on the tailored synthesis of a ternary catalyst. The desired characteristic is a mixture of CeO_2 and Fe_2O_3 on particle scale and partial deposition of Pt on the Fe_2O_3 surface. A selective variation of the catalyst structure, due to parameter adjustment in the synthesis process, helps to determine essential insights on the synthesis process. It further provides a basic understanding of the reaction mechanism and is therefore a milestone on the way to a tailored catalyst design.

4.1 Fundamentals of the Fischer-Tropsch-synthesis

The Fischer-Tropsch (FT) synthesis is an industrial process to produce energy rich hydrocarbon-chains from syngas mixture of CO and H_2 [10-12]. The applied syngas can be gained from different raw materials such as coal (Coal to Liquid - CTL), natural gas (Gas to Liquid - GTL) or biomass (Biomass to Liquid - BTL). Figure 25 illustrates the basic reaction of the FT-reaction on the surface of a heterogeneous catalyst. The basic reactions of the FT process are the formation of paraffinic (8) and olefinic (9) chains, where n is typically in the range of 10-20.



Next to the advantage of a sulphur- and nitrogen-free synthesis, the FT process can have, depended on the applied catalyst, a high selectivity for straight-chain alkanes which are suitable as diesel fuel. Undesirable side reactions are the formation of methane ($n = 1$). In addition to alkanes, small amounts of alkenes, as well as alcohols and other oxygenated hydrocarbons form as side products.

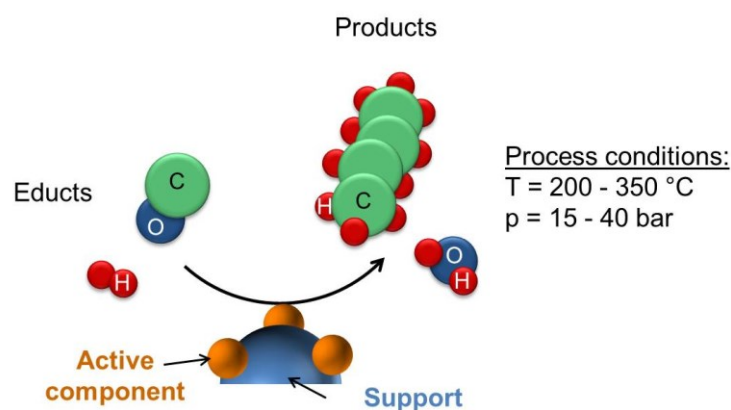


Figure 25: Schematic representation of the Fischer-Tropsch reaction on the catalyst surface.

The development of the technology started in the early 1900s. In Germany this method was applied during the 1930s and 1940s to produce liquid fuels from syngas-derived coal [190, 191]. After the Second World War, the company Sasol started the production of gasoline and diesel fuel via the Coal to Liquid - CTL route [11, 15, 192]. The economic viability of the CTL approach is significantly influenced by the political situation of the producing country (e.g. existing embargoes) and got financially unattractive with decreasing oil price in the 90's [11]. One economic way to produce synthesis gas is the direct usage of natural gas, obtained as by-product from oil production. Sasol and Qatar Petroleum have realized this Gas to Liquid - GTL route on industrial scale, for example, in Qatar [193].

The most promising route regarding the future feasibility is the Biomass to Liquid – BTL one. Because of the limited crude oil reserves, an increasing awareness for the climate change and the duty toward future generations to economize responsible with our energy resources, the FT process is undergoing a renaissance. The research effort in

this field drastically increased within the last years. Next to the development of new reactor technologies, the development of new catalysts with high activity and selectivity are essential to secure the profitability of the process in the long term [194].

4.1.1 Fischer-Tropsch-catalysts

The two main functions of the catalyst are the activation and dissociation of CO bonds and the formation of C-C and C-H bonds. Temperatures in the range of 200–350°C and a pressure in the range of 1.5–4.0 MPa are characteristic conditions for the FT synthesis. The employed catalysts typical consist of group VIII transition metal oxides. Vannice et al. [195] showed that the molecular average weight of hydrocarbon chains produced by FT synthesis decreased in the following sequence: Ru > Fe > Co > Rh > Ni > Ir > Pt > Pd. Only Ru, Fe, Co and Ni have catalytic characteristics that are appropriate to consider them for a commercial production. However, under practical reaction conditions, Ni based catalysts produce specific methane. Ru is too expensive and its worldwide reserves are insufficient for large-scale industry [191]. Therefore, Co and Fe-based catalysts are the preferred choice for FT diesel synthesis. Especially Co based catalysts have a high hydrocarbon selectivity, thus, a yield of straight-chain alkanes, and low activity for the water gas shift reaction [196]. To reach the required activity of the catalysts a high dispersion of small cobalt particles ideally in the range of 6 – 10 nm [197, 198] on a stable support is mandatory. [11, 191, 199-201]

Silica has intensively investigated as support materials, since it offer high specific surface areas [202, 203]. However, industrial Co-based FT catalysts are routinely prepared on an alumina support. This support has the advantage of high mechanical strength, a good thermal stability and advanced textural structures [202-206]. Yet, a major problem associated with the use of alumina is the potential formation of cobalt aluminates. Cobalt aluminum spinels are only reducible in hydrogen at very harsh conditions. This characteristic can result in a significant and undesired loss in catalytic activity [207, 208].

4.1.2 Flame made Fischer-Tropsch-catalysts

So far, two authors worked on the flame-based preparation of Co catalysts specifically for the FT reaction. Chaisuk and co-workers proved the general scalability of the FSP process to produce ZrO₂ supported Co-FT catalysts resulting in catalysts with different Co dispersion by varying the preparation parameters, such as precursor feed rate and the concentration of the solution [209]. The catalyst testing in the FT reaction occurred at atmospheric pressure and at an operation temperature of 220°C. Teoh et al. studied a

flame made Ru-doped cobalt-zirconia catalysts with the outcome that their performance is competitive with a benchmark catalyst obtained by classical impregnation under industrially relevant conditions [210]. This demonstrates the potential of the FSP process to synthesis Co-based FT catalysts. Further, flame made cobalt oxide on different supports was tested for reactions other than FT. Turrà et al. e.g. investigated Co/SiO₂ structures, synthesized using FSP [211]. Høj et al. studied the preparation of Al₂O₃ supported Mo/Co nanoparticles for hydrotreating applications and faced the difficulty of cobalt aluminate formation during single flame synthesis [81].

4.2 Flame synthesis of a supported catalysts for the Fischer-Tropsch reaction

The following study explores the DF synthesis of a catalyst which consists of small cobalt particles deposited on Al₂O₃ as a state of the art support for FT reactions. The aim within this deposited system is to achieve a mixture on particle scale (3). The challenge in the synthesis of this multicomponent catalyst is to suppress the formation of inactive mixed metal oxide phases.

Whereas the single flame process (SF) forms the undesired cobalt aluminate spinel phase (1), the double flame approach offers the potential to suppress its formation and to result in a reducible and active Co catalyst supported on Al₂O₃. The hypothesis of the study is that the systematic variation of the intersection distances of the two aerosol streams influences the characteristic of the synthesized catalysts as illustrated in Figure 26. Small intersection distances are assumed to result in the formation of mixed-metal-oxides, eventually in form of polycrystalline particles with Al and with Co rich areas (2). The adjustment of higher intersection distances offers the desired mixture on particle scale (3).

A further increase in intersection distance is assumed to result in a mixture on cluster scale and is therefore related with an undesired decrease in the degree of mixing (4). In the physically mixed sample (PM), the mixture of the two components is on aggregate scale, lacking the formation of chemical bonding at the interface (5). Both the mixture on cluster and aggregate scale would result in reduced temperature stability, because of an intimate contact between the sinter active Co-particles and the missing stabilization on the Al₂O₃ support.

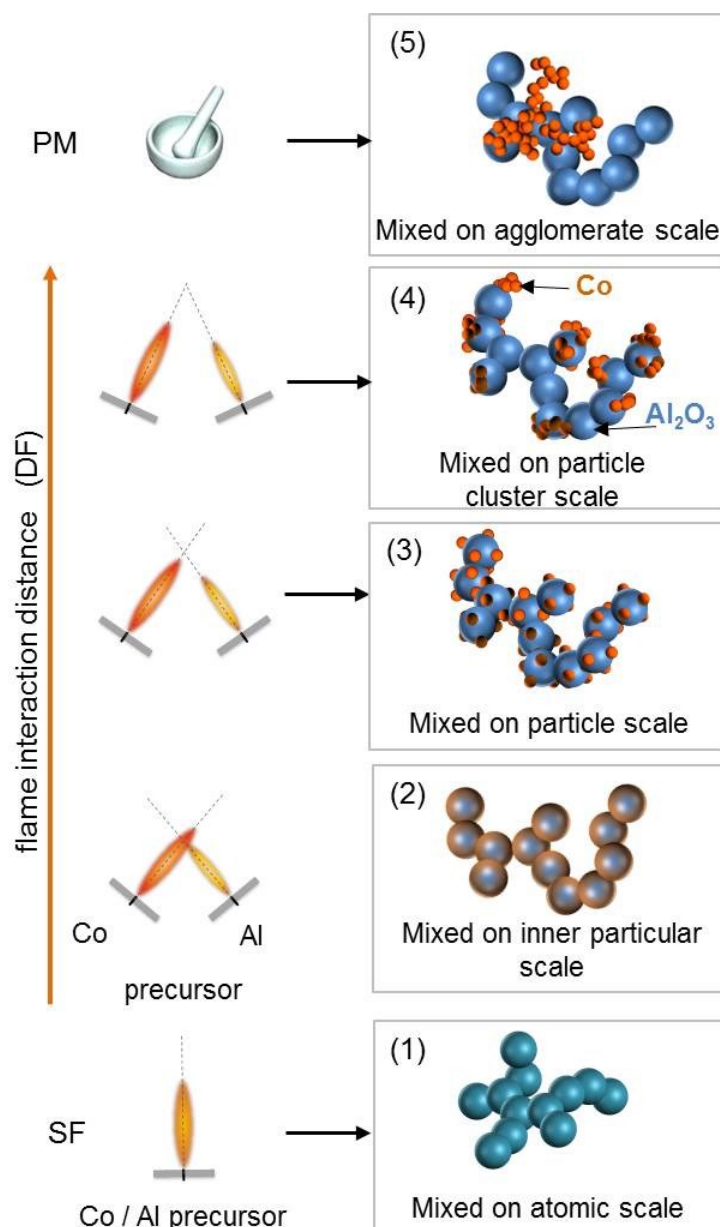


Figure 26: Working hypothesis for the formation of the resulting catalysts sprayed with different flame geometries (SF = single flame, DF = double flame, PM = physical mixture).

The purpose of the study is to find the specific intersection distance for the Co / Al₂O₃ material system, where a mixture on particle scale takes place. The requirement is a stable and uniform dispersion of the Co particle on the Al₂O₃ support. A final test of the synthesized particles demonstrates its catalytic activity and selectivity in the FT-reaction.

4.2.1 Synthesis and characterization of binary Al₂O₃ / Co catalysts

Different catalysts with a Co content of 10 wt. % help to get a full picture regarding the influence of the intersection distance on the material formation. The DF synthesis

process provides samples synthesized with four different intersection distances of the flames. The SF process offers the base for synthesizing additional two types of alumina-supported catalysts: The first way is a subsequent deposition of flame made cobalt particles / aggregates on an alumina support. The second way is to spray the two metals combined in the single flame. For the latter conditions two different settings are synthesized: one with the same 10 wt. % Co loading as used for the DF samples and one with a distinctly higher cobalt loading of 50 wt. %. This helps to understand the effect of increasing Co content in the spinel phase. Pure cobalt oxide and alumina nanoparticles serve as references from the SF approach. Table 2 lists all specifications of the samples, notation, synthesis method, amount of cobalt in the powder, flame parameter including intersection distance and angle and the specific surface area of the samples.

Table 2: Overview of the synthesis conditions and the specific surface areas (SSA)

Notation	Synthesis method	Amount Co [wt. %]	Intersection distance l [cm]	Intersection angle α [°]	SSA [m²/g]
Co₃O₄	SF	100	---	---	98
Al₂O₃	SF	0	---	---	153
SF 10 % Co	SF	10	---	---	130
SF 50 % Co	SF	50	---	---	129
DF 15	DF	10	15	20	94
DF 17	DF	10	17	20	92
DF 26	DF	10	26	20	123
DF 51	DF	10	51	10	178

While the two single flame made Co/Al₂O₃ powders exhibit a similar surface area independent of the Co content, a significant increase in the specific surface areas (SSA) of the DF powders is observable. Its increase rises from around 90 m²/g for the DF 15 and DF 17 sample to 178 m²/g for DF 51. This trend leads to the conclusion that the particle formation differs dependent on the intersection distance. Spraying in the single flame or adjusting small intersection distances leads to an interaction of the alumina and cobalt molecules, respectively particles, in the nucleation and coalescence dominated regime as already discussed in chapter 3.3. Here, the temperature is still high and primary particle formation is in progress. A mixture of Co and Al on atomic scale is likely, resulting in a formation of an Al-Co spinel. When the flames intersect at high distances, the temperature in the mixing zone is lower and primary particle formation completed. In this stage, aggregation and deposition instead of coalescence dominates the mixing process of the two components.

The observed differences in primary particle size indicate a significant difference in the mixed oxide composition for the small intersection distance (DF 15) compared to the SF powder. STEM and EDX analysis of various particles in different areas of the sample (exemplary presented in Figure 27) confirm this assumption. Co is homogeneous distributed within a single particle in the SF sample. The DF 15 samples in contrast exhibits large pure alumina areas and small Co enrichments forming deposits (bright spots). The conduction of zero loss images and Co mappings is necessary to determine changes in the particle size distribution of this Co deposits. They are carried out for all DF samples and presented exemplary for DF 15 and DF 51 in Figure 28. For all as-prepared DF powders, the cobalt deposits disperse well on the alumina support. Changes in the intersection distance do not affect the size of the cobalt rich particle significantly. They have an average diameter of about 12 nm. The TEM diameters of the alumina support particles are in the range of 4 to 40 nm (Figure 32), showing a decreasing trend for higher intersection distances.

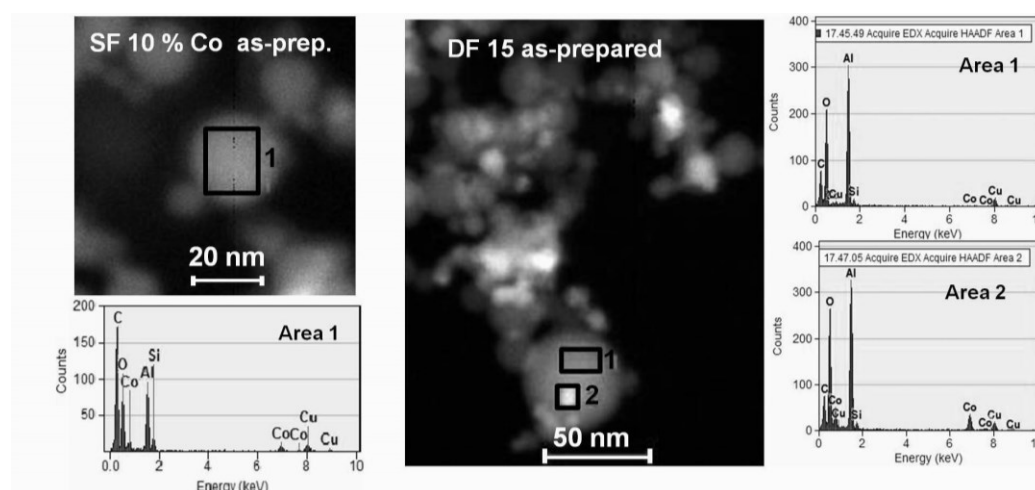


Figure 27: STEM images and EDX analysis indicating a homogeneous Co distribution within a single particle for the SF 10 % Co sample (left). The DF 15 catalyst (right) in contrast exhibiting large pure alumina areas (1) and small Co enriched areas (2).

The measurable changes in particle size and distribution of the DF samples are clearly associated with the increase in intersection distance and base on several physical and chemical reasons. These reasons presumably arise all simultaneously: First, the temperature history of particles travelling through the flame changes with intersection distance. For small intersection distances, the entrainment flow, which has a cooling effect on the flames, is limited. Secondly, a higher combustion enthalpy density (higher energy per volume ratio) [212] is provided through the second flame, leading to a longer residence time of the particles at high temperatures. Both effects result in an increase of primary particle size due to an extended coalescence dominated phase. For high

intersection distances, the second aerosol stream might increase the degree of turbulence and the entrainment. This results in an additional cooling of the aerosol streams and in a lowering of the primary particle size. However, detailed CFD calculations are required for the validation of this assumption. Strobel et al. [76] and Høj et al. [184] reported a trend of decreasing particle size with increasing intersection distance for different material systems. Besides this, the limitation of entrainment also leads to higher particle concentrations in the mixing zone when the two flames interact at small distances compared to individual flames (full entrainment from all directions). The coalescence rate increases and promotes the synthesis of large particles. This effect explains why the alumina particle size of as-prepared DF catalysts decreases with increasing intersection distance. The cobalt oxide particle size stays constant, even so different cobalt spinel phases are formed and this formation can be related with different particle sizes [213].

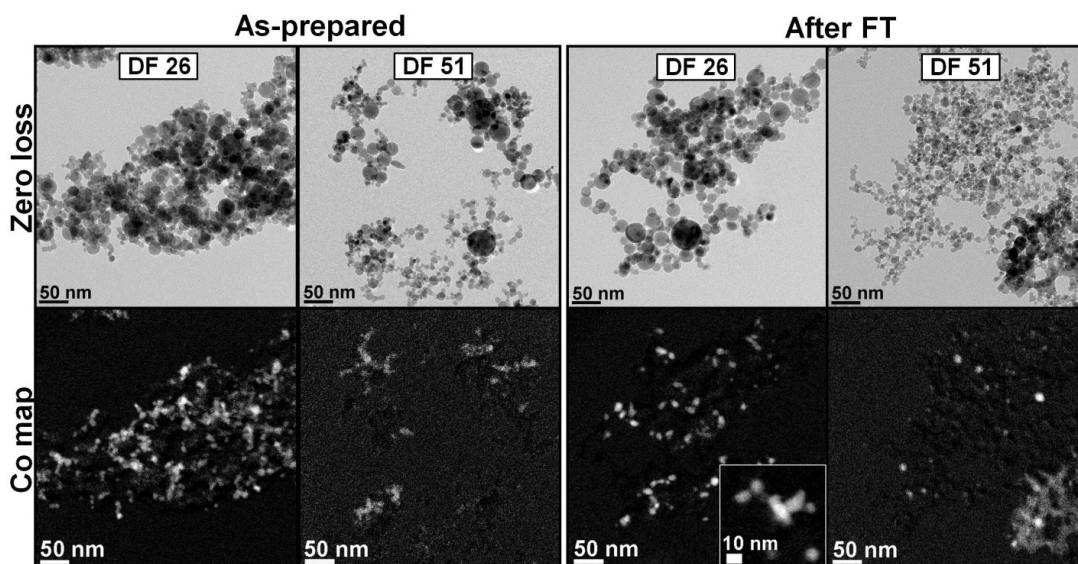


Figure 28: Zero loss and Co EF-TEM mappings of the FT active DF 26 and DF 51 catalysts before (left) and after FT catalysis (right). The inset shows Co particles with a higher magnification.

To get a more detailed insight in the different catalysts formed using DF, the determination of the crystal phases is essential and realized using XRD analysis (Figure 29). The patterns of the pure cobalt and the pure alumina samples, synthesized in the SF approach, help to indicate the major phases. Cobalt forms Co_3O_4 while the alumina crystallizes in the $\gamma\text{-Al}_2\text{O}_3$ phase. In contrast to the pure oxides, a detailed phase assignment for all alumina-supported cobalt FT-catalysts is highly complex, since the formation of mixed metal oxides is related with nearly identical crystal structures. Pure

Co_3O_4 , as well as the cobalt aluminates Co_2AlO_4 and CoAl_2O_4 crystallize in the same cubic spinel structure and show only minor differences in their lattice constants: 8.036 Å for Co_3O_4 , 8.087 Å for Co_2AlO_4 and 8.092 Å for CoAl_2O_4 [214]. Next to this three stoichiometric spinels a large variety of non-stoichiometric cobalt aluminate spinel phases ($\text{Co}_{3-x}\text{Al}_x\text{O}_4$, $0 \leq x < 3$) exist [214]. This brings about very similar peak positions for all different material compositions and causes limitation in the exact phase determination. Nevertheless, based on the position of the reflexes, which shift to higher angles for increasing aluminum content, qualitative changes of the cobalt content within the spinel structure and the formation of pure alumina can be identified.

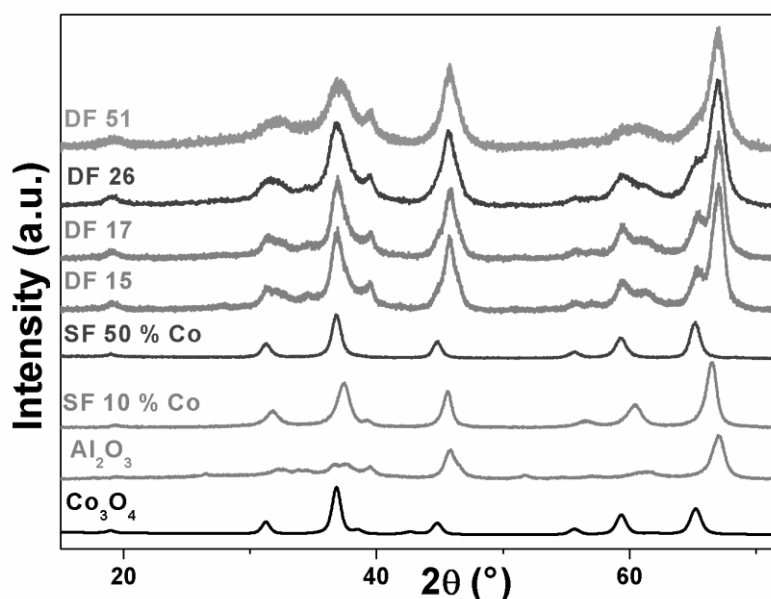


Figure 29: XRD patterns for the DFSP samples prepared with different intersection distances compared to patterns for samples prepared using the single flame (10 and 50 wt. % Co, pure Co_3O_4 and Al_2O_3).

The SF 10 % Co sample has a small alumina reflex at $2\theta = 38.5^\circ$ and all major cobalt aluminate spinel peaks. However, none of the stoichiometric spinels fit the recorded pattern of the SF 10 % Co sample exactly. The CoAl_2O_4 phase which contains the highest amount of aluminum in the stoichiometrically phases, has a strong reflex at $2\theta = 65.8^\circ$. In the SF 10 % Co sample this reflex is shifted 0.9° in direction of the pure alumina peak which is positioned at $2\theta = 67^\circ$. This shift reflects a calculated composition of $\text{Co}_{0.2}\text{Al}_{2.8}\text{O}_4$ and is an indication for either a high amount of Al bonded within a cobalt alumina spinel phase or a combination of pure alumina and CoAl_2O_4 . A specific differentiation between the two options is not possible based on the XRD results. For the SF 50 % Co sample, the main peak at $2\theta = 36.8^\circ$ is congruent with the characteristic Co_3O_4 reflex at $2\theta = 36.8^\circ$ and the spinel phases CoAl_2O_4 and Co_2AlO_4 at $2\theta = 36.7^\circ$.

The calculated composition of the SF 50 % Co sample matches nearly the CoAl_2O_4 spinel phase.

The DF samples present separate cobalt oxide and alumina peaks. The peak at $2\theta = 34.6^\circ$ clearly indicates the formation of pure CoO in the DF process. A possible explanation for the formation of CoO, rather than cobalt oxide in the highest oxidation state +3 (Co_3O_4) is the limitation of O_2 supply in the DF compared to the SF process, as discussed in the literature [213]. In addition, either pure Co_3O_4 or cobalt aluminate spinel phases are formed for the DF samples, a distinction between both is, however, not possible. The peak broadening of the DF samples indicates decreasing particle sizes, which is consistent with BET and TEM results. In addition, the observed increase in background noise reveals an increasing content of X-ray amorphous phases. The calculated content of the amorphous phase for the DF 26 sample is 17 % and increases to 37 % for the DF 51 sample.

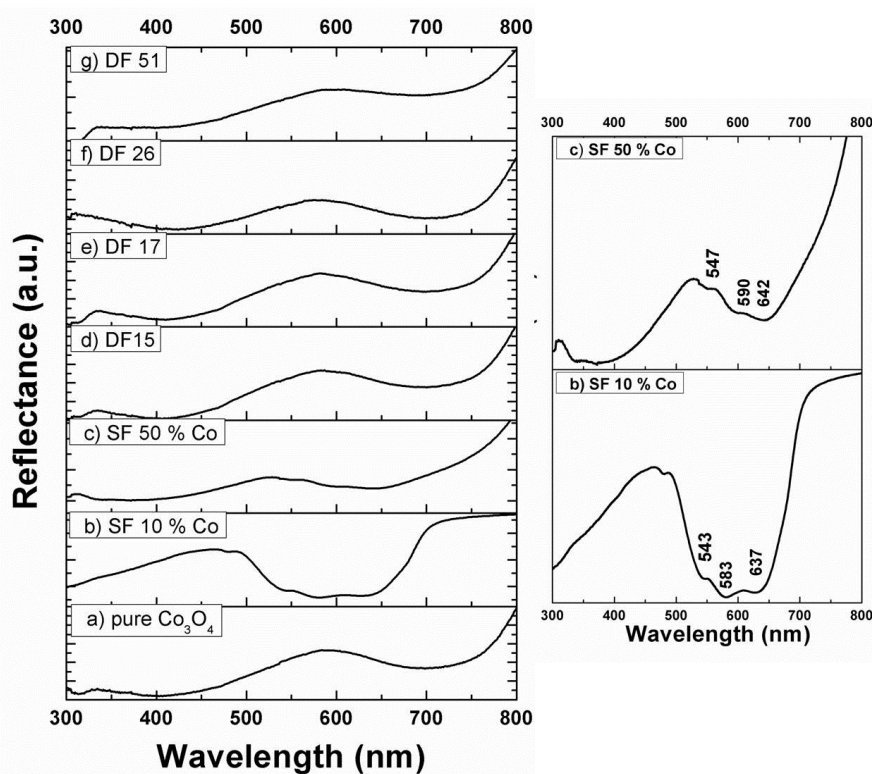


Figure 30: UV-Vis spectra of the SF 10 % Co and 50 % Co catalyst, all DF samples and pure cobalt oxide nanoparticles.

The determination of the oxidation state of the Co using UV-Vis gives more detailed insights in the stoichiometry of the formed spinel. Figure 30 shows the UV-Vis spectra in reflection mode. The pure cobalt oxide nanoparticles which are black in color show two broad bands at 400 and 700 nm attributed to the $^1\text{A}_{1g} \rightarrow ^1\text{T}_{2g}$ and $^1\text{A}_{1g} \rightarrow ^1\text{T}_{1g}$ transitions

of octahedral coordinated Co^{3+} [191, 215]. On the contrary, cobalt is tetrahedral coordinated in the SF 10 % Co sample, indicating an alumina rich spinel. The blue color of the SF 10 % Co sample corresponds to adsorption bands with minima at 543, 583 and 637 nm highlighted in the right part of Figure 30. The increase of the cobalt amount to 50 wt. %, results in a decrease of intensity of the three bands that are characteristic for tetrahedral coordinated Co^{2+} . Instead, a strong band at around 400 nm appears, attributed to the presence of Co^{3+} ions in octahedral sites. The powders synthesized with the DF have a greenish/black color. The UV-Vis spectra of all four samples exhibit similar features. No trend is visible which would provide a clear indication for changes in phase composition. Two broad bands at around 420 and 720 nm are characteristic for the observed color of the samples and represents cobalt in the oxidation state +3 [214, 216]. In contrast to the single flame prepared samples, the formation of an alumina-rich spinel with tetrahedral coordinated Co^{2+} is not observed, evidenced through the absence of the dominant triplet at 540-650 nm.

Temperature programmed reduction (TPR) is used to investigate the reduction behavior of the catalysts, since XRD and UV-Vis analysis are unable to indicate significant differences in the crystal structure of the Co rich mixed phases. Figure 31 presents the results. The FSP synthesized pure cobalt oxide nanoparticles show a two-step reduction behavior typically observed in the literature [217]. Whereas the first peak represents the reduction of Co_3O_4 to CoO , the second peak stands for a further reduction to metallic cobalt, consuming three times more hydrogen than the first step. The TPR spectrum for the SF 10 % Co catalyst only shows a dominant peak in the high temperature regime above 800°C while the catalyst with increased Co content (SF 50 % Co) exhibits low temperature peaks between $300\text{-}500^\circ\text{C}$ in addition to high temperature reduction peaks ($> 500^\circ\text{C}$). The peaks in the temperature regime below 500°C result from the reduction of pure cobalt oxide. The reduction of Co particles, which strongly interacting with the alumina support or the cobalt aluminates, takes place at higher temperatures [218, 219].

Combined with the information received from the XRD and UV-Vis analysis, the formation of cobalt aluminates in spinel phase, instead of pure cobalt oxide particles supported on alumina, is obvious when cobalt and aluminum precursors are sprayed as one feedstock in the single flame. The triplet band in the UV-Vis spectra (Figure 30) between 540 and 650 nm indicate the formation of an alumina-rich spinel with cobalt in the oxidation state +2 ($\text{Co}_{3-x}\text{Al}_x\text{O}_4$, $2 \leq x < 3$) for the SF 10 % Co catalyst. This is congruent with the XRD analysis even indicating the existents of pure $\gamma\text{-Al}_2\text{O}_3$ crystallites.

The high temperature peak above 800°C in the TPR profile indicated that this aluminum-rich spinel is hardly reducible under normal FT conditions [220] (Figure 31).

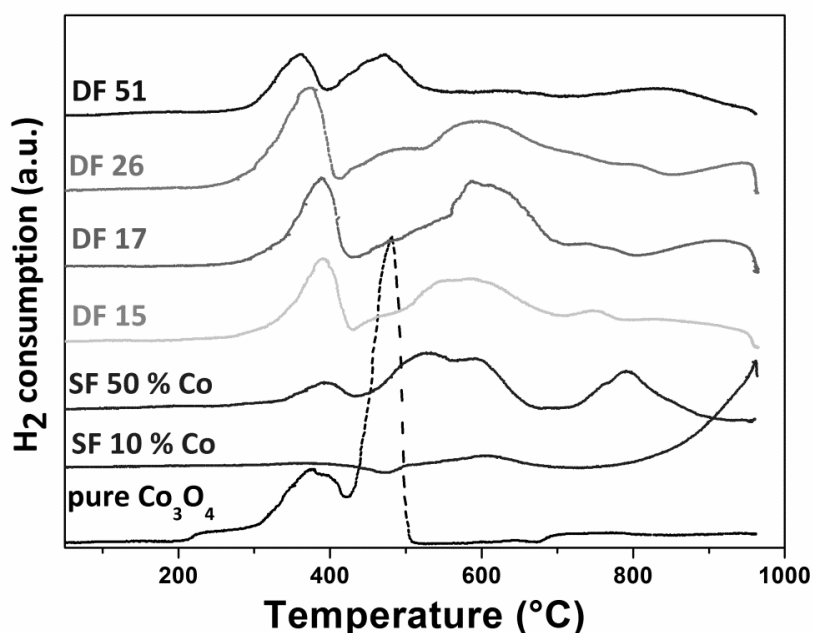


Figure 31: TPR profiles of pure cobalt oxide nanoparticles and in-situ alumina-supported cobalt catalysts (10 and 50 wt. % Co) synthesized using SFSP and DFSP catalysts with different intersection distances. The reduction profiles are recorded with a heating rate of 10°C/min.

To fully investigate the effect of an increased cobalt content on the resulting structure when using the single flame approach, the catalyst SF 50 % Co completes the study. The comparison of this sample to the SF 10 % Co identifies no structural changes with respect to surface area, particle size and shape (BET, TEM). However, the UV-Vis and TPR results point to the formation of pure cobalt oxide combined with cobalt aluminates. This formation is in agreement with the phase diagram [213] in regions where more cobalt is present than required for the formation of a stoichiometric spinel. The triplet UV-Vis band indicates the presence of octahedral coordinated Co^{3+} as found in pure Co_3O_4 and/or cobalt-rich aluminates as well as Co^{2+} . The later species points to an alumina-rich spinel, as cobalt exists exclusively in the oxidation state +2 in such an aluminate. The intensity of the corresponding band, however, is reduced compared to the SF 10 % Co catalyst. The work of Khodakov et al. supports that the formation of large amounts of hardly reducible spinel ($\text{Co}_{3-x}\text{Al}_x\text{O}_4$, $2 \leq x < 3$) can, thus, be excluded [191]. While UV-Vis is not able to distinguish between Co_3O_4 and cobalt-rich aluminates ($\text{Co}_{3-x}\text{Al}_x\text{O}_4$, $0 \leq x < 2$); TPR measurements clearly prove the presence of Co_3O_4 in the SF 50% Co sample. The typically observed two reduction peaks in the low temperature regime below 500°C indicate formation of pure cobalt oxide. The peaks with reduction

temperatures above 500°C, in contrast, are assigned to cobalt aluminates ($\text{Co}_{3-x}\text{Al}_x\text{O}_4$, $0 < x \leq 2$) with different Co compositions [220]. In summary, the structural data reveal the formation of cobalt oxide nanoparticles deposited on a cobalt aluminate support. Supposedly, such a system is catalytically active for FT; however, the high overall Co-content is not economically reasonable so any further investigation of this SF approach are conducted. As already stated in Figure 26 (a), cobalt and aluminum oxide prepared using the SF approach result in a mixture on atomic scale with variable compositions. The samples are either unreducible and FT inactive or economically unreasonable.

The DF approach reduces the spinel formation when generating alumina and cobalt oxide nanoparticles in individual flames. The process produces, depended of the intersection distance, individual and well-dispersed cobalt oxide particles on the alumina support. The TPR analysis in Figure 31 identifies significant differences between the four DF catalysts depended on the intersection distance of the flames: The low-temperature reduction peak at around 390°C for DF 15 shifts to 360°C for the DF 51 sample. In addition, the intensity of the peak positioned at 480°C (CoO to Co) increases from the DF 15 to the DF 51 sample. The lower intensity in the temperature regime above 500°C suggests that the amount of irreducible cobalt aluminate spinel is significantly smaller for the DF 51 compared to all other DF samples. In fact, the ratio between the areas of the peaks above 500°C and the areas of the peaks below 500°C decrease with flame intersection distance.

Hanssteen et al. investigated the reduction behavior for different cobalt aluminates with variable cobalt and alumina contents ($\text{Co}_{3-x}\text{Al}_x\text{O}_4$; $0 \leq x < 3$) in more detail [220]. As mentioned before, they reported an increase in reduction temperature with aluminum content. Based on their results, the DF 15 and DF 17 consist of greenish $\text{Co}_{2,5}\text{Al}_{0,5}\text{O}_4$ spinel with high cobalt content in the +3 oxidation state. The UV-Vis results support this assumption. The first reduction peak centered at about 390°C indicates that in this spinel type structure Co^{3+} reduces to Co^{2+} in the temperature regime below 500°C. Further reduction to metallic cobalt only occurs at temperatures higher 500°C since the alumina containing spinel matrix still incorporates the cobalt (Co^{2+}). This result indicates the formation of non-reducible cobalt aluminate particles deposited on an Al_2O_3 support. TPR measurements suggest that with a further increase in intersection distance (DF 26 and DF 51), the amount of hardly reducible $\text{Co}_{2,5}\text{Al}_{0,5}\text{O}_4$ decreases in favor of Co_3O_4 . The increase of the reduction peak at 480°C is one indicator. The first reduction peak for the catalysts DF 26 and DF 51 at around 360°C cannot only be assigned to the reduction of

Co^{3+} to Co^{2+} of the $\text{Co}_{2.5}\text{Al}_{0.5}\text{O}_4$ phase but also to the reduction of Co_3O_4 to CoO as already observed for pure cobalt oxide. The peak centered at 480°C indicates the second reduction from CoO to metallic cobalt. This leads to the assumption that the synthesis parameter of the DF 26 configuration and even more the one of the DF 51 configuration are suitable for the synthesis of reducible Co particles on an Al_2O_3 support.

4.2.2 Sinter stability and catalytic performance in the FT reaction

As discussed in chapter 2.1 not only the material itself plays an important role, when it comes to activity and stability of the catalyst, also the way in which the active component is deposited on the support has major influence. The FT activity is tested for all powders with 10 wt. % Co at 20 bar and 230°C in a fixed bed reactor.

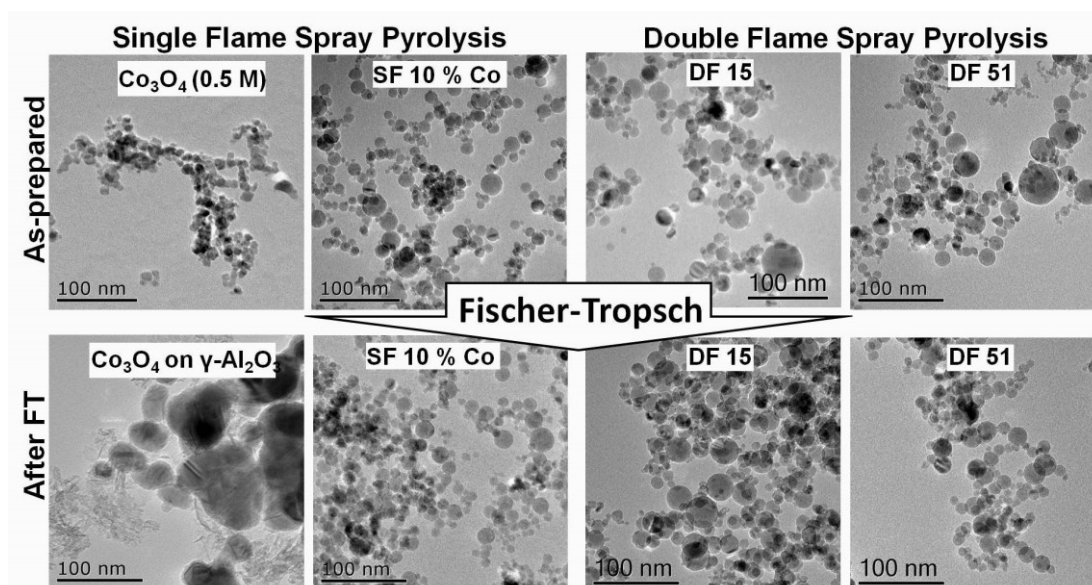


Figure 32: TEM images of the single flame made pure Co_3O_4 and SF 10 % Co catalysts and double flame made DF 15 and DF 51 catalyst before and after FT reaction.

For detailed investigations of the sinter stability, and to benchmark the activity of pure cobalt particles, eliminating any type of spinel formation, Co_3O_4 nanoparticles are synthesized in the SF approach, and subsequently supported on commercial alumina. The structures of the materials, before and after FT reaction, are exemplary illustrated on the TEM images in Figure 32. The significantly larger dark particles after FT indicate a high sinter activity, most likely during activation in pure H_2 . This high sinter activity results in a significant loss of FT-active metal surface area. In the catalytic testing, no FT activity is observed under the investigated conditions for the subsequently supported sample. The procedure of a physical mixing of the components followed by a heat treatment does not result in sufficiently strong interactions between the pure cobalt oxide nanoparticles

and the alumina support. The applied ultrasonic pretreatment, to break up the large cobalt oxide agglomerates that are typically formed during flame synthesis, is ineffective and the pure cobalt oxide aggregates cannot be disintegrated prior to the dilution with alumina in ethanol. As a result, sintering is favored due to close contact of the cobalt oxide nanoparticles. Although mechanical mixing with a ball mill is a common measure to overcome this problem, the FT performance of such systems is usually inferior in comparison to that of catalysts prepared by the standard incipient wetness impregnation (IWI) technique [210]. This is the reason why this approach is not further investigated.

The in-situ supported cobalt-alumina samples, however, regardless of whether they are prepared by single or double flame did not show any structural changes in the TEM images acquired before and after FT. The zero loss images and Co mappings after the reaction of the DF 26 and DF 51 catalyst showed, if at all, only a slight increase in Co particle size (Figure 28).

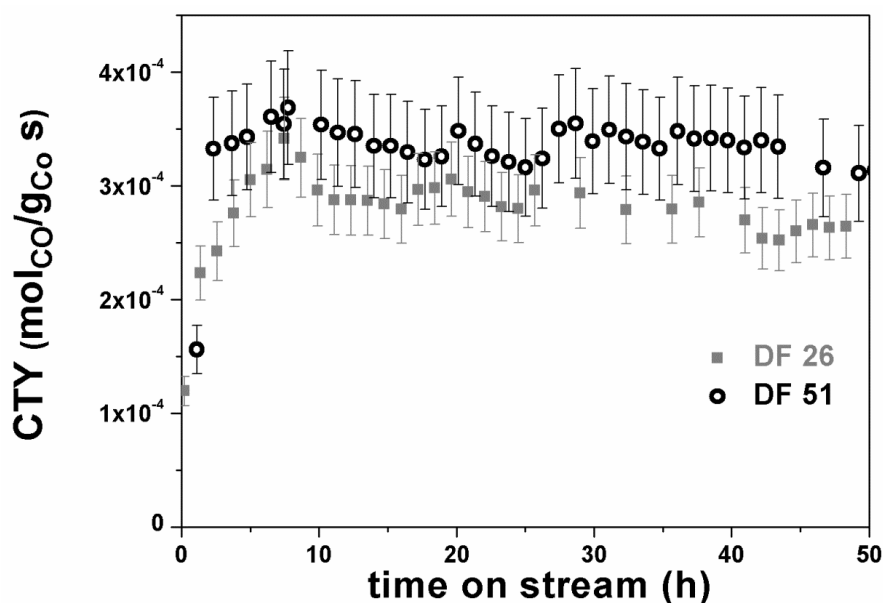


Figure 33: Evolution of cobalt time yield over 50 h time on stream (CTY = moles CO converted per gram Co-metal per second). The FT reaction is performed at 230°C, 20 bar and a total gas velocity of 62.5 mL/min ($H_2:CO:N_2 = 6:3:1$) in a fixed bed reactor.

Even so, all flame made catalysts exhibit good sinter stability, established due to the strong metal support interaction accomplished in the flame process, the SF Co/Al₂O₃ catalysts and the catalysts prepared with the double flame approach, using short intersection distances (DF 15 and DF 17) showed any FT activity. This is in agreement with the results of the structural analysis, that all this samples exhibit a large amount of irreducible cobalt aluminates. On the contrary, catalysts prepared using higher

intersection distances (DF 26 and DF 51) showed FT activity with a constant Co time yield over 50 hours on stream (Figure 33). Of the two catalysts, the FT activity is slightly higher for the DF 51 compared to DF 26.

The main products for the flame made catalysts, DF 26 and DF 51, are linear paraffin's (Table 3). For both catalysts, a similar selectivity pattern is observed, with the DF 51 sample producing slightly more methane. As compared to the standard IWI catalyst showing a methane selectivity of 12 wt. %, the flame synthesized catalysts produced somewhat more methane (17 – 20 wt. %). Smaller C₅₊ yields and lower olefin to paraffin ratios (3-5 times) are further observed for the DF 26 and DF 51 catalysts in the investigated hydrocarbon-fractions C₄-C₆ as well (Table 3). These observations indicate stronger hydrogenation activity of the flame made catalysts leading to chain termination and paraffin formation due to hydrogen adsorption. In contrast, the CO₂ selectivity with about 1 wt. % for all catalysts is not affected by the intersection distance.

Table 3: FT performance of the double flame and reference catalysts investigated at 230°C, 20 bar and a total gas velocity of 62.5 mL/min (H₂:CO:N₂ = 6:3:1) in a fixed bed reactor.

	CTY* (mol _{CO} /g _{Co} s)	Sel. (wt. %)				Olefin/Paraffin		
		CO ₂	CH ₄	C ₂ -C ₄	C ₅₊	C ₄	C ₅	C ₆
DF 15	---	---	---	---	---	---	---	---
DF 17	---	---	---	---	---	---	---	---
DF 26	2.8·10 ⁻⁴	1.3	17.0	20	62	0.9	0.6	0.3
DF 51	3.4·10 ⁻⁴	1.0	19.6	16	64	0.7	0.5	0.3

*CTY: cobalt-time yield: moles CO converted per gram Co-metal per second.

4.2.3 Conclusion

The obtained results confirm the hypothesis proposed in Figure 26 (1)–(5). The synthesis in the SF involves a mixture on atomic scale (1) in form of the non-reducible mixed metal oxide CoAl₂O₄. When the synthesis takes place in the DF setting and the flames intersect at distances up to 17 cm (DF 15 and DF 17) the coalescence phase is still fully developed. This proposes a mixture on inner particulate scale, respectively on particle scale (2), indicated by the formation of Co- rich spinels next to Al -rich regions. Intersection distance of 26 and 51 cm (DF 26 and DF 51) leads to the formation of individual cobalt oxide particles which are deposited on an alumina support (3). However, this mixing on particle scale is still accompanied with the formation of clearly identifiable amounts of irreducible cobalt rich-spinels. A mixture neither on particle cluster

scale (4) nor on agglomerate scale (5) are detected even for the highest intersection distance of 51 cm.

The results further indicate that the spinel phase is the thermodynamically favored crystal phase. Even for the catalyst synthesized with an intersection distance of 51 cm a full elimination of the spinel phase does not occur. The ratio of cobalt and alumina within the spinel phases changes, however, from an alumina rich spinel phase CoAl_2O_4 in the SF to cobalt rich spinel phase $\text{Co}_{2.5}\text{Al}_{0.5}\text{O}_4$ for the DF setting. In contrast to the SF approach, where variable Co contents (10 and 50 wt. % Co) lead to similar particle sizes, the support particle size for DF made catalysts is influenced by the flame reactor geometry: smaller particles are obtained with increasing intersection distance. The decrease in particle sizes can either be based on changes in the material composition of the final product (predominantly spinel phase for DF 15 and DF 17 and pure cobalt oxide + alumina for the DF 51) or on temperature and velocity profiles of the DF setting. Chapter 5 shows the influence of the geometric parameter in the DF process on the temperature and velocity profile in detail. A further issue at high intersection distances, which has to be investigated in more detail, is an advanced flame spreading due to ambient air entrainments. The jet propagation is advanced and the entrainment region of the flames in the mixing zone is already highly developed. This leads to the situation, that the probability to get in contact with a particle synthesized in the opposed flame is significant higher for particles, following a streamline near the inner entrainment region than for particles positioned at a streamline in the outer entrainment region. This may lead to significant differences in the material structure which emphasizes the necessity of a fundamental study on the mixing parameter in the DF process.

Combining all results the most promising intersection distance of the investigated samples for the syntheses of FT-active Co-alumina catalysts is in the range of 51 cm. Here the individual particle formation is nearly completed; significant agglomeration of the Co has not started. The high sinter stability of the DF samples indicates that the aerosol streams still provide enough energy at the intersection point, that partial sintering of the cobalt oxide particles on the support is possible. This sinter stability is essential to face harsh reaction conditions during the following FT process. However, to further increase the FT-activity the remaining spinel phase in the DF 51 has to be decrease, while keeping the sinter stability of the cobalt oxide. A further increase of the intersection distance combined with an increase in the intersection angle to increase the mixing process of the jets could be one approach. Another approach to increase the activity is to tune the particle size of the active component and the support, which can be adjusted

individual, through variations in precursor concentration, gas velocities, and ratio of the oxygen stream in the different flames as discussed in chapter 3.2.1. Adjusting these parameters results in the synthesis of cobalt particle with an optimum size about 6-8 nm, independent of the concentration ratio between active component and support.

4.3 Catalysts for the preferential oxidation of carbon monoxide

In proton exchange membrane fuel cells (PEMFC) the chemical energy is present in a fuel, e.g. H₂. The conversion of the H₂ into water using O₂ generates directly electrical energy [221-224]. This approach is a promising alternative to combustion engines because of its high efficiency, low operation temperature, and limited pollutant emission [221]. Due to their fast reaction kinetics, cells fueled with H₂ are preferred compared to e.g. methane. One way to produce the consumed H₂ is the photocatalytic water splitting process. However, this production route is still under investigation, since efficiencies are still considerably low. An alternative way is the production of hydrogen based on the reformation of a hydrocarbon fuel produced e.g. from biomass. This approach comes, though, with the challenge to reduce the CO content in the H₂ feed stock stream. Already small traces of CO in the hydrogen stream can significantly depress the performance of the PEMFC due to the strong adsorption of CO on the mostly Pt based electro catalysts. This is especially an issue, in cases where an on-board generation of the H₂ is considered, to bypass a risky storage of pure H₂ in the vehicles. A supplemented water-gas-shift (WGS) reaction can reduce the CO concentration to 1,000-10,000 ppm [221]. A reduction to 10-100 ppm, however, is required to ensure the efficiency of the PEMFC. The application of the preferential oxidation of CO (CO-PrOx) realizes this additional reduction of the CO concentration. Here, a heterogeneous catalyst oxidizes the CO selectively to CO₂ (10) as presented in Figure 34.



Since the CO is present within a H₂ atmosphere, the competing reaction is the combustion of hydrogen (11):



The goal of the catalysts design is to ensure a reasonable selectivity of oxygen to CO instead of H₂ oxidation [225]. To implement this, a fundamental understanding of the characteristic of the catalyst and reaction mechanism is essential. This helps to realize the design of catalyst with a high turnover frequency and a high selectivity and thus, the implementation of the CO-PrOx as commercial tool.

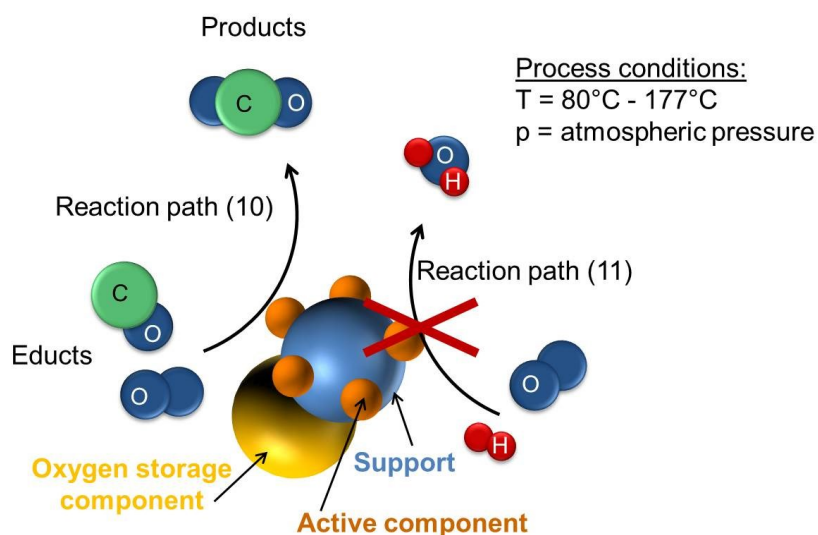


Figure 34: Schematic representation of the preferential oxidation of CO (PrOx).

4.3.1 CO-PrOx- catalysts

Oh and Sinkevitch published 1993 an overview on the activity and selectivity of PrOx catalysts by testing a variety of catalytic materials, supported on alumina, in a laboratory reactor feed stream containing CO, H₂, and O₂ [226]. They investigated noble metals such as Pt, Pd, Rh, and Ru and oxidation catalysts including Co/Cu, Ni/Co/Fe, Ag, Cr, Fe, and Mn to identify promising catalytic systems. Until now, the most appropriate catalysts for the CO-PrOx reaction are Pt, Rh and Ru, since they achieved nearly complete CO conversion at low temperatures. Kahlich et al. demonstrated the influence of the temperature on the CO selectivity using a Pt/Al₂O₃ catalyst [225]. CO displaces H₂ from the metal surface at temperatures lower than 150°C. This fact results in a preferred oxidation of CO compared to H₂ and a significant selectivity increase for the CO oxidation. The application of higher temperatures leads to a lower surface coverage of the CO and results an increase in H₂ adsorption. The selectivity shifts in direction of H₂ oxidation.

Liu et al. stated that several bimetallic systems (active component on support) exhibit much improved PrOx performances compared to the monometallic counterparts [227]. The improved activity is based on geometric (high dispersion of the catalytic component) and/or electronic effects (modification of the electronic structure of the catalytic active component due to interaction with the support) [228]. Pt is so far the most common active component for the PrOx reaction and its interactions with several support systems has been investigated: Pt/Al₂O₃ [225, 229-231], Pt/FeO_x [232-234], Pt/CeO₂ [223, 235]. Al₂O₃ is an irreducible support and the oxidation of CO takes place by a relatively straightforward Langmuirian-type adsorption on the Pt surface. The reaction mechanism

becomes more complex in cases Pt deposited on a reducible support such as CeO_2 . A high oxygen conversion at low temperatures and a maximum in selectivity is observed at much lower temperatures for the Pt/CeO_2 system than for $\text{Pt/Al}_2\text{O}_3$ [229]. This shift towards low temperature reactions is often related to the reducibility as well as the oxidation state of the support. CeO_2 is active in transient oxygen storage and it promotes, applied as a support, the oxidation even under oxygen-poor conditions [236]. Several studies have presented that CeO_2 supported catalysts are able to oxidize carbon monoxide even in the absence of oxygen due to its oxygen storage capacity [237-239]. The reducibility and the oxygen mobility abilities of CeO_2 can be further improved in multicomponent systems e.g. by doping different cations with smaller ionic radii such as Fe [240]. Fe-modified CeO_2 systems combining the redox behavior of the cerium ($\text{Ce}^{4+}/\text{Ce}^{3+}$) and iron ($\text{Fe}^{3+}/\text{Fe}^{2+}$) cations leading to a remarkable improvement of their oxygen mobility which is directly related to the formation of oxygen vacancies [241, 242].

4.3.2 Flame made CO-PrOx- catalysts

Kydd et al. are the only group so far, focusing on the synthesis of CO-PrOx catalysts using the FSP approach. They investigated the CuO/CeO_2 system with Cu loading from 1-12 wt.% and demonstrated that the rapid and high-temperature synthesis that occurs during the FSP process is an effective and simple strategy for producing highly active CO-PrOx catalysts [172, 243]. Christensen et al. synthesized CeO_2 in a SF process and tested its activity in catalytic soot oxidation [244]. Further catalytic active systems e.g. $\text{Pt/Al}_2\text{O}_3$ [139, 245] have been synthesized using FSP, the particles are, however, tested in reactions different from the preferential oxidation of CO.

4.4 Flame synthesis of ternary catalysts for CO-PrOx

The aim of the second study is the synthesis of CeO_2 and Fe_2O_3 support particles which are mixed on particle scale. This intimate interaction between the FeO_x and CeO_2 particles is supposed to have a positive influence on the reducibility of the catalyst. Additionally, it is assumed that the exclusive deposition of Pt on the Fe_2O_3 favors H-spillover effects. The performance of experiments with varying intersection distances, as illustrated in Figure 35, helps to identify the intersection distance which results in the desired mixing of FeO_x and CeO_2 on particle scale (3). A synthesis with small intersection distances is supposed to result in the formation of Fe-doped CeO_2 particle decorated with Pt since the flame synthesis of Fe and Ce is known to result in a doped crystal structure [246]. The product characteristic is supposed to vary slightly from the one achieved in the SF process (1), since the SF process offers the possibility of a uniform

atomic mixture within the primary particles. In the DF process, the formation of polycrystalline particles is conceivable, since mixing in the coalescence phase takes place (2).

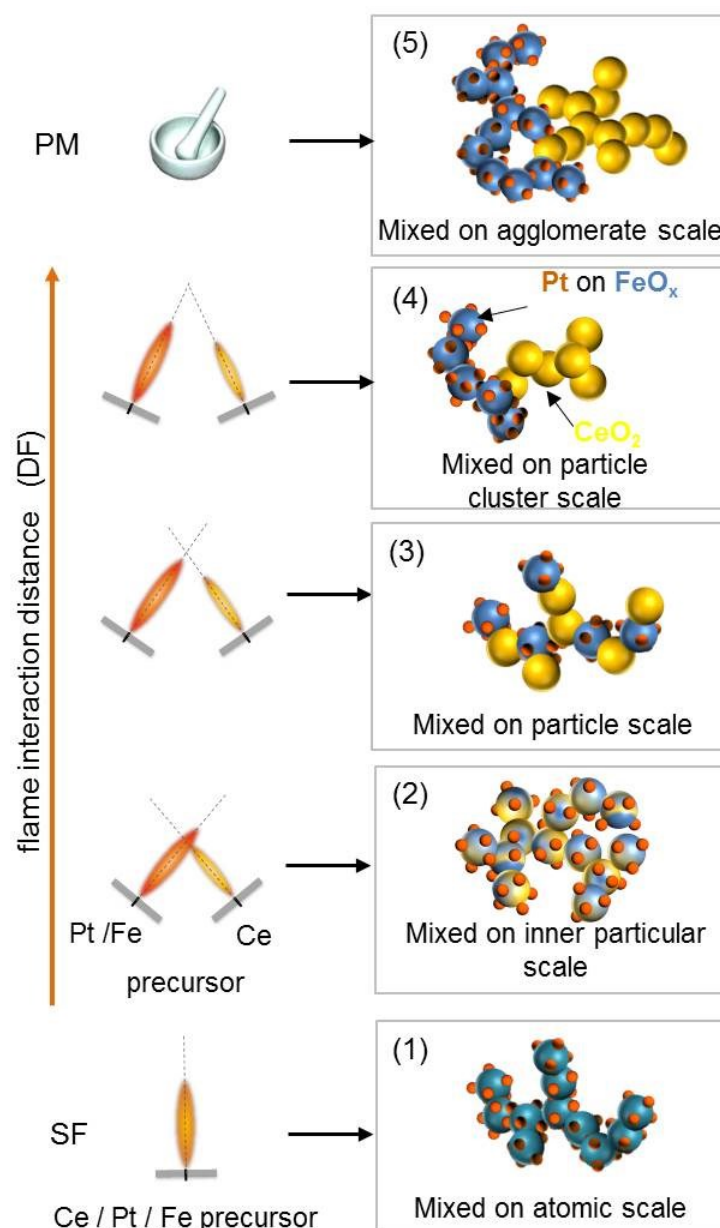


Figure 35: Working hypothesis of the formation of the resulting catalysts sprayed with different flame geometries (SF = single flame, DF = double flame, PM = physical mixing).

An increase of the intersection distance enables the synthesis of the desired mixture of CeO_2 and Fe_2O_3 on particle scale (3). The formation of individual particles allows taking advantage of the particular properties of the single oxide materials, e.g. the oxygen reduction capacity. A mixture on particle scale and a stable interphase between the support components ensures the required oxygen mobility between the two components.

The addition of Pt, exclusively on the Fe₂O₃, further favors a low temperature activity due to the application of a reducible support. Mixtures on cluster (4) and on aggregate scale (5), are supposed to take place at high intersection distances or in a physical mixture, respectively. This mixing state limits the oxygen mobility between the CeO₂ and Fe₂O₃ components significantly and is, thus, undesired. The following section presents the results of the catalyst characterization to determine the influence of the intersection distance on the mixing state and the resulting CO-PrOx activity.

4.4.1 Synthesis and characterization of ternary Fe+Pt / Ce catalysts

The study includes in total eight different flame synthesized samples. Five catalysts are set up in the SF and three catalysts in the DF with systematically varying intersection distances. Table 4 gives an overview of the parameter and the received specific surface area. All tested multicomponent catalysts have a final composition of 5 wt.% Pt, 8 wt.% FeO_x (as Fe₂O₃) and 87 wt.% CeO₂.

Table 4: Overview of the synthesizes conditions and the specific surface areas (SSA)

Notation	Synthesis method	Molratio Fe-Ce	Intersection distance l [cm]	Intersection angle α [°]	SSA [m ² /g]	Pt- size [nm]
FeO _x	SF	---	---	---	258	---
Pt-Fe ₂ O ₃	SF	---	---	---	244	2.1 ± 0.7
CeO ₂	SF	---	---	---	138	---
Pt-CeO ₂	SF	---	---	---	147	0.8 ± 0.2
Pt-Fe-Ce	SF	1 : 5	---	---	116	0.7 ± 0.2
DF 18	DF	1 : 5	18	20	128	1.1 ± 0.3
DF 23	DF	1 : 5	23	20	139	1.3 ± 0.4
DF 33	DF	1 : 5	33	20	158	1.9 ± 0.6

XRD measurements give first insight which of the crystal structure is the most dominant in the synthesized powders. Figure 36 illustrates the XRD patterns for pure Fe₂O₃ and CeO₂, the SF and all three DF samples. The patterns indicates the formation of γ -Fe₂O₃ analog to earlier FSP synthesized Fe₂O₃ by Li at al. [247] and of CeO₂ analog to Mädler at al. [171]. The comparison of the pure CeO₂ pattern and the SF pattern containing Fe and Ce allows no clear statement, in which crystalline form the Fe is present, when spraying both materials in the SF. A significant shift of the characteristic CeO₂ (200) reflex at $2\theta = 33^\circ$ due to Fe doping, visible e.g. for the sol-gel synthesis of Fe-doped CeO₂ [248], misses in the pattern of the FSP sample. However, there is still the possibility of Feⁿ⁺ cationic doping in CeO₂. Since the ionic radius of Fe²⁺ (ionic radius of

0.097 nm) is quite similar to the one of Ce^{4+} (0.092 nm) [249], a substitution along with the formation of oxygen vacancy to preserve charge neutrality is likely. Since this substitution comes with a negligible variation in the lattice cell parameters, no peak shifting in the XRD pattern is expected.

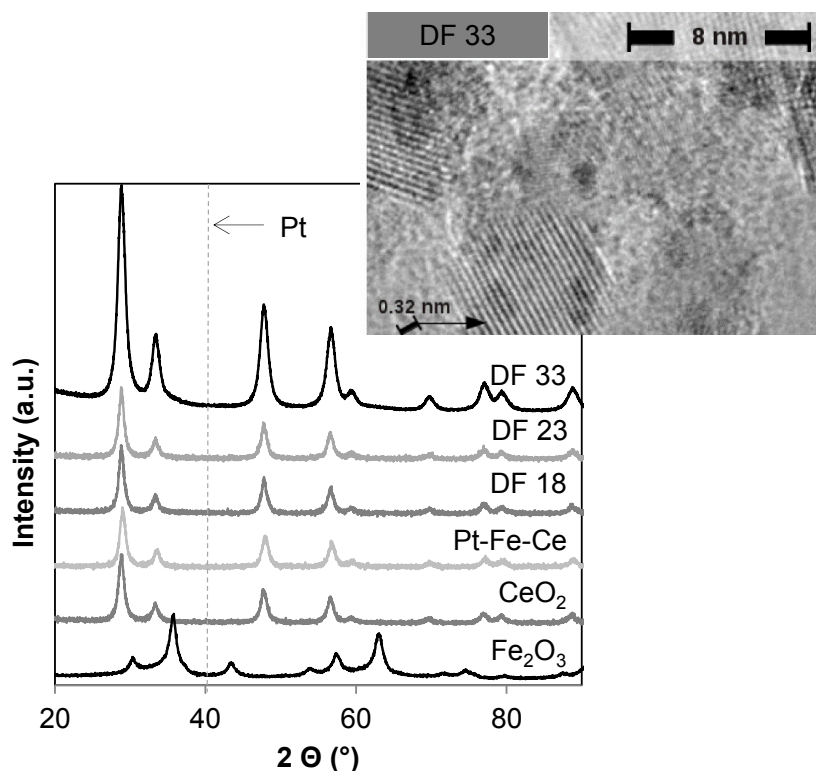


Figure 36: XRD pattern of pure Fe_2O_3 and CeO_2 , the SF sample containing Pt-Fe-Ce and the three DF samples with increasing intersection distances, Inset: HR-STEM of the DF 33 sample

Pure Fe_2O_3 reflex cannot be identified, even for the sample with the highest intersection distance. However, the presence of crystalline Fe_2O_3 is nevertheless possible, since small crystals are almost invisible to XRD due to the significant X-ray scattering [247]. The HR-TEM image in Figure 36 clearly indicates the presence of small Fe_2O_3 crystals in the sample, since the indicated lattice distance of 0.32 nm corresponds to the $\gamma\text{-Fe}_2\text{O}_3$ crystal plane [247, 250]. The explanation for an absence of Fe_2O_3 peaks in the XRD could be the low Fe content (8 wt. %) and the small crystallite size.

Figure 37 presents STEM images of the single flame samples: Pt- Fe_2O_{x3} (a), Pt- CeO_2 (b) and Pt-Fe-Ce (c) and of all three DF samples (d-f). The Pt- FeO_x contains spherical Fe_2O_3 particles. Because of the lower boiling point of Pt compared to Fe_2O_3 , the Pt particle formation starts at a later stage compared to the nucleation of the metal oxide support, resulting in the typical deposit structure straight out of the SF setting (clearly visible as bright spots) [139].

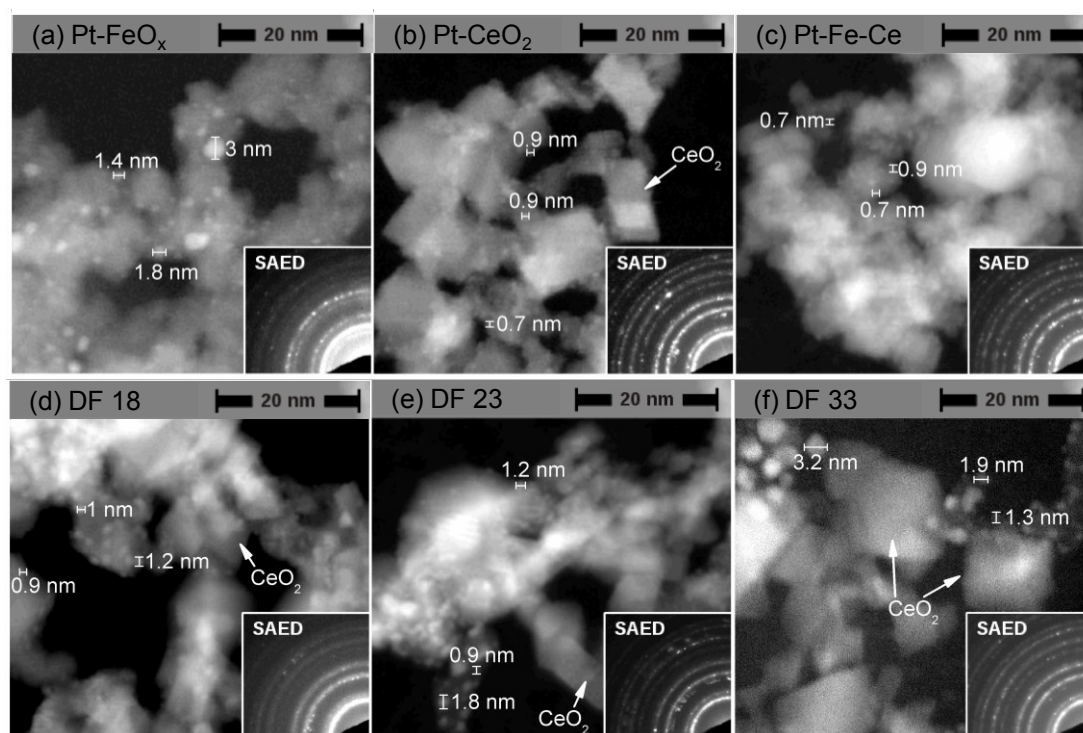


Figure 37: STEM images of the (a) Pt-FeO_x, (b) Pt-CeO₂ and (c) Pt-Fe-Ce sample synthesized in the SF and the three DF samples with increasing intersection distance (d-f). Insets: SAED pattern of the corresponding samples.

The precursor concentration in the pure Fe flame is considerably low resulting in a high specific surface area of the Fe₂O₃ with 258 m²/g. The deposition of Pt results in a slight decrease of the specific surface area to 244 m²/g. The average diameter of the Pt deposits is with $d_D = 2.1 \pm 0.7$ nm the highest for all samples, since the Pt concentration related to the pure Fe₂O₃ weight is 59.5%. The high Pt concentrations results in Pt mobility on the surface and sintering effects during the synthesis process and explains the decrease of the specific surface area. When the Pt concentration is significant lower compared to the support concentration, the addition of noble metals leads, however, to an increase of the specific surface area [1]. This described increase is visible when Pt is deposited on the CeO₂ component. The pure CeO₂ has a specific surface area of 138 m²/g and the addition of platinum increases the specific surface area to 147 m²/g. The STEM image indicates that the synthesis of Pt-CeO₂ results in angular CeO₂ deposited with Pt of an average particle size of $d_D = 0.8 \pm 0.2$ nm.

The lowest specific surface area 116 m²/g is achieved when spraying the Ce, Fe and Pt combined in the single flame. The platinum deposits have an average size of $d_D = 0.7 \pm 0.2$. In this synthesis case Fe doping of the CeO₂ is expected as presented e.g. from Channei et al. [246]. Even so, small amounts of Fe-doping in the flame made CeO₂

is known to increase the specific surface area, the opposite trend is observed for the SF case. One reason for this observed decrease is a slight increase in the overall precursor concentration due to the addition of 1/5 Fe compared to the pure and Pt decorated CeO₂ SF samples.

The STEM images of the DF samples indicate significant differences between all DF samples, which are coherent with the BET results. In the later one, an increase of the specific surface area with increasing intersection distance is visible from 128, 139 to 158 m²/g for the DF 18, 23 and 33 samples, respectively. Because the temperature in the intersection zone is lower with increasing intersection distance, less sintering is expected, represented by an increasing specific surface area. The significant increase in the SSA is in addition an indicator that separate Fe₂O₃ forms at increased intersection distances. Since the Fe- content is considerably low, this result in the formation of small Fe₂O₃ particles deposited on the CeO₂ particles, visible in Figure 37(f). It is further interesting to note the general increase in Pt size with increasing nozzle distance in Figure 38, which at first sight, may appear to contradict the trend on support particle sintering.

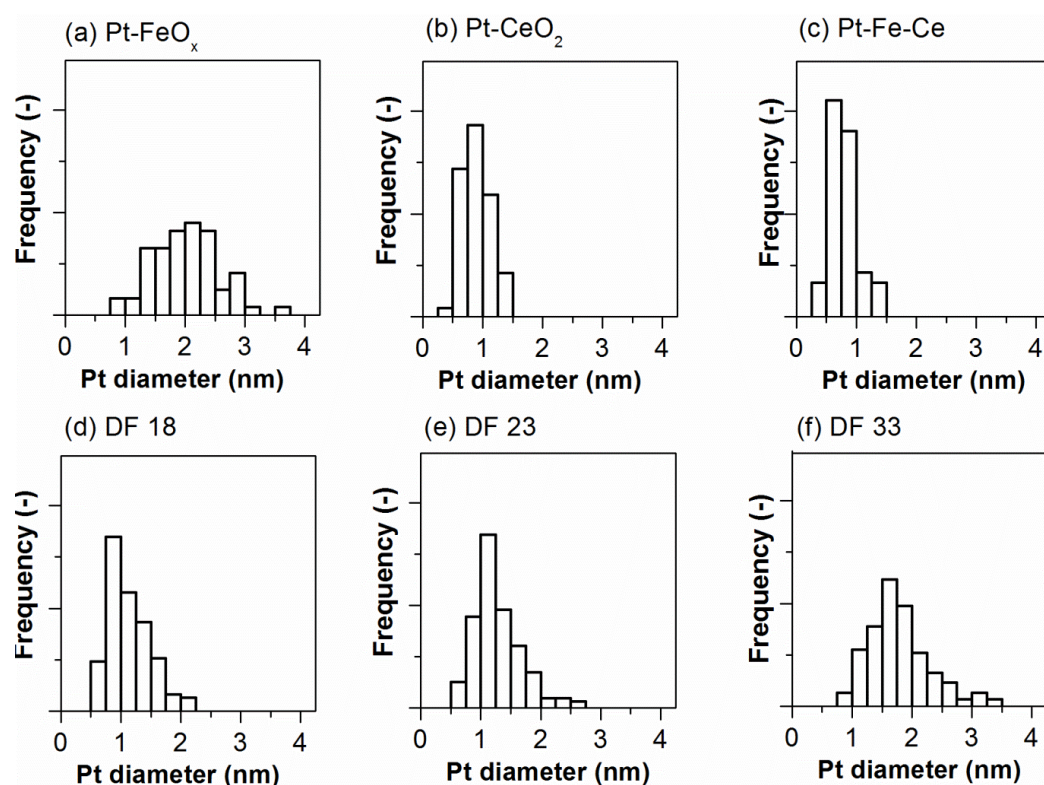


Figure 38: STEM - Pt particle size distribution based on 200 particle counts for all 6 Pt containing samples with the average Pt size listed in Table 4.

At small nozzle distances (e.g. DF 18) the Pt particles deposits after the Fe and Ce flames have intersected and a deposition of Pt takes place on the mixing phase of the Fe and Ce components. This results in average Pt dimeters of $d_D = 1.1 \pm 0.3$ nm. An increase in intersection distance leads to a mixture of the two particle streams after primary particle formation has started for both components, Fe and Ce. Here, the Pt deposits partly on the pure Fe_2O_3 particles. These results in the formation of larger deposits $d_D = 1.3 \pm 0.4$ nm for the DF 23. Most of the Pt would be isolated on the Fe_2O_3 support for the sample synthesized at high nozzle distance DF 33. Since the available surface area of the pure Fe component is significantly smaller than the joint surface of Ce and Fe, sintering of the Pt on the surface of the Fe_2O_3 particles is favored. This results in an increase of Pt particle size to $d_D = 1.9 \pm 0.6$ nm for the DF 33 sample.

To get a more detailed picture on the reducibility of the catalysts again H_2 temperature programmed reduction (H_2 -TPR) is conducted and presented in Figure 39. The H_2 -TPR results further underline the observed changes in material structure related to an increase of intersection distance. The most prominent characteristic comparing the DF samples is the shift of the reduction peak at 25 °C (for the SF) towards lower temperature as a function of increasing intersection distance. The inset illustrates the merging of the peak with the Lorentzian peak at -6 °C. This peak can be attributed to the reduction of PtO_x on FeO_x , while the TPR peak at ~ 25 °C is attributed to the reduction of PtO_x on CeO_2 .

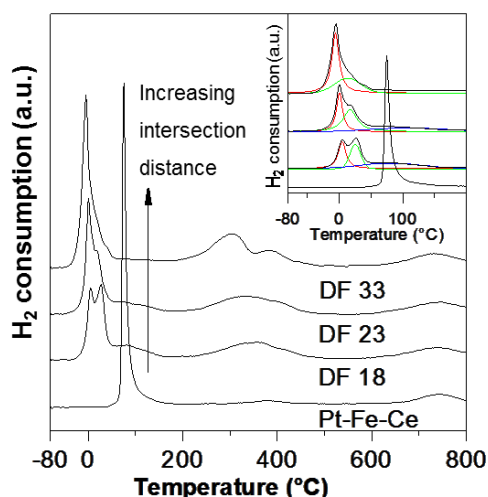


Figure 39: (a) H_2 -TPR profiles of DF samples with increasing intersection distances as well as the SF synthesized Pt-Fe-Ce sample. Inset: Peak deconvolution of the DF and the SF samples.

These results clearly indicate that with an increasing intersection distance, the formation of Pt selective deposited on pure Fe_2O_3 particles is predominant. The reduction peak for

PtO_x on CeO₂ misses almost completely for the DF 33 sample. In comparison to the SF: Pt-Fe-Ce sample where no reduction peak of Pt on Fe₂O₃ is present, inferring the absence of segregated FeO_x and CeO₂ phases.

4.4.2 Catalytic performance in the PrOx- reaction

The differences in the mixing state of the catalyst have also a significant influence on the catalytic performance, tested in a H₂-rich stream. Figure 40 illustrates the CO conversion (a) and CO₂ selectivity (b) over the temperature. The graphic presents the results for the DF synthesized catalysts with different intersection distances and the physically mixed Pt-FeO_x and CeO₂ (PM) and SF Pt-Fe-Ce sample. The applied reaction conditions are as followed: amount of catalysts = 20 mg, 50 mL min⁻¹ of PrOx gas mixture (1% CO, 2% O₂, 88% H₂ in He; O/CO ratio of λ=4), GHSV = 7640 h⁻¹.

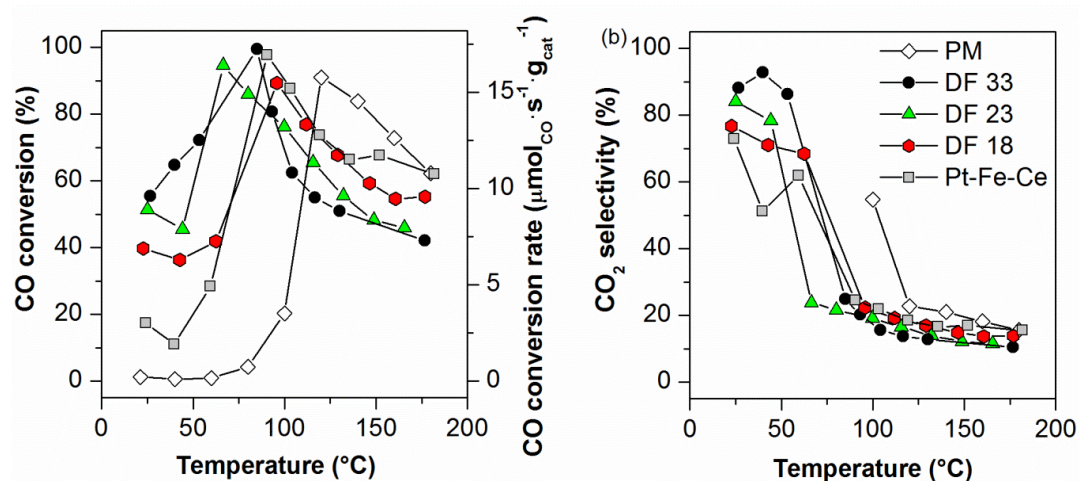


Figure 40: a) CO conversion and (b) CO₂ selectivity plots over the temperature of the DF catalysts synthesised with different intersection distances and the mechanically mixed Pt-FeO_x and CeO₂ (PM) and SF sample.

In PrOx reactions of CO, the CO conversion trend is typically divided in two regions: the low- temperature reaction regime ($T < T$ of maximum conversion) and high-temperature reaction regime ($T > T$ of maximum conversion). These two characteristic regions are visible for all the catalysts, however, the temperature for the maximum CO-conversion is significant higher for the PM sample compared to the flame made samples. The DF 33 sample exhibits the highest CO conversion at lower temperatures followed by the DF 23, DF 18 and the SF Pt-Fe-Ce sample. This trend is comparable with the trend of the low temperature reducibility in Figure 39. The PM sample has by far the lowest CO conversion at low temperatures. The order of CO conversion changes after passing the maximum conversion temperature. In the high-temperature reaction regime the PM

sample has the highest conversion, followed by the SF, DF 18, DF 23 and DF 33 sample. The decrease in CO conversion comes due to a drop in selectivity, illustrated in Figure 40 (b). In the high temperature regime, the CO₂ selectivity decreases for all samples down to 20%. The significant decrease in selectivity is based on the competitive adsorption of H₂ and CO on the Pt active sites [225].

The catalytic results emphasize the significant influence of the different mixing states on the catalytic activity and selectivity. The catalyst synthesized with the highest intersection distances (DF 33) exhibits the lowest reduction temperature and the highest CO₂ selectivity. This fact highlights that the selective deposition of Pt on the Fe-support particles favors H-spillover. The combination of CeO₂ and Fe₂O₃ on particle scale, present in the DF 33 sample, further influences the catalytic performance in a positive direction. This becomes apparent when comparing the performance of the DF 33 sample with the one of the PM sample. The latter has only physical bonds and no chemical (sinter) bonds between the CeO₂ and the Fe₂O₃ particles. The chemical bonds between the CeO₂ and the Fe₂O₃ particles are, therefore, the precondition for taking advantage of the oxygen storage capacity of the CeO₂. A mixture of Fe and Ce on atomic scale (Fe doping of CeO₂) decorated with Pt, which is present at smaller intersection distances and the SF adjustment, increases again the reduction temperature and decreases the selectivity.

4.4.3 Conclusion

The presented results are in line with the introduced working hypothesis stated in Figure 35 (1) – (5). The synthesis in the SF is assumed to result in the formation Fe-doping of the crystalline CeO₂ (1) even so a XRD peak shift is missing. At an intersection distance of 18 cm (DF 18), the particle formation is still in the nucleation / coalescence phase. Since singular Fe₂O₃ peaks misses in XRD pattern and no Fe₂O₃ particles are visible in the TEM image, again Fe doping is expected. However, the reduction behavior for the DF 18 and the SF sample differs significantly. This reveals a significant change in the mixing state even so this is not visible in TEM and XRD. Since the Pt has a lower boiling point compared to Fe and Ce, it forms deposits on the Fe-doped CeO₂ particles. The increase in intersection distance to 23 cm, results still in extensive sintering and doping between FeO_x and CeO₂. The conducted analysis does not provide a clear insight, whether the Fe is uniformly distributed into the Ce matrix or if the primary particles containing different crystal phases (2). The best result regarding the suppression of Fe-doping and the formation of a mixture of individual particles achieves the synthesis at an intersection distance of 33 cm. Here, the formation of individual Fe₂O₃ particles takes

place formed next to the formation of cubic CeO₂ (3). STEM analysis indicates a nearly exclusive deposition of the Pt on the spherical Fe₂O₃ particles. Due to the higher amount of Ce compared to Fe (5:1), CeO₂ cluster formation takes place. The mixing state present in sample DF 33 is, thus, a combination of mixing on particle and cluster scale (3-4). The sample characteristic of the DF 33 further differs significantly from the PM sample, where a mixture on agglomerate scales is present due to the preparation process (5).

The specific surfaces area of the powders increases, related with a decreases of the particle diameter, from the SF sample in direction of the samples synthesized with higher intersection distances. The explanation for this trend is the separation of small Fe₂O₃ particles with a high specific surface area and larger CeO₂ particles. The Pt particle size exhibits an opposing trend with increasing particle sizes for increasing intersection distances. The reason for this contrary trend is the fact that Pt deposits for higher intersection distances exclusively on the Fe₂O₃ particles. This fact significantly reduces the available overall surface area and favors Pt sintering.

The different mixing states of the synthesized samples result in considerable changes in reducibility and catalytic activity. The TPR results reveal a decrease in reducibility of the catalysts synthesized with increasing intersection distances, with a clearly visible shift of the reduction peak of the SF at 25 °C towards lower temperature. These results are consistent with the results of the catalytic tests, where a reduced reduction temperature and a good selectivity towards CO in the low temperature region is visible for the DF 33 sample compared to the SF and PM samples.

At the intersection distance of 33 cm, the DF offers the synthesis of a tailored mixture of CeO₂ and Fe₂O₃ particles with a chemical particle bonding and the exclusive deposition of Pt only on the Fe₂O₃ particles. An aerosol synthesis in this high temperature environment promises further a high sinter stability of the catalysts. The catalyst synthesized with an intersection distance of 33 cm is, therefore, the most promising sample for further catalytic testing.

So far, little knowledge on the detailed reaction mechanism is present, hindering the specific design of the catalyst and consequently the essential increase in activity and selectivity. The synthesis of the previously investigated catalysts with a specific design helps to understand the interplay between the different support components CeO₂ and FeO_x and to gain a deeper understanding of the CO-PrOx mechanisms. The joined publication of Dreyer et al. [5] includes a detailed discussion on the catalytic performance

of the synthesized model catalysts and proposes a detailed reaction path for the preferential oxidation of CO when applying ternary flame synthesized catalysts.

4.5 Evaluation of the DF set-up for the synthesis of multicomponent catalysts

Both the synthesis of the Fischer-Tropsch and the synthesis of the PrOx catalyst indicate the flexibility and suitability of the DF process to design multicomponent catalyst in a single step. The studies demonstrate that the tailored adjustment of the intersection distances of the two flames changes the mixing state of the synthesized catalysts significantly from a mixture on atomic scale to mixtures on particle/ cluster scale. The different distributions of the components result already in remarkable changes in catalytic performance; however, the full potential of the DF setting is not fully achieved. The catalytic activity and selectivity could be further enhanced by changing the particle characteristics e.g. particle size of the different components separately and independent of the overall material concentration. The DF process offers this process flexibility, since adjustments of the flame parameters (precursor and gas flow rate and precursor concentration) influence the particle sizes of the different component individually, while the overall ratio of the two components stays stable. A further demonstrated advantage of the DF process is that the synthesized catalysts exhibit a high sinter stability, which results from the high temperature during the synthesis process.

These facts are the main reasons why the number of publications reporting novel catalytic materials using the DF process has increased significant within the recent years [76, 77, 180-189]. All these studies, including the presented ones, focus more on the synthesis of the desired multicomponent materials rather than on investigations of the underlying process conditions in the DF set up. The fundamental understanding of the DF process including the resulting temperature profile of the merging flames and the mixing process of the two particle streams is thus still missing. This detailed process understanding of the DF setting is, however, essential to further tailor the catalyst characteristic and enhance the catalytic performance of the DF catalysts.

The following chapter presents the required basic investigations on the DF process parameters, including temperature diagnostics of varying flame profiles and for the first time a quantitative characterization of the the mixing states of the different synthesized particle samples.

5 Characterization of the mixing process during the DF synthesis of heterostructured nanoparticles

The appropriate flame adjustment to achieve a certain mixing state in the double flame process is one key to significantly influence the catalytic activity and selectivity of the synthesized catalysts. To enable the synthesis of a tailored mixing state in the DF process three questions are in focus:

1. Which process conditions (temperature profile, mixing characteristic) are present in a double flame system?
2. How do these process conditions influence the resulting mixing state of the synthesized samples?
3. What are suitable methods to quantitatively characterize the mixing states in nanosized multicomponent samples?

The answers of these three questions are essential to predict the influence of parameter changes in intersection distance and angle. The following sections try to give first answers to these questions, since detailed temperature studies of the double flame process are lacking and the mixing process of the DF setting is largely unknown so far.

The first section 5.1 presents investigations regarding the variation of the temperature profile from two intersecting xylene flames. Fourier-transform infrared (FTIR) technique and thermocouple measurements are the base for the experimental analysis of the temperature profile. Computational fluid dynamics simulations (CFD) complement the temperature measurements. The aim is to determine, how the additional heat source of the second flame and the limited entrainment of air within the DF setting influence the temperature profile of the reaction zone compared to the well-known SF configuration. The section further discusses the effect of the geometric configuration on the mixing process of the two individual gas streams based on the results of a CFD simulation.

Section 5.2 experimentally investigates the influence of varying flame parameters on the mixing process in a deposited system. The influence of the expanded high temperature zone of the DF on the resulting particle characteristic is examined in detail. The quantitative determination of the degree of mixing in a deposited system takes place for the first time using TEM image-based statistical analyses (quadrat method).

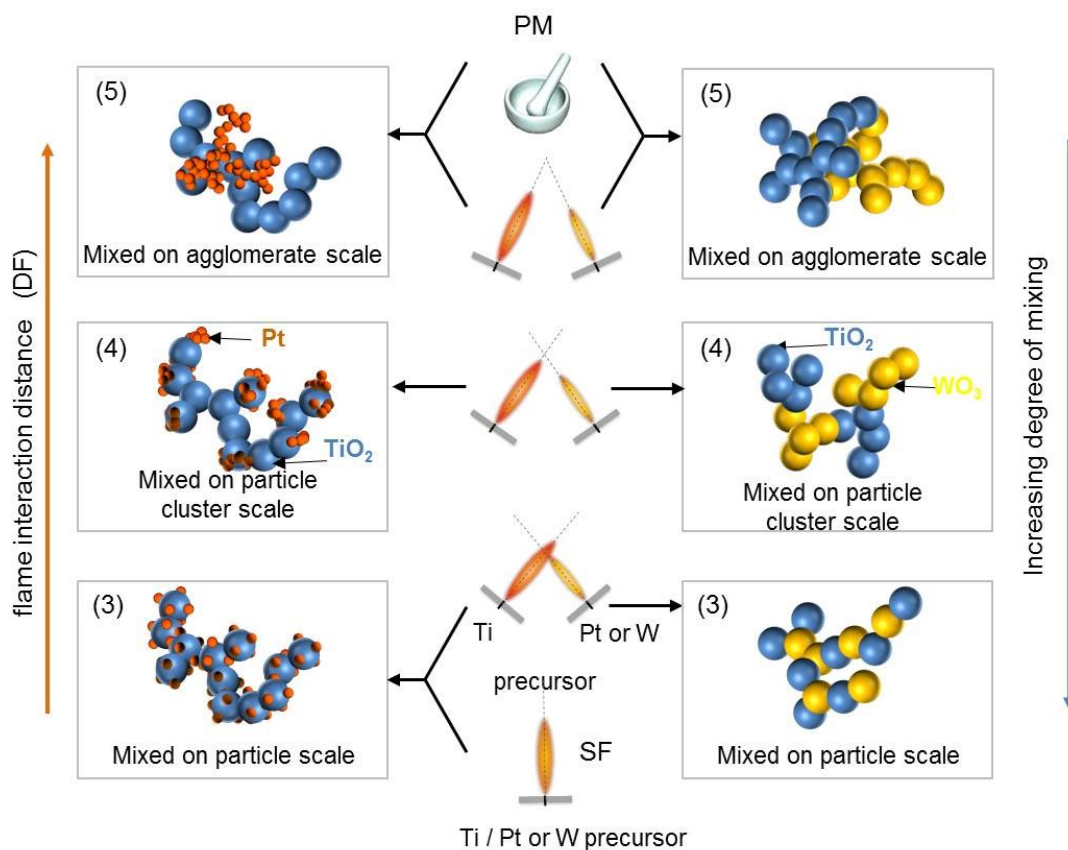


Figure 41: Working hypothesis of the formation of the particles sprayed with different flame geometries (SF = single flame, DF = double flame, PM = physical mixture) left: Deposited system: Pt on TiO₂ and right: aggregated system with TiO₂ and WO₃ primary particles

The investigations focus on the multicomponent system Pt and TiO₂ since this model system offers two main advantages: Firstly, an undesired formation of a mixed metal oxides and the occurrence of doping effects which can be neglected for the synthesis of Pt on TiO₂ [80]. Secondly, the system offers the possibility of an independent particle size determination of support and Pt particles using H₂/CO chemisorption and STEM analysis. Additionally is the influence of parameters such as concentration and precursor flow rates on the Pt dispersion in the single flame setting well known and has been investigated for different supports such as TiO₂ or Al₂O₃ [80, 139, 168]. Figure 41 (left side) illustrates the working hypothesis for the performed experiments. The Pt – TiO₂ system forms a uniform mixture on particle scale in the SF. It can be assumed that a synthesis in the DF set up will result in mixtures on cluster scale or even on aggregate scale. To confirm this assumption a method to quantify the degree of mixing in a deposited system is developed and tested. An additional intention of the experiments is to investigate the influence of the intersection angle on the mixing process and to

determine the DF configuration which results in the same uniform mixture on particle scale achieved in the SF.

Section 5.3 identifies a suitable method to quantify the degree of mixing in aggregated systems. The investigations are based on the multicomponent particle system TiO_2 and WO_3 . The advantage of applying TiO_2 and WO_3 is the components significantly differ in their atomic number. This allows an individual particle analysis based on their contrast. Therefore, gray scale pictures are generated using scanning transmission electron microscopy (STEM) combined with annular dark-field imaging (ADF-STEM).

Pre-experiments determine the characteristic flame configuration (intersection distance and angle) which results in a mixture on particle scale for the TiO_2 - WO_3 system. In a second step, samples with three different configurations are synthesized and the average hetero coordination number of the particles within a particle collective is determined. The discussion of the results includes the influence of the intersection distances and angles on the mixing state and the uniformity on the sample. Figure 41 (right side) illustrates the expected mixing states based on the adjustment of the flames.

5.1 Temperature profile and mixing characteristic in the DF process

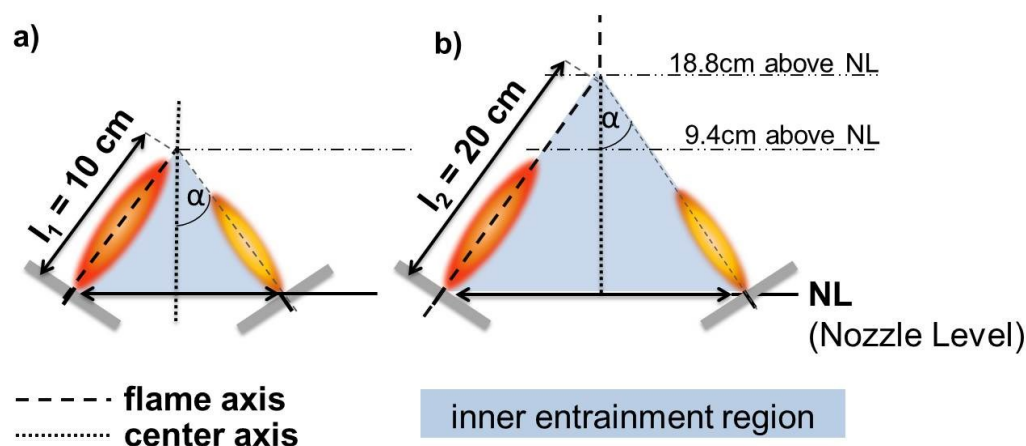


Figure 42: Geometric configuration of the double flame (DF) set-up (not true to scale) with a) $l_1 = 10$ cm and b) $l_2 = 20$ cm intersection distance at constant intersection angle $\alpha = 20^\circ$, resulting in intersection points of the flame axes at a) 9.4 cm and b) 18.8 cm above nozzle level (NL). The shaded area indicates the inner entrainment region between the flames.

The temperature in the reaction zone plays an essential role within the DF synthesis process since it directly influences the resulting mixing state illustrated in Figure 24 page

54. In this section the well-known temperature profile of the SF process is compared with the temperature profiles of two different flame configurations having intersection distances of 10 and 20 cm and an angle of $\alpha = 20^\circ$, see Figure 42.

Fourier transform infrared spectroscopy (FTIR) measurements give information on the vertical temperature profile along the flame axis (dashed line) and thermocouple measurements along the center axis (black dotted line). The position of both axes is illustrated in Figure 42. In Figure 43 are the FTIR-measured line-of-sight (symbols) and the thermocouple (gray line) based flame temperature matched with DFT simulated flame temperature profiles (black lines).

As described in section 3.2.1 the temperature profile of the single flame involves a constant temperature region within the first 5 cm up to 2800 K where most of the combustion takes place. A significant temperature decrease follows, resulting from flame expansion due to entrainment of ambient air. The simulation (solid line) are in good agreement with Schulz et al. [168] and Gröhn et al. [251] reporting similar temperature profiles for such xylene-based FSP flames.

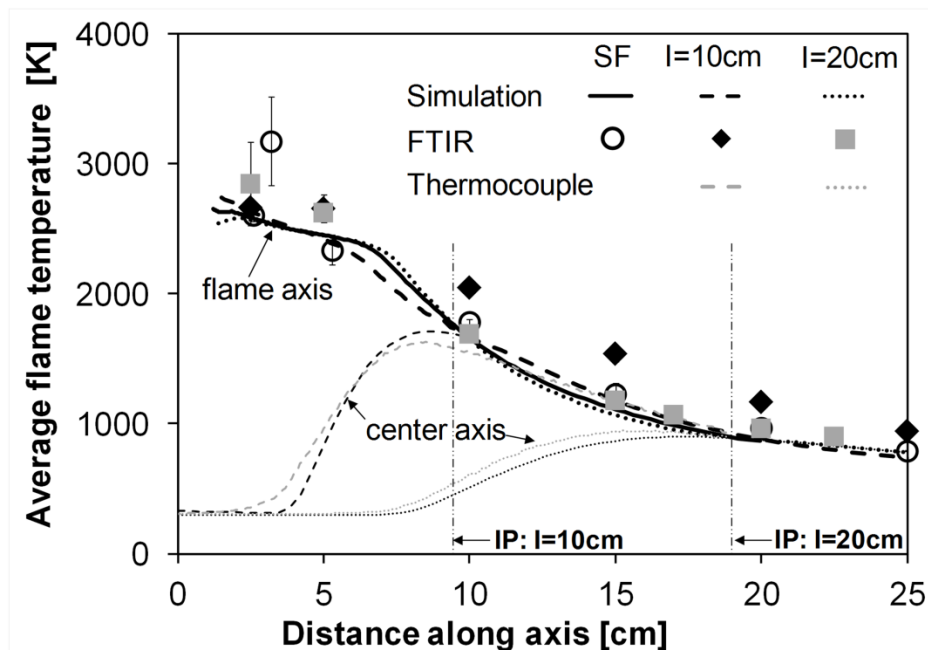


Figure 43: FTIR-measured line-of-sight (symbols) and CFD-predicted centerline flame temperatures (thick black lines) along the flame axis for the single flame (circles, solid line) as well as the DF with $l = 10$ cm (diamonds, dashed line) and $l = 20$ cm (squares, dotted line) at constant $\alpha = 20^\circ$. Furthermore thermocouple-measured temperatures along the center axis (thin gray lines) are compared with the CFD-predicted ones (thin black lines) for $l = 10$ and 20 cm.

The FTIR-measured single flame temperature profile (open circles) shows a maximum of about 3000 K within the first 5 cm before it rapidly decreases to around 1800 K at 10 cm

and 1000 K at 20 cm distance above nozzle level. FTIR measurements are line-of-sight averages that typically underestimate the centerline temperature in regions with steep radial gradients [252]. They show the largest experimental uncertainties (~12%) and the highest deviation to the simulated temperatures within the high temperature zone of the flame. This tendency is, however, attributed to low signal intensities in this optically thick part of the flame and steep temperature gradients which are especially observed at low heights above the burner [145, 168]. A reduced temperature in the flame center, due to droplet evaporation and maximum temperatures slightly off center, are additional reasons why minor changes in the measurement alignment can result in significant temperature changes in the high temperature part. This circumstance promotes measurement uncertainties and might be the explanation why the maximum temperature is higher in the FTIR measurements compared to the simulated flame center temperatures. The estimated parameters for the combustion model of the CFD simulation also have a significant influence on the temperature profile of the high temperature zone and may have to be further optimized in future. However, since the focus of the study is to investigate the temperature in the region of flame intersection these uncertainties play a tangential role. For the crucial distances higher than 5 cm, where radial temperature gradients become less pronounced, good agreement between the measurement and the simulated SF set-up is attained.

In all temperature measurements, FTIR and thermocouple, as well as in the CFD simulation only xylene combustion is considered and precursor combustion is neglected. This is a reasonable procedure considering the fact that there are only minor variations in the combustion enthalpy due to the addition of a precursor (e.g. 4.5% for a 0.5 M TiO₂-flame compared to a pure xylene flame).

Figure 43 further illustrates the flame temperature profiles of two varying intersection distances $l = 10$ (diamonds, dashed line) and $l = 20$ (squares, dotted line) at a constant $\alpha = 20^\circ$. In the $l = 10$ configuration the FTIR-measured average temperature is 200-300 K higher along the flame axis (between 10 and 20 cm) compared to the SF configuration. This higher temperature can be attributed to a reduced supply of cold ambient air in the inner entrainment region (see illustration in Figure 42). Around the geometric intersection point, mutual entrainment of hot gas seems to decelerate the cooling process of the flame compared to the SF set-up. These conditions result in higher temperatures along the flame axis for the DF set-up. This assumption was already suspected by Strobel et al. for similar double FSP configurations [76]. For the $l = 20$ cm configuration the FTIR measurements indicate a lower temperature deviation between

the DF and SF set-up. This suggests a significant reduction of the interaction along the flame axes of the two flames.

The comparison of the maximum thermocouple- measured temperature at a horizontal of 9.4 cm above the nozzle level in Figure 44 (black solid lines) indicates that the $I = 10$ (a) configuration has an approx. 200 K increased temperature compared to the $I = 20$ (b) one at this height. This is in good agreement with the FTIR results and a further verification of the assumption that the average temperature is increased for the $I = 10$ setting due to limitations in the entrainment. The higher flame axis temperature, after passing the geometric intersection point, however, is less pronounced in the simulations. It can be assumed that the reason for this circumstance mainly results from differences in the entrainment conditions of the simulations compared to the experimental set-up. In the experimental setting, the nozzle holder geometry of the DF arrangement differs and therefore significantly influences the supply of cold ambient air into the inner region. This actual nozzle plate geometry may not be described accurately enough in the computational grid leading to the observed differences.

The thermocouple- measured (thin gray dashed lines in Figure 43) and the simulated (thin black dashed lines) temperature profile along the center axis for the $I = 10$ configuration indicate a rapid rise in temperature from ambient conditions at 3 cm to 1650 K at 8 cm. This increase originates from the interaction of the two expanding flame jets (see simulated flow profiles in Figure 45) with outer aerosol stream boundaries already merging before the geometric intersection point. Simulation (thin black dotted line) and thermocouple measured (thin gray dotted line) temperatures for the $I = 20$ configuration indicate an approximately ambient temperature up to 8 cm on the center axis. Downstream the temperature slowly rises to a maximum of ~950 K attained shortly before the intersection point (18.8 cm on the center axis). This confirms that in the high temperature where most of the nucleation and primary particle growth takes place is only little interaction between the two flames, zone [168]. The illustration of the thermocouple- measured temperature in Figure 43 slightly underestimates the maximal measured temperature, since it is shifted in radial direction due to an experimental offset, visible in Figure 44.

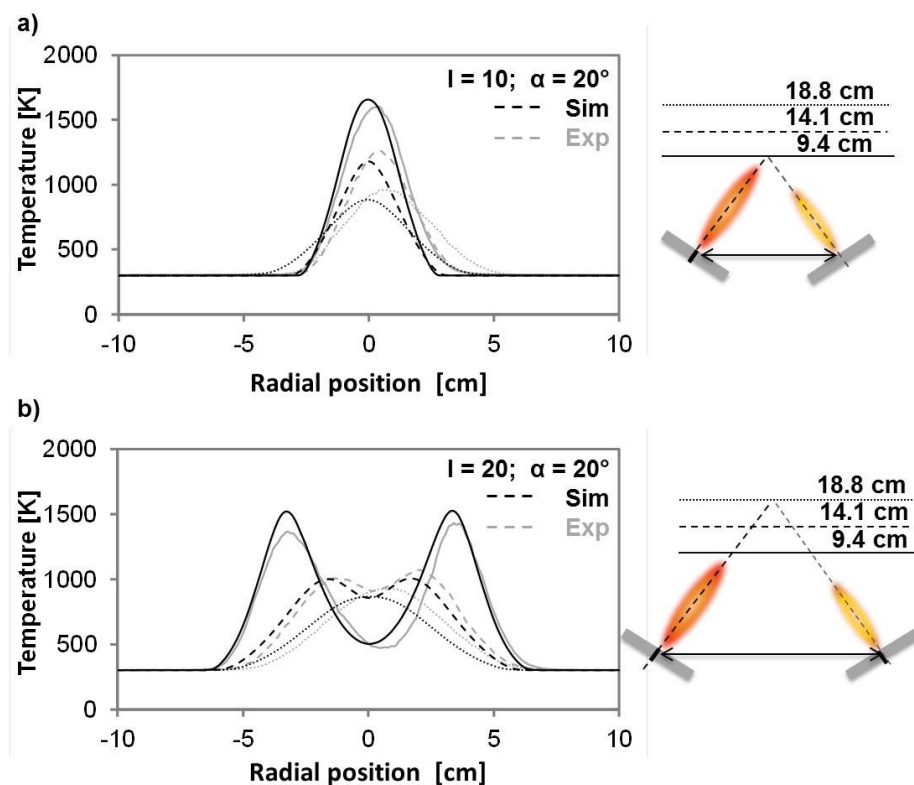


Figure 44: Thermocouple-measured (gray lines, Exp) and simulated (black lines, Sim) temperature profiles along three horizontals 9.4 (solid lines), 14.1 (dashed lines) and 18.8 cm (dotted lines) above nozzle level for the double flame setting with a) $I = 10$ cm and b) $I = 20$ cm.

Figure 44a illustrates the temperature profiles measured by thermocouple as well as CFD-predictions along horizontal lines at 9.4 (solid line), 14.1 (dashed line) and 18.8 cm (dotted line) distance from the nozzle level. Thermocouple and simulated temperatures are in good agreement considering the model limitations for the high temperature zone addressed earlier and the fact that thermocouple measurements are not corrected for radiation and convection [253]. Small radial shifts between measured and computed profiles result from the mentioned limited accuracy of the experimental alignment. Similar to the FTIR results, the thermocouple-measured temperature in Figure 44 is higher after passing the intersection point compared to the simulations (~ 80 K at a horizontal of 18.8 cm and 14.1 cm). For higher temperatures (horizontal at 9.4 cm) inaccuracies for the thermocouple measurements due to radiation and convection are more important [253]. This leads to a lower experimentally determined temperature in contrast to the simulated ones. As thermocouple measurements tend to underestimate the temperature especially in the high temperature regime, it can be assumed that the actual temperature is significantly higher than the measured and the simulated one.

For the $l = 10$ cm setting, all profiles show only one maximum around the centerline confirming that the two flames have merged to a single one at 9.4 cm which corresponds to the geometric intersection point. This merging of the two individual flames doubles the hot aerosol mass flow, enthalpy and entrainment air requirement compared to a single flame, further explaining the higher temperatures downstream the intersection point observed with FTIR (Figure 43). Since the horizontal temperature profile gives an indication of the degree of flame expansion it is thereby indirectly a first indication for the mixing process of the aerosol streams. The results demonstrate that for small intersection distances $l \leq 10$ cm the aerosol streams have already fully merged at temperatures above 1500 K where particle formation is still in progress. Mixtures on atomic and inner particulate scale are thereby conceivable.

For higher intersection distances, $l = 20$ the merging of the temperature profiles is only completed for the horizontal at 18.8 cm above nozzle level (see Figure 44 b), where the temperatures are already below 1000 K and the primary particle formation process is presumably completed. Dependent on the precursor, mixtures on particle and particle cluster scale can be expected. For the horizontal profiles recorded at 9.4 cm and 14.1 cm two local temperature maxima and a local minimum along the horizontals are visible. This characteristic of the temperature profile is an evidence for the existence of two individual spray flames in the outer regions. However, the temperatures increase in the inner entrainment region of the flames, distinctive visible for the horizontal one at 14.1 cm, indicating a partial intersection of the flames upstream of the geometric intersection point (18.8 cm at the center axis).

In summary, the experimental studies of the temperature profile suggest a slightly higher flame axis temperature for small intersection distances ($l \leq 10$ cm) compared to the SF or higher intersection distances ($l = 20$ cm), due to limitations of the entrainment flow. Within the next section 5.2, the influence of this temperature increase on the product characteristic is investigated in more detail.

How the interaction of the two flames takes place in detail is described by the status of the mixing process of the two aerosol streams. The status of the mixing process gives insight into the probability distribution of the components in the reaction zone. The mixing process is in progress as long as one component's probability of presence changes with the position in the merged reaction zone of the flames. The mixing process is considered to be completed, when both components have the same probability of presence within the whole reaction zone of the flames. One way to visualize the status of the mixing process of the aerosol streams depending on the position in the reaction zone are CFD-

simulated contour plots of the fraction ratio of scalars. Figure 45 illustrates these contour plots for the central plane of the $l = 10$ and $l = 20$ cm ($\alpha = 20^\circ$) setting. In this approach the simulations did not consider any particles and their migration e.g. by diffusion or thermophoresis. However, the particles typically present within the flame are small enough (Stokes $\ll 1$) to closely follow gas streamlines. It is further assumed that the formation of nanoparticles takes place after vaporization and combustion of the liquid precursor in the spray flame and its dynamics have no significant influence on the multiphase flow characteristics [169, 254].

The two nozzles release different types of scalars blue (0) and red (1) in the ratio 1:1. The mixing process of the aerosol streams is completed, when a fraction of 0.5 (gray) is achieved since this is the final component's probability of presence as soon as the system is in equilibrium. A completed mixture process is a necessary requirement to achieve a uniform mixture, as defined in section 2.2 on page 13.

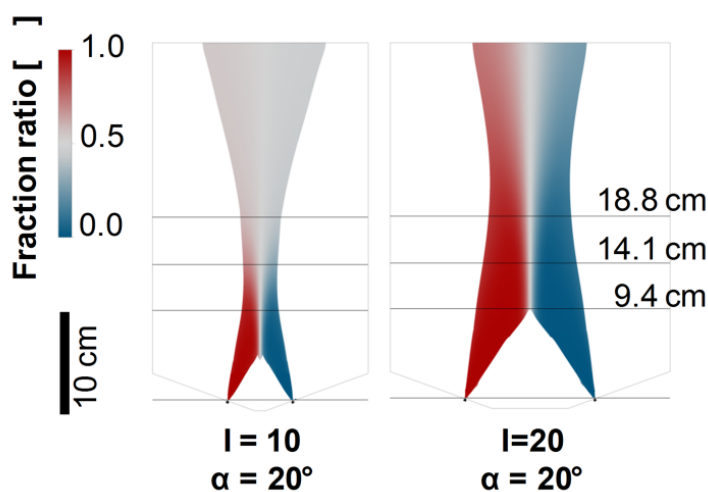


Figure 45: Central plane contour plots of the fraction ratio of scalars released from nozzles 1 (red) and 2 (blue) for the $l = 10$ cm and $l = 20$ cm setting both with $\alpha = 20^\circ$.

Comparing the $l = 10$ and the $l = 20$ setting significant differences in the mixing process and in the resulting uniformity of the sample are visible. In the $l = 10$ configuration the inner flame boundaries intersect at 4.7 cm above nozzle level resulting in a uniform mixture of the two scalars (fraction ratio ~ 0.5) around the centerline where temperatures are around 500°K . In contrast, blue and red scalars exist off-center in unmixed regions. These unmixed regions, however, diminish rapidly after passing the intersection point at a horizontal of 9.4 cm above nozzle level, since the mixing region quickly spreads to the outer boundaries of the combined reaction zone. At a horizontal height of 18.8 cm the mixing process of the aerosol streams is completed and a uniform mixture is achieved

throughout the whole reaction zone. During the mixing process of the aerosol streams, the temperature in the reaction zone is continuously above 600°K.

For higher intersection distance ($l = 20$), the flame boundaries of the two expanding aerosol streams intersect significantly later compared to the $l = 10$ set up. The first interaction of the inner flame boundary takes place at a horizontal height of roughly 9.4 cm above nozzle level and results in the formation of a uniform mixture around the center axis at temperatures around 600 K. This region slightly expands radially up to the intersection point at 18.8 cm but the expansion is limited in direction of the outer flame boundaries. Even at twice the intersection height, at a horizontal of 38 cm above nozzle level, a uniform mixture across the combined flame has not been achieved. Less intense turbulent mixing at lower gas velocities leads to this restricted mixing. Additionally, the overall domain of the aerosol streams is significantly broader for the $l = 20$ cm flame. It is more than twice as thick as the $l = 10$ cm flame at the intersection point, since for higher intersection distances the expansion and deceleration of the aerosol streams by air entrainment is even more pronounced.

The contour plots further give a first indication that the mixing process of the flames highly depends on the adjusted flame configuration. Regions, where the mixing process of the two aerosol streams have already taken place at the high temperature and within the particle formation zone (inner entrainment region), can be present in parallel to regions, where mixing with the other aerosol stream takes place at significantly lower temperatures or a mixing of the two aerosol streams is completely absent. The DF process, however, offers a variety of geometric parameters to modify the mixing process of two aerosol streams and therefore the final product uniformity.

In the next section, experimental investigations give for the first time systematic insights regarding the influence of the intersection distance and the intersection angle on the degree of mixing and the uniformity of the synthesized sample.

5.2 Analysis of the DF mixing process in a deposited system

For a detailed study regarding the influence of the flame configuration on the crystallinity and the individual particle sizes one SF and three DF samples ($l = 10, 20, 35$ with $\alpha = 20^\circ$) within the Pt and TiO_2 system are synthesized. Table 5 lists the geometric parameters and the resulting SSA.

Table 5: Overview of the synthesizes conditions and the specific surface areas (SSA)

Notation	Synthesis method	Amount Pt [wt. %]	Intersection distance l [cm]	Intersection angle α [°]	SSA [m ² /g]
TiO ₂	SF	0	---	---	119
SF	SF	5	---	---	117
l=10 $\alpha=20^\circ$	DF	5	10	20	129
l=20 $\alpha=20^\circ$	DF	5	20	20	120
l=35 $\alpha=20^\circ$	DF	5	35	20	120
l=10 $\alpha=37.5^\circ$	DF	5	10	37.5	108

The crystallinity and particle size are determined using X-ray diffraction, BET and H₂-dispersion measurements. Figure 46 shows the X-ray diffraction patterns of pure TiO₂ synthesized in the SF as well as 5 wt.% Pt/TiO₂ produced with the SF and the three DF settings. The characteristic Bragg peaks in the pattern reveal that the titania consists of the crystal phases anatase and rutile. The ratio of the two phases is determined based on Rietveld fittings and reveal a ratio of 75 / 25 wt.% for the SF TiO₂ and all DF samples. The average crystallite sizes are 21 nm for anatase and 5 nm for the rutile crystals. The anatase to rutile ratio and the average particle sizes are in good agreement with the work of Teoh et al. who synthesized Pt/TiO₂ in the SF process [80]. Figure 46 further illustrates that the crystallinity of the titania support and the crystal sizes are both unaffected by the flame configuration and linked temperature changes in the reaction zone of the l = 10 setup.

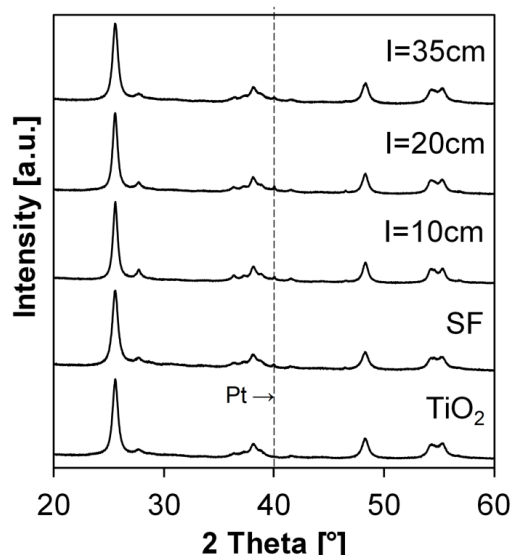


Figure 46: XRD patterns of pure TiO₂ as well as 5 wt.% Pt/TiO₂ nanopowders prepared with the single flame (SF) or the double flame (DF) with l = 10, 20 cm or 35 cm intersection distance and $\alpha = 20^\circ$.

Next to the crystallite size is the titania BET-equivalent diameter (open triangles) unaffected from the different double flame configuration as presented in Figure 47. All three double flame settings: $l = 10$ cm, 20 cm and 35 cm at $\alpha = 20^\circ$ have an average BET-equivalent diameter in the range of 12.5 ± 0.6 nm. This diameter does not vary significantly from the one of the SF, which is 13.0 ± 0.3 nm. This result is in agreement with the work of Schulz et al. [168] who demonstrated the completion of the titania growth under comparable synthesis conditions at around 8 cm from the nozzle level. Therefore at the intersection distance of $l = 10$ cm the titania particle growth is expected to have already stopped. Molecular dynamics studies of Buesser et al. further corroborate the results since they illustrate in their work that rapid coalescence of small titania nanoparticles does not occur below approx. 1800 K [166]. This temperature is reached in the DF setting at ~ 10 cm from the nozzle (Figure 43).

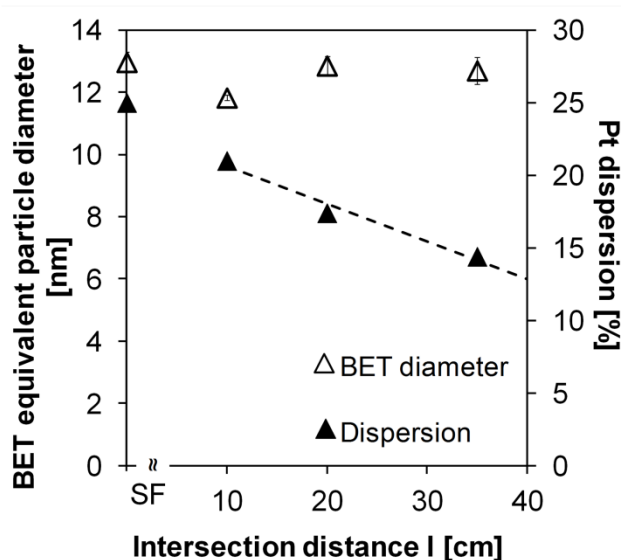


Figure 47: BET-equivalent diameter of the TiO_2 particles (open triangles, left axis) and Pt dispersion (filled triangles, right axis) in the SF product powder and for the DF with $\alpha = 20^\circ$ and $l = 10, 20$ and 35 cm. The titania primary particle size stays approximately constant for all conditions while the Pt dispersion determined by H_2 adsorption isotherms is highest for the SF and decreases with increasing intersection distances of the DF indicating increasing Pt particle sizes.

In comparison to the constant support particle characteristic the Pt particle size is affected by the different synthesis conditions. The X-ray diffraction patterns show a small peak at $2\theta = 40^\circ$ (vertical line in Figure 46) for all Pt-containing samples. This peak is attributed to metallic platinum. Only for the DF sample made with $l = 35$ cm a quantitative Rietveld analysis is possible resulting in a fitted Pt content of 4.71 ± 0.8 wt.%. This content reflects the nominal precursor composition of 5 wt.%. The determined Rietveld Pt

size is 2.7 ± 0.3 nm. In case of the other Pt-containing samples a sufficient signal-to-noise ratio is missing referring to smaller Pt crystallites compared to the $l = 35$ sample.

H₂ chemisorption helps to achieve detailed insights into the Pt-particle size. While nitrogen adsorption is a measure for the size of the support particles, which constitute 95 wt.-% of the product powder, H₂ chemisorption provides an indicator for the Pt particle size in terms of Pt dispersion. The determined dispersion is the ratio of the H₂-accessible Pt surface atoms to the total number of Pt atoms in the system. The highest dispersion, which correlates with the smallest Pt particle size, is obtained for the single flame configuration with a dispersion of $25\% \pm 2.4\%$, see Figure 47 (filled triangles, right axis). An increase of the intersection distance in the DF setting results in a decrease of the Pt dispersion and thus increases the Pt particle size. The lowest dispersion of 14.4 % is obtained for the highest intersection distance of $l = 35$ cm. This result is in qualitative agreement with Strobel et al. who also observed a size increase of alumina-supported Pt particle for higher intersection distances [76]. These results illustrate that the Pt particle size is significantly affected by the DF setting in contrast to the TiO₂ support particles.

The dispersion measurements are carried out with H₂ and CO resulting in equivalent dispersions for both gases. XRD and TEM measurements performed before and after the chemisorption (sample $l = 35$ cm, $\alpha = 20^\circ$; data not shown) resulted in the same Pt crystallite size ruling out sintering during H₂ pre-treatment. Previous single flame studies of Teoh et al. [80] and Schulz et al. [168] report Pt dispersions on TiO₂ of 40% and above. Compared to this study the measured dispersions are considerably lower. However, it should be noted that in both cited studies the dispersion is measured differently using CO pulse chemisorption. A significant influence of the type of analysis method, here static adsorption isotherms vs. dynamic pulse chemisorption, on the absolute dispersion values is known [255]. The results are further affected by the choice of the evaluation method of the isotherms (extrapolation, rucketing, langmuir). Strobel et al. obtained comparable dispersion in the range of 30% for FSP-made 5 wt.% Pt/Al₂O₃ using H₂ chemisorption and the isotherm method [139].

These results give a first indication that the different physical properties of the particular material respectively the applied precursors highly influence the final product characteristic. Precursor with low boiling points and an extended region of nucleation and surface growth (e.g. noble metals like Pt) are more effected by geometric changes in the DF configurations (within the investigate parameter range) than materials, respectively precursors, where the particle formation process is completed within the high temperature regime of the flame (e.g. TiO₂).

All investigated intersection distances, including the SF, result in mixtures on particle scale (Figure 50). However, significant differences in the uniformity of the deposition are visible (Figure 48). Distributions of different parameters such as Pt particle size and number of particles per cell help to experimentally quantify the uniformity of the synthesized samples. The analysis on bases of a distribution has certain advantages compared to average values. The form of the resulting distribution gives an insight into the uniformity of the investigated parameter. A resulting distribution which is bell-shaped with high symmetry (the difference between the median and the arithmetic mean is small and the skewness approaches zero [70]) and a small standard deviation indicates a uniform product quality. In contrast, a low uniformity is indicated by an asymmetric distribution (high skewness) and a large standard deviation. One appropriate way to illustrate the form of the investigated distribution is the use of boxplot representations, see section 2.4.2.

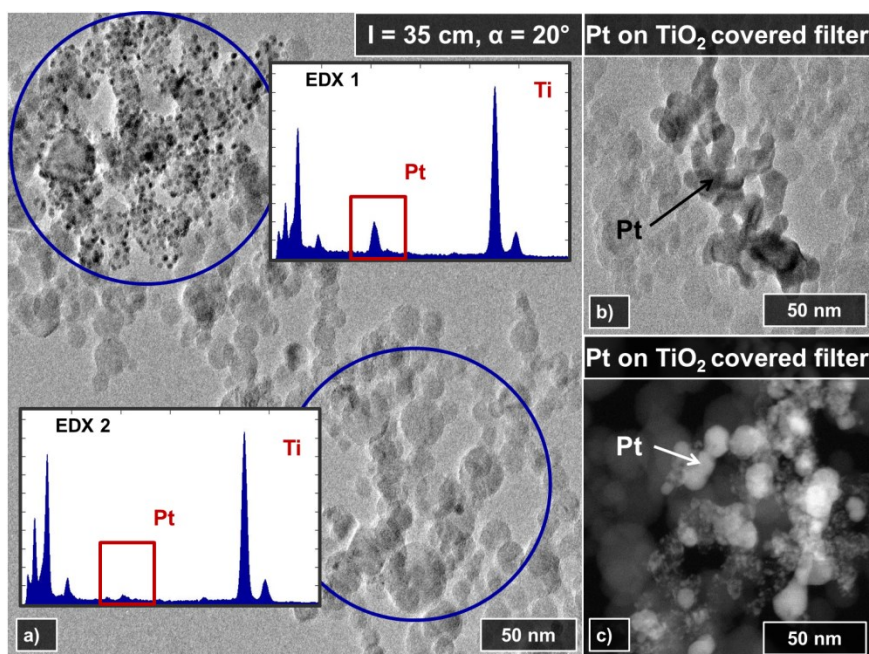


Figure 48: a) TEM micrograph of a powder made in the DF with $I = 35 \text{ cm}$ and $\alpha = 20^\circ$. Upon mixing Pt particles deposit on titania supports which limits their further growth to $\leq 5 \text{ nm}$ (top region). EDX reveals Pt-rich (EDX 1, top) and Pt-lean regions (EDX 2, bottom) in the produced powder. b) TEM and c) STEM images of Pt nanoparticles made in a pure Pt SF and deposited on a previously TiO_2 -coated glass-fibre filter. Primary Pt particles grow by homogeneous nucleation, coalescence and/or vapor condensation to sizes up to 20 nm.

In a first step, changes within the Pt particle size distribution give an insight into the mixing characteristic of different flame configurations. Whereas a uniform Pt particle size distribution on the TiO_2 support is known for the SF process (Figure 50a), a non-uniform distribution is observed for the DF process with high intersection distance $I = 35 \text{ cm}$

(Figure 48a). The Pt diameter distributions (Figure 49) are obtained using TEM and STEM images of the SF (a) and DF with $\alpha = 20^\circ$ and $l = 10, 20$ and 35 cm (b-d). Table 6 provides the corresponding mean diameters and geometric standard deviations.

In the SF, the formation of TiO_2 support particles and Pt deposits take place consecutively. As discussed before, TiO_2 nanoparticles formation takes place initially followed by a heterogeneous nucleation of small Pt atomic clusters on the TiO_2 surface. The formed Pt atomic clusters then subsequently grow by Pt vapor condensation and rearrangement forming Pt particles [168]. Sintering of the Pt particles is hindered due to the immobilization on the TiO_2 surface. The synthesis results in a log-normal Pt-size distribution with a Pt particle size of $d_{\text{TEM}} = 1.1$ nm and a geometric standard deviation in the range of $\sigma_g \sim 1.35$ represented in Figure 49 (a). The σ_g of the SF is considerably smaller than the value representing coagulation and rapidly coalescing primary particles in the free molecular regime approaching their self-preserving size ($\sigma_g = 1.46$) [256]. The narrow size distribution, therefore, further supports that formation and growth of Pt particles mainly occurs by vapor condensation on pre-existing titania particles.

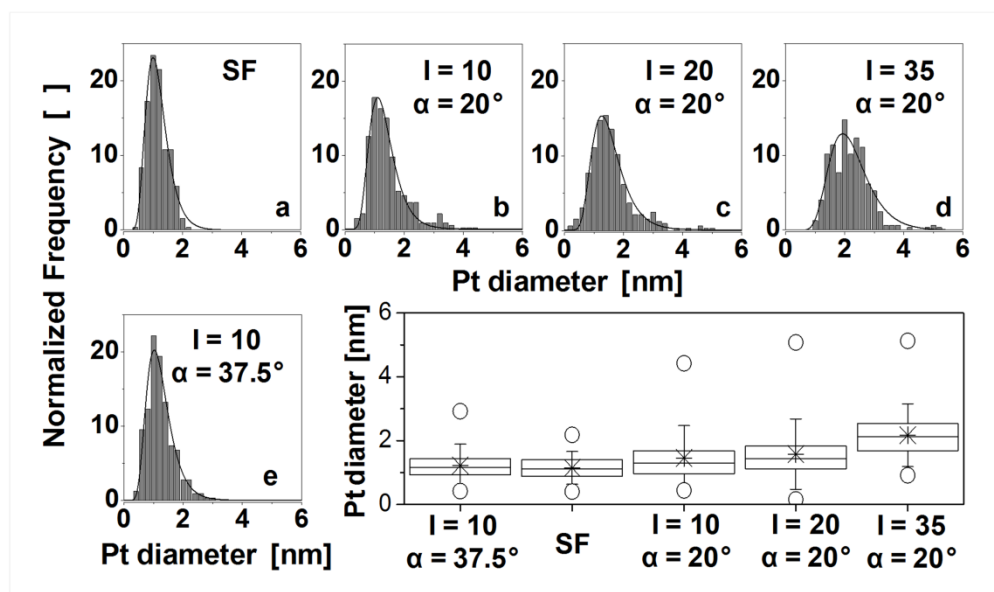


Figure 49: Pt particle size distributions for the SF (a) and DF settings of $l = 10$ (b), 20 (c) and 35 cm (d) with $\alpha = 20^\circ$, based on $n=325$ evaluated Pt particles each. A size distribution for $l = 10$ cm and $\alpha = 37.5^\circ$ (e) is shown as well. The corresponding boxplot representations provide the lower quartile, the median and the upper quartile values (box), the lower and upper limit of the results (\circ), the arithmetic mean (\times) and 1.5 times the standard deviation (whisker).

When the Pt synthesis takes place without the presence of TiO_2 support, Pt undergoes homogeneous nucleation before growth takes place by coalescence and/or condensation of additional Pt vapor. The primary particle growth stops at low particle

concentrations or when the temperature falls below the Pt sintering temperature (about 450°C for Pt, [139]). This case is represented, due to a SF fed, only with Pt precursor. The primary Pt particle sizes go up to 20 nm when the Pt powder is collected on a (previously) TiO₂-covered glass-fiber filter (Figure 48 b and c - no particle size distribution present).

In double flame configuration, the Pt particle size depends strongly on the intersection distance. For short intersection distances, homogeneous nucleation of Pt has not or only partly started in the intersection region, leading to a Pt particle size in the range of the SF powder. For higher intersection distances, the Pt nucleation starts in the absence of TiO₂ support particles. The Pt particles then collide with the TiO₂ particles of the second flame which inhibits further growth by Pt – Pt particle coalescence. The higher the intersection distance the longer the Pt particle growth takes place. This trend is visible in the increase of the mean particle size from 1.3 nm for $l = 10$ cm to 2.1 nm for $l = 35$ cm and $\alpha = 20^\circ$. This observation is also in agreement with the dispersion measurements (Figure 47) and close to the XRD Pt size of 2.7 ± 0.3 nm for the $l = 35$ cm sample (Figure 46).

The Pt particle sizes of samples DF with $l = 10$ cm and $l = 20$ cm are log-normal distributed and have increasing geometric standard deviations σ_g compared to the SF (see Table 6 and boxplots in Figure 49). For $l = 10$ and $l = 20$ cm, the size distribution broadens due to a more pronounced large tail. This indicates that some particles form by homogeneous nucleation and subsequently grow to a larger size without any TiO₂ support contact while others remain small by growth or early deposition on TiO₂. At $l = 35$ cm the σ_g seems to decrease to 1.3 again. It must be noted, however, that the distribution deviates from log-normal shape and may in fact consist of two overlapping distributions, associated with the two different particle formation and growth regimes. Very small particles < 1nm are not observed as aerosol mixing begins at a rather high distance above nozzle level. A significant number of larger Pt particles indicate a continuous growth by Pt-Pt coalescence in regions of the flame where TiO₂ aerosol has not entered yet. This shows that the mixing process in the DF process plays a key role for the final product uniformity.

Table 6: Geometric mean (d_{mean}) and geometric standard deviation (σ_g) of the TEM based Pt diameter distributions of Figure 49 along with the empty cell ratio and F-Test results of the Pt number distribution (Figure 51).

Sample	Pt diameter distribution		Pt number distribution			
			10nm x 10nm cell		50nm x 50nm cell	
	d_{mean} [nm]	σ_g	Empty cell ratio	F-Test*	Empty cell ratio	F-Test*
I=10 $\alpha=37.5^\circ$	1.1	1.40	0.52±0.04	fail	0.00±0.01	pass
SF	1.1	1.35	0.53±0.05	---	0.00±0.00	---
I=10 $\alpha=20^\circ$	1.3	1.52	0.54±0.03	fail	0.01±0.02	fail
I=20 $\alpha=20^\circ$	1.4	1.60	0.59±0.05	fail	0.05±0.07	fail
I=35 $\alpha=20^\circ$	2.1 [▲]	1.30 [▲]	0.73±0.12	fail	0.14±0.11	fail

* Testing the null hypothesis (sample and SF distributions have the same variance ($\alpha_0=0.05$))

▲ A deviation from log normal distribution shape is observed Figure 49

One main difference between the SF and the DF process could be the present aggregate state of the Pt in the reaction zone. In the SF Pt nucleation and condensation coexist all over the reaction zone. In the DF, Pt might be present in solid phase after heterogeneous nucleation in the inner entrainment region and in the outer regions due to the absence of TiO₂ in the gas phase. For adjustments with higher intersection distances is the probability for a TiO₂ supported Pt contact significantly higher along the center axis compared to the outer flame regions. In the outer regions of the Pt flame homogeneous nucleation and growth by coalescence and/or condensation occurs, leading to larger Pt particles. This is reflected in the broader Pt size distributions and larger mean particle diameters for higher intersection distances (Figure 49 and Figure 47). At the same time, undecorated TiO₂ particles are formed at the outer region of the TiO₂ flame resulting in Pt-lean and Pt-rich regions in the produced powders, visible in Figure 48c for I = 35 cm and confirmed by EDX (insets). This non-uniform Pt deposition significantly reduces the degree of mixing,

For I = 10 cm in contrast, a balance in concentration gradients is obtained in an earlier stage of the reaction zone. A uniform Pt deposition is obtained for an intersection distance of 10 cm, indicated by small geometric standard deviation of the Pt particle size distribution. The case where all TiO₂ support particles have the same amount of similarly sized Pt deposits reflects the ideal case regarding the uniformity of a mixture.

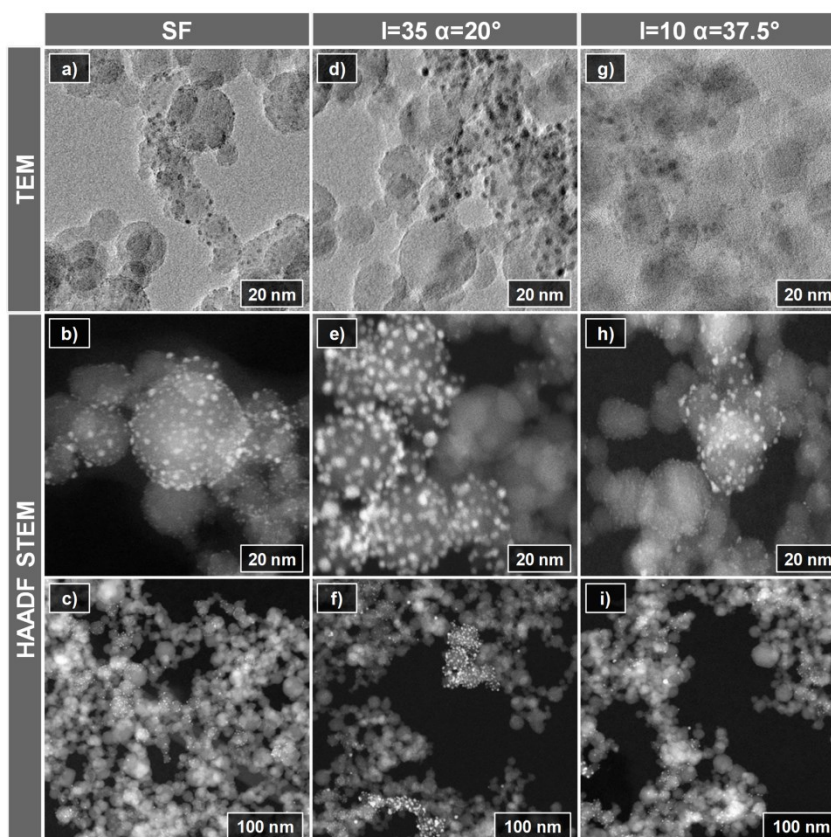


Figure 50: TEM and HAADF-STEM images of Pt / TiO₂ particles made in the SF (a - c) and in double flames with $l = 35$ cm, $\alpha = 20^\circ$ (d - f) or $l = 10$ cm, $\alpha = 37.5^\circ$ (g - i).

To quantify this definition of uniformity the quadrat method [103] is applied to HAADF-STEM images of the produced powders (Figure 50). Equally sized cells divide the images and enable to quantify the number of Pt particles per cell. A large number of cells having approximately the same amount of Pt particles result in a symmetric bell-shaped distribution with a small standard deviation and skewness value. This case represents a uniform Pt deposition, correlated with a high degree of mixing. In a non-uniform mixture some quadrats contain no or only a few Pt particles along with others displaying a high number of Pt particles. Since the result of the quadrat method can depend on the cell size [70, 102], two cell sizes are investigated. The smaller 10 x 10 nm quadrats have a size similar to the average BET-equivalent diameter of the TiO₂ particles, whereas the larger 50 x 50 nm quadrat size is more sensitive regarding the regions of high Pt density (approximately 150 nm, see Figure 48).

While Appendix 1 shows the detailed Pt particle number distributions of each sample for cell sizes of 10 x 10 nm and 50 x 50 nm, Figure 51a summarizes the resulting characteristics of the distributions for 50 x 50 nm cells in the form of boxplots.

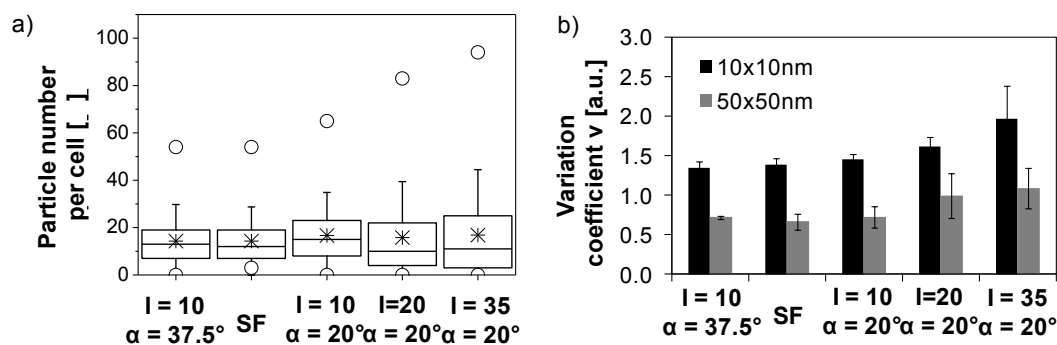


Figure 51: a) Boxplots of the Pt particle number distributions (50 x 50 nm cells) and b) the variation coefficient for cell sizes 10 x 10 nm and 50 x 50 nm indicating a decrease in the uniformity for increasing intersection distances.

For the SF sample the median is nearly centered within the box, whereas for increasing intersection distances from $I = 10$ to 35 cm at constant $\alpha = 20^\circ$ the median shifts to the lower quartile representing an asymmetric, right-skewed distribution. This increase in skewness is accompanied with an increased upper limit (circles) and increased standard deviation (whiskers) indicating that the Pt distribution becomes less uniform and the degree of mixing decreases with higher intersection distance, as predicted by the contour plots (Figure 45). A detailed boxplot analysis of the 10 x 10 nm is impossible since the amount of empty (not with Pt decorated TiO_2 covered cells) is dominating the distribution considerably. A numeric comparison of DF distributions and SF ones takes place with the help of the F-test. The F-test is passed if the variances are not significantly different from that of the SF sample (null hypothesis) and otherwise failed (level of significance $\alpha_0 = 0.05$). Here the F-test is failed for all Pt distributions obtained with the $\alpha = 20^\circ$ DF flames, indicating that mixing process and the resulting uniformity of the sample significantly differs from the SF (Table 6).

The variation coefficient v is a well-known and routinely applied parameter to quantify the uniformity of a mixture [257]. It reflects the deviation to a predefined target value. In this case, the target value is defined as the state, where all TiO_2 -covered cells within the STEM image contain an equal amount of Pt particles (ideal uniform mixture). Thus, an increase in the variation coefficient correlates with a decrease in uniformity. The SF sample reveals a variation coefficient of 1.39 ± 0.08 for the cell size of 10 x 10 nm and 0.67 ± 0.1 for 50 x 50 nm (Figure 51b). This indicates a slightly non-uniform Pt particle deposition even for the well-mixed single flame, qualitatively observed also by Teoh et al. [80]. In the DF configuration the variation coefficient increases with higher intersection distances to 1.96 ± 0.43 (10 x 10 nm) and 1.09 ± 0.25 (50 x 50 nm) at $I = 35$ cm, $\alpha = 20^\circ$.

Although the two cell sizes result in different absolute values for the variation coefficient, the trend is the same for both cell sizes (Figure 51).

Another promising indicator for the uniformity of the samples is the ratio of the empty cells to the overall number of investigated TiO₂ covered cells (Table 6). The requirement for an empty cell is the complete absence of Pt particle deposits on the TiO₂ support. The uniformity of the mixture increases with a reduction of the empty cells ratio. The 50 x 50 nm analysis results in an empty cell ratio from 0% for the SF to 14% for $l = 35$ cm. The increasing empty cell ratio with increasing intersection distance correlates with the boxplot results of the Pt-particle number (cell size of 50 x 50 nm) and confirms a lower uniformity of the mixture for increasing intersection distances. The empty cell ratio determined with cell sizes of 10 x 10 nm also confirms the trend of increasing empty cell ratio with increasing intersection distance. The absolute value of the ratio, however, increases significantly from 52% for the SF to 73% for $l = 35$ cm.

The successful implementation of the quadrat method as a tool to analyze the Pt particle distribution indicates a significant decrease in uniformity with increasing intersection distance. This trend is visible for all applied evaluation methods. The value for the minimal height of the intersection distance, however, significantly depends on the applied material system and the desired mixing state and is commonly $l > 10$ cm as presented in section 4.2 and 4.4. In these cases, the adjustment of the intersection angle can help to ensure a uniform mixture even at higher intersection distances.

Effect of the intersection angle on the mixing process

Figure 52 illustrates the effect of the intersection angle α on the Pt dispersion for $l = 10$ cm (open diamond) and 20 cm (filled diamond). An increase of the intersection angle from 10° to 37.5° significantly increases the Pt dispersion. The trend is valid for both intersection distances, even though shorter intersection distances result in higher dispersions for all angles. A modification of the intersection angle, from $\alpha = 20^\circ$ to $\alpha = 37.5^\circ$, increases the Pt dispersion to ~22.3%. These results point out that the adjustment of an adequate intersection angle enables the similar uniformity achieved in the SF for samples synthesized with an intersection distances in the range of 20 cm samples. The adjustment of smaller intersection angles results in a more parallel alignment of the flames. This comes with a decreased radial velocity component and results in a reduced mixing of the two aerosol streams. In contrast, higher intersection angles enhance the mixing process and result in higher Pt dispersions (smaller particle size).

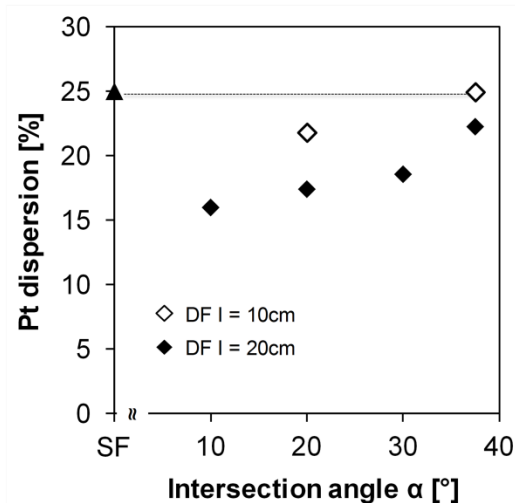


Figure 52: Effect of the intersection angle α on the Pt dispersion for $l = 10$ cm (open triangles) and 20 cm (filled triangles). Intersecting the flames at higher angles increases the Pt dispersion for both configurations.

At $\alpha = 37.5^\circ$ and $l = 10$ cm a dispersion of $\sim 25\%$, similar to the SF (filled triangle), is obtained. The similar Pt dispersion for the SF and the $l = 10$ cm, $\alpha = 37.5^\circ$ sample is further confirmed by the Pt particle size distribution from TEM analysis (Figure 49 a and e). Both samples follow a log normal distribution with a similar geometric mean diameter and standard deviation (Table 6). A qualitative comparison of the corresponding (S)TEM images (Figure 50 a-c and g-i) already suggests a similar Pt deposition pattern on TiO_2 associated with a comparable uniformity for both samples. The boxplots representing the Pt number distribution (Figure 51) present equivalent mean values and standard deviations (passed F-Test for cell size: 50×50 nm). Variation coefficient (Figure 51b) and the empty cell ratio (Table 6) are similar, too. The results of this section reveal that the choice of the intersection angle is a key parameter to ensure the uniformity of a sample, especially at high intersection distances.

5.3 Analysis of the DF mixing process in an aggregated system

For a detailed study regarding the influence of the flame configuration on the degree of mixing and the uniformity of the mixture in an aggregated system three SF and four DF samples ($l = 9, 20, 33$ and 66 with varying α) of the WO_3 and TiO_2 system are synthesized. Table 7 lists the geometric parameters and the resulting SSA. The molar ratio between the W and Ti is 1:2.8 which correlates with a weight ratio of 1:1 for the oxides and similar BET diameter of 11.2 nm for both components.

Table 7: Overview of the synthesis conditions and the specific surface areas (SSA)

No-tation	Syn-thesis method	Weight ratio TiO ₂ / WO ₃	Intersec-tion distance l [cm]	Intersection angle α [°]	SSA [m ² /g]	BET diameter [nm]
TiO ₂	SF	---	---	---	134	11.2
WO ₃	SF	---	---	---	73	11.2
SF	SF	1:1	---	---	127	---
DF 9	DF	1:1	87	20	92	---
DF 20	DF	1:1	20	35	96	11.2
DF 33	DF	1:1	33	20	104	10.3
DF 66	DF	1:1	66	10	100	10.7
PM	PM	1:1	---	---	96	11.1

Before the degree of mixing in the different samples can be quantified the critical intersection distance, which results in the formation of a mixture on particle scale, has to be determined. This is essential to exclude samples with mixtures on atomic and inner particulate state, which would distort the results.

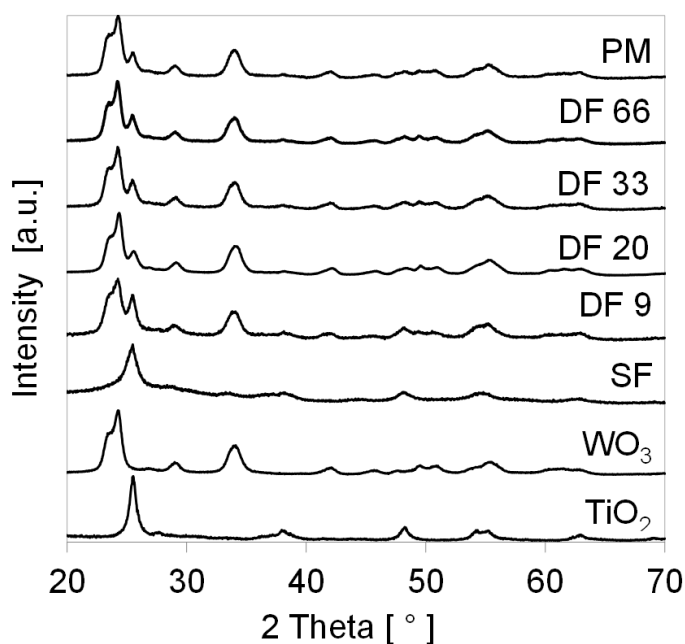


Figure 53: XRD patterns of pure TiO₂ and WO₃ and of the multicomponent powders prepared with the single flame (SF), the double flame (DF) intersection distance: $l = 9, 20, 33$ and 66 cm and the physical mixture (PM).

The XRD pattern indicates that the synthesis of both components (Ti and W) in the SF suppresses the formation of crystalline WO₃. The characteristic double peak, around 24° 2 θ for monoclinic WO₃, is completely missing in this sample (Figure 53). Although no peak shift for the main TiO₂ peaks is visible W doping of the TiO₂ is expected in the FSP

synthesis as already discussed by Akurati et al. [258]. The STEM image of the sample further indicates the formation of an amorphous WO_3 layer on the crystalline TiO_2 . The specific surface area is significantly higher compared to the other multicomponent samples. The synthesis of the two components in the single flame thus results in a mixture on atomic respectively inner particulate scale.

The synthesis in the DF set up with an intersection distance of 9 cm results in the formation of crystalline WO_3 and a significant decrease in SSA. However, the peak ratio between the main peak of the TiO_2 and the WO_3 still reveals the existence of non-crystalline WO_3 . The adjustment of an intersection distance of 20 cm enables the synthesis of crystalline WO_3 and TiO_2 particles. For this and the other two DF samples, the peak ratio of the TiO_2 and the WO_3 peak is equivalent to the one of the PM sample. The resulting BET diameter of all DF and the PM samples are within the same range without a clear trend. This confirms the conclusion of the previous section for materials, which grow by homogeneous nucleation like TiO_2 , an influence of the flame adjustment on the individual particle size can be excluded.

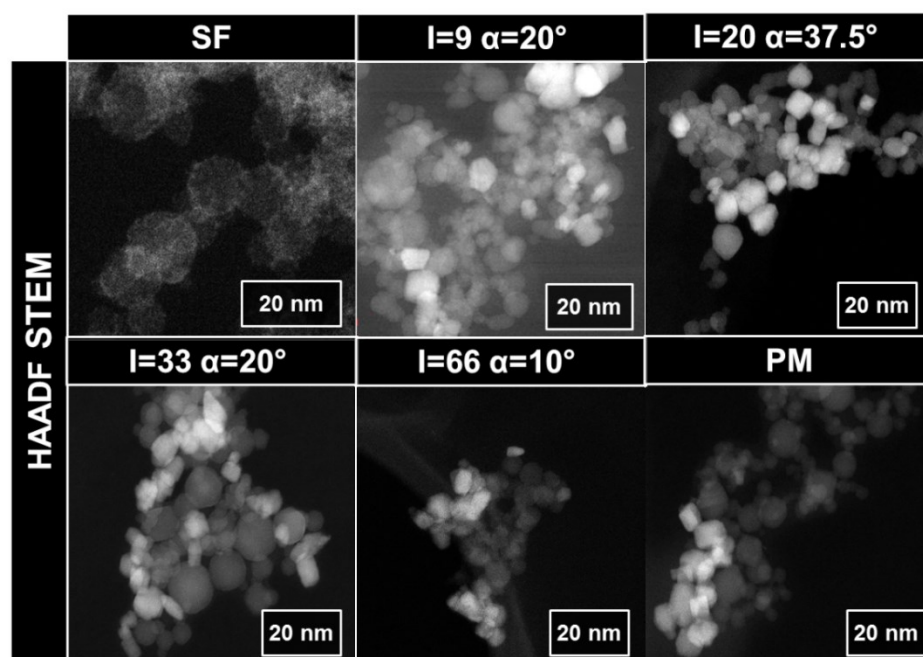


Figure 54: High angle annular dark-field (HAADF)-STEM images of TiO_2 (gray) and WO_3 (white) particles, synthesized using the SF, different parameter in the DF and a PM.

A detailed study of the degree of mixing and the uniformity of the samples is conducted based on the following samples: $I = 20$, $I = 33$, $I = 66$ cm and PM and the working hypothesis is illustrated in Figure 41. Since the atomic number significantly differs for the system, STEM combined with high angle annular dark-field imaging (HAADF-STEM) is

an appropriate method to achieve a gray scale picture of the present mixing state. The individual components considerably differ in contrast as visible in Figure 54. The spherical gray particles are TiO_2 and the cubic bright ones are WO_3 . To determine the mixing state and the uniformity of the samples minimum 39 agglomerates are analyzed regarding their average cluster sizes (Table 8) and their cluster size distributions (Figure 55). Therefore, all presented particles are assigned to either TiO_2 or WO_3 and the number of surrounding particles with the same type are counted and the resulting parameter like cluster size and heterocoordination are listed in Table 8.

Table 8: Key parameter of the investigated agglomerates within the three DF and the PM sample.

	l = 20 $\alpha = 37.5^\circ$	l = 33 $\alpha = 20^\circ$	l = 66cm $\alpha = 10$	PM
Amount of investigated particles	1598	1865	2093	2285
Amount of investigated agglomerates	41	39	52	47
Amount of WO_3 cluster	71	80	60	29
Amount of TiO_2 cluster	111	104	130	67
Arithmetic mean of the overall cluster size	8.8	10.1	11.01	23.8
Arithmetic mean of the WO_3 cluster size	4.8	7.8	7.0	22.7
Arithmetic mean of the TiO_2 cluster size	11.3	11.9	12.9	24.3
Heterocoordination	0.27	0.28	0.21	0.08

Based on the results of the previous section 5.2 it can be assumed that a flame adjustment with an intersection distance of $l = 20$ and an intersection angle $\alpha = 37.5$ results in a uniform mixture throughout the sample. Thus the $l = 20, \alpha = 37.5^\circ$ is set as a benchmark with an arithmetic mean of the TiO_2 cluster size of 11.3. and 4.8 for the WO_3 . Even for this geometric arrangement, a significant skewness of both distributions is visible in the box plot of Figure 55. The ratio of the TiO_2 and WO_3 particles is $\neq 0.5$ since in total more TiO_2 particles are present compared to the number of WO_3 (average over all samples: 62% TiO_2 particles and 38% WO_3 particles). This imbalance automatically leads to the formation of larger TiO_2 clusters with a higher standard deviation. The WO_3 in comparison has significantly smaller clusters and a reduced standard deviation.

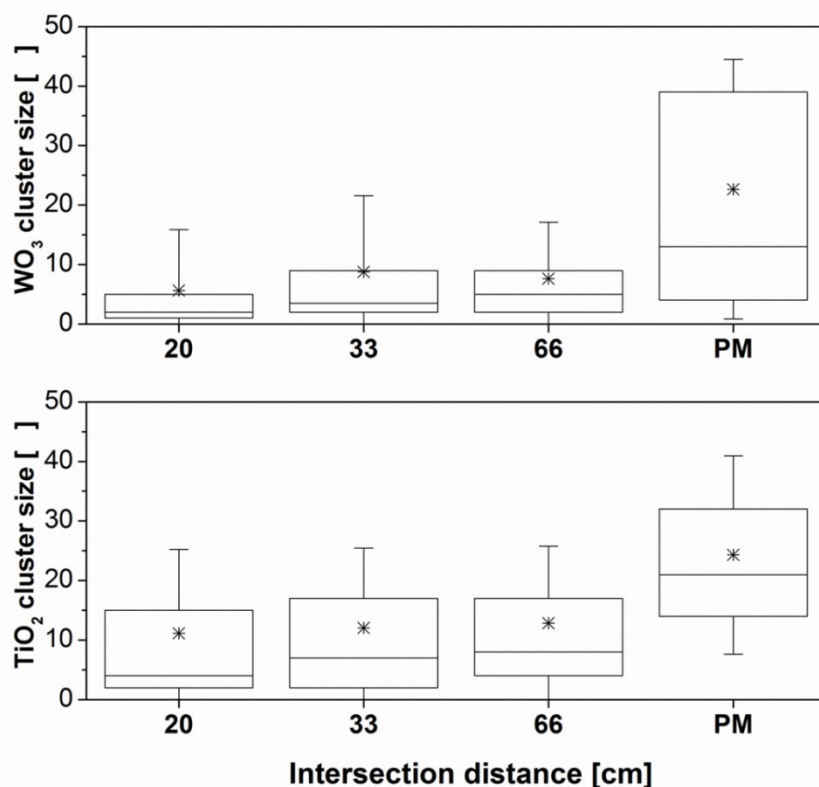


Figure 55: Boxplots of the determined cluster sizes for TiO_2 and WO_3 within the three DF samples $l = 20, 33$ and 66 and the PM sample. The corresponding boxplot representations provide the lower quartile, the median and the upper quartile values (box), the lower and upper limit of the results (\circ), the arithmetic mean (\times) and 1.5 times the standard deviation (whisker).

Based on the previous results it can be assumed that an increase in intersection distance and a decrease in the intersection angle significantly reduce the uniformity of the mixtures. The hypothesis is that a decreased degree of mixing is indicated by a larger average cluster size and an increasing standard deviation reveals a decrease in uniformity of the mixture. However, the determined average number of clusters for the three different DF samples does not considerably change and stays in the ranges of 182 to 190 clusters for all DF samples. For both the TiO_2 and the WO_3 a slight increase in the arithmetic mean of the cluster size distribution (\times) is visible from 8.8 to 10 for the TiO_2 and from 4.8 to 7.8 for the WO_3 . In addition, the skewness of the distribution slightly decreases with increasing intersection distance. This is valid for both materials TiO_2 and WO_3 and might indicate that the number of single clusters decreases with increasing intersection distance. These results are linked with a decrease in the degree of mixing and less uniform mixtures for an increasing intersection distance and decreasing intersection angles.

A significant drop in the degree of mixing and in uniformity, however, is observed for the PM sample. Whereas for all DF samples mixtures on particle / cluster scale are present, the PM consists of a mixture on aggregate scale for both TiO_2 and WO_3 . This confirms the working hypothesis of Figure 41. For both components, the distribution of the physical mixture significantly differs. Compared to the TiO_2 the PM sample of the WO_3 reveals a considerably broader and skewed distribution, indicating that next to large agglomerates also small particle cluster are present. For further interpretation of the data, aggregate size distributions for both components are required e.g. determined by a scanning mobility particle sizer or a disc centrifuge. Another opportunity to determine the degree of mixing is the analysis of the number of contacts between the different components, the hetero coordination described in section 2.4.2. The hetero coordination shows the same trend as the average cluster size: a slight decrease from 0.27 to 0.21 for the DF samples and a significant drop for the PM sample to 0.08. The hetero coordination deviates from 0.5 since in total more TiO_2 particles are present than WO_3 .

The overall results for the TiO_2/WO_3 systems show the same trend as already observed for the Pt/TiO_2 system: a decrease in the degree of mixing (average cluster size) and in uniformity (distribution of the cluster size) for increasing intersection distances and angles. However, the influence of the increasing intersection distances and decreasing intersection angles are minor compared to the results obtained in the Pt/TiO_2 system where the highest investigated intersection distance was 35 cm. This leads to the assumption that intersection distance and angle have a higher influence on systems when one component grows by heterogeneous nucleation (e.g. Pt) compared to systems where both components undergo homogeneous nucleation (e.g. TiO_2 or WO_3) in the high temperature regime of the flame.

It is further demonstrated, that for all three investigated geometric settings of the TiO_2/WO_3 synthesis, even for the intersection distances of 66 cm, a reasonable degree of mixing and an acceptable uniformity of the samples is achieved. This is the first time that such a characterization of an aggregated particle system synthesized in the DF set up is quantitatively conducted and key insights into the mixing process are provided. However, the validity for other material systems next to the TiO_2/WO_3 system has to be provided in the near future.

So far, the STEM based approach is the only experimental opportunity to obtain a quantitative evaluation of the degree of mixing and the uniformity of the mixture in aggregated systems. However, this approach is related with several experimental uncertainties, which have to be carefully discussed while data interpretation. Even so,

the contrast for the TiO_2 and the WO_3 particles significantly differs in the HAADF-STEM images, a distinction between both compounds is still limited, especially with increasing sample thickness. In the TiO_2 and WO_3 system, the individual particle shape can provide additional evidence within the investigated system; nevertheless, a careful interpretation of the data is a prerequisite. It should further be mentioned that the conducted analysis of the uniformity and the degree of mixing is based on a 2D projection of a 3D problem. How this 2D projection of 3D nanoparticles influences the determined degree of mixing and the interpreted uniformity of the mixture is so far unknown and under detailed investigation using Diffusion Limited Cluster Aggregation (DCLA) simulations.

5.4 Conclusions

The analysis of the temperature profile indicates significant differences between DF settings with different geometric adjustments. The temperature along the flame axis is slightly increased for an intersection distance of $l = 10$ cm and $\alpha = 20^\circ$ due to limitations of the entrainment flow. The horizontal temperature profiles, which describe the merging of the different flame aerosol streams, are a first indicator for the influence of the adjustment on the mixing process. The merging of the temperature profiles is a mandatory requirement for a uniform particle formation process. However, it is not sufficient for postulating a uniform particle mixture within the flames as underlined by the detailed image based product analysis.

The studies present the effect of the geometric arrangement of the DF set up on the individual particle characteristic and on uniformity and the degree of mixing in the Pt/ TiO_2 and the TiO_2/WO_3 system. While the crystallinity and size of the high melting point particles like TiO_2 and WO_3 are almost unaffected by the investigated geometric flame configurations, a significant influence on the size of Pt particles and its distribution on TiO_2 is observed. The quadrat method in combination with the variation coefficient is shown to be an effective tool for evaluating the uniformity of a deposited system. High intersection distances and small intersection angles lead to a non-uniform mixing of the two flames and the formation of large and broadly distributed Pt particles on the TiO_2 support particles. High intersection angles enhanced the mixing process of the aerosol streams significantly and for a geometric adjustment of $l = 10$ cm, $\alpha = 37.5^\circ$ a high Pt dispersion and a uniform mixing comparable to the single flame is achieved. This result shows the importance of the intersection angle as an adjustment parameter to increase the uniformity of a particle mixture synthesized in the DF. When increasing the intersection angle, the degree of mixing significantly increases presented quantitatively for intersection angles up to $\alpha = 37.5^\circ$. The overall result for the TiO_2/WO_3 systems show

the same trend as already observed for the Pt/TiO₂ system: a slight decrease in the degree of mixing (average cluster size) and in uniformity (distribution of the cluster size) for increasing intersection distances and angles. However, the effect seems to be less pronounced compared to the Pt/TiO₂ system because both components undergo homogeneous nucleation.

These presented results are a first indication how geometric parameter in the DF process influence the mixing process. Initial computational fluid dynamics help to identify preferred process configurations for a uniform product quality without requiring time consuming experiments and product analysis. However, this approach should be further extended to predict optimal synthesis condition with respect to the resulting uniformity of the product. This is a necessary step to ensure a constant product quality in the DF process while keeping all the advantages of the DF process.

6 Scope and potential of the double flame system

The investigated material systems successfully reveal that the double flame (DF) set up offers high process flexibility and the possibility of a tailored multicomponent catalyst synthesis. The presented experiments demonstrate that an appropriate flame configuration in the DF process enables the synthesis of multicomponent catalysts that show superior catalytic performances. The reason for this superior performance is a mixture of the components on a scale, which supports an interaction of the components that favor a specific catalytic activity. The presented studies clearly show that the DF process is a fast and flexible synthesis technique which is suitable for the synthesis of FT active Co//Al₂O₃ and CO-PrOx active CeO₂ // Pt-Fe₂O₃ catalysts. The FT catalysts show the highest activity when a mixture on particle scale exists. This mixing state is achieved at $l = 50$ cm and enables the reduction of the formation irreducible spinels ensures a high specific surface area of the catalytic active CoO_x phase. The high temperatures during the synthesis process further offer a sinter stable material interphase between the Al₂O₃ support and the CoO_x phase. The CO-PrOx- study demonstrates that in the DF setting an exclusive deposition of the active component on one of two support particles is possible in a single step. Again, a mixture on particle scale with an exclusive deposition of Pt on the Fe₂O₃, results in the most active low-temperature catalyst. The necessity of intimate particular contact between the CeO₂ and the Fe₂O₃ is obvious since a mixture of the two components on aggregate scale (PM) leads to a reduced activity.

In summary, the thesis provides important insights on the process characteristics of the DF process (e.g. temperature profile and particle mixing characteristic of the flame jets). Two novel methods for the quantification of the degree of mixing and the uniformity of the mixture in deposited and aggregated particle systems are developed. They are applied to quantify the impact of variations in the geometric configuration of the flames (intersection distance and angle). This new characterization method offers the possibility to quantify the influence of different geometric configurations on the degree of mixing, in the deposited Pt/TiO₂ and the aggregated WO₃/TiO₂ systems for the first time. By definition, the degree of mixing decreases from mixtures on particle scale in direction of mixtures on agglomerate scale. The results demonstrate that an increase in intersection distance significantly decreases the uniformity of the synthesized particles. An increase in the intersection angle, however, enhances the uniformity of the mixture. The results of the aggregated system reveal that an intersection distance of 66 cm still results in a relatively high degree of mixing. The achieved mixing state differs significantly from that of a physical mixture. This indicates that even for high intersection distances, where

advanced jet propagation is present, a mixture on cluster scale can be realized in the DF. This outcome eliminates the potential assumption that at higher interaction distances ($l > 50$ cm) an insufficient low degree of mixing is present.

The presented results are a first step to gain insights into the temperature and mixing process of the DF setting. However, investigations on this topic have to be enlarged to build up a full picture of the process- influencing variables. One way is to extend the (CFD) simulations with variable intersection distances and angles. This approach requires, however, the additional implementation of the particle formation process in the simulations. Only if this step is realized the mixing process within the flame can be fully understood. Another strategy is to experimentally investigate further material combinations with respect to their degree of mixing at different flame configurations. However, the number of possible material combinations is very limited since a mandatory difference in contrast, as present for the Ti || W system, is required for a successful conduction of an STEM image based analysis

Until now, the full potential of the DF process for the tailored syntheses of multi component materials is by far untapped. The results of the thesis suggest two major fields of action:

1. A detailed understanding of the combustion and particle formation process for different metals and metal oxides in the FSP process is essential. Depending on the applied material system, this would enable **the prediction of the required intersection distance** to synthesize particles of the required mixing state.
2. **The full usage of all variable synthesis parameters** in the DF process (e.g. asymmetric synthesis conditions) is essential to further tune the catalytic performance of the synthesized catalysts.

The following section presents first insights on these two fields and introduces recommendations for potential procedures and research approaches:

Prediction of the required intersection distance: Figure 56 schematically visualizes the relation between intersection distance and the particle characteristic for the four investigated combinations and one additional material combination Ce || Zr. The experimental and the detailed results for the last material combination are listed in chapter III in the appendix. For this material combination, the product characteristic is classified based on XRD. Figure 56 indicates that the intersection distance which is related to a certain scale of mixture (mixing on atomic (1), inner particular (2), particle (3),

cluster (4) and agglomerate (5) scale) significantly depends on the applied material combinations.

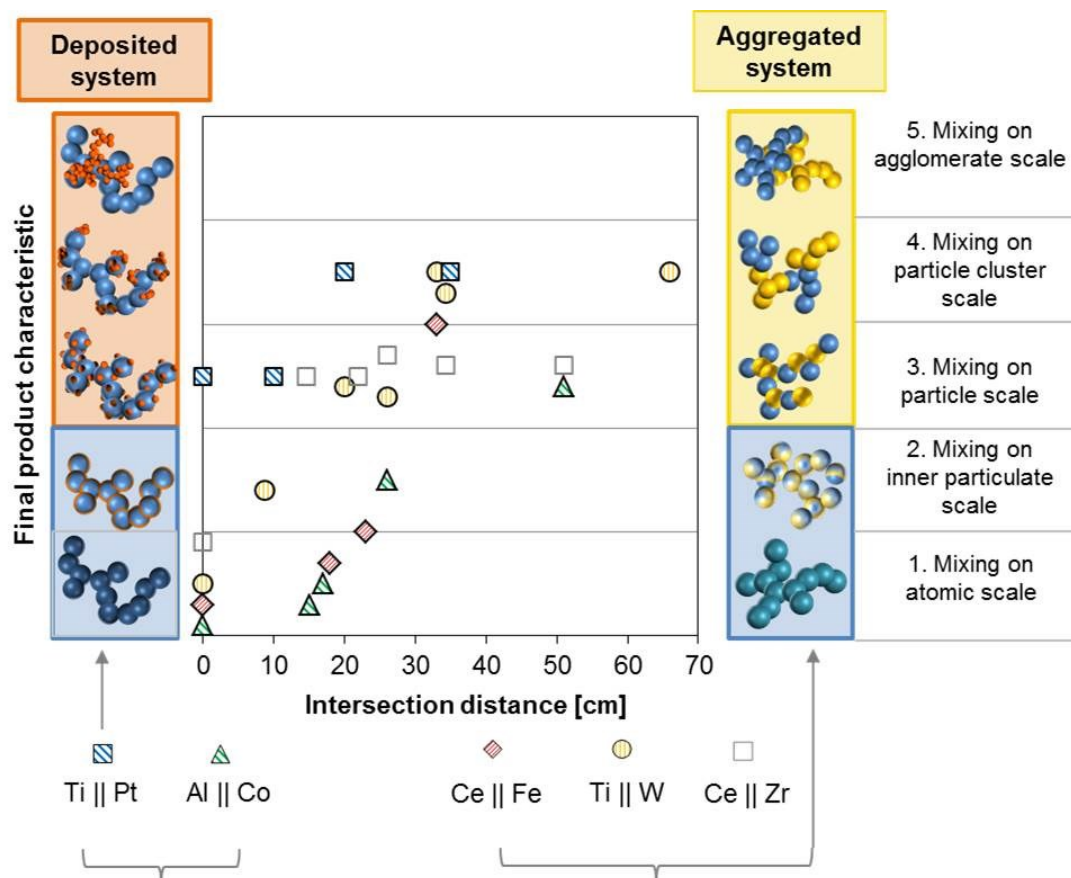


Figure 56: Schematic visualization of the relation between intersection distance and the particle characteristic for different material combinations, synthesized in the DF process using standard flame conditions. The position of the data points within a box has no relevance. In cases where two mixing states are assumed present is the data point is positioned on the boundary line.

Within the Ti || Pt system a mixture on particle scale is already achieved in the single flame setting and for small intersection distances (>10cm). Within the Ti || W system an intersection of 20 cm is required to realize a mixture on particle scale and for the Ce || Fe+Pt system even an intersection distance of 33 cm is necessary. In the Co || Al system, an intersection distance of 51 cm is still insufficient to obtain a uniform mixture on particle scale and to fully suppress the formation of Co-rich alumina spinels. In contrast, the separation of Ce and Zr in two flames leads to a complete suppression of the favored mixed metal oxide phase $Ce_{0.5}Zr_{0.5}O_2$. At an intersection distance of 15 cm. One indication for this different mixing behavior could be varying physical properties of the oxides. Whereas Co_3O_4 has e.g. a melting point in the range of $900^\circ C$, have Al_2O_3 , ($2053^\circ C$), CeO_2 ($2400^\circ C$) and ZrO_2 ($2709^\circ C$) considerably higher melting points [259]. This variation in melting points can be one indicator, next to variations in the boiling point and vapor pressures of the materials, why the intersection distance that leads to a

mixture on particle scale is significantly higher for the Co || Al system. However, combustion and particle formation characteristics in the flame might be additional key factors with respect to the resulting product characteristic. Rosebrock et al. give first important insights on the combustion and particle formation characteristic with their recently published work on the field of single droplet combustion [146, 147]. However, so far there are only limited investigations which focus on the combustion and particle formation characteristic in the FSP process especially regarding the formation of multicomponent materials. A detailed knowledge on the influence of precursor and solvent characteristic during the combustion process is therefore missing. Comparative analysis focusing on the influence of the physical properties e.g. boiling and melting point on the synthesis of metals and metal oxides would give further necessary insights. The coagulation behavior of fractal aggregates, based on discrete element modeling (DEM), is investigated in detail, however, so far only for single materials [159-163] e.g. TiO_2 [164-166], SiO_2 [131], or ZrO_2 [158]. The goal has to be that the mixing characteristic of a multi component system during the coalescence and aggregation process is included in the present DF models.

The results of the thesis suggest that a predomination of the ideal intersection distance / regime requires a comprehensive database which contains the key parameter of the combustion and the particle formation process for different components. The presented results can serve as a first basis; however, it is mandatory to enlarge the number of investigated material combinations and to increase the knowledge on the combustion and particle formation characteristics within the flames to make the DF technology even more attractive as a straightforward single step synthesis route for multicomponent catalysts.

The full usage of all variable synthesis parameters: The future scope for the synthesis of multi component material in the DF system should aim on two promising process parameters. Firstly, an asymmetric adjustment of the combustion parameters to tune the individual particle sizes independently from the overall concentration ratio of the components. Compared to the SF process the DF process offers this possibility due to a separate adjustment of the synthesis parameters in the flames (e.g. precursor flow rate, type and flow rate of the dispersion gas and the precursor concentration). The particle sizes, especially of the active component, directly influence the catalytic performance. A fine-tuning of the particle sizes, thus, comes with the potential to significantly increase the catalytic activity. Secondly, the implementation of an asymmetric flame configuration can help to overcome limitations, resulting e.g. from different physical properties of the individual materials. One example is a significant difference in the vapor pressures of the

component which leads to a consecutive particle formation instead of a simultaneous one [260]. Stark et al. presented the phenomena for the V_2O_5/TiO_2 system [138]. V_2O_5 is very volatile and has a much higher vapor pressure than TiO_2 . The synthesis of these two components in the SF would always result in the formation of a V_2O_5 layer on a spherical TiO_2 core (core shell structure) illustrated at the bottom of Figure 57.

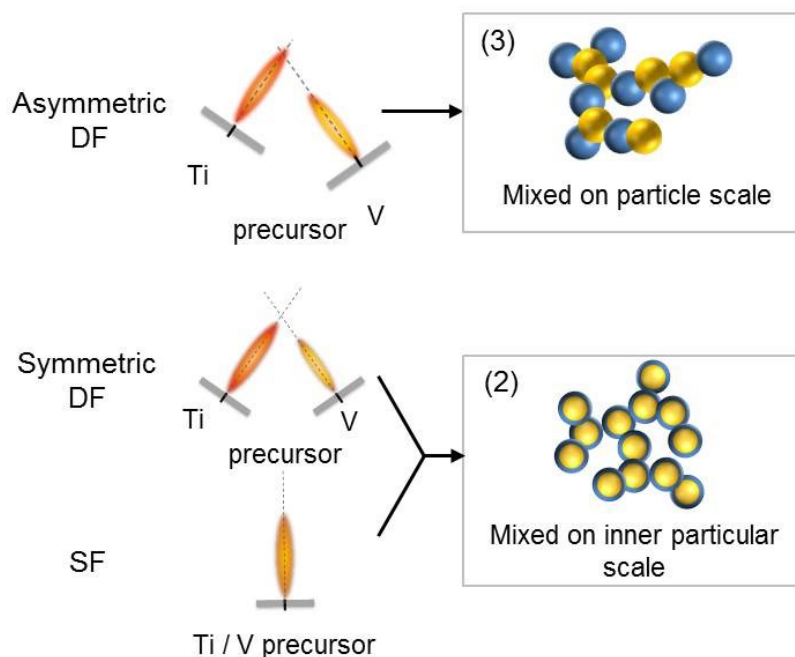


Figure 57: Example for the synthesis options for a multi component material based on two materials with a significantly different vapor pressure $p_{V_2O_5} \gg p_{TiO_2}$

The DF system provides the possibility to overcome this issue by separating the material synthesis in two flames. A symmetric configuration of the flames, however, would still lead to the formation of a core shell structure. Only an asymmetric configuration of the flames has the potential to form a mixture on particle scale illustrated on the top of Figure 57. A prerequisite is a higher intersection distance for the material with the high vapor pressure (e.g. V-flame) compared to the other material (e.g. Ti-flame). The asymmetric configuration can help to tailor the interaction region of two materials with significantly different physical properties. Currently the asymmetric configuration is under investigation for the synthesis of particulate mixed SiO_2 and $Ce_{0.7}Zr_{0.3}O_2$ supports for carbon dioxide reforming of methane. An additional future step could be the application of a third flame which is also under investigation and extends the variety of material combinations. For a triple flame setting, however, a detailed knowledge of the process parameters in the double flame setting is essential, since the complexity of the system even further increases with the addition of a third flame.

Bibliography

- [1] W.Y. Teoh, R. Amal, L. Mädler, Flame spray pyrolysis: An enabling technology for nanoparticles design and fabrication, *Nanoscale* 2 (2010) 1324-1347.
- [2] L. Mädler, H.K. Kammler, R. Mueller, S.E. Pratsinis, Controlled synthesis of nanostructured particles by flame spray pyrolysis, *Journal of Aerosol Science* 33 (2002) 369-389.
- [3] H.K. Grossmann, T. Grieb, F. Meierhofer, M.J. Hodapp, D. Noriler, A. Gröhn, H.F. Meier, U. Fritsching, K. Wegner, L. Mädler, *Nanoscale mixing during double-flame spray synthesis of heterostructured nanoparticles*, *J Nanopart Res* 17 (2015) 1-16.
- [4] M. Minnermann, H.K. Grossmann, S. Pokhrel, K. Thiel, H. Hagelin-Weaver, M. Bäumer, L. Mädler, Double flame spray pyrolysis as a novel technique to synthesize alumina-supported cobalt Fischer–Tropsch catalysts, *Catalysis Today* 214 (2013) 90-99.
- [5] J.A.H. Dreyer, H.K. Grossmann, J. Chen, T. Grieb, B.B. Gong, P.H.L. Sit, L. Mädler, W.Y. Teoh, Preferential oxidation of carbon monoxide over Pt–FeO_x/CeO₂ synthesized by two-nozzle flame spray pyrolysis, *Journal of Catalysis* 329 (2015) 248-261.
- [6] J.L. Sawin, F. Sverrisson, W. Rickerson, *Renewables 2015 Global Status Report*, Paris, (2015).
- [7] T.A. Semelsberger, R.L. Borup, H.L. Greene, Dimethyl ether (DME) as an alternative fuel, *Journal of Power Sources* 156 (2006) 497-511.
- [8] G.W. Huber, S. Iborra, A. Corma, Synthesis of transportation fuels from biomass: Chemistry, catalysts, and engineering, *Chem. Rev.* 106 (2006) 4044-4098.
- [9] D.M. Alonso, J.Q. Bond, J.A. Dumesic, Catalytic conversion of biomass to biofuels, *Green Chem.* 12 (2010) 1493-1513.
- [10] H. Schulz, Short history and present trends of Fischer–Tropsch synthesis, *Applied Catalysis A: General* 186 (1999) 3-12.
- [11] M.E. Dry, The Fischer–Tropsch process: 1950–2000, *Catalysis Today* 71 (2002) 227-241.
- [12] M.V. Landau, R. Vidruk, M. Herskowitz, Sustainable Production of Green Feed from Carbon Dioxide and Hydrogen, *ChemSusChem* 7 (2014) 785-794.
- [13] J.P. Longwell, E.S. Rubin, J. Wilson, Coal: Energy for the future, *Progress in Energy and Combustion Science* 21 (1995) 269-360.
- [14] D. Leckel, Diesel Production from Fischer-Tropsch: The Past, the Present, and New Concepts, *Energy Fuels* 23 (2009) 2342-2358.
- [15] M.E. Dry, J.C. Hoogendoorn, Technology of the Fischer-Tropsch process, *Catal. Rev.-Sci. Eng.* 23 (1981) 265-278.
- [16] X.B. Chen, S.H. Shen, L.J. Guo, S.S. Mao, Semiconductor-based Photocatalytic Hydrogen Generation, *Chem. Rev.* 110 (2010) 6503-6570.
- [17] A. Kudo, Development of photocatalyst materials for water splitting, *Int. J. Hydrog. Energy* 31 (2006) 197-202.
- [18] A. Kudo, Y. Miseki, Heterogeneous photocatalyst materials for water splitting, *Chemical Society Reviews* 38 (2009) 253-278.
- [19] G. Sahara, O. Ishitani, Efficient Photocatalysts for CO₂ Reduction, *Inorganic Chemistry* 54 (2015) 5096-5104.
- [20] J. Bonin, M. Robert, M. Routier, Selective and Efficient Photocatalytic CO₂ Reduction to CO Using Visible Light and an Iron-Based Homogeneous Catalyst, *Journal of the American Chemical Society* 136 (2014) 16768-16771.
- [21] C.D. Windle, E. Pastor, A. Reynal, A.C. Whitwood, Y. Vaynzof, J.R. Durrant, R.N. Perutz, E. Reisner, Improving the Photocatalytic Reduction of CO₂ to CO through Immobilisation of a Molecular Re Catalyst on TiO₂, *Chemistry – A European Journal* 21 (2015) 3746-3754.

- [22] Ş. Neaţu, J. Maciá-Agulló, H. Garcia, Solar Light Photocatalytic CO₂ Reduction: General Considerations and Selected Bench-Mark Photocatalysts, *International Journal of Molecular Sciences* 15 (2014) 5246.
- [23] D.L. Trimm, Z.I. Önsan, Onboard fuel conversion for hydrogen-fuel-cell-driven vehicles, *Catalysis Reviews* 43 (2001) 31-84.
- [24] G. Ercolino, M.A. Ashraf, V. Specchia, S. Specchia, Performance evaluation and comparison of fuel processors integrated with PEM fuel cell based on steam or autothermal reforming and on CO preferential oxidation or selective methanation, *Applied Energy* 143 (2015) 138-153.
- [25] O. Deutschmann, H. Knözinger, K. Kochloefl, T. Turek, Heterogeneous Catalysis and Solid Catalysts, *Ullmann's Encyclopedia of Industrial Chemistry*, Wiley-VCH Verlag GmbH & Co. KGaA (2000).
- [26] F. Schüth, Heterogene Katalyse. Schlüsseltechnologie der chemischen Industrie, *Chemie in unserer Zeit* 40 (2006) 92-103.
- [27] G. Mul, J.A. Moulijn, Preparation of Supported Metal Catalysts, *ChemInform* 36 (2005).
- [28] J.A. Dumesic, G.W. Huber, M. Boudart, Principles of Heterogeneous Catalysis, *Handbook of Heterogeneous Catalysis*, Wiley-VCH Verlag GmbH & Co. KGaA (2008).
- [29] Y. Chen, D. Zeng, M.B. Cortie, A. Dowd, H. Guo, J. Wang, D.-L. Peng, Seed-Induced Growth of Flower-Like Au–Ni–ZnO Metal–Semiconductor Hybrid Nanocrystals for Photocatalytic Applications, *Small* 11 (2015) 1460-1469.
- [30] M. Gharibi, F.T. Zangeneh, F. Yaripour, S. Sahebdehfar, Nanocatalysts for conversion of natural gas to liquid fuels and petrochemical feedstocks, *Applied Catalysis A: General* 443–444 (2012) 8-26.
- [31] D. Wei, R. Dave, R. Pfeffer, Mixing and Characterization of Nanosized Powders: An Assessment of Different Techniques, *J Nanopart Res* 4 (2002) 21-41.
- [32] S. Schauermaun, N. Nilius, S. Shaikhutdinov, H.-J. Freund, Nanoparticles for Heterogeneous Catalysis: New Mechanistic Insights, *Accounts of Chemical Research* 46 (2013) 1673-1681.
- [33] K. Philippot, P. Serp, Concepts in Nanocatalysis, *Nanomaterials in Catalysis*, Wiley-VCH Verlag GmbH & Co. KGaA (2013) 1-54.
- [34] J.Q. Wang, H.W. Gu, Novel Metal Nanomaterials and Their Catalytic Applications, *Molecules* 20 (2015) 17070-17092.
- [35] Z.C. Zhang, B. Xu, X. Wang, Engineering nanointerfaces for nanocatalysis, *Chemical Society Reviews* 43 (2014) 7870-7886.
- [36] S.J. Tauster, Strong metal-support interactions, *Accounts of Chemical Research* 20 (1987) 389-394.
- [37] A.L. Rogach, C.J. Murphy, T.K. Sau, Complex-shaped metal nanoparticles: bottom-up syntheses and applications, Wiley-VCH, Weinheim D, 2012.
- [38] A.T. Bell, The impact of nanoscience on heterogeneous catalysis, *Science* 299 (2003) 1688-1691.
- [39] J.R.H. Ross, Chapter 4 - Catalyst Preparation, in: J.R.H. Ross (Ed.), *Heterogeneous Catalysis*, Elsevier, Amsterdam, (2012), 65-96.
- [40] J.M. Thomas, W.J. Thomas, Principles and practice of heterogeneous catalysis, VCH, Weinheim Germany, (1997).
- [41] S. Sinthika, S.T. Vala, Y. Kawazoe, R. Thapa, CO Oxidation Prefers the Eley–Rideal or Langmuir–Hinshelwood Pathway: Monolayer vs Thin Film of SiC, *ACS Applied Materials & Interfaces* 8 (2016) 5290-5299.
- [42] I. Chorkendorff, J.W. Niemantsverdriet, Kinetics, *Concepts of Modern Catalysis and Kinetics*, Wiley-VCH Verlag GmbH & Co. KGaA (2005) 23-78.
- [43] N. Lopez, J.K. Nørskov, Catalytic CO Oxidation by a Gold Nanoparticle: A Density Functional Study, *Journal of the American Chemical Society* 124 (2002) 11262-11263.

- [44] H. Xiong, H.N. Pham, A.K. Datye, Hydrothermally stable heterogeneous catalysts for conversion of biorenewables, *Green Chem.* 16 (2014) 4627-4643.
- [45] A.M. Ruppert, B.M. Weckhuysen, Metal–Support Interactions, *Handbook of Heterogeneous Catalysis*, Wiley-VCH Verlag GmbH & Co. KGaA (2008).
- [46] J.A. Bergwerff, B.M. Weckhuysen, Oxide–Support Interactions, *Handbook of Heterogeneous Catalysis*, Wiley-VCH Verlag GmbH & Co. KGaA (2008).
- [47] R. Strobel, A. Baiker, S.E. Pratsinis, Aerosol flame synthesis of catalysts, *Adv. Powder Technol.* 17 (2006) 457-480.
- [48] G.C. Bond, The origins of particle size effects in heterogeneous catalysis, *Surface Science* 156, Part 2 (1985) 966-981.
- [49] O. Dulub, W. Hebenstreit, U. Diebold, Imaging Cluster Surfaces with Atomic Resolution: The Strong Metal-Support Interaction State of Pt Supported on TiO₂ (110), *Physical Review Letters* 84 (2000) 3646-3649.
- [50] G.L. Haller, D.E. Resasco, Metal–Support Interaction: Group VIII Metals and Reducible Oxides, *Advances in Catalysis* 36 (1989) 173-235.
- [51] J.L. Falconer, W.C. Conner, Second international conference on spillover, *Applied Catalysis* 56 (1989) N28-N29.
- [52] U. Roland, T. Braunschweig, F. Roessner, On the nature of spilt-over hydrogen, *Journal of Molecular Catalysis a-Chemical* 127 (1997) 61-84.
- [53] W.C. Conner, J.L. Falconer, Spillover in Heterogeneous Catalysis, *Chem. Rev.* 95 (1995) 759-788.
- [54] R. Prins, Hydrogen Spillover. Facts and Fiction, *Chem. Rev.* 112 (2012) 2714-2738.
- [55] A. Ibhaddon, P. Fitzpatrick, Heterogeneous Photocatalysis: Recent Advances and Applications, *Catalysts* 3 (2013) 189.
- [56] J.-M. Herrmann, Heterogeneous photocatalysis: fundamentals and applications to the removal of various types of aqueous pollutants, *Catalysis Today* 53 (1999) 115-129.
- [57] E.S. Kim, N. Nishimura, G. Magesh, J.Y. Kim, J.W. Jang, H. Jun, J. Kubota, K. Domen, J.S. Lee, Fabrication of CaFe₂O₄/TaON Heterojunction Photoanode for Photoelectrochemical Water Oxidation, *Journal of the American Chemical Society* 135 (2013) 5375-5383.
- [58] R. Marschall, Semiconductor Composites: Strategies for Enhancing Charge Carrier Separation to Improve Photocatalytic Activity, *Adv. Funct. Mater.* 24 (2014) 2421-2440.
- [59] M.L. Eggersdorfer, D. Kadau, H.J. Herrmann, S.E. Pratsinis, Aggregate morphology evolution by sintering: Number and diameter of primary particles, *Journal of Aerosol Science* 46 (2012) 7-19.
- [60] K. Schuh, W. Kleist, M. Høj, V. Trouillet, A.D. Jensen, J.D. Grunwaldt, One-step synthesis of bismuth molybdate catalysts via flame spray pyrolysis for the selective oxidation of propylene to acrolein, *Chem. Commun.* 50 (2014) 15404-15406.
- [61] J.A.H. Dreyer, S. Pokhrel, J. Birkenstock, M.G. Hevia, M. Schowalter, A. Rosenauer, A. Urakawa, W.Y. Teoh, L. Mädler, Decrease of the required dopant concentration for δ-Bi₂O₃ crystal stabilization through thermal quenching during single-step flame spray pyrolysis, *CrystEngComm* 18 (2016) 2046-2056.
- [62] M.B. Gawande, R.K. Pandey, R.V. Jayaram, Role of mixed metal oxides in catalysis science-versatile applications in organic synthesis, *Catalysis Science & Technology* 2 (2012) 1113-1125.
- [63] I.E. Wachs, Recent conceptual advances in the catalysis science of mixed metal oxide catalytic materials, *Catalysis Today* 100 (2005) 79-94.
- [64] Z. Shan, Y. Wang, H. Ding, F. Huang, Structure-dependent photocatalytic activities of MWO₄ (M = Ca, Sr, Ba), *Journal of Molecular Catalysis a-Chemical* 302 (2009) 54-58.

- [65] M. Ni, M.K.H. Leung, D.Y.C. Leung, K. Sumathy, A review and recent developments in photocatalytic water-splitting using TiO_2 for hydrogen production, *Renewable and Sustainable Energy Reviews* 11 (2007) 401-425.
- [66] S. George, S. Pokhrel, Z. Ji, B.L. Henderson, T. Xia, L. Li, J.I. Zink, A.E. Nel, L. Mädler, Role of Fe Doping in Tuning the Band Gap of TiO_2 for the Photo-Oxidation-Induced Cytotoxicity Paradigm, *Journal of the American Chemical Society* 133 (2011) 11270-11278.
- [67] M.B. Cortie, A.M. McDonagh, Synthesis and Optical Properties of Hybrid and Alloy Plasmonic Nanoparticles, *Chem. Rev.* 111 (2011) 3713-3735.
- [68] C.J. Zhong, M.M. Maye, Core-shell assembled nanoparticles as catalysts, *Adv. Mater.* 13 (2001) 1507.
- [69] J.S. Wang, X. Li, S.F. Zhang, R.W. Lu, Facile synthesis of ultrasmall monodisperse "raisin-bun"-type $\text{MoO}_3/\text{SiO}_2$ nanocomposites with enhanced catalytic properties, *Nanoscale* 5 (2013) 4823-4828.
- [70] D. Kim, J.S. Lee, C.M.F. Barry, J.L. Mead, Microscopic measurement of the degree of mixing for nanoparticles in polymer nanocomposites by TEM images, *Microscopy Research and Technique* 70 (2007) 539-546.
- [71] J.M. Campelo, D. Luna, R. Luque, J.M. Marinas, A.A. Romero, Sustainable Preparation of Supported Metal Nanoparticles and Their Applications in Catalysis, *ChemSusChem* 2 (2009) 18-45.
- [72] H. Zhang, S. Pokhrel, Z. Ji, H. Meng, X. Wang, S. Lin, C.H. Chang, L. Li, R. Li, B. Sun, M. Wang, Y.P. Liao, R. Liu, T. Xia, L. Mädler, A.E. Nel, PdO doping tunes band-gap energy levels as well as oxidative stress responses to a Co_3O_4 p-type semiconductor in cells and the lung, *Journal of the American Chemical Society* 136 (2014) 6406-6420.
- [73] Y. Shimizu, N. Nakashima, T. Hyodo, M. Egashira, NO_x Sensing Properties of Varistor-Type Gas Sensors Consisting of Micro p-n Junctions, *Journal of Electroceramics* 6 (2001) 209-217.
- [74] R. Sasikala, A. Shirole, V. Sudarsan, T. Sakuntala, C. Sudakar, R. Naik, S.R. Bharadwaj, Highly dispersed phase of SnO_2 on TiO_2 nanoparticles synthesized by polyol-mediated route: Photocatalytic activity for hydrogen generation, *Int. J. Hydrog. Energy* 34 (2009) 3621-3630.
- [75] Q.X. Jia, A. Iwase, A. Kudo, $\text{BiVO}_4\text{-Ru/SrTiO}_3$: Rh composite Z-scheme photocatalyst for solar water splitting, *Chem. Sci.* 5 (2014) 1513-1519.
- [76] R. Strobel, L. Mädler, M. Piacentini, M. Maciejewski, A. Baiker, S.E. Pratsinis, Two-Nozzle Flame Synthesis of $\text{Pt/Ba/Al}_2\text{O}_3$ for NO_x Storage, *J. Am. Chem. Soc.* 18 (2006) 2532-2537.
- [77] R. Strobel, F. Krumeich, S.E. Pratsinis, A. Baiker, Flame-derived $\text{Pt/Ba/Ce}_x\text{Zr}_{1-x}\text{O}_2$: Influence of support on thermal deterioration and behavior as NO_x storage-reduction catalysts, *Journal of Catalysis* 243 (2006) 229-238.
- [78] H.-J. Kim, J.-H. Lee, Highly sensitive and selective gas sensors using p-type oxide semiconductors: Overview, *Sensors and Actuators B: Chemical* 192 (2014) 607-627.
- [79] M. Tepluchin, D.K. Pham, M. Casapu, L. Mädler, S. Kureti, J.-D. Grunwaldt, Influence of single- and double-flame spray pyrolysis on the structure of $\text{MnO}_x/\gamma\text{-Al}_2\text{O}_3$ and $\text{FeO}_x/\gamma\text{-Al}_2\text{O}_3$ catalysts and their behaviour in CO removal under lean exhaust gas conditions, *Catalysis Science & Technology* (2014).
- [80] W.Y. Teoh, L. Mädler, D. Beydoun, S.E. Pratsinis, R. Amal, Direct (one-step) synthesis of TiO_2 and Pt/TiO_2 nanoparticles for photocatalytic mineralisation of sucrose, *Chemical Engineering Science* 60 (2005) 5852-5861.
- [81] M. Høj, K. Linde, T.K. Hansen, M. Brorson, A.D. Jensen, J.D. Grunwaldt, Flame spray synthesis of $\text{CoMo/Al}_2\text{O}_3$ hydrotreating catalysts, *Appl. Catal. A-Gen.* 397 (2011) 201-208.
- [82] S. Hannemann, J.D. Grunwaldt, P. Lienemann, D. Günther, Krumeich, S.E. Pratsinis, A. Baiker, Combination of flame synthesis and high-throughput

experimentation The preparation of alumina-supported noble metal particles and their application in the partial oxidation of methane, *Applied Catalysis A: General* (2007) 226–239.

[83] R. Marschall, J. Soldat, M. Wark, Enhanced photocatalytic hydrogen generation from barium tantalate composites, *Photochem. Photobiol. Sci.* 12 (2013) 671–677.

[84] H.G. Kim, P.H. Borse, J.S. Jang, E.D. Jeong, O.-S. Jung, Y.J. Suh, J.S. Lee, Fabrication of $\text{CaFe}_2\text{O}_4/\text{MgFe}_2\text{O}_4$ bulk heterojunction for enhanced visible light photocatalysis, *Chem. Commun.* (2009) 5889–5891.

[85] M. Liu, W. You, Z. Lei, G. Zhou, J. Yang, G. Wu, G. Ma, G. Luan, T. Takata, M. Hara, K. Domen, C. Li, Water reduction and oxidation on Pt-Ru/ $\text{Y}_2\text{Ta}_2\text{O}_5\text{N}_2$ catalyst under visible light irradiation, *Chem. Commun.* (2004) 2192–2193.

[86] I. Chorkendorff, J.W. Niemantsverdriet, *Catalyst Characterization, Concepts of Modern Catalysis and Kinetics*, Wiley-VCH Verlag GmbH & Co. KGaA (2005) 129–166.

[87] S. Brunauer, P.H. Emmett, E. Teller, Adsorption of Gases in Multimolecular Layers, *Journal of the American Chemical Society* 60 (1938) 309–319.

[88] A. Dąbrowski, Adsorption — from theory to practice, *Adv. Colloid Interface Sci.* 93 (2001) 135–224.

[89] G. Fagerlund, Determination of specific surface by the BET method, *Materials and Structures*, (1973) 239–245.

[90] K.S.W. Sing, J. Rouquerol, Surface Area and Porosity, *Handbook of heterogeneous Catalysis*, Wiley- VCH, Weinheim, 1997.

[91] G. Bergeret, P. Gallezot, Particle Size and Dispersion Measurements, in: G. Ertl, H. Knözinger, F. Schüth, J. Weitkamp (Eds.), *Handbook of Heterogeneous Catalysis*, Wiley-VCH Verlag GmbH & Co. KGaA (2008).

[92] D. Murzin, *Engineering catalysis*, de Gruyter, Berlin, Germany, (2013).

[93] R.J. Farrauto, Introduction to catalysis and industrial catalytic processes, in: L. Dorazio, C.H. Bartholomew (Eds.) (2016).

[94] L. Torrente-Murciano, The importance of particle-support interaction on particle size determination by gas chemisorption, *J Nanopart Res* 18 (2016) 87.

[95] N. Tanaka, K. Saitoh, Basics of STEM, *Scanning Transmission Electron Microscopy of Nanomaterials*, Imperial College Press (2014) 41–108.

[96] P.D. Christofides, M.H. Li, L. Mädler, Control of particulate processes: Recent results and future challenges, *Powder Technology* 175 (2007) 1–7.

[97] E.L. Dreizin, Metal-based reactive nanomaterials, *Progress in Energy and Combustion Science* 35 (2009) 141–167.

[98] B. Daumann, H. Nirschl, Microscopic Measurement of the Homogeneity of Nanoscale Mixtures, *Ind. Eng. Chem. Res.* 50 (2011) 877–882.

[99] B. Daumann, J.A. Weber, H. Anlauf, H. Nirschl, Discontinuous powder mixing of nanoscale particles, *Chem. Eng. J.* 167 (2011) 377–387.

[100] O.O. Ayeni, C.L. Wu, J.B. Joshi, K. Nandakumar, A discrete element method study of granular segregation in non-circular rotating drums, *Powder Technology* 283 (2015) 549–560.

[101] M. Camesasca, M. Kaufman, I. Manas-Zloczower, Quantifying Fluid Mixing with the Shannon Entropy, *Macromolecular Theory and Simulations* 15 (2006) 595–607.

[102] P.A. Karnezis, G. Durrant, B. Cantor, Characterization of reinforcement distribution in cast Al-alloy/SiCp composites, *Mater. Charact.* 40 (1998) 97–109.

[103] A. Rogers, *Statistical Analysis of Spatial Dispersion: The Quadrat Method*, Pion Ltd London, 1974.

[104] N. Riefler, L. Mädler, Structure–conductivity relations of simulated highly porous nanoparticle aggregate films, *J Nanopart Res* 12 (2009) 853–863.

[105] G.R. Chandratilleke, A.B. Yu, J. Bridgwater, A DEM study of the mixing of particles induced by a flat blade, *Chemical Engineering Science* 79 (2012) 54–74.

- [106] G.R. Chandratilleke, A.B. Yu, J. Bridgwater, K. Shinohara, A particle-scale index in the quantification of mixing of particles, *AIChE J.* 58 (2012) 1099-1118.
- [107] M. Halidan, G.R. Chandratilleke, S.L.I. Chan, A.B. Yu, J. Bridgwater, Prediction of the mixing behaviour of binary mixtures of particles in a bladed mixer, *Chemical Engineering Science* 120 (2014) 37-48.
- [108] R. Hogg, *Mixing and Segregation in Powders: Evaluation, Mechanisms and Processes*, KONA Powder Part. J. (2009) 3-17.
- [109] Köhler, *Nanotechnologie*, Wiley VCH (2001).
- [110] H.K.D.H. Bhadeshia, Mechanically alloyed metals, *Materials Science and Technology* 16 (2000) 1404-1411.
- [111] C. Suryanarayana, Mechanical alloying and milling, *Progress in Materials Science* 46 (2001) 1-184.
- [112] B. Kubias, M.J.G. Fait, R. Schlögl, *Mechanochemical Methods, Handbook of Heterogeneous Catalysis*, Wiley-VCH Verlag GmbH & Co. KGaA (2008).
- [113] O.B. Lapina, A.A. Shubin, A.V. Nosov, E. Bosch, J. Spengler, H. Knözinger, Characterization of V_2O_5 - TiO_2 Catalysts Prepared by Milling by ESR and Solid State 1H and 51V NMR, *The Journal of Physical Chemistry B* 103 (1999) 7599-7606.
- [114] M.T. Uddin, Y. Nicolas, C. Olivier, T. Toupance, L. Servant, M.M. Müller, H.-J. Kleebe, J. Ziegler, W. Jaegermann, Nanostructured SnO_2 - ZnO Heterojunction Photocatalysts Showing Enhanced Photocatalytic Activity for the Degradation of Organic Dyes, *Inorganic Chemistry* 51 (2012) 7764-7773.
- [115] B.L. Cushing, V.L. Kolesnichenko, C.J. O'Connor, Recent Advances in the Liquid-Phase Syntheses of Inorganic Nanoparticles, *Chem. Rev.* 104 (2004) 3893-3946.
- [116] F.E. Kruis, H. Fissan, A. Peled, Synthesis of nanoparticles in the gas phase for electronic, optical and magnetic applications—a review, *Journal of Aerosol Science* 29 (1998) 511-535.
- [117] R. Koirala, S.E. Pratsinis, A. Baiker, Synthesis of catalytic materials in flames: opportunities and challenges, *Chemical Society Reviews* 45 (2016) 3053-3068.
- [118] L. Lloyd, *Industrial Catalysts, Handbook of Industrial Catalysts*, Springer US (2011) 1-22.
- [119] V. Gupta, A.R. Gupta, V. Kant, *Synthesis, Characterization and Biomedical Applications of Nanoparticles*, *Science International* 1 (2013) 167-174
- [120] R. Overney, *Lecture: Nanothermodynamics and Nanoparticle Synthesis*, Washington (2010).
- [121] D. Sun, J. Liu, J. Li, Z. Feng, L. He, B. Zhao, T. Wang, R. Li, S. Yin, T. Sato, Solvothermal synthesis of spindle-like WO_3 - TiO_2 particles with enhanced photocatalytic activity, *Materials Research Bulletin* 53 (2014) 163-168.
- [122] H.B. Li, S.C. Xu, M. Liu, M. Feng, J.Z. Yin, Structure and Magnetic Properties of $FeCo/Al_2O_3$ Nanocomposites, *Chemical Research in Chinese Universities* 26 (2010) 344-347.
- [123] P.M. Ajayan, *Bulk Metal and Ceramics Nanocomposites, Nanocomposite Science and Technology*, Wiley-VCH Verlag GmbH & Co. KGaA (2004) 1-75.
- [124] D. Kerner, M. Rochnia, *Flame Hydrolysis, Handbook of Heterogeneous Catalysis*, Wiley-VCH Verlag GmbH & Co. KGaA (2008)
- [125] U. Backman, U. Tapper, J.K. Jokiniemi, An aerosol method to synthesize supported metal catalyst nanoparticles, *Synthetic Metals* 142 (2004) 169-176.
- [126] S. Thybo, S. Jensen, J. Johansen, O. Hansen, U.J. Quaade, Flame spray deposition of porous catalysts on surfaces and in microsystems, *Journal of Catalysis* (2004) 271-277.
- [127] T. Johannessen, J.R. Jensen, M. Mosleh, J. Johansen, U. Quaade, H. Livbjerg, *Flame Synthesis of Nanoparticles: Applications in Catalysis and Product/Process Engineering*, *Chemical Engineering Research and Design* (2004) 1444-1452.
- [128] L. Mädler, *Liquid-fed Aerosol Reactors for One-step Synthesis of Nanostructured Particles*, *KONA* (2004) 107-120.

- [129] C. Burda, X.B. Chen, R. Narayanan, M.A. El-Sayed, Chemistry and properties of nanocrystals of different shapes, *Chem. Rev.* 105 (2005) 1025-1102.
- [130] A. Gurav, T. Kodas, T. Pluym, Y. Xiong, *Aerosol Processing of Materials, Aerosol Science and Technology* (1993) 411-152.
- [131] S. Tsantilis, S.E. Pratsinis, Soft- and Hard-Agglomerate Aerosols Made at High Temperatures, *Langmuir* (2004) 5933-5939.
- [132] I.S. Shim, C.S. Lee, Synthesis and characterization of $\text{Al}_2\text{O}_3/\text{ZrO}_2$, $\text{Al}_2\text{O}_3/\text{TiO}_2$ and $\text{Al}_2\text{O}_3/\text{ZrO}_2/\text{TiO}_2$ ceramic composite particles prepared by ultrasonic spray pyrolysis, *Bull. Korean Chem. Soc.* 23 (2002) 1127-1134.
- [133] J. Sourice, A. Quinsac, Y. Leconte, O. Sublemontier, W. Porcher, C. Haon, A. Bordes, E. De Vito, A. Boulineau, S. Jouanneau Si Larbi, N. Herlin-Boime, C. Reynaud, One-Step Synthesis of Si@C Nanoparticles by Laser Pyrolysis: High-Capacity Anode Material for Lithium-Ion Batteries, *Acs Applied Materials & Interfaces* 7 (2015) 6637-6644.
- [134] N.A. Vainos, 1 - Laser growth and processing of photonic structures: an overview of fundamentals, interaction phenomena and operations, in: N.A. Vainos (Ed.), *Laser Growth and Processing of Photonic Devices*, Woodhead Publishing (2012) 1-52.
- [135] Y.C. Kang, D.J. Seo, S.B. Park, H.D. Park, Direct synthesis of strontium titanate phosphor particles with high luminescence by flame spray pyrolysis, *Materials Research Bulletin* 37 (2002) 263-269.
- [136] B. Guo, H. Yim, A. Khasanov, J. Stevens, Formation of Magnetic Fe_xO_y /Silica Core-Shell Particles in a One-Step Flame Aerosol Process, *Aerosol Science and Technology* 44 (2010) 281-291.
- [137] P.F. Miquel, C.-H. Hung, J.L. Katz, Formation of V_2O_5 -based mixed oxides in flames, *Journal of Materials Research* 8 (1993) 2404-2413.
- [138] W.J. Stark, K. Wegner, S.E. Pratsinis, A. Baiker, Flame Aerosol Synthesis of Vanadia-Titania Nanoparticles: Structural and Catalytic Properties in the Selective Catalytic Reduction of NO by NH_3 , *Journal of Catalysis* 197 (2001) 182-191.
- [139] R. Strobel, W.J. Stark, L. Mädler, S.E. Pratsinis, A. Baiker, Flame-made platinum/alumina: structural properties and catalytic behaviour in enantioselective hydrogenation, *Journal of Catalysis* 213 (2003) 296-304.
- [140] H. Schulz, W.J. Stark, M. Maciejewski, S.E. Pratsinis, A. Baiker, Flame-made nanocrystalline ceria/zirconia doped with alumina or silica: structural properties and enhanced oxygen exchange capacity, *Journal of Materials Chemistry* 13 (2003) 2979-2984.
- [141] H.H. Kung, M.C. Kung, Nanotechnology: applications and potentials for heterogeneous catalysis, *Catalysis Today* (2004) 219-224.
- [142] B. Thiebaut, Flame Spray Pyrolysis: A Unique Facility for the Production of Nanopowders, *Platin. Met. Rev.* 55 (2011) 149-151.
- [143] K. Wegner, B. Schimmoeller, B. Thiebaut, C. Fernandez, T.N. Rao, Pilot Plants for Industrial Nanoparticle Production by Flame Spray Pyrolysis, *KONA Powder Part. J.* (2011) 251-265.
- [144] R. Strobel, S.E. Pratsinis, Flame aerosol synthesis of smart nanostructured materials, *Journal of Materials Chemistry* 17 (2007) 4743-4756.
- [145] A.J. Gröhn, S.E. Pratsinis, K. Wegner, Fluid-particle dynamics during combustion spray aerosol synthesis of ZrO_2 , *Chem. Eng. J.* 191 (2012) 491-502.
- [146] C.D. Rosebrock, N. Riefler, T. Wriedt, L. Mädler, S.D. Tse, Disruptive Burning of Precursor/Solvent Droplets in Flame-Spray Synthesis of Nanoparticles, *AIChE J.* 59 (2013) 4553-4566.
- [147] C.D. Rosebrock, T. Wriedt, L. Mädler, K. Wegner, The role of microexplosions in flame spray synthesis for homogeneous nanopowders from low-cost metal precursors, *AIChE J.* 62 (2016) 381-391.
- [148] J. Polte, Fundamental growth principles of colloidal metal nanoparticles - a new perspective, *CrystEngComm* 17 (2015) 6809-6830.

- [149] Y. Fukumori, T. Nomura, T. Adschiri, S. Ohara, F. Saito, M. Naito, K. Okuyama, M. Kawahara, H. Suzuki, T. Sasaki, M. Fuji, S. Inagaki, H. Takeuchi, Y. Ando, Chapter 2 - Structural control of nanoparticles, in: M.H.N.N. Yokoyama (Ed.), Nanoparticle Technology Handbook, Elsevier, Amsterdam (2008) 49-112.
- [150] M. Suzuki, M. Kagawa, Y. Syono, T. Hirai, Synthesis of ultrafine single-component oxide particles by the spray-ICP technique, *J Mater Sci* 27 (1992) 679-684.
- [151] T. Tani, L. Mädler, S. Pratsinis, Homogeneous ZnO Nanoparticles by Flame Spray Pyrolysis, *J Nanopart Res* 4 (2002) 337-343.
- [152] S.E. Pratsinis, Flame aerosol synthesis of ceramic powders, *Progress in Energy and Combustion Science* 24 (1998) 197-219.
- [153] T. Hawa, M.R. Zachariah, Coalescence kinetics of unequal sized nanoparticles, *Journal of Aerosol Science* 37 (2006) 1-15.
- [154] S.K. Friedlander, *Smoke, dust, and haze: fundamentals of aerosol behavior*, Wiley (1977).
- [155] R.S. Windeler, K.E.J. Lehtinen, S.K. Friedlander, Production of Nanometer-Sized Metal Oxide Particles by Gas Phase Reaction in a Free Jet. II: Particle Size and Neck Formation—Comparison with Theory, *Aerosol Science and Technology* 27 (1997) 191-205.
- [156] C.-s. Wang, S.K. Friedlander, L. Mädler, Nanoparticle aerosol science and technology: an overview, *China Particuology* 3 (2005) 243-254.
- [157] B.B. Mandelbrot, J.A. Wheeler, *The Fractal Geometry of Nature*, *American Journal of Physics* 51 (1983) 286-287.
- [158] M.L. Eggersdorfer, A.J. Gröhn, C.M. Sorensen, P.H. McMurry, S.E. Pratsinis, Mass-mobility characterization of flame-made ZrO₂ aerosols: Primary particle diameter and extent of aggregation, *Journal of Colloid and Interface Science* 387 (2012) 12-23.
- [159] M.L. Eggersdorfer, D. Kadau, H.J. Herrmann, S.E. Pratsinis, Multiparticle Sintering Dynamics: From Fractal-Like Aggregates to Compact Structures, *Langmuir : the ACS journal of surfaces and colloids* 27 (2011) 6358-6367.
- [160] E. Goudeli, M.L. Eggersdorfer, S.E. Pratsinis, Coagulation of Agglomerates Consisting of Polydisperse Primary Particles, *Langmuir* 32 (2016) 9276-9285.
- [161] E. Goudeli, S.E. Pratsinis, Gas-phase manufacturing of nanoparticles: Molecular dynamics and mesoscale simulations, *Particulate Science and Technology* 34 (2016) 483-493.
- [162] E. Goudeli, M.L. Eggersdorfer, S.E. Pratsinis, Coagulation–Agglomeration of Fractal-like Particles: Structure and Self-Preserving Size Distribution, *Langmuir* 31 (2015) 1320-1327.
- [163] G.A. Kelesidis, E. Goudeli, S.E. Pratsinis, Flame synthesis of functional nanostructured materials and devices: Surface growth and aggregation, *Proceedings of the Combustion Institute* 36 (2017) 29-50.
- [164] S. Tsantilis, H.K. Kammler, S.E. Pratsinis, Population balance modeling of flame synthesis of titania nanoparticles, *Chemical Engineering Science* 57 (2002) 2139-2156.
- [165] S. Tsantilis, S.E. Pratsinis, Evolution of primary and aggregate particle-size distributions by coagulation and sintering, *AIChE J.* 46 (2000) 407-415.
- [166] B. Buesser, A.J. Gröhn, S.E. Pratsinis, Sintering Rate and Mechanism of TiO₂ Nanoparticles by Molecular Dynamics, *J. Phys. Chem. C* 115 (2011) 11030-11035.
- [167] S. Salameh, R. Scholz, J.W. Seo, L. Mädler, Contact behavior of size fractionated TiO₂ nanoparticle agglomerates and aggregates, *Powder Technology* 256 (2014) 345-351.
- [168] H. Schulz, L. Mädler, R. Strobel, R. Jossen, S.E. Pratsinis, T. Johannessen, Independent control of metal cluster and ceramic particle characteristics during one-step synthesis of Pt/TiO₂, *Journal of Materials Research* 20 (2005) 2568-2577.

- [169] D. Noriler, C.D. Rosebrock, L. Mädler, H.F. Meier, U. Fritsching, Influence of atomization and spray parameters on the flame spray process for nanoparticle production, *Atom. Sprays* 24 (2014) 495-524.
- [170] L. Mädler, S.E. Pratsinis, Bismuth Oxide Nanoparticles by Flame Spray Pyrolysis, *Journal of the American Ceramic Society* 85 (2002) 1713-1718.
- [171] L. Mädler, W.J. Stark, S.E. Pratsinis, Flame-made ceria nanoparticles, *Journal of Materials Research* 17 (2002) 1356-1362.
- [172] R. Kydd, W.Y. Teoh, K. Wong, Y. Wang, J. Scott, Q.-H. Zeng, A.-B. Yu, J. Zou, R. Amal, Flame-Synthesized Ceria-Supported Copper Dimers for Preferential Oxidation of CO, *Adv. Funct. Mater.* 19 (2009) 369-377.
- [173] R.N. Grass, T.F. Albrecht, F. Krumeich, W.J. Stark, Large-scale preparation of ceria/bismuth metal-matrix nano-composites with a hardness comparable to steel, *Journal of Materials Chemistry* 17 (2007) 1485-1490.
- [174] L. Mädler, W.J. Stark, S.E. Pratsinis, Rapid synthesis of stable ZnO quantum dots, *Journal of Applied Physics* 92 (2002) 6537-6540.
- [175] T. Tani, L. Mädler, S.E. Pratsinis, Synthesis of zinc oxide/silica composite nanoparticles by flame spray pyrolysis, *J Mater Sci* 37 (2002) 4627-4632.
- [176] J. Xiao, A. Kuc, S. Pokhrel, L. Mädler, R. Pöttgen, F. Winter, T. Frauenheim, T. Heine, Fe-Doped ZnO Nanoparticles: The Oxidation Number and Local Charge on Iron, Studied by ^{57}Fe Mößbauer Spectroscopy and DFT Calculations, *Chemistry – A European Journal* 19 (2013) 3287-3291.
- [177] W.Y. Teoh, R. Amal, L. Mädler, S.E. Pratsinis, Flame sprayed visible light-active Fe-TiO₂ for photomineralisation of oxalic acid, *Catalysis Today* 120 (2007) 203-213.
- [178] W.J. Stark, L. Mädler, M. Maciejewski, S.E. Pratsinis, A. Baiker, Flame synthesis of nanocrystalline ceria-zirconia: effect of carrier liquid, *Chem. Commun.* (2003) 588-589.
- [179] Y.K. Kho, W.Y. Teoh, A. Iwase, L. Maedler, A. Kudo, R. Amal, Flame Preparation of Visible-Light-Responsive BiVO₄ Oxygen Evolution Photocatalysts with Subsequent Activation via Aqueous Route, *Acs Applied Materials & Interfaces* 3 (2011) 1997-2004.
- [180] M. Piacentini, R. Strobel, M. Maciejewski, S.E. Pratsinis, A. Baiker, Flame-made Pt-Ba/Al₂O₃ catalysts: Structural properties and behavior in lean-NO_x storage-reduction, *Journal of Catalysis* 243 (2006) 43-56.
- [181] F.O. Ernst, R. Buechel, R. Strobel, S.E. Pratsinis, One-step flame-synthesis of carbon-embedded and -supported platinum clusters, *J. Am. Chem. Soc.* 130 (2008) 2117-2123.
- [182] R. Buchel, R. Strobel, F. Krumeich, A. Baiker, S.E. Pratsinis, Influence of Pt location on BaCO₃ or Al₂O₃ during NO_x storage reduction, *Journal of Catalysis* 261 (2009) 201-207.
- [183] R. Buchel, S.E. Pratsinis, A. Baiker, Influence of controlled spatial deposition of Pt and Pd in NO_x storage-reduction catalysts on their efficiency, *Appl. Catal. B- Environ.* 101 (2011) 682-689.
- [184] M. Høj, D.K. Pham, M. Brorson, L. Mädler, A.D. Jensen, J.D. Grunwaldt, Two- Nozzle Flame Spray Pyrolysis (FSP) Synthesis of CoMo/Al₂O₃ Hydrotreating Catalysts, *Catalysis Letters* 143 (2013) 386-394.
- [185] Z. Wang, S. Pokhrel, M. Chen, M. Hunger, L. Mädler, J. Huang, Palladium-doped silica-alumina catalysts obtained from double-flame FSP for chemoselective hydrogenation of the model aromatic ketone acetophenone, *Journal of Catalysis* 302 (2013) 10-19.
- [186] M. Tepluchin, D.K. Pham, M. Casapu, L. Mädler, S. Kureti, J.-D. Grunwaldt, Influence of single- and double-flame spray pyrolysis on the structure of MnO_x/γ-Al₂O₃ and FeO_x/γ-Al₂O₃ catalysts and their behaviour in CO removal under lean exhaust gas conditions, *Catalysis Science & Technology* (2014).

- [187] M. Schubert, S. Pokhrel, A. Thome, V. Zielasek, T.M. Gesing, F. Roessner, L. Mädler, M. Baumer, Highly active Co-Al₂O₃-based catalysts for CO₂ methanation with very low platinum promotion prepared by double flame spray pyrolysis, *Catalysis Science & Technology* 6 (2016) 7449-7460.
- [188] K.D. Kim, S. Pokhrel, Z. Wang, H. Ling, C. Zhou, Z. Liu, M. Hunger, L. Mädler, J. Huang, Tailoring High-Performance Pd Catalysts for Chemoselective Hydrogenation Reactions via Optimizing the Parameters of the Double-Flame Spray Pyrolysis, *ACS Catalysis* 6 (2016) 2372-2381.
- [189] R. Büchel, A. Baiker, S.E. Pratsinis, Effect of Ba and K addition and controlled spatial deposition of Rh in Rh/Al₂O₃ catalysts for CO₂ hydrogenation, *Applied Catalysis A: General* 477 (2014) 93-101.
- [190] R.B. Anderson, H. Kölbl, M. Rálek, *The Fischer-Tropsch Synthesis*, Academic Pr1984.
- [191] A.Y. Khodakov, W. Chu, P. Fongarland, Advances in the development of novel cobalt Fischer-Tropsch catalysts for synthesis of long-chain hydrocarbons and clean fuels, *Chem. Rev.* 107 (2007) 1692-1744.
- [192] R. Guettel, U. Kunz, T. Turek, Reactors for Fischer-Tropsch Synthesis, *Chemical Engineering & Technology* 31 (2008) 746-754.
- [193] A.P. Vogel, H.G. Nel, J.A. Stadler, R.G. Jordi, B.B. Breman, Intensification of the Sasol SPD Reactor - Realizing Potential, *Ind. Eng. Chem. Res.* 53 (2014) 1768-1774.
- [194] Q.H. Zhang, J.C. Kang, Y. Wang, Development of Novel Catalysts for Fischer-Tropsch Synthesis: Tuning the Product Selectivity, *ChemCatChem* 2 (2010) 1030-1058.
- [195] M.A. Vannice, The catalytic synthesis of hydrocarbons from H₂CO mixtures over the group VIII metals: II. The kinetics of the methanation reaction over supported metals, *Journal of Catalysis* 37 (1975) 462-473.
- [196] S. Zinoviev, F. Muller-Langer, P. Das, N. Bertero, P. Fornasiero, M. Kaltschmitt, G. Centi, S. Miertus, Next-Generation Biofuels: Survey of Emerging Technologies and Sustainability Issues, *ChemSusChem* 3 (2010) 1106-1133.
- [197] G.L. Bezemer, J.H. Bitter, H. Kuipers, H. Oosterbeek, J.E. Holewijn, X.D. Xu, F. Kapteijn, A.J. van Dillen, K.P. de Jong, Cobalt particle size effects in the Fischer-Tropsch reaction studied with carbon nanofiber supported catalysts, *Journal of the American Chemical Society* 128 (2006) 3956-3964.
- [198] G. Prieto, A. Martínez, P. Concepción, R. Moreno-Tost, Cobalt particle size effects in Fischer-Tropsch synthesis: structural and in situ spectroscopic characterisation on reverse micelle-synthesised Co/ITQ-2 model catalysts, *Journal of Catalysis* 266 (2009) 129-144.
- [199] E. Iglesia, Design, synthesis, and use of cobalt-based Fischer-Tropsch synthesis catalysts, *Appl. Catal. A-Gen.* 161 (1997) 59-78.
- [200] M.E. Dry, Present and future applications of the Fischer-Tropsch process, *Appl. Catal. A-Gen.* 276 (2004) 1-3.
- [201] M.E. Dry, *Fischer-Tropsch Technology*, Elsevier Science, Amsterdam (2004) 1-700.
- [202] A.R. de la Osa, A. De Lucas, A. Romero, J.L. Valverde, P. Sánchez, Influence of the catalytic support on the industrial Fischer-Tropsch synthetic diesel production, *Catalysis Today* 176 (2011) 298-302.
- [203] Ø. Borg, V. Frøseth, S. Storster, E. Rytter, A. Holmen, M.S. Fábio Bellot Noronha, S.-A. Eduardo Falabella, Fischer-tropsch synthesis. recent studies on the relation between the properties of supported cobalt catalysts and the activity and selectivity, *Studies in Surface Science and Catalysis*, Elsevier (2007) 117-122.
- [204] S. Storsaeter, B. Totdal, J.C. Walmsley, B.S. Tanem, A. Holmen, Characterization of alumina-, silica-, and titania-supported cobalt Fischer-Tropsch catalysts, *Journal of Catalysis* 236 (2005) 139-152.

- [205] S. Bessell, Support effects in cobalt-based fischer-tropsch catalysis, *Applied Catalysis A: General* 96 (1993) 253-268.
- [206] M. Sadeqzadeh, H. Karaca, O.V. Safonova, P. Fongarland, S. Chambrey, P. Roussel, A. Griboval-Constant, M. Lacroix, D. Curulla-Ferre, F. Luck, A.Y. Khodakov, Identification of the active species in the working alumina-supported cobalt catalyst under various conditions of Fischer-Tropsch synthesis, *Catalysis Today* 164 (2011) 62-67.
- [207] J. van de Loosdrecht, B. Bazhinmaev, J.A. Dalmon, J.W. Niemantsverdriet, S.V. Tsybulya, A.M. Saib, P.J. van Berge, J.L. Visagie, Cobalt Fischer-Tropsch synthesis: Deactivation by oxidation?, *Catalysis Today* 123 (2007) 293-302.
- [208] P.J. van Berge, J. van de Loosdrecht, S. Barradas, A.M. van der Kraan, Oxidation of cobalt based Fischer-Tropsch catalysts as a deactivation mechanism, *Catalysis Today* 58 (2000) 321-334.
- [209] C. Chaisuk, P. Boonpitak, J. Panpranot, O. Mekasuwandumrong, Effects of Co dopants and flame conditions on the formation of Co/ZrO₂ nanoparticles by flame spray pyrolysis and their catalytic properties in CO hydrogenation, *Catal. Commun.* 12 (2011) 917-922.
- [210] W.Y. Teoh, R. Setiawan, L. Mädler, J.D. Grunwaldt, R. Amal, S.E. Pratsinis, Ru-doped cobalt-zirconia nanocomposites by flame synthesis: Physicochemical and catalytic properties, *J. Am. Chem. Soc.* 20 (2008) 4069-4079.
- [211] N. Turra, A.B. Acuna, B. Schimmoller, B. Mayr-Schmolzer, P. Mania, I. Hermans, Aerobic Oxidation of Cyclohexane Catalyzed by Flame-Made Nano-Structured Co/SiO₂ Materials, *Top. Catal.* 54 (2011) 737-745.
- [212] R. Jossen, S.E. Pratsinis, W.J. Stark, L. Mädler, Criteria for flame-spray synthesis of hollow, shell-like, or inhomogeneous oxides, *Journal of the American Ceramic Society* 88 (2005) 1388-1393.
- [213] J. Azurdia, J. Marchal, R.M. Laine, Synthesis and characterization of mixed-metal oxide nanopowders along the CoO_x-Al₂O₃ tie line using liquid-feed flame spray pyrolysis, *Journal of the American Ceramic Society* 89 (2006) 2749-2756.
- [214] F. Tielens, M. Calatayud, R. Franco, J.M. Recio, J. Perez-Ramirez, C. Minot, Theoretical investigation of the inversion parameter in Co_{3-s}Al_sO₄ (s=0-3) spinel structures, *Solid State Ion.* 180 (2009) 1011-1016.
- [215] S. Velu, K. Suzuki, S. Hashimoto, N. Satoh, F. Ohashi, S. Tomura, The effect of cobalt on the structural properties and reducibility of CuCoZnAl layered double hydroxides and their thermally derived mixed oxides, *Journal of Materials Chemistry* 11 (2001) 2049-2060.
- [216] S. Kurajica, E. Tkalcec, B. Grzeta, D. Ivekovic, V. Mandic, J. Popovic, D. Kranzelic, Evolution of structural and optical properties in the course of thermal evolution of sol-gel derived cobalt-doped gahnite, *J. Alloys Compd.* 509 (2011) 3223-3228.
- [217] B. Jongsomjit, J. Panpranot, J.G. Goodwin, Co-Support Compound Formation in Alumina-Supported Cobalt Catalysts, *Journal of Catalysis* 204 (2001) 98-109.
- [218] D.J. Moodley, A.M. Saib, J. van de Loosdrecht, C.A. Welker-Nieuwoudt, B.H. Sigwebela, J.W. Niemantsverdriet, The impact of cobalt aluminate formation on the deactivation of cobalt-based Fischer-Tropsch synthesis catalysts, *Catalysis Today* 171 (2011) 192-200.
- [219] Y.T. Tsai, X.H. Mo, A. Campos, J.G. Goodwin, J.J. Spivey, Hydrotalcite supported Co catalysts for CO hydrogenation, *Appl. Catal. A-Gen.* 396 (2011) 91-100.
- [220] O.H. Hansteen, H. Fjellvag, B.C. Hauback, Reduction, crystal structure and magnetic properties of Co_{3-x}Al_xO_{4-δ} (0.0 ≤ x ≤ 2.0, 0.0 ≤ δ ≤ 1.0). Comparison with the Co/γ-Al₂O₃ Fischer-Tropsch catalyst, *Acta Chem. Scand.* 52 (1998) 1285-1292.
- [221] J.M. Zalc, D.G. Löffler, Fuel processing for PEM fuel cells: transport and kinetic issues of system design, *Journal of Power Sources* 111 (2002) 58-64.

- [222] D. Widmann, E. Hocking, R.J. Behm, On the origin of the selectivity in the preferential CO oxidation on Au/TiO₂ – Nature of the active oxygen species for H₂ oxidation, *Journal of Catalysis* 317 (2014) 272-276.
- [223] C.S. Polster, R. Zhang, M.T. Cyb, J.T. Miller, C.D. Baertsch, Selectivity loss of Pt/CeO₂ PROX catalysts at low CO concentrations: mechanism and active site study, *Journal of Catalysis* 273 (2010) 50-58.
- [224] E.D. Park, D. Lee, H.C. Lee, Recent progress in selective CO removal in a H₂-rich stream, *Catalysis Today* 139 (2009) 280-290.
- [225] M.J. Kahlich, H.A. Gasteiger, R.J. Behm, Kinetics of the Selective CO Oxidation in H₂-Rich Gas on Pt/Al₂O₃, *Journal of Catalysis* 171 (1997) 93-105.
- [226] S.H. Oh, R.M. Sinkevitch, Carbon-monoxide removal from hydrogen-rich-fuel-cell feedstreams by selective catalytic-oxidation, *Journal of Catalysis* 142 (1993) 254-262.
- [227] K. Liu, A. Wang, T. Zhang, Recent Advances in Preferential Oxidation of CO Reaction over Platinum Group Metal Catalysts, *ACS Catalysis* 2 (2012) 1165-1178.
- [228] A. Moscu, Y. Schuurman, F.C. Meunier, Recent progresses on the use of supported bimetallic catalysts for the preferential oxidation of CO (PROX), *Catalysis: Volume 28, The Royal Society of Chemistry* (2016) 237-267.
- [229] A. Wootsch, C. Descorme, D. Duprez, Preferential oxidation of carbon monoxide in the presence of hydrogen (PROX) over ceria-zirconia and alumina-supported Pt catalysts, *Journal of Catalysis* 225 (2004) 259-266.
- [230] O.S. Alexeev, S.Y. Chin, M.H. Engelhard, L. Ortiz-Soto, M.D. Amiridis, Effects of reduction temperature and metal-support interactions on the catalytic activity Pt/ γ -Al₂O₃ and Pt/TiO₂ for the oxidation of CO in the presence and absence of H₂, *Journal of Physical Chemistry B* 109 (2005) 23430-23443.
- [231] M.M. Schubert, M.J. Kahlich, H.A. Gasteiger, R.J. Behm, Correlation between CO surface coverage and selectivity/kinetics for the preferential CO oxidation over Pt/ γ -Al₂O₃ and Au/ α -Fe₂O₃: an in-situ DRIFTS study, *Journal of Power Sources* 84 (1999) 175-182.
- [232] S. Li, M. Jia, J. Gao, P. Wu, M. Yang, S. Huang, X. Dou, Y. Yang, W. Zhang, Infrared Studies of the Promoting Role of Water on the Reactivity of Pt/FeOx Catalyst in Low-Temperature Oxidation of Carbon Monoxide, *The Journal of Physical Chemistry C* 119 (2015) 2483-2490.
- [233] Q. Fu, W.-X. Li, Y. Yao, H. Liu, H.-Y. Su, D. Ma, X.-K. Gu, L. Chen, Z. Wang, H. Zhang, B. Wang, X. Bao, Interface-Confined Ferrous Centers for Catalytic Oxidation, *Science* 328 (2010) 1141-1144.
- [234] H. Xu, Q. Fu, Y. Yao, X. Bao, Highly active Pt-Fe bicomponent catalysts for CO oxidation in the presence and absence of H₂, *Energy & Environmental Science* 5 (2012) 6313-6320.
- [235] O. Pozdnyakova, D. Teschner, A. Wootsch, J. Kröhnert, B. Steinhauer, H. Sauer, L. Toth, F.C. Jentoft, A. Knop-Gericke, Z. Paál, R. Schlögl, Preferential CO oxidation in hydrogen (PROX) on ceria-supported catalysts, part I: Oxidation state and surface species on Pt/CeO₂ under reaction conditions, *Journal of Catalysis* 237 (2006) 1-16.
- [236] A. Trovarelli, Catalytic properties of ceria and CeO₂-containing materials, *Catal. Rev.-Sci. Eng.* 38 (1996) 439-520.
- [237] S. Johansson, L. Osterlund, B. Kasemo, CO oxidation bistability diagrams for Pt/CeO_x and Pt/SiO₂ model catalysts prepared by electron-beam lithography, *Journal of Catalysis* 201 (2001) 275-285.
- [238] R. Taha, D. Martin, S. Kacimi, D. Duprez, Exchange and oxidation of (CO)-O-16 on O-18-predosed Rh-Al₂O₃ and Rh-CeO₂ catalysts, *Catalysis Today* 29 (1996) 89-92.
- [239] T. Bunluesin, H. Cordatos, R.J. Gorte, Study of CO oxidation-kinetics on Rh/ceria, *Journal of Catalysis* 157 (1995) 222-226.

- [240] A.B. Kehoe, D.O. Scanlon, G.W. Watson, Role of Lattice Distortions in the Oxygen Storage Capacity of Divalently Doped CeO₂, *J. Am. Chem. Soc.* 23 (2011) 4464-4468.
- [241] O.H. Laguna, M.A. Centeno, M. Boutonnet, J.A. Odriozola, Fe-doped ceria solids synthesized by the microemulsion method for CO oxidation reactions, *Applied Catalysis B: Environmental* 106 (2011) 621-629.
- [242] H. Bao, X. Chen, J. Fang, Z. Jiang, W. Huang, Structure-activity Relation of Fe₂O₃-CeO₂ Composite Catalysts in CO Oxidation, *Catalysis Letters* 125 (2008) 160-167.
- [243] R. Kydd, D. Ferri, P. Hug, J. Scott, W.Y. Teoh, R. Amal, Temperature-induced evolution of reaction sites and mechanisms during preferential oxidation of CO, *Journal of Catalysis* 277 (2011) 64-71.
- [244] J.M. Christensen, D. Deiana, J.D. Grunwaldt, A.D. Jensen, Ceria Prepared by Flame Spray Pyrolysis as an Efficient Catalyst for Oxidation of Diesel Soot, *Catalysis Letters* 144 (2014) 1661-1666.
- [245] B. Schimmoeller, F. Hoxha, T. Mallat, F. Krumeich, S.E. Pratsinis, A. Baiker, Fine tuning the surface acid/base properties of single step flame-made Pt/alumina, *Applied Catalysis A: General* 374 (2010) 48-57.
- [246] D. Channei, B. Inceesungvorn, N. Wetchakun, S. Phanichphant, Kinetics Study of Photocatalytic Activity of Flame-Made Unloaded and Fe-Loaded CeO₂ Nanoparticles, *International Journal of Photoenergy* 2013 (2013) 9.
- [247] D. Li, W.Y. Teoh, C. Selomulya, R.C. Woodward, P. Munroe, R. Amal, Insight into microstructural and magnetic properties of flame-made gamma-Fe₂O₃ nanoparticles, *Journal of Materials Chemistry* 17 (2007) 4876-4884.
- [248] O.H. Laguna, M.A. Centeno, G. Arzamendi, L.M. Gandía, F. Romero-Sarria, J.A. Odriozola, Iron-modified ceria and Au/ceria catalysts for Total and Preferential Oxidation of CO (TOX and PROX), *Catalysis Today* 157 (2010) 155-159.
- [249] R. Shannon, Revised effective ionic radii and systematic studies of interatomic distances in halides and chalcogenides, *Acta Crystallographica Section A* 32 (1976) 751-767.
- [250] R. Strobel, S.E. Pratsinis, Direct synthesis of maghemite, magnetite and wustite nanoparticles by flame spray pyrolysis, *Adv. Powder Technol.* 20 (2009) 190-194.
- [251] A.J. Gröhn, M.L. Eggersdorfer, S.E. Pratsinis, K. Wegner, On-line monitoring of primary and agglomerate particle dynamics, *Journal of Aerosol Science* 73 (2014) 1-13.
- [252] H.K. Kammler, S.E. Pratsinis, P.W. Morrison Jr, B. Hemmerling, Flame temperature measurements during electrically assisted aerosol synthesis of nanoparticles, *Combustion and Flame* 128 (2002) 369-381.
- [253] M.V. Heitor, A.L.N. Moreira, Thermocouples and sample probes for combustion studies, *Progress in Energy and Combustion Science* 19 (1993) 259-278.
- [254] H. Torabmostaedi, T. Zhang, P. Foot, S. Dembele, C. Fernandez, Process control for the synthesis of ZrO₂ nanoparticles using FSP at high production rate, *Powder Technology* 246 (2013) 419-433.
- [255] G. Ertl, H. Knözinger, F. Schüth, J. Weitkamp, *Handbook Of Heterogeneous Catalysis*. 2, WILEY-VCH Verlag, Weinheim (2008).
- [256] S. Vemury, S.E. Pratsinis, Self-Preserving Size Distributions of Agglomerates, *Journal of Aerosol Science* 26 (1995) 175-185.
- [257] B. Daumann, H. Nirschl, Assessment of the mixing efficiency of solid mixtures by means of image analysis, *Powder Technology* 182 (2008) 415-423.
- [258] K.K. Akurati, A. Vital, J.P. Delleman, K. Michalow, T. Graule, D. Fetti, A. Baiker, Flame-made WO₃/TiO₂ nanoparticles: Relation between surface acidity, structure and photocatalytic activity, *Appl. Catal. B-Environ.* 79 (2008) 53-62.
- [259] M.L. Williams, *CRC Handbook of Chemistry and Physics*, 76th ed., CRC Press (1995).

- [260] T. Johannessen, J.R. Jensen, M. Mosleh, J. Johansen, U. Quaade, H. Livbjerg, Flame Synthesis of Nanoparticles, *Chemical Engineering Research and Design* 82 (2004) 1444-1452.
- [261] M. Minnermann, S. Pokhrel, K. Thiel, R. Henkel, J. Birkenstock, T. Laurus, A. Zargham, J.I. Flege, V. Zielasek, E. Piskorska-Hommel, J. Falta, L. Mädler, M. Baumer, Role of Palladium in Iron Based Fischer-Tropsch Catalysts Prepared by Flame Spray Pyrolysis, *J. Phys. Chem. C* 115 (2011) 1302-1310.
- [262] H. Lux, *Praktikum der quantitativen anorganischen Analyse*, J. F. Bergmann Verlag München, Berlin (1988).
- [263] R. Colmyer, Using nanoparticle oxides as supports for Cobalt based Fischer Tropsch catalysts, *Departement of chemical engineering, University of Florida, Gainesville* (2011).
- [264] C.K. Westbrook, F.L. Dryer, Simplified Reaction Mechanisms for the Oxidation of Hydrocarbon Fuels in Flames, *Combustion Science and Technology* 27 (1981) 31-43.
- [265] J. Birkenstock, R.X. Fischer, T. Messner, BRASS, The Bremen Rietveld Analysis and Structure Suite, Ver. 2.2 beta, in: <http://www.brass.uni-bremen.de/> (Ed.), University of Bremen (2010).
- [266] J.E. Benson, M. Boudart, Hydrogen-oxygen titration method for the measurement of supported platinum surface areas, *Journal of Catalysis* 4 (1965) 704.
- [267] P.B. Wells, Characterization of the standard platinum/silica catalyst europt-1. 5. chemisorption of carbon monoxide and of oxygen, *Applied Catalysis* 18 (1985) 259-272.
- [268] C.A. Schneider, W.S. Rasband, K.W. Eliceiri, NIH Image to ImageJ: 25 years of image analysis, *Nat Meth* 9 (2012) 671-675.
- [269] H.K. Kammler, L. Mädler, Characterization of fine dry powders, in: B. Lee, S. Komarneni (Eds.), *Chemical Processing of Ceramics*, CRC Press Taylor & Francis Groups, Boca Raton (2005) 233-266.
- [270] J.W. Tukey, *Exploratory Data Analysis*, Addison-Wesley Publishing Company Reading (1977).

Danksagung

„Die Dankbarkeit ist ein Gefühl, welches das Herz veredelt und bessert, wohlthätig für den, der empfängt, wie für den, welcher gibt.“

Adolph Freiherr von Knigge

Die vorliegende Arbeit entstand während meiner Tätigkeit als wissenschaftliche Mitarbeiterin am Institut für Werkstofftechnik (IWT) der Universität Bremen.

Herrn Prof. Dr. Lutz Mädler danke ich herzlich für die Anregung zu dieser Arbeit, für seine sehr geschätzte fachliche und persönliche Unterstützung während der Zeit meiner Promotion und darüber hinaus. Vielen Dank für das Eröffnen vieler Kontakte und Möglichkeiten, die mich als Person nachhaltig geprägt haben.

A special thanks to Prof. Dr. Degen for being my second reviewer.

Dank an meine Kollegen und Kolleginnen der Verfahrenstechnik am IWT für das Arbeitsklima, das mich jeden Tag wieder mit Freude zur Arbeit gehen lassen hat. Ein besonderer Dank geht an Lydia und Claudia für die Unterstützung über das Wissenschaftliche hinaus.

Dank an Prof. Dr. Bäumer von der Arbeitsgruppe für Angewandte und Physikalische Chemie und Dr. Melanie Minnermann für die erfolgreiche Zusammenarbeit auf dem Gebiet der Fischer-Tropsch Synthese. Melanie, ich freue mich, dass aus wissenschaftlicher Zusammenarbeit Freundschaft wurde.

Thanks to Dr. Jochen Dreyer und Prof. Wey Yang Teoh from the “School of Energy and Environment” at the City University of Hong Kong for the fruitful international cooperation and the frequent exchange.

Thanks a lot to Prof. Dr. Rose Amal and Dr. Yun Hau Ng for hosting me during my research stay at the “Particles and Catalysis Research Laboratory” (PartCat) at the University of New South Wales (UNSW) in Sydney.

Dank für die gute Zusammenarbeit geht auch an die Kollegen und Kolleginnen folgender Arbeitsgruppen der Universität Bremen:

Arbeitsgruppe von Prof. Dr. Thöming (Verfahrenstechnik der Wertstoffrückgewinnung), von Prof. Dr. Gesing (Chemische Kristallographie fester Stoffe), von Prof. Dr. Rosenauer (Kristallographie) und von Prof. Dr. Fischer (Electron Microscopy).

Dank an die Stiftung der Deutschen Wirtschaft (sdw), welche die finanzielle Grundlage für meine Promotion gelegt hat und meine persönliche Entwicklung durch ideelle Förderung, ein breites Netzwerk und entstandene Freundschaften bedeutend geprägt hat.

Dank an Sabine, Melanie und Glenn für die tatkräftige Unterstützung bei Wort und Grammatik.

Besonderer Dank geht an meine Familie und Tobias, dafür dass Ihr mich auf dem Weg zur Promotion begleitet und mir zu jeder Zeit zur Seite gestanden habt.

Studentische Arbeiten

„In der vorliegenden Arbeit sind Ergebnisse enthalten, die im Rahmen der Betreuung folgender studentischer Arbeiten entstanden sind:

The thesis further contains results that were generated during my supervision of the following master and bachelor theses:

Bachelor Thesis: Valentin Baric, In der Flamme synthetisierte TiO_2/Pt Nanopartikel für die photokatalytisch aktivierte Wasserspaltung, 2012

Master Thesis: Udo Schwientek, Synthese photokatalytisch aktiver Nanopartikeln im Doppel-Flammen-Sprüh-Pyrolyse Prozess, 2013

Bachelor Thesis: Niklas Jüngst, Experimentelle Studie zum Einfluss der Prozessparameter im Doppel-Flammen-Sprüh- Pyrolyse Prozess, 2013

Master Thesis: Nikolai Gulow: Experimentelle Studie über in der Flamme synthetisierte Mischoxid-Heterojunctions für die photokatalytisch aktivierte Wasserspaltung, 2013

Master Thesis: Desiree Rist, Exploration binärer Mischoxidphasen für die photokatalytische Wasserspaltung, 2015

Erklärung

Hiermit erkläre ich, dass ich die vorliegende Arbeit ohne unerlaubte fremde Hilfe angefertigt habe. Darüber hinaus habe ich keine anderen, als die von mir angegebenen Quellen und Hilfsmittel benutzt, sowie die den benutzten Werken wörtlich oder inhaltlich entnommenen Stellen als solche kenntlich gemacht.

Bremen, den

Henrike Großmann

Appendix

I. Experimental procedures

All experimental procedures are summarized in the following sections and linked to the related chapter. The experimental procedures are a reprint of the corresponding publications.

I.I. Experimental procedures for chapter 4.2 reprinted from ref. [4]

Catalyst preparation

The metal organic precursors for the FSP synthesis of either the pure oxides or the mixed $\text{CoO}_x/\text{Al}_2\text{O}_3$ powders are Aluminum-sec-butoxide (Alfa Aesar 95% purity) and cobalt naphthenate (Stream chemicals 53% in mineral spirits). In the latter case, a 10 wt. % loading of Co is prepared as a standard. Only for comparison, a catalyst with 50 wt. % Co on Al_2O_3 is also synthesized.

For the single flame process, 50 mL of Al-sec-butoxide in xylene and 4.6 mL of cobalt naphthenate dissolved in xylene (both 0.5 M by metal) are mixed in order to obtain 10 wt. % Co-loading. For the preparation of 50 wt. % Co Al_2O_3 catalyst, 43.1 mL of cobalt precursor (0.5 M by metal) are mixed with 50 mL of Al-sec-butoxide in xylene (0.5 M by metal). For each synthesis, a syringe pump delivers the liquid precursor at a rate of 5 mL/min using. The precursor atomization takes place using a two-phase nozzle. The precursor flow rate is 5 L/min O_2 and a constant pressure drop of 1.5 bar exists at the nozzle tip. A supporting CH_4 and O_2 premixed flame (1.5 L/min, 3.2 L/min) ignites the self-sustaining spray flame. The particle formation steps: gas phase reaction, nucleation, surface growth, coagulation and coalescence take place within the created flame environment. The combination of a vacuum pump and a glass fiber filter with a diameter of 257 mm helps to collect the synthesized particles [1].

In the double flame spray pyrolysis process (DFSP), 50 mL of each metal oxide precursor solution are individually sprayed through two independent nozzles with the standard flow rate of 5 mL/min and with the aerosol streams intersecting at a defined distance l . The nozzle distance d and the intersection angle α adjust the intersection distance l . Table 2 lists all important parameters. The metal ion concentration for the Al^{3+} flame is 0.5 M while the concentration of the Co^{2+} solution is 0.048 M. This results in an overall Co loading of 10 wt. %.

The synthesis of the pure cobalt oxide and pure alumina references samples in the SFSP set up uses Al-sec-butoxide and cobalt naphthenate, both dissolved in xylene with a concentration of 0.5 M by metal. In order to prepare a physically mixed catalyst the flame made CoO_x particles are subsequently dispersed in ethanol and ultrasonicated for 30 minutes. The addition of $\gamma\text{-Al}_2\text{O}_3$ (Alfa Aesar) as support follows until achieving a 10 % Co weight content. The mixture run through an ultrasonic treatment until all of the ethanol evaporates. For the careful stirring of the dried mixture, a spatula is applied and the following calcination takes place at 400°C for 4 h.

Catalyst Characterization

A FEI Tecnai F20 S-TWIN microscope operated at an accelerating voltage of 200 kV carries out the transmission electron microscopy (TEM) measurements for characterizing the as-prepared particles as well as the catalysts after FT reaction. A slow-scan CCD camera with an integrated Gatan Image Filter Model 2001 records the TEM and energy-filtered images (EF-TEM). The three-window method is the basis to acquire the EF-TEM maps. Energy dispersive X-ray (EDX) microanalysis determines the elemental composition of the nanoparticles (see [261] for further experimental details). The suspension of the powder sample takes place using ethanol and a 5 minutes long ultrasonic treatment. A droplet of the suspension is placed on a carbon coated copper grid.

Atomic absorption spectroscopy (AAS, Unicam 989QZ Zeeman Solaar) measures the cobalt metal content of the as-prepared samples. Before each analysis, about 5 mg of each sample digest with 200 mg of potassium hydrosulfate and 3 mL 5 % sulfuric acid as described in ref. [262].

Nitrogen adsorption-desorption isotherms (Brunauer-Emmett-Teller (BET) measurements) are recorded using a Quantachrome NOVA 4000e within a pressure range of P/P_0 between 0.01 and 0.99. Before the determination of the specific surface area of the sample starts, a 2 h outgas procedure at 200°C under vacuum takes place. The conduction temperature of the measurement is at a liquid nitrogen temperature of 77 K.

A Philips PW1800 diffractometer equipped with a secondary monochromator conducts the X-ray diffraction (XRD) measurements using Cu K_α ($\lambda = 0.154 \text{ nm}$) radiation. It records continuous scans in the 2θ range of 10° to 140° with an integration step width of $2\theta \sim 0.03^\circ$ and 15 s per step. The samples fill a circular Si-single-crystal sample holder with a diameter of 16 mm. With the help of a 50 wt.% mixture of the sample with crystalline ZnO the quantification of potential amorphous fractions of selective samples takes place.

A Shimadzu UV-Visible spectrophotometer UV-2600 equipped with an ISR-2600 plus two-detector and integrating sphere, conducts the Ultraviolet-Visible (UV-Vis) diffuse reflectance measurements of the as-prepared samples. Small amounts of each sample are pressed into sample holders filled with barium sulfate and reflection spectra are measured in the wavelength range between 200 - 800 nm in 2 nm steps.

Temperature programmed reduction (TPR) profiles are recorded for as-prepared catalysts using a Quantachrome CHEMBET-3000 instrument. To remove any traces of water before the analysis, a N₂ flow at 200°C purges 50 mg of each sample for 30 min. The experiment is performed with a gas mixture of 5 vol % H₂ in Ar at a flow rate of 60 mL/min. A thermal conductivity detector (TCD) monitors the hydrogen uptake, while the samples are heated from room temperature to 1000°C with a rate of 10°C/min.

Catalyst testing

The catalytic activity and selectivity measurements are performed in a fixed-bed reactor system described in ref. [263]. For each reaction experiment, 1 g of catalyst (10 wt. % Co) with agglomerate sizes up to 250 µm are diluted with glass beads (MO-SCI Corporation) of similar particles sizes (180-250 µm). In total, a catalyst bed volume of 8 ml is loaded in the stainless steel reactor (I_D = 11.8 mm). To check the reproducibility of the FSP synthesis, catalysts sprayed with the same intersection distance but obtained from different batches are tested in the FT reaction. An axially placed thermocouple which is directly in contact with the catalyst, helps to monitor and control the temperature inside the reactor. The temperature for the activation of the catalysts in a H₂-stream of 100 mL/min prior to the FT measurements is 500°C for 4 h. The conditions for the FT measurement are 230°C, 20 bar and a total flow rate of 62.5 mL/min (H₂/CO/N₂=6:3:1). N₂ is the internal standard in the experiments. Long-time tests of the catalytic performance (activity and selectivity) for each catalyst last up to 65 h on stream. A three-channel on-line gas chromatograph (Varian 450GC), equipped with two thermal conductivity detectors (TCD) and a flame ionization detector (FID) to quantify the reaction species, monitors the progress of the FT reaction. Two parallel Hayseep Q 80/100 mesh columns, each connected to a TCD, separate the permanent gases such as H₂, CO, CO₂, N₂, and CH₄. The third parallel channel with a CP Sil PONA CB column connected to the FID determines the hydrocarbon selectivity (C₁-C₈). Catalyst activity is defined as moles CO converted per gram Co-metal per second (cobalt-time yield (CTY)). Therefore, the CO/N₂ peak ratio in the stream before reaction is determined and compared with the different component-to-N₂ peak ratios of the gas stream leaving the reactor.

I.II. Experimental procedures for chapter 4.4 reprinted from ref. [5]

Catalyst preparation

The Pt-FeO_x-CeO₂ catalysts are synthesized using one respectively two conventional FSP nozzles. The FeO_x and CeO₂ synthesis takes either place separately in the SF setting, in certain cases decorated with 5wt% Pt with respect to the final catalyst weight. Mechanically grinding Pt-FeO_x powder and CeO₂ in an agate mortar in Ce to Fe ratio of 5:1 is the production step for the physically mixed sample (PM). In the DF setting the CeO₂ is synthesis in one and FeO_x decorated with Pt in the second flame. The intersection distance carries between $l = 18, 23$ and 33 cm, with an constant intersection angle $\alpha = 20^\circ$. Table 4 lists all samples notation and its synthesis parameter.

The liquid precursor for the synthesis of CeO₂ consists of 0.22 M cerium (III) 2-ethylhexanoate (49% in 2-ethylhexanoic acid, Strem Chemicals) dissolved in xylene (Aldrich), while that for the synthesis of FeO_x contains 0.044 M iron (III) 2-ethylhexanoate (52% in mineral spirits, Alfa Aesar) in xylene. The concentrations result in a Ce to Fe ratio of 5:1. The added platinum (II) acetylacetonate (95%, Aldrich) has an overall Pt concentration of 0.0107 M.

In all SF and the DF settings, delivers a syringe pump the liquid precursors at a rate of 5 mL min⁻¹. The nozzle atomizes the precursor with an O₂ gas flow rate of 5 L min⁻¹ and pressure of 1.5 bar at the tip. A supporting flame containing premixed CH₄ (1.5 L min⁻¹) and O₂ (3.2 L min⁻¹) ignites the dispersed precursor droplets. A glass fiber filter with a diameter of 257 mm collects with the aid of a vacuum pump the formed particles.

Catalyst Characterization

A Quantachrome NOVA 4000e records nitrogen adsorption-desorption isotherms (Brunauer-Emmett-Teller (BET) measurements) within a pressure range of P/P_0 between 0.01 and 0.99. Before the specific surface area is determined, an outgassing procedure at 200°C under vacuum takes place for 2 h. The measurement temperature is 77 K (liquid nitrogen temperature).

A FEI Titan 80/300 operating at 300 kV and equipped with a high-angle annular dark field (HAADF) detector us applied to record scanning transmission electron microscopy (STEM) images of the catalysts. Powder of each sample is dispersed on carbon-coated copper grids. In the conventional TEM mode, selected-area electron diffraction (SAED) patterns are obtained.

A Bruker D8 diffractometer equipped with a secondary monochromator records X-ray diffraction (XRD) pattern of the as-prepared catalyst powders. Cu K_α ($\lambda = 0.154$ nm) is the applied radiation source. The integration step width is $2\theta \sim 0.02^\circ$ combined with a

residence time of 5 s per step. To achieve a high resolution XRD of the DF 33 sample, a Philips PW1800 diffractometer, operating with a monochromatic Cu K α ($\lambda=0.154$ nm) radiation source, and primary and secondary soller slits and an aperture of 0.1 rad is applied. The step width is 0.04° with a measuring time of 18 s per step.

Temperature programmed studies are conducted in an AutoChem 2950 HP Chemisorption Analyzer (Micromeritics) equipped with an internal temperature conductivity detector (TCD) and MicroStar Mass Spectrometer (Micromeritics). Accurately weighed 20 mg of catalysts supported on quartz wool plug in a quartz U-tube are used in all experiments. For H $_2$ temperature programmed reduction (H $_2$ -TPR) the sample is first cooled to -80°C with aid of a CryoCooler (Micromeritics) under 50 mL min $^{-1}$ of Ar, followed by temperature ramping at 10°C min $^{-1}$ up to 800°C under 50 mL min $^{-1}$ of 5% H $_2$ /Ar.

Catalyst testing

Catalytic PrOx assessments are carried out in a glass tubular reactor (I.D. = 5 mm, GHSV = 7640 h $^{-1}$) filled with 20 mg of the as-prepared catalyst diluted in 0.4 g silicon carbide (Aldrich, 200–450 mesh particle size). Quartz wool plugs are used to support the catalyst beds. A K-type thermocouple is inserted into the middle of the packed catalyst bed. The exhaust gas is passed through an ice bath and analyzed by an online gas chromatograph (GC 2010, Shimadzu) equipped with a flame ionization detector (FID) and a temperature conductivity detector (TCD). Gaseous H $_2$ and O $_2$ are separated in the MXT-Msieve column (30 m, ID 0.53 mm, Restek) connected to the TCD detector, while CO, CO $_2$, and CH $_4$ are separated in the Rt-U-BOND column (30 m, ID 0.53 mm, Restek) connected to the methanizer and FID detector.

The inlet gas flows are controlled with calibrated mass flow controllers (Aalborg). Prior to each PrOx experiment, the catalyst is subjected to standard reduction under 50 mL min $^{-1}$ 10% H $_2$ /Ar at 200°C for 1 h. The PrOx is carried out under standard PrOx condition of 50 mL min $^{-1}$ of 1% CO, 2% O $_2$, 88% H $_2$ and balance He to give an O/CO ratio of $k = 4$. The CO conversion (C) and CO $_2$ selectivity (S) are defined as

$$C = \frac{CO_{in} - CO_{out}}{CO_{in}} \cdot 100 \quad (1)$$

$$S = \frac{CO_{in} - CO_{out}}{2(O_{2,in} - O_{2,out})} \cdot 100 \quad (2)$$

with the inlet flow rate CO $_{in}$, O $_{2,in}$ and outlet flow rate CO $_{out}$, O $_{2,out}$.

I.III. Experimental procedures for chapter 5.1 partly reprinted from ref. [3]

Temperature diagnostics

A conventional two-phase FSP nozzle as well as a double nozzle set-up provide the base for the experimental analysis of the temperature profiles. Pure xylene is supplied either in the single or in the double flame setting, adjusting an intersection distance of $l = 10$ and 20 cm. The centers of the FSP nozzles are located on the “nozzle level” (NL) and the intersection angle α amounts 20° . The standard flow rate of the syringe pump (KDS-100-CE, KDS Scientific) delivering the xylene, is 5 mL/min. The nozzle atomizes the xylene with 5 L/min of co-flowing O_2 at constant 1.5 bar pressure drop. A premixed supporting flame of 1.5 L/min CH_4 and 3.2 L/min O_2 ignites and stabilizes the spray flame.

A Fourier-transform infrared (FTIR) spectrometer (Bomem MB 155S) equipped with a deuterated triglycine sulfate detector records the emission and transmission spectra of the xylene flames. The wavenumber range of the measurements is $6500\text{--}500$ cm^{-1} at 32 cm^{-1} resolution and with the iris fully open (~ 1 cm beam diameter).

Fitting a blackbody Planck function using the hot CO_2 radiance spectra helps to obtain line-of-sight average flame temperatures [145, 252]. In the DF configuration, the temperature measurement is proceeds along the flame axis to the intersection point and then vertically upward along the center axis (dashed line in Figure 42). Moving a thermocouple (k-type; outer diameter: 0.5 mm) mounted on a computer-controlled 2D traverse unit, results in horizontal temperature profiles of the two xylene flames for both double flame configurations. The spatial temperature is measured in 1 mm steps at heights of 9.4 , 14.1 and 18.8 cm above the nozzle level (Figure 42) which correspond to flame intersection distances of 10 , 15 and 20 cm, respectively. In addition, vertical scans are conducted along the center axis (dotted line in Figure 42). The thermocouple rested for about 1 s at each location to achieve a steady temperature readout. The averages of three repeated thermocouple measurements are within an error of 5% . No correction for radiation or convection is applied to the data [253].

CFD Simulations

A mathematical model describing the spray and fluid dynamics of the xylene flames in the single and double FSP configurations is established and solved by a CFD method. Following Noriler et al., a two-phase Euler-Lagrange approach is chosen to describe the continuous gas phase and discrete liquid droplets, respectively [169]. The turbulence is modeled by the k-omega-SST two-equations Reynolds average Navier-Stokes model. Between the phases a two-way coupling with turbulent dispersion is used, while the

mass and heat interphase transfers of the vaporizing droplets are accounted by the Ranz-Marshall (1952) correlation to the Sherwood and Nusselt numbers. Radiation is described by the simple P-1 model considering a grey gas model. The Eddy Dissipation Concept (EDC) model describes the interaction between turbulence and chemistry, assuming that the reactions occur in the fine scale turbulent structures, where the reactants are homogeneously mixed. Simulation are carried out for flame settings of $l = 10$ and 20 cm and $\alpha = 20^\circ$. Compared to Noriler et al. describing a single flame set-up [169], two modifications are made: First, a fully three-dimensional hexahedral mesh (2.4 to 2.8 million cells) is used for the discretization of each domain, as the double flame configuration does not allow a two-dimensional approach. Second, the liquid fuel is changed: Instead of ethanol, xylene is used, employing, however, the kinetic rate of toluene [264] since a fundamental study of the combustion mechanism of xylene seems not been published yet. The temperature distributions are numerically evaluated along the flame and center axis for the SF and DF settings as well as at 9.4, 14.1 and 18.8 cm above the nozzle level. Additionally, the mixing characteristic of the gas jets is analyzed and defined with the fraction ratio, a dimensionless relation between arbitrary scalars released from each nozzle, following the established flow. This analysis can be related to nanoparticles trajectories, since they only follow and do not interfere with the gas flow (Stokes number $\ll 1$). The boundary of the mixing profile is defined by a limiting velocity (1% of the maximum velocity) for the jet region, disregarding any downward flow in the domain.

Particle synthesis

To investigate the degree of mixing in a deposited system a conventional FSP single nozzle and a double nozzle set-up are employed for synthesis of TiO_2 -supported Pt nanoparticles. Titanium(IV)-isopropoxide (Sigma Aldrich, >97 %) is diluted with xylene (VWR, 98.7 %) to 0.5 M Ti concentration. For the single flame (SF) experiments, platinum-acetylacetonate ($\text{Pt}(\text{acac})_2$, Strem Chemicals, 98 %) is added to yield a Pt content of 5 wt-% in the product powder.

The flame operates at the same standard conditions, already described for the flame diagnostics. Particles collection takes place 60 cm above the nozzle on glass fiber filters (Pall A/E Glass, \varnothing 25.7 cm) with the help of a vacuum pump.

In the double flame (DF) experiments, the precursor solution containing 5 wt-% Pt with respect to the final powder is dissolved in xylene separately and delivered to a second FSP reactor, that operates with the same flow rates as the first one. In the first set of experiments, the intersection angle is constant at $\alpha = 20^\circ$ while the intersection distances changes to $l = 10, 20$ and 35 cm. In the second set, the intersection angle varies ($\alpha = 10,$

20 and 37.5°) while the intersection distance is constant at $l = 10$ and 20 cm, respectively. For reference, pure unsupported Pt nanoparticles are collected by first operating only the TiO₂ flame to form a titania filter cake on the glass fiber filter and subsequently operating only the Pt-producing flame.

TiO₂ and WO₃ are chosen as model material to determine the mixing in aggregated systems because of the high difference in the atomic number of Ti and W (22 and 74, respectively). This results in a high z-contrast in TEM examination. Titan(IV)-isopropoxid (Sigma Aldrich, >97 %) dissolved as 0,288 M solution in xylene (VWR, 98.7 %) served as precursor for the TiO₂ synthesis. The WO₃ flame (tungsten carbonyl Strem Chemicals Inc., >99,9%) has a metal concentration of 0.1M and uses Tetrahydrofuran (THF) as solvent (Strem Chemicals Inc.). Before spraying the tungsten precursor solution is gently heated to 35 °C and stirred for 15 min to increase the solubility of the solid precursor. The investigation of three different double flame adjustments, with varying intersection distances l and intersection angles α includes the following parameter combinations: 1: $l = 20$ cm, $\alpha = 35^\circ$, 2: $l = 33$ cm, $\alpha = 20^\circ$ and 3: $l = 66$ cm, $\alpha = 10^\circ$. The fourth sample is a physical mixture (PM) of pure TiO₂ and WO₃ which are synthesized in a single flame, respectively. The mass ratio of the powders mixture is 1:1.

Particle characterization

The specific surface area (SSA) of the product powders is determined with the nitrogen adsorption method at 77 K (Quantachrome NOVA 4000e Autosorb). Powders degassing takes place for 2 h at 200°C in flowing nitrogen before recording a 5-point BET adsorption isotherm over a relative pressure range of 0.1-0.3. The analysis includes at least two samples produced with the same synthesis setting. The resulting average specific surface area is related to an average primary particle size, d_{BET} , assuming monodisperse spheres with a homogenous density of TiO₂ with $\rho_{\text{Rutil}} = 4.26 \text{ g cm}^{-3}$ and $\rho_{\text{Anatase}} = 3.84 \text{ g cm}^{-3}$: $d_{\text{BET}} = \frac{6}{\rho_p \cdot \text{SSA}}$. For the calculations of the BET equivalent diameter is the Pt mass fraction neglected [80, 168].

A Philips PW1800 diffractometer with secondary monochromator for pure Cu K_α radiation ($\lambda = 0.154 \text{ nm}$) and primary and secondary Soller slits with 0.1 rad aperture helps to determine the product powder crystallinity. The scan range of the X-ray diffraction is $2\theta = 20 - 60^\circ$ with a 0.02° step width and a retention time of 6 s per step. Rietveld refinement are the base to determine the phase composition and average crystallite sizes (BRASS program [265]), including the following structure models: TiO₂ anatase (ICSD # 172916); TiO₂ rutile (ICSD # 9161); Pt (ICSD # 77944).

For investigations of the Pt dispersion on the TiO₂ support H₂ and CO chemisorption is realized on a Quantachrome Autosorb-1. The sample reduction takes place for 2 h at 350°C in flowing hydrogen, followed by an evacuation procedure of 2 h at the same temperature [139]. Chemisorption is carried out at 35°C with 5 % H₂/ He applying the two isotherm bracketing method [255] in a pressure range of 250-712 mmHg. The definition of the Pt dispersion is the ratio of atoms accessible to H₂ to the total number of Pt atoms in the system assuming a stoichiometric factor (H/Pt) of 1 [266]. The measurements conducted in H₂ atmosphere are confirmed in a CO atmosphere, also assuming a stoichiometric factor (CO/Pt) of 1 [267].

A FEI Titan 80/300 microscope is applied to obtain TEM and scanning TEM (STEM) images as well as energy dispersive X-ray spectroscopy (EDX) measurements. To distinguish between different chemical elements based on the Z contrast, an HAADF (high-angle annular dark-field) detector is applied in the STEM analysis. For the dispersion of the powder before the deposition on a carbon-coated copper TEM grid, an ultrasonic treatment of 2 mg of product in 5 mL of ethanol is conducted for 10 min. A single drop of this dispersion is deposited on the grid

ImageJ is applied to determine a STEM-equivalent particle size is from the area of the particles in high resolution images [268]. The analysis includes 325 particles per sample, this number ensures the representative results of the Pt size distribution [269]. The illustration of the particle size distribution occurs using boxplots [270]. The box itself represents the lower quartile, the median and the upper quartile values. The lower and upper limits of the results (○), the arithmetic mean (×) and 1.5 times the standard deviation of the distribution (whisker) complete the boxplot.

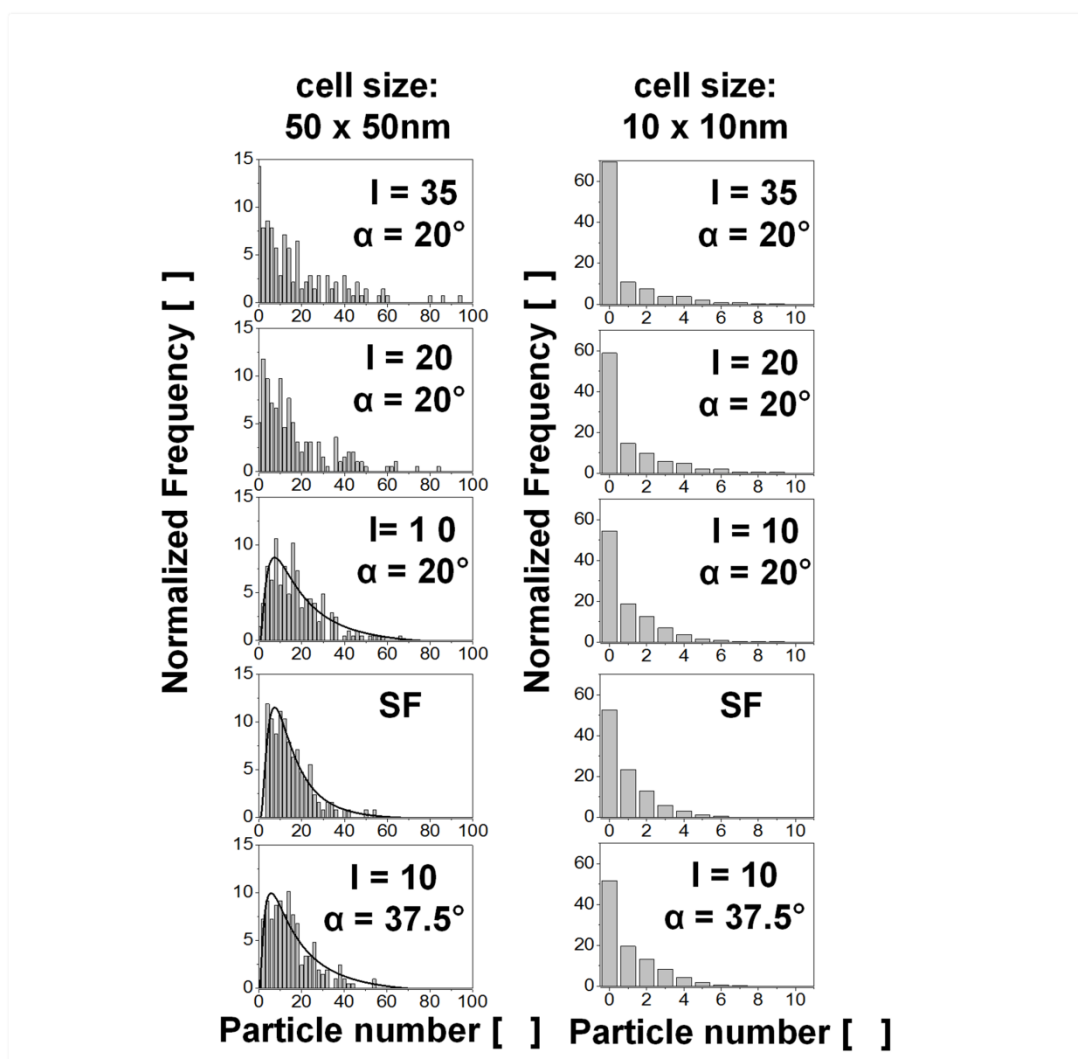
Experimental determination of the degree of mixing in deposited and aggregated systems

The quadrat method based on Rogers [103] forms the base for the determination of the degree of mixing between Pt and TiO₂ particles. This method was also applied and adjusted e.g. by Karnezis et al. characterizing the reinforcement distribution in composites [102] or Kim et al. for nanocomposites [70]. The first step of this method is the division of three or more STEM images of each investigated sample into at least 2000 cells of 10 nm x 10 nm as well as 100 cells of 50 nm x 50 nm. This step helps to evaluate the influence of cell size on the results. Here, a particle / support particle system is investigated, where the second component possess no continuous background, compared to the analysis of metal-matrix composite (MMC) materials [70]. This brings the challenge to distinguish between quadrat filled with TiO₂ support particles and empty quadrat. As a rule, only the Pt particles within cells covered to at least 75%

with TiO_2 are counted. The resulting Pt-distribution per quadrat is the base to examine the degree of mixing. Whereas a high degree of mixing represents a uniform Pt-particle dispersion over all TiO_2 particles and a low degree of mixing characterizes a non-uniform spread of Pt and TiO_2 particles. In addition to this, the variation coefficient v is used to quantify the degree of mixing [257]. The higher the variation coefficient, the higher is the percentage deviation from a defined target value of an ideal mixture. In this case the target value is defined as the average amount of Pt-particles per cell taking all investigated cells within an image into consideration. As an additional indicator, the ratio of empty cells (TiO_2 cells without Pt) to the total amount of counted cells is calculated.

To quantify the degree of mixing in an aggregated system an average of 40 aggregates and 1960 primary particles are examined per sample with respect to their mixing characteristic.

II. Additional material chapter 5.2:



Appendix 1: Spatial Pt particle distributions for the SF and DF setting based on analysis of STEM images with the quadrat method as a function of cell size (left: 50 x 50 nm and right: 10 x 10 nm). The frequency is normalized with respect to the evaluated number of cells per sample.

III. Additional material chapter 6:

Experimental and results CeO₂||ZrO₂:

The metallorganic precursors, cerium (III) 2-ethylhexanoate (49% in 2-ethylhexanoic acid) and zirconium butoxide (80% in butanol, Sigma-Adrich) were used for the synthesis of CeO₂ and ZrO₂. All the precursors were dissolved in xylene (99.95%, Strem) with a given concentration of the metal ions (0.116 M Ce³⁺, 0.097 M Zr⁴⁺). The liquid precursors were delivered to the nozzle tip using a syringe pump at a flow rate of 5 mL/min. The precursor solutions were combined with dispersant O₂ at a flow rate of 5 mL/min maintaining a pressure drop of 1.5 bar at the nozzle tip. Combustion of the dispersed droplets was initiated by the co-delivery of CH₄ and O₂ (1.5 L/min, 3.2 L/min) to form a flame. The Ce and Zr precursors during FSP were designed such that the mixture of CeO₂ and ZrO₂ are 50/50 by weight. Intersection distances for different flame angles and nozzle distances were derived using the flame geometry listed in Appendix Table 1.

Appendix Table 1:

Notation	Synthesis method	Weight ratio ZrO ₂ -CeO ₂	Intersection distance l [cm]	Intersection angle α [°]	SSA [m ² /g]
Ce Zr SF	SF	1 : 1	---	---	172
Ce Zr DF 15	DF	1 : 1	15	20	125
Ce Zr DF 22	DF	1 : 1	22	15	121
Ce Zr DF 26	DF	1 : 1	26	20	124
Ce Zr DF 34	DF	1 : 1	34	20	114
Ce Zr DF 51	DF	1 : 1	51	10	121

For the X-ray diffraction measurements, the Ce or Zr based nanoparticles obtained from FSP were loaded in a PANalytical X'Pert MPD PRO diffracting system, equipped with Ni-filtered Cu-K_α (λ=0.154 nm) radiation, 1/4° fixed divergence, primary and secondary Soller slit with 0.04 rad aperture, circular sample holder with 16 mm diameter, and X'Celerator detector (position sensitive in a range of 2.122° 2θ with 127 channels, yielding a channel width of 0.01671° 2θ), applying a continuous scan in the range of 15-100° 2θ and an integration step width of 0.0334° 2θ. The structural and microstructural parameters were extracted using Rietveld refinement by applying BRASS program [265]. Background, scale factor, unit cell parameters, Gaussian as well as Lorentzian peak widths

parameters were simultaneously refined followed by crystallite size and microstrain analysis. Finally, the crystal structures were refined to yield accurate positions of the metal atoms. As a starting point, the following structural models were used: CeO₂ (ICSD-157419) with cubic space group FM-3M and ZrO₂ (ICSD-66782) with tetragonal space group P42/nmc and ZrO₂ (ICSD-105553) with cubic space group FM-3M, respectively. The results are listed in Appendix Table 2. The present phases and the crystallite sizes indicating the formation of pure ZrO₂ and CeO₂ on particulate scale for all DF settings. The differentiation between mixing on particle and cluster scale is not possible using XRD.

Appendix Table 2:

Notation	Present phases	Phases [%]	Crystallite size [nm]
SF	Ce _{0.6} Zr _{0.4} O ₂	100	8.3
DF 15	t-ZrO ₂	41.78	20.8
	c-ZrO ₂	12.44	10.7
	c-CeO ₂	45.78	10.7
DF 22	t-ZrO ₂	43.17	20.8
	c-ZrO ₂	12.09	10.6
	c-CeO ₂	44.74	10.2
DF 26	t-ZrO ₂	41.44	21.2
	c-ZrO ₂	12.48	11
	c-CeO ₂	46.09	10.1
DF 34	t-ZrO ₂	42.56	20.5
	c-ZrO ₂	12.89	10.4
	c-CeO ₂	44.54	10
DF 51	t-ZrO ₂	42.9	20.9
	c-ZrO ₂	14.32	10.4
	c-CeO ₂	42.78	9.8